Optimum design for sustainable ‘green’ overlays **controlling flexural failure**

Lin, Yougui

Award date:
2014

Awarding institution:
Coventry University

Optimum Design for Sustainable 'Green' Overlays: Controlling Flexural Failure

By

Yougui Lin

May, 2014

Optimum Design for Sustainable ‘Green’ Overlays: Controlling Flexural Failure

By

Yougui Lin

May, 2014

A thesis submitted in partial fulfilment of the University’s requirements

For the degree of Doctor of Philosophy

ABSTRACT

The target of the 'Green Overlays' research was a cost effective, minimal disruption, sustainable and environmentally friendly alternative to the wholesale demolition, removal and complete reconstruction of the existing structural concrete pavement. The important problem of flexural resistance for strengthening concrete pavements with structural overlays has been scrutinised.

A new mix design method for steel fibre reinforced, roller compacted, polymer modified, bonded concrete overlay has been proposed. The mixes developed were characterized of high flexural strength and high bond strength with the old concrete substrate. '*Placeability'* and '*compactability'* of the mix were two dominant issues during laboratory investigation.

An innovative approach for establishing the relationship between Stress and Crack Face Opening Displacement for steel fibre reinforced concrete beams under flexure was developed. In addition, a new and simple method for calculating the interfacial Strain Energy Release Rate of both, a two-dimensional specimen and a three-dimensional model of the overlay pavement system were developed. This method can be readily and easily used by practicing engineers.

Finally, a new test specimen and its loading configuration for measuring interfacial fracture toughness for concrete overlay pavements were established. The interfacial fracture toughness of a composite concrete beam, consisted of steel fibre-reinforced roller compacted polymer modified concrete bonded on conventional concrete and undergoing flexure, was assessed.

In summary, this thesis presents four key findings:
A new mix design method for steel fibre-reinforced roller compacted polymer modified concrete bonded on conventional concrete.
A new method for establishing the fibre bridging law by an inverse analysis approach.
A new, simplified method for calculating strain energy release rate at the interface of a composite beam.
A new, innovative technique for calculating strain energy release rate at the interface of an overlaid pavement.
The thesis contains a plethora of graphs, data-tables, examples and formulae, suitable for future researchers.

Key-words: steel fibre-reinforced, roller-compacted, polymer-modified concrete, bonded concrete overlay pavement, mix design method, flexural strength, fibre bridging law, interfacial strain energy release rate, interfacial fracture toughness, beam on elastic foundation.

PREFACE

This thesis was part of the research project, "Optimum Design for: Sustainable 'Green' Overlays", funded by Engineering and Physical Sciences Research Council (EPSRC).

The supervisory team consisted by Dr John N Karadelis as director of studies, and Professor Peter Claisse as second supervisor.

During the progress of the research, two journal papers extracted from the research were published, are listed below. Paper marked with a "*" are presented in appendix.

*Lin, Y.; Karadelis, J.N.; Xu, Y.; 2013, A new mix design method for steel fibre-reinforced, roller compacted and polymer modified bonded concrete overlays, *Construction and Building Materials* 48 (2013) 333–341

Karadelis, J.N.; Lin, Y.; Olubanwo, A.; Xu, Y.; 2012, Sustainable bonded overlays for the repair and strengthening of concrete pavements, *Concrete*, Vol. 46, Issue 07, pp.34 – 36.

ACKNOWLEDGEMENTS

First, I would like to express my deepest gratitude and love to my wife Wei Pan.

I am very grateful to my director of studies Dr. John N Karadelis, and to my second supervisor Professor Peter Claisse, for their guidance and friendship during these four years.

I am also very grateful to my colleague Ms. Yi Xu for helping me with the laboratory work.

My special thanks to all the technicians of the Sir John Laing Building at Coventry University, Ian Breakwell, Terry and Kieran Teeling, Kieran Lehane and Steve Hutton.

The financial support of the Engineering and Physical Sciences Research Council (EPSRC), and Aggregate Industries, Ltd UK, is gratefully acknowledged. Special mention should also be made of Tarmac, AGS Mineraux, Power Minerals and Nippon Gohsei EU for providing materials for research.

TABLE OF CONTENTS

LIST OF FIGURES

LIST OF TABLES

ABBREVIATIONS

3PB = Three-point bend

4PB = Four-point bend

BCO = Bonded concrete overlay

CF = Cement stabilized aggregate foundation

Con.SBRPMC1.5%-35 = ID of a mix, indicating that the mix is conventional SBR modified concrete, reinforced with 35-mm length steel fibre with the content of 1.5% in volume faction, fabricated on vibrating table.

Con.SBRPMC0% = ID of a mix, indicating that the mix is the matrix of mix Con.SBRPMC1.5%-35, its mix proportion is the same as the mix Con.SBRPMC1.5%-35 except for no steel fibre addition, fabricated by vibrating table.

CMOD = Crack mouth opening displacement

$CMOD_a$ = Crack mouth opening displacement induced by applied load

$CMOD_b$ = Crack mouth opening displacement induced by fibre bridging traction

CRBCO = Continuously reinforced bonded concrete overlay

CTOD = Crack tip opening displacement or notch tip opening displacement

$CTOD_C$ = Critical crack tip opening displacement

CRCP = Continuously reinforced concrete pavement

ERR = Energy release rate

FE= Finite element

FEA = Finite element analysis

JPCP = Jointed plain concrete pavement

K_I = Stress intensity factor in opening loading (mode-I)

K_{IC} = Critical stress intensity factor or fracture toughness in mode-I loading

K_{II} = Stress intensity factor in sliding loading (mode-II)

K_{IIC} = Critical stress intensity factor in sliding loading (mode-II)

K_{IC}^{init} = Crack initiation toughness in Double-K model

M-P = Modified Proctor (compaction test)

M-VB = Modified Vebe test

MOR = Modulus of Rupture

MTK = Matakaolin

OPCC = Ordinary Portland cement concrete

OPCC-on-OPCC = A type of composite specimen: ordinary Portland cement concrete overlaid on ordinary Portland cement concrete base

PFA = Pulverised fuel ash

PMC = Polymer modified concrete

PMCBO = Polymer modified concrete bonded overlay

PMC-on-OPCC= A type of composite specimen: polymer modified concrete overlaid on ordinary Portland cement concrete base

PVA = Poly-vinyl Alcohol, a type of polymer in powder form.

PVA-MCM = PVA modified cement mortar

PVA-MCP = PVA modified cement paste

PVAPMC = PVA modified concrete

PVAPMC1.5%-35 = ID of a mix, indicating that the mix is roller - compacted PVA modified cement concrete, reinforced with 35mm-length steel fibre with the content of 1.5% in volume faction, consolidated by vibrating compactor.

RC = Roller compacted

RCC = Roller compacted concrete

RC-PMCBO = Roller-compacted polymer modified concrete bonded overlay

RF = Rubber foundation

SBR = Styrene Butadiene Rubber, a type of polymer in liquid form

SBR-MCM = SBR modified cement mortar

SBR-MCP = SBR modified cement paste

SBRPMC = SBR polymer modified concrete

SBRPMC1.5%-35 = ID of a mix, indicating the mix is roller compacted SBR modified concrete reinforced with 35-mm length steel fibre with the content of 1.5% in volume faction, fabricated by vibrating compactor.

SBRPMC0% = ID of a mix, indicating the mix is matrix of mix SBRPMC1.5%-35, its mix proportion is the same as SBRPMC1.5%-35 except no fibre addition, fabricated by vibrating compactor.

SBRPMC1.5%-50 = ID of a mix, indicating the mix is roller-compacted SBR modified concrete reinforced with 50-mm length steel fibre with the content of 1.5% in volume faction, fabricated by vibrating compactor

SCI = Structural conditions index

SFRC = Steel fibre-reinforced concrete

SFR-RC-SBRPMC = Steel fibre-reinforced roller-compacted SBR polymer modified concrete

SFR-RC-PMCBO = Steel fibre-reinforced roller-compacted polymer modified concrete bonded overlay

SFR-RC-SBRMC-BO = Steel fibre-reinforced roller-compacted SBR modified concrete bonded overlay

SFRPMC = Steel fibre-reinforced polymer modified concrete

SIF = Stress intensity factor

S-P = Standard Proctor (compaction test)

1 Introduction

Since the beginning of the 20th century concrete pavements have been one of the main structural materials in highways, streets and airfields. Concrete pavements can be technically classified into jointed plain concrete pavement (JPCP), and continuously reinforced concrete pavement (CRCP). A great number of concrete pavements need to be rehabilitated in the world every year. Asphalt overlays are currently popular in worn concrete pavement rehabilitation projects.

It is well known that asphalt overlays on existing concrete pavement do not constitute successful structures because serious reflective cracking would inevitably occur in asphalt overlay, leading to poor durability. Thus, in order to avoid the disadvantage of asphalt overlay, the old concrete pavement rubblization is currently widely used, such as in the USA, China, etc. However, the construction cost using rubblization technology is much higher than that of overlays because the additional courses, such as graded aggregate base, are necessary, so it seems to be economically unviable. Thus, it is natural to consider looking into the bonded concrete overlay which makes use of the remaining strength of the existing pavement.

Thus in order to avoid the disadvantage of asphalt overlay in the 1980's bonded concrete overlay (BCO) began to be experimentally used in concrete pavement rehabilitation, including the USA, Canada, Belgium and Japan (Delatte 1998). In the 1990's, more and more test projects of BCO pavements were constructed in the USA. Based on the accumulated achievements, since 2001 many BCOs have been successfully used in worn concrete pavement rehabilitation projects (Illinois Department of Transportation, 2002, 2005; NCPTC USA 2008). The BCOs were recommended to be used on worn JPCP. The BCOs are in structure characteristic of overlay joints being in alignment with those in existing JPCPs, and the width of overlay joints being equal to or greater than the width of underlying crack at JPCP.

The utilisation of BCOs can be more sustainable, environmentally friendly and cost effective than the complete removal and replacement of the old concrete pavement. Conventional concrete overlays bonded on old concrete pavements are increasingly gaining acceptance (Delatte 1998; Delatte and Sehdev 2003; Illinois Department of Transportation, 2002, 2005; NCPTC USA 2008). When being bonded together the key to success is to ensure the two composite structures –the overlay and the existing pavement - move as one structure under the action of thermal and vehicle loadings (NCPTC, USA 2008). BCO is intended to add life to existing concrete pavements. The design intent is for the BCO to bond fully with the existing concrete pavement, leading to a thicker composite section, a much stiffer pavement, and a considerable decrease in pavement stresses.

Although BCOs of concrete pavement have been successfully used in the USA, and become more and more popular, several disadvantages exist as follows: used conventional concrete mixes and slip-form paver lead to slow construction, causing long traffic disruptions; careful surface treatment of existing pavement, such as shot-blasting or water-blasting, is needed to achieve good bond, leading to higher costs.

Therefore, it is natural to consider using proper materials and construction methods to avoid these disadvantages mentioned above. The steel fibre-reinforced roller-compacted polymer modified concrete bonded overlay (SFR-RC-PMCBO) appears to be a reasonable material for avoiding the disadvantages; the reasons being as follows: Steel fibre in mix is intended to retard the reflective cracking; the polymer to achieve good bond with old concrete; and the roller compaction to achieve quick construction.

The SFR-RC-PMCBO pavement system may possibly fail in three modes: flexural failure, de-lamination failure and shear failure. The control to flexural failure is investigated by the author of this thesis.

In this research PMC (polymer modified concrete) overlay will be directly placed on the CRCP, and will not be sawed to joints. This may probably lead to serious reflection cracking in overlay due to the existence of numerous underlying cracks in old pavement. Therefore,

successful control of flexural failure and reflective cracking will be the key to the proposed overlay pavement structures.

Based on the analysis above, the research work focuses on:

(1) Developing mixes, which have high flexural strengths, high bond strength and high resistance to reflection crack, and also have the workability suitable to be placed by asphalt paver and compacted by roller.

(2) Studying experimentally the mechanical properties of mixes developed, including flexural strengths, fracture parameters, and so on.

(3) Establishing mechanical models for the composite structure on elastic foundation to simulate the steel fibre-reinforced roller-compacted polymer modified concrete bonded overlay pavement system.

In order to achieve the objectives above, mixes of high flexural strength and high bond strength, and at the same time displaying proper workability for placement by asphalt pavers and compaction by rollers, will be firstly developed; followed by extensive experiments for measuring mechanical properties; Finally, finite element analysis will be used to model the overlay pavement system by applying fracture mechanics and interface fracture mechanics, to analyse the strain energy release rate of interface between overlay and existing concrete pavements.

2 Literature Review

A bonded concrete overlay (BCO) pavement rehabilitation method is intended to add life to an existing concrete. The design intent is for the BCO to bond fully with the existing concrete pavement, leading to a thicker composite section, a much stiffer pavement, and a considerable decrease in pavement stresses.

In the 1980's, attempt was made to use BCOs in concrete pavement rehabilitation in the USA, Canada, Belgium and Japan (Delatte 1998). However, only parts of the projects were successful, and others failed at early stages (Delatte 1998). In the 1990's more and more test projects of BCO pavements were constructed in the USA. Based on cumulative achievements, since 2001 many BCOs have been successfully used in worn JCJP concrete pavement rehabilitation projects (NCPTC USA 2008). All the BCO materials were conventional concrete and constructed by employing slip-form pavers. Based on the BCO research achievements and construction experience the 'National Concrete Pavement Technology Centre (NCPTC) of the USA' published the 'Guide to Concrete Overlays' first edition in 2007, and second edition in 2008. This guide and the AASHTO 'Guide for Design of Pavement Structures' (1993, 1998) sufficiently provide a design and construction method for conventional concrete overlays. The BCO is in the structure characteristic of overlay joints in alignment with those in the existing concrete pavement, and the width of overlay joints is equal to or greater than the underlying crack width at the bottom of the existing joints. It is in the construction characteristic of the treatment of the surface of old concrete pavement to ensure the two structures, the overlay and the existing pavement, move as one structure under the action of thermal and vehicle loadings (NCPTC USA 2008).

Although BCOs of concrete pavement have been successfully used in the USA, several disadvantages still exist as follows: Used conventional concrete mixes and slip-form paver lead to slow construction, causing longer traffic disruption, Careful surface treatment of

existing pavement, i.e. shot-blasting and water-blasting, is needed to achieve good bond, leading to higher costs.

Roller-compacted concrete (RCC) has been widely used in pavement and dam construction. The USA code '*Guide for roller-compacted concrete pavements'* (NCPTC USA 2010) sufficiently provides the design and construction for RCC pavement usage. The main advantage of RCC pavement compared to other pavement structures is reduced cost and time for construction (ACI Committee 207 1999; NCPTC USA 2010). This is particularly suitable to worn pavement rehabilitation, because short traffic disruption is highly desired for old pavement repair. The rapid construction of RCC pavement is mainly attributed to the construction method, i.e. placement by asphalt paver and compaction by vibrating roller.

Recently Aggregate Industries (AI) and Coventry University have collaborated successfully to develop a polymer modified concrete (PMC) for pavement repairs, which is capable of being laid by an asphalt paver and compacted by a vibrating roller (Hughes 2006; Hughes and Karadelis 2007; Koutselas 2011). In order to eliminate the disadvantages of BCO as outlined above, and to use the very high flexural and bond strength, the roller compacted (RC) polymer modified concrete bonded overlay (PMCBO) appears reasonable, Firstly, slighter surface treatment of existing pavement seems feasible due to very high bond strength of PMC; Secondly, RC-PMCBO used in the pavements in fair and good conditions appears viable; Thirdly, it is worth an attempt not to saw cut joints of RC-PMCBO on continuously reinforced concrete pavements (CRCP).

These three changes, compared with those currently used in the USA, in materials and overlay structures, lead to extensive investigation being necessary.

2.1 Reflective Cracking of Overlay

Reflective cracking often occurs on overlays on old pavement rehabilitation; this usually leads to poor riding quality and poor durability. Controlling reflective cracking has been one of the main concerns in pavement overlay design and construction. Numerous cracks exist in

deteriorated concrete pavements, such as the construction joints and the aged cracks in jointed plain concrete pavement (JPCP), and the inherent contraction cracks in worn continuously reinforced concrete pavements (CRCP). The joints of JPCPs are typical of spacing of 400 - 500 cm, while the contraction cracks of CRCP are typical of spacing of 90 - 150 mm during normal service life.

A series of RILEM conferences on cracking in pavements (Scarpas et al. 2012) have clearly demonstrated that cracking constitutes one of the most detrimental, frequent and costly pavement deterioration modes. Reflective cracking in concrete pavements is usually caused by the stresses induced by both environmental loading and vehicular loading. In order to control reflective cracking on overlays, much effort has been made by both academic and engineering sides. Ryu et al. (2013) recently reported a test section of continuously-reinforced concrete bonded overlay (CRCBO) on deteriorated JPCP conducted in the USA, and stated that nine percent of existing underlying joints of old pavement reflected to overlay in twenty days after CRCBO placement. For the CRCBOs on worn CRCPs, reflective cracking on overlays occurred within a few years (NCPTC USA 2008).

Since reflective cracking in overlay in worn JPCP rehabilitation is inevitable, bonded concrete overlay is recommended to be saw-cut in coincidence with existing joints by a USA code (NCPTC USA 2008). However, saw-cut scheme is obviously not viable to overlay on CRCPs due to the presence of numerous inherent cracks.

The addition of steel fibre is able to greatly improve the flexural strength, particularly the residual strength after cracking. Hence, SFRC exhibits much higher fracture energy than plain concrete, which is a typical brittle material. The additional tensile stress offered by the steel fibre bridging across the crack resists further crack extension, so high fibre content and thick SFRC overlay may be able to control reflective cracking. Therefore, for the overlay on CRCP, steel fibre-reinforced RCC is an alternative and worth a trial.

2.2 Bond Strength

Interface of overlay pavements experiences normal and shear stress under the action of vehicular loading and environmental loading. As has been discussed previously, high flexural strength is targeted for overlay on CRCPs to obtain high resistance to reflective cracking. This may lead to the need of higher bond strength between overlay and existing pavements to ensure the overlay system behaves as a monolithic structure. The criterion of bond strength for ordinary Portland cement concrete (OPCC) overlay, which was obtained by direct testing in field or core samples taken in the field, may not be suitable for a high strength overlay system. Therefore, the mixes should be carefully selected to achieve high bond strength. Polymers seem to be able to fulfil the task.

The addition of polymer modifiers into concrete could greatly improve bond strength, freezing and thawing resistance, abrasion resistance, flexural and tensile strengths, and reduce permeability and elastic modulus (ACI Committee 548 2003; Ohama 1995; Ohama 1997). The polymers in common use are Styrene Butadiene Rubber (SBR) and Polyvinyl Alcohol (PVA) (Ohama 1997). During cement hydration, the polymer particles become concentrated in the void spaces at the beginning; and then continue to coalesce into a polymer film, resulting in a mixture or comatrix that coats the aggregate particles. (ACI Committee 548 2003).

The polymer SBR (Styrene Butadiene Rubber) has been widely used in the repair of concrete structures, in which SBR served as modifier and water reducer (ACI Committee 548 2003). Hughes and Lubis (1996) used a particular PVA to modify the cement mortar. High flexural strength and high bond strength with steel reinforcement were achieved using a small roller compactor in the laboratory. Details about the PVA product are not available in the paper. Jenni et al. (2005) investigated the PVA modified cement mortar and the adhesive strength between mortar and tiles. The two studies mentioned above indicated high bond strength was achieved using PVA modifier. However, the influence of the polymers on workability was not investigated in the two literatures.

So, it seems that the polymers SBR and PVA might be the proper additives to improve bond strength, and thus worth a trial.

2.3 Mixes for Roller-compacted Bonded Concrete Overlay

The constituents and proportion of RCC (roller compacted concrete) for pavements have been extensively investigated**.** The RCC mix designs are mainly focusing on determining the optimal water content. The methods currently available for determining optimal water content are the modified Proctor (M-P) compaction method (BS 1377-4:1990 2002; ACI Committee 211 2002), and the modified Vebe (M-VB) method (ASTM C 1170-06 2006; ACI Committee 207 1999), although they relate exclusively to plain RCC (without steel fibres).

Recently, Kagaya et al. (2001) carried out laboratory studies with steel fibre reinforced RCC, using the M-VB method. Neocleous et al. (2011) employed the M-P method to develop mixes containing recycled steel fibre reinforced in RCC pavements. However, the abovementioned mix design methods were for pavements resting on a sub-base or a sub-grade. The mixes of conventional RCC found to be very dry, and are adequately placed by asphalt pavers and compacted by vibrating rollers. However, dry mixes may lead to poor bond with existing concrete pavements. On the other hand, good bond could be achieved by using wet mixes due to wet paste sufficiently moistening the interface. So, it is necessary to properly define the mix workability, and in the meantime to search for appropriate ingredients and constituents to achieve good bond with substrate concrete.

For RCC bonded overlays in construction, mixes should be dry enough to be placed by pavers. However, it may well introduce problems while being placed by pavers due to the mix being 'lumpy'. Also, high water content will result in high water to cement ratio and hence low strength. Therefore, the appropriate workability of a RCC bonded overlay mix is defined in terms of "*roller compactability*" and "*paver placeability*", namely a mix with the appropriate workability should be suitable for roller compaction, whilst in the meantime, be viable to be placed by asphalt pavers. Therefore, it is deemed to be necessary to develop a new mix design method.

Mixes with poor workability during construction may result in poor quality concrete. Therefore, the selection of appropriate polymers is important to obtain the desired mixes satisfying the requirement of bond strength and workability. The workability of mixes for roller-compacted bonded concrete overlay, defined in terms of the placeability and compactability, may probably be sensitive to both water content and type of polymers. Some polymers in concrete matrix may deteriorate the mix workability, though they are favourable for bond strength. The combination of SBR and PVA in an adequate ratio, forming a hybrid polymer modifier, can be another good alternative for obtainment of high bond strength, whilst having appropriate workability.

It is clear that the constituent of ingredient materials and their proportion needed extensive experimental investigation, and a new mix design method needs development. This is a difficult assignment as the mixes need to comply with the requirements of high flexural strength and high bond strength with proper workability.

2.4 Flexural Strength of SFR-RC-PMC

The main advantage of steel fibre-reinforced concrete (SFRC) is the improvement in flexural strength in post-peak (Jenq and Shah 1986; Gopalaratnam et al. 1991; Banthia and Trottier 1995a; Banthia and Trottier 1995b), i.e. the toughness, and in fatigue life (Johnston and Zemp 1991; Sun et al. 1996; Paskova and Meyer 1997; Zhang and Stang 1998; Singh and Kaushik 2001).

Flexural performance of steel fibre reinforced concrete (SFRC) has been investigated since the 1980's (Jenq and Shah 1986; Gopalaratnam et al 1991; Banthia and Trottier 1995; Armelin and Banthia 1997; Lok and Pei 1998; Jeng et al. 2002; Neocleous et al. 2006; Denennam et al. 2011). A great number of articles are involved in flexural strength, residual flexural strength (toughness), crack propagation, fibre bridging law, fracture energy, and so on. Compared to plain concrete, the most important enhancement in adding fibre is the toughness of SBRC. The toughness is often characterised by residual strength, equivalent flexural strength and toughness indices (Altoubat et al. 2008; Jeng et al. 2002). Among the

definitions, the ASTM code (ASTM C 1609/C 1609M-06 2006) and British Standard (BS EN 14651:2005+A1:2007 2007) may be the most authoritative ones. The former uses a four-point bending test and the latter uses a three-point bending notched beam test.

For the structures subjected to cyclic loading, such as pavements, the service life is mainly dependent on the fatigue strength. Although the fatigue performance of SFRC has been extensively investigated (Johnston and Zemp 1991; Sun et al. 1996; Paskova and Meyer 1997; Zhang and Stang 1998; Singh and Kaushik 2001; Saleh et al. 2012), it has not been adopted in pavement design codes. For example, the design code for SFRC slab on ground proposed by ACI Committee 360R-92 (1997) does not consider the contribution to fatigue life by steel fibres.

Recently, Altoubat et al. (2008) conducted the test of full-scale SFRC slab on elastic foundation, and related the load carrying capacity to the equivalent flexural strength proposed by the Japan Society of Civil Engineers JSCE-SF4 (1984), and then proposed a simple design method for SFRC pavement. This approach may be an expedient method to incorporate the fibre effect since authoritative codes are not available.

However, all the aforementioned SFRCs are conventional concrete, the steel fibre-reinforced roller-compacted polymer-modified concrete (SFR-RC-PMC) has not been investigated yet to date. Therefore, the flexural performance of SFR-RC-PMC is necessarily investigated to provide mechanical parameters for pavement design.

Fibres become active after matrix cracking. Compared to plain concrete, the improvement in flexural performance of SFRC is mainly attributed to the tensile stress induced by fibre traction. The stress-crack face opening displacement relationship, called fibre bridging law, has been extensively investigated since the 1980's. Single fibre pullout test, aligned fibres pullout tests have been carried out to reveal the tensile stress provided by fibres in cracked bodies to better understand the role of fibres in concrete matrix (Stroeven et al. 1978; Baggott and Abdel-monem 1992; Li and Chan 1994). However, fibre pullout test (including single fibre and aligned fibres pullout test) cannot directly provide the tensile stress-crack opening

width relationship for prediction and design, and needs to be combined with the analysis of fibre content and length and aspect ratio and so on to offer bridging law (Jenq and Shah 1986; Armelin and Banthia 1997). For RCC, unlike conventional SFRC, both fibre implantation in dry mixes and dog-bone specimen formation for uniaxial tension are quite difficult. Thus it is ideal to use experimental results from beams under bending tests to obtain bridging law by inverse analysis.

Steel fibre in RCC may not be effective due to the lean cement paste compared to conventional SFRC. Poor efficiency of steel fibre may increase the fibre content to achieve the identical strength, leading to higher cost and poor workability. Kagaya et al. (2001) carried out laboratory studies with steel fibre reinforced RCC; and Neocleous et al. (2011) develop RCC mixes containing recycled steel fibre. However, the efficiency of steel fibre in RCC has not been investigated. The fibre bridging law may probably offer deeper insight into the efficiency of fibres in RCC.

2.5 Toughness of Interface

The interface of bonded concrete overlay pavement experiences normal stress and shear stress during normal service life. Tensile bond strength and direct shear bond strength may be used in fields for quality control during overlay construction. However, because stress distribution in the crack line at the vicinity of the crack tip varies greatly due to stress singularity at the crack tip, the strength-based criterion (tensile and shear bond strengths) method for evaluating interface fracture is no longer the appropriate approach.

Owing to the differences of modulus of elasticity and Poisson's ratio of the two layers, shear stress always exists in interface of overlay pavement system; moreover, stress intensity factor or strain energy release rate instead of stress is a proper parameter due to the singularity of stress at the vicinity of the crack tip. In reality, interface fracture mechanics has been used to evaluate interfacial fracture toughness since the 1990's. Büyüköztürk and Lee (1993) measured the interfacial fracture toughness of mortar-granite interface using four-point

bending test illustrated by Figure 2-1. Klingbeil and Beuth (1997) employed a four-point bending test to measure the interfacial toughness of two metal layers; Watanabe (2009) investigated interfacial delamination of mortar and ceramic tiles under shear loading; Shi et al. (2006) tested compacted mixed-mode specimens to measure interfacial toughness of adhesive joints; Lau and Büyüköztürk (2010) studied the interfacial toughness of cement/epoxy interface using four-point bending test.

Under the subjection to the symmetrical load (see Figure 2-1), the interfacial crack may symmetrically propagate in both side interfaces for those homogeneous materials, such as metal layer and cement mortar; however, the loading configuration may not be suitable for concrete overlay composite beams, due to the non-uniform bond of the interface.

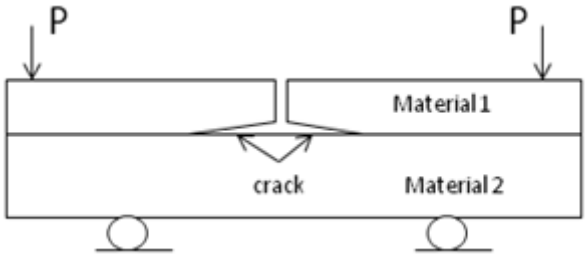

Figure 2-1 Four-point bending test for measuring interfacial toughness of bi-material

Therefore, it is necessary to develop a new loading configuration for measuring interfacial fracture toughness of overlay composite specimen. Consequently, the development of a new calculation method for obtaining interfacial toughness may be needed, due to that analytical solution for interfacial crack problem is usually not available.

2.6 Interfacial Toughness of Overlay Pavement System

General literature review by Ioannides (2006) presented the eighty years history of stress analysis of concrete pavements. Gaedicke and Roesler (2009) reviewed the state-of-the art application of fracture mechanics in concrete pavements, and pointed out that the lag time in usage of fracture mechanics is caused by several factors, one of them being the difficulty in developing simple fracture mechanic analysis for slabs. Ramsamooj (1999) presented a method for analysing stress intensity factors (SIF) K_I and K_{II} of cracks in infinite-length

concrete slab by combining FEA and general analytical solutions. Gotlif et al. (2006) analysed the SIFs of partial crack in concrete pavements. All the literatures aforementioned were about stress or SIFs in the single material. Jayawickrama and Lytton (1987) analysed SIFs K_I and K_{II} of overlay pavement system. Kazimierowicz-Frankowska (2008) analysed the stress ahead of a 1mm-width crack in the overlay pavement system, but did not consider the interfacial crack problems. It is clear that the method for calculating the energy release rate of interface in overlay pavements is not available to date.

2.7 Flexural Performance of SFRC Beams on Elastic Foundation

It is ideal to test full-scale concrete slab on elastic foundation to simulate the pavement system. However, the large scale test needs complicated experimental set-up, and is expensive. Analytical solution to load-deflection of cracked SFRC slab on elastic foundation is not currently available. Falkner et al. (1995) tested SFRC slab on cork and rubber subbase for simulating SFRC slab on subgrade to evaluate load bearing capacity by yield line theory, and employed ANSYS code simulating the load-deflection relationship; Belletti et al. (2008) performed the experiment of SFRC slabs, in which the SRFC slabs were laid on springs to simulate subgrade, and simulated the experimental results with a nonlinear fracture mechanics method by using ABAQUS code. Meda and Plizzari (2004) proposed a design method for SFRC slabs on the ground. Altoubat et al. (2008) conducted a test of full-scale SFRC slabs on subgrade to validate a design method for SFRC pavement.

Although a finite element code could successfully simulate cracked SFRC slabs on elastic foundation, it is not convenient to analyse the performance affected by fibre bridging law due to multiple cracking occurrences. Experiments of beam on elastic foundation are obviously more viable and much cheaper than full-scale slab. A beam on elastic foundation may be regarded as an approximate system for simulating slab, and the experiment may offer deeper insight into the mechanism of SFRC beam on elastic foundation, and moreover the mechanism of flexural behaviour may be revealed from the beam test.

Parmerter (1976), Parmerter and Mukherji (1975) proposed a method to calculate the bending moment on the cracked section and SIFs at the crack tip for un-reinforced beam on Winkler foundation, but the relationship of load-CMOD was not available in the literatures; moreover, to the author's best knowledge, it has not been experimentally verified. Olesen (2001) gave a closed-form solution to infinitely long SFRC beam on Winkler foundation by using a crack-hinge model and bilinear fibre-bridging law, but details are not available and this has not been experimentally validated.

Therefore, if the Winkler foundation model is suitable, Parmerter's theory needs to be verified and development of load-CMOD relationship is firstly needed for the simulation of the flexural performance. Furthermore, if the Winkler foundation model is not able to properly characterise the elastic foundation for SFRC beam, the finite element method may have to be employed to establish the load-CMOD relationship, because analytical solutions to cracked beam on elastic solid foundation is not available to date to the author's best knowledge (Gallagher 1983).

2.8 Thickness of Bonded Plain Concrete Overlay

The thickness of concrete pavements is currently determined by both loading stress analysis and empirical calibration. The most commonly used equation determining thickness of concrete overlay is that of the US Army Corps of Engineers', which was developed in the 1950's from full-scale accelerated traffic tests, and which takes the form (Kohn and Rollings 1988):

$$H_1^n = H_e^n - CH_2^n \qquad 2.1$$

where n=power to represent bond conditions between the base and overlay, H_1= thickness of overlay, H_e=thickness of equivalent new pavement to support the design traffic if no base pavement exists, H_2=thickness of base pavement to be overlaid, C=structural condition factor of the base pavement (1.00 for no or little structural cracking; 0.75 if some initial structural cracks but no progressive distress such as spalling and multiple cracking).

For fully bonded concrete overlay overlaid on the base pavement in good structural conditions, c=1.0, the equation becomes:

$$H_1 = H_e - H_2 \quad 2.2$$

Although a form of this equation has been found as far back as 1924 (Kohn and Rollings 1988), the original basis and derivation of the equation is uncertain; it is only an empirical equation without theoretical foundation, and ignores the fatigue effect of base pavements.

Fwa (1990) analyzed the AASHTO (1986) 'Code for Pavement Design' concept of remaining-life and then pointed out that it is fundamentally correct. However, the expression for the remaining-life factor used in its design equation is incomplete, and then derived a general expression for determining remaining-life factor of existing pavement, F_{RL}, for BCO the equation becomes:

$$H_1 = H_{e-} - F_{RL}H_2 \quad 2.3$$

For bonded plain concrete overlay, AASHTO (1993) provides the following equation for evaluating the thickness of bonded plain concrete overlays, which is still currently valid (National Concrete Pavement Technology Centre (NCPTC) USA 2008; Texas Department of Transportation USA 2011; Ryu et al. 2013):

$$\mathrm{D_{ol}} = \mathrm{D_f} - \mathrm{D_{eff}} \quad 2.4$$

where D_{ol} is the required thickness of BCO, D_f is the required thickness of concrete pavement equivalent new pavement to support the design traffic if no base pavement exists, D_{eff} is effective thickness of existing pavement, depending on the structural condition of existing concrete pavements.

The structural conditions index (SCI) and remaining life of existing pavement are key parameters in BCO pavement design and stress analysis. 'Guide to Concrete Overlays' (NCPTC USA 2008) provides a procedure of evaluating existing concrete pavement conditions, including coefficient of thermal expansion of concrete, FWD test, coring, strength of concrete and so on. Based on the evaluation an appropriate solution is determined.

In the UK, BCO has not been used in concrete pavement rehabilitations yet. The UK pavement design code 'Design Manual for Roads and Bridges' (The Highways Agency UK, 2006) provides a simple design method for new concrete pavement, and no concrete overlay design method is available.

However, the thickness design method for SFRC overlay is not available so far. For expediency, the equivalent flexural strength of SFRC proposed by Altoubat et al. (2008) may be used for the overlay thickness design.

2.9 Proposed BCOs of PMC Pavement Structures

It is seen that from the literature review above, continuously reinforced bonded concrete overlay (CRBCO) on worn JPCP and CRCP could not effectively retard the reflective cracking. Therefore, in this study, two types of bonded overlays for two types of worn concrete pavements are proposed. The overlay for worn JPCP rehabilitation, joints of overlay need to be saw cut in alignment with the existing underlying joints, therefore, the mix should contain polymer to obtain good bond with old concrete pavement. However, the addition of steel fibre is not necessary, and thus the mix is roller compacted polymer modified concrete (RC-PMC). For the overlay for CRCP rehabilitation, steel fibres should be incorporated in mixes to retard reflective cracking, and polymer is needed to obtain good bond strength; thus the mix is steel fibre-reinforced roller compacted polymer modified concrete (SFR-RC-PMC); The construction method for both overlays is the same, i.e. the mix is placed by asphalt pavers and compacted by vibrating rollers. Table 2-1 summarise the mix constituents and construction method, and Figure 2-2 illustrates the overlay pavement system.

This thesis will focus on the investigation of SFR-RC-PMC materials and their overlay on worn CRCP pavement systems.

Table 2-1 Proposed overlay structures for worn JPCP and CRCP rehabilitation

Old concrete pavement	Mix of overlay	Joint of overlay	Construction method
JPCP	RC-PMC	Joints of overlay in coincidence with underlying existing joints	Mix placed by paver, compacted by roller
CRCP	SFR-RC-PMC	No joints on overlay	Mix placed by paver, compacted by roller

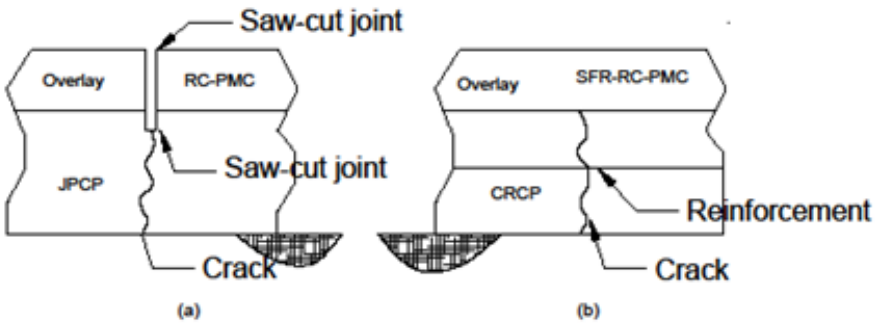

Figure 2-2 (a) RC-PMC overlay on old JPCP: saw-cut joints of BCO in coincidence with joints of underlying pavement; (b) SFR-RC-PMC overlay on old CRCP.

3 Methodology

The objectives were set up in the preceding Chapters 1 and 2. To achieve this goal, the methodology used in this study is as follows:

Firstly, mechanical experiment of ingredient materials, such as coarse aggregate and sand and polymers, will be first carried out for optimal selection of most appropriate materials; meanwhile constituents of mix will be experimentally investigated for the achievement of good bond strength and proper workability.

Secondly, the mix design method for bonded concrete overlay will be developed. For this purpose, the applicability of existing mix design method for RCC will be necessarily investigated. The development of a new mix design method appears necessary, because the expected mix workability for bonded overlays is quite different from conventional RCC. The mix workability, thus, needs to be properly defined.

Thirdly, flexural mechanical properties of SFR-RC-PMC developed will experimentally investigated. Based on the mechanical properties tested, flexural behaviour of beam under bending and on elastic foundation will be simulated to further reveal the mechanism of flexural performance.

Fourthly, PMC-on-OPCC composite beam will be experimentally studied to explore the interfacial delamination under flexure.

Theoretical analysis will follow after the experiments. The concrete fracture mechanics will be employed to simulate the process of crack propagation of beam under bending also, on elastic foundation; and interface fracture mechanics will be used to explore the behaviour of interfacial delamination of composite beam under bending with the aid of finite element analysis code, such as ANSYS. MATLAB programme for the establishment of fibre bridging law will be developed.

The following processes show the research procedure in a specific mode. Figure 3-1

demonstrates the research procedure based on the main objectives, as set in the Introduction. Figure 3-2 shows the additional work that had to be undertaken in order to achieve the principal aim.

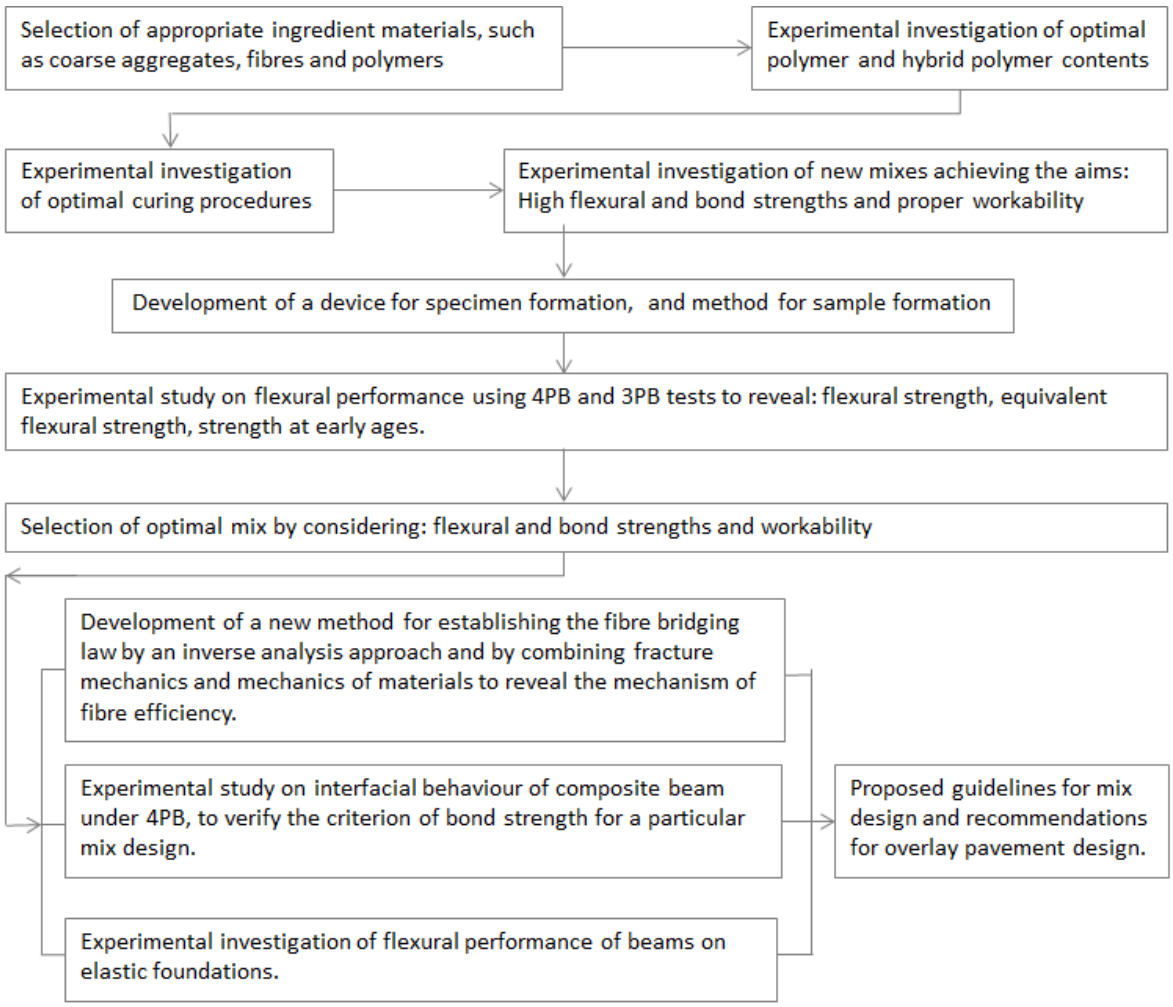

Figure 3-1 Research procedure for main objectives

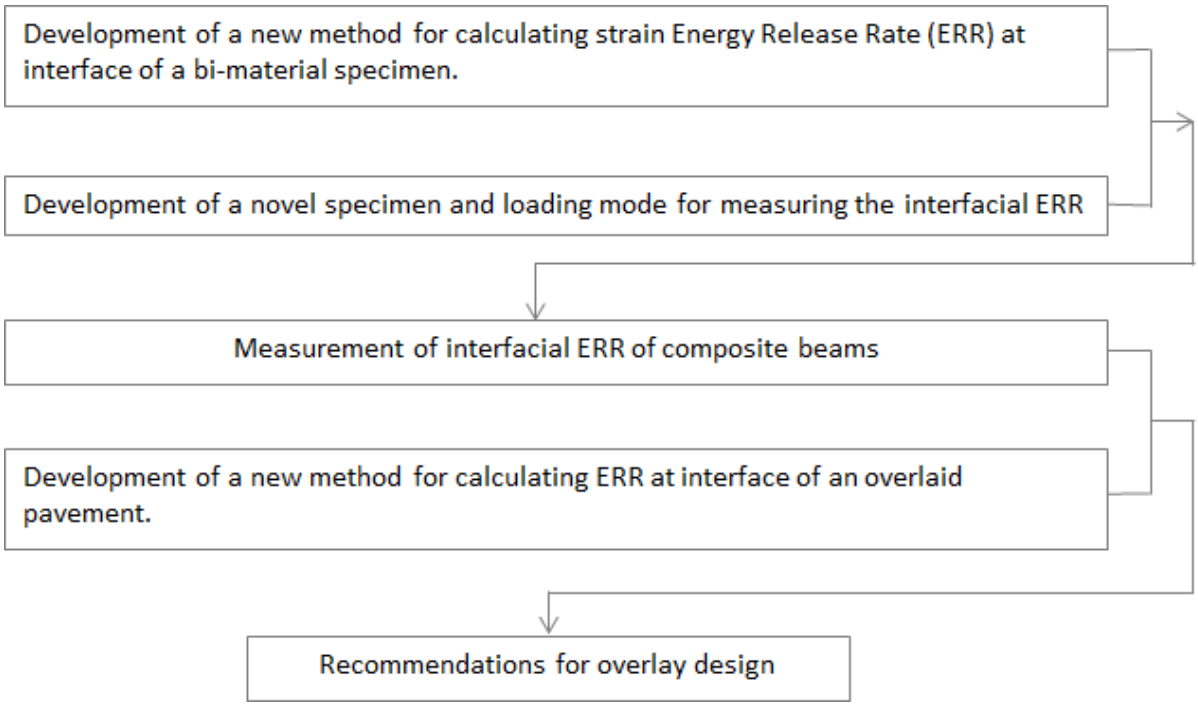

Figure 3-2 Research procedure for additional work

Following the methodology described above, the objectives will be achieved.

4 Optimum Design for Mixes

This research started from the selection of ingredient materials and mix proportion design. In this study, a variety of local materials were firstly experimentally investigated to select appropriate materials, and two types of polymers were tested and selected by comparing both mixes strength and workability. Design method for mixes suitable for asphalt paver placement and roller compaction, and high bond strength was then investigated, and finally specimen formation was experimentally studied.

4.1 Ingredient Materials Used

As discussed in Chapter 2, in order to achieve high flexural strength and high bond strength, the constituents of mixes studied incorporated steel fibre and polymers, in addition to the materials commonly used in conventional concrete.

Selection of coarse aggregates

The selection of aggregates used in this research was based on both strength and availability. Based on previous experience, two types of aggregate, grit-stone and granite-stone were selected to experimentally evaluate the strength in accordance with British standard (BS812-110.1990). Crush value tests were carried out complying with British Standard (BS812-110.1990). The experimental results were listed below:

The crush value of crushed grit-stone aggregate: 11.4%
The crush value of crushed granite-stone aggregate: 19.98%

It is obvious from the results that the grit-stone aggregate exhibited much higher strength than the granite-stone one; therefore it was selected for the present research. The various physical and mechanical properties of crushed grit-stone aggregate were tested in accordance with relevant British Standards, and the results are listed in Table 4-1 and Table 4-7, and illustrated in Figure 4-1.

Table 4-1 Gradation of crushed grit-stone aggregate

Cumulative passing by weight (%)				
14mm	10mm	6.3mm	4.75mm	4mm
100	92.86	16.36	3.25	2.41

Figure 4-1 Materials used

Fine aggregate (sand)

The fine aggregate used was natural river quartz sand (shown in Figure 4-1). Experiments for sieve analysis, water absorption and particle density (BS 812: Part 2: 1995) were carried out, and the experimental results are tabulated in Table 4-5 and Table 4-7. Among these tests, fineness modulus was determined as follows: fineness modulus is defined as 1/100 of the sum of the cumulative percentage retained on the sieves of the standard series: 150μm, 300μm, 600μm, 1.18mm, 2.36mm, 5.00mm and up to the largest sieve size used (Neville 1995). In this study, sand ratio is defined as sand (fine aggregate) to total aggregate (fine aggregate plus coarse aggregate) ratio by weight. The gradations of combined aggregates with sand ratio of 0.345, 0.4 and 0.5 are presented in Table 4-4. It is noted that the water absorption of sand was zero.

SBR (Styrene Butadiene Rubber)

Styrene Butadiene Rubber (SBR) was used to improve the bond strength of interface between overlay and old concrete substrate and enhance the flexural strength. The latex of SBR contained solid content of 46% and water content of 54% by weight, and PH was 8.5-9.0. The SBR can serve as polymer modifier and water-reducing admixture (ACI 548.3R-03 2003).

The water contained in SBR was taken into account in the determination of water-cement ratio in the following sections. SBR has been widely used as polymer modifier in cement concrete and cement mortar (Ohama 1995; ACI 548.3R-03 2003). The SBR used in the present research is pictured in Figure 4-1 and listed in Table 4-7.

Cement and PFA and Matakaolin

Cement and Pulverised Fuel Ash (PFA) and Matakaolin (MTK) used are illustrated in Figure 4-1. The physical properties and chemical compositions of cement, MTK and PFA, provided by the corresponding manufacturers are listed in Tables 4-2, 4-3, 4-6 and 4-7.

Selection of PVAs

PVA is the abbreviation of Polyvinyl Alcohol, a type of polymer in powder form. There are many different products of the PVA family. A particular PVA was used by Hughes and Lubis (1996) to modify cement mortar. High flexural strength and high bond strength with steel reinforcement were achieved using a small roller compactor in laboratory. Details about the PVA product, such as the specific name of the product and the manufacturer, are not available in the paper. In this study, two PVA products, GH-17S and NH-18S, were experimentally investigated. The experimental results indicated that the addition of NH-18S did not enhance the concrete bond strength and flexural strength. In contrast, the inclusion of GH-17S drastically improved the bond strength, and therefore, GH-17S was adopted for further extensive studies. The PVA used in the present research was white powder (Figure 4-1), and water soluble; manufactured by NIPPON GOHSEI.

Superplasticizer

The superplasticizer used was liquid and is shown in Figure 4-1, FOSROC AURACAST.400. It was used to reduce the water content in an effort to improve the flexural strength and bond strength. It is shown in Figure 4-1.

Table 4-2 Physical properties and chemical composition of Cement-I of Hanson Heidelberg of UK

Physical property	Chemical compound by weight (%)								
Loss on ignition	SiO_2	Al_2O_3	Fe_2O_3	CaO	MgO	SO_3	K_2O	Na_2O	Cl
3.30%	20.06	4.42	2.67	64.04	1.19	3.1	0.71	0.21	0.05

Table 4-3 Physical properties and chemical composition of PFA from Drax Power Station, UK

Physical Properties		Basic Oxide Composition (average by weight, %)						
Loss on ignition	Fineness	SO_3	CaO	MgO	K_2O	Al_2O_3	Fe_2O_3	SiO_2
4.80%	25.10%	0.77	2.8	1.5	3.1	24.7	8.8	51.2

Table 4-4 Gradation of combined aggregate (coarse aggregate and sand)

Sand ratio	Cumulative passing by weight (%)							
	14mm	10mm	6.3mm	4.75mm	2.36mm	1.18mm	600μm	300μm
0.345	100	95.32	45.21	37.53	30.35	28.28	23.65	3.81
0.4	100	95.72	49.82	41.95	35.19	32.78	27.42	4.41
0.5	100	96.43	58.18	51.63	43.99	40.98	34.28	5.52

Table 4-5 Physical properties of fine aggregate (sand)

Type of sand	Water absorption %	Particle density Kg/m³	Sieve analysis/ cumulative passing, % 4.75mm	2.36mm	1.18mm	600µm	300 µm	150 µm	75 µm
Quartz river sand	0%	2670	100	87.97	81.96	68.56	11.03	2.84	0.44

Table 4-6 Physical properties of metakaolin (MTK)

Physical Characteristics			Basic Oxide Composition (average by weight, %)					
Loss on ignition	Pozzolanic. Index (Chapelle test)	Specific area (BET)	TiO_2	CaO+MgO	Na_2O+K_2O	Al_2O_3	Fe_2O_3	SiO_2
1%	1100mg $Ca(OH)_2/g$	17m²/g	1.5	0.3	0.8	40	1.4	55

Table 4-7 Materials used and properties

Materials	Properties	Supplier/Manufacturer
Cement	Cement-I, 52.5N, specific density 3150 kg/m3	Hanson Heidelberg Cement Group,UK
Coarse aggregate(CA)	Crushed grit-stone, size 4.75 to 10 mm, impact value 12.9%, apparent particle density on oven dry 2790kg/m^3, particle density on saturated surface-dried basis 2770kg/m^3, water absorption 0.5%.	Tarmac Ltd, UK
Fine aggregate (FA)	Quartz river sand, apparent particle density 2670kg/m3, fineness modulus 2.476, water absorption 0%.	Coventry Building Supplies, UK
SBR	White liquid, solid ingredient content 46% by weight, water content 54%, specific density 1040kg/m^3.	Everbuild Building Products, UK
PVA	Polyvinyl Alcohol, GH-17S, white powder and water soluble, specific density 1250 kg/m^3.	NIPPON GOHSEI, Japan
Steel fibre-35	length 35 mm, hooked-end, rectangular section 0.45 mm×0.6 mm, tensile strength 1050MPa, aspect ratio 60.	Propex Concrete Systems Corp., UK
Steel fibre-50	length 50 mm, hooked-end, diameter 0.62 mm, tensile strength 1270MPa, aspect ratio 80.	Dramix, UK
MTK	Matakaolin, white powder, the specific density 2507kg/m^3, loss on ignition 1%, water demand (Mars cone) 900g/kg.	AGS MINERAUX, France
PFA	Pulverized Fuel Ash, powder, specific density 2090kg/m^3	Drax Power station, UK
Superplasticizer	Auracast 400, liquid, dark straw, specific density 1020kg/m^3.	Fosroc Ltd, UK

4.2 Optimal Design of the Dosage of SBR and PVA

In hardened cement paste, microcracks are induced by stresses such as those caused by evaporation of excess mixing water. Polymer modification helps in two ways: reducing the extent of moisture movement by blocking the passages and bridging the microcracks and restricting propagation by the polymer film (ACI Committee 548 2003). Excessive usage of polymers may be not only detrimental to flexural strength and workability but also not cost effective. The optimal dosage of polymers should be helpful for mixes achieving high flexural and bond strength, and at the meantime obtaining proper workability for placement by pavers and compaction by rollers.

The specimens for investigating were cubes of polymer modified cement paste and polymer modified cement mortar. The mix proportion and cube formation are presented below.

Curing procedure

The curing procedure used with polymer modified concrete (PMC) requires initial moist-curing to prevent plastic-shrinkage cracking, followed by air curing. The air curing should be considered as drying rather than curing. After initial moist curing, the latex particles at the surface coalesce into a film, preventing further moisture loss (ACI Committee 548 2003). The entrapped moisture hydrates the cement particles. The air curing process with PMC is necessary for the polymer to form films in the cement paste and between the cement paste and aggregates. Ohama (1995) recommended 2-day moist curing and five-day water curing followed by dry curing for SBR-modified cement concrete. The curing procedure recommended by ASTM Committee C-9 and C099.44 (1999) is to store specimens in a moist tank for four days and then move out to cure in air until testing date. The moist tank should be of temperature of 23 ± 2^0C and relative humidity higher than 95%.

It is noted that the ASTM (1999) moist curing procedure is for conventional PMC, which contains much more water than roller compacted concrete; in addition, concrete modified with different polymers may require slightly different curing procedure. In this study SBR

modified cement mortar (SBR-MCM) and PVA modified cement mortar (PVA-MCM) were tested to optimise the curing procedure. The mix proportion and mix parameters of the two mixes are listed in Table 4-8. The water-cement ratios of SBR-MCM and PVA-MCM were 0.206 and 0.261, respectively. These were similar to those of mix SBRPMC1.5%-35 and PVAPMC1.5%-35, whose water to cement ratios were 0.212 and 0.228, respectively. The mixing procedure was the same as polymer modified concrete (PMC) presented in Section 4.4.1. All specimens were cubes of 50 mm x 50 mm x 50 mm, and were fabricated by hammering due to their glue-like behaviour. After casting, the specimens were covered with polythene sheets to minimise moisture evaporation, and demoulded in 24h, and then taken through the following different curing procedures: (1) procedure-1: 3-day water curing and 24-day air curing, (2) procedure-2: 5-day water curing and 22-day air curing; (3) procedure-3: 7-day water curing and 20-day air curing; (4) procedure-4: 14-day water curing and 13-day air curing (for PVA-MCM). Figure 4-2 shows specimens in water curing and air curing. The cubes were tested in compression at the age of 28 days for compressive strength, and the results are tabulated in Table 4-9 and Table 4-10, and pictured in Figure 4-3.

(a) (b)

Figure 4-2 (a) specimens in water curing; (b) specimens in air curing

In this study, SBR content is defined as the ratio of SBR solid to cement by weight, while the PVA content is the ratio of PVA to cement by weight. The water in the column of 'mix proportion' listed in Table 4-8 is the added water not including the water contained in SBR, whereas the water to cement ratio is determined by the expressions shown below. The following eqns. 4.1 - 4.4 describe the definition of the parameters of mix proportions.

$$\text{SBR content} = \frac{\text{SBR}\times 46\%}{\text{Cement}} \times 100\% \qquad 4.1$$

$$\text{PVA content} = \frac{\text{PVA}}{\text{Cement}} \times 100\% \quad 4.2$$

$$W/C = \frac{\text{SBR}\times 54\% + \text{added water}}{\text{Cement}} \quad 4.3$$

$$\text{Superplasticizer content} = \frac{\text{Sup.}}{\text{Cement}} \times 100\% \quad 4.4$$

where *SB*, *PVA*, Cement and *Sup.* are the mass of SBR, PVA, cement and superplasticizer, respectively. Note that SBR used in this study contained 46% solid and 54% water by weight.

Table 4-8 Mix proportion of SBR-MCM) and PVA-MCM

Mix ID of PMM	SBR or PVA content	Mix parameter	Mix proportion
SBR-MCM	10%	SBRx46%=Cx10% (SBRX54%+W)/C=0.206	C:Sand:SBR:W= 1:1.26:0.217:0.0889
PVA-MCM	2%	W/C=0.261, PVA/C=2% Sup./C=1.5%	C:Sup.:Sand:PVA:W= 1:0.015:1.26:0.02:0.261

Table 4-9 Compressive strength of cubes of mix SBR-MCM (in Table 4-8) in various water curing times

Water curing time (days)		3	5	7	14	27
Compressive strength	Average	51.43	55.95	52.65	54.13	47.57
(MPa)	STDEV	5.32	1.35	1.7	4.96	1.19

Table 4-10 Compressive strength of cubes of PVA-MCM (in Table 4-8) in various water curing times

Water curing time (days)		3	5	7	14
Compressive strength (MPa)	Average	59.77	69.17	70.04	64.03
	STDEV	10.85	6.30	1.42	7.49

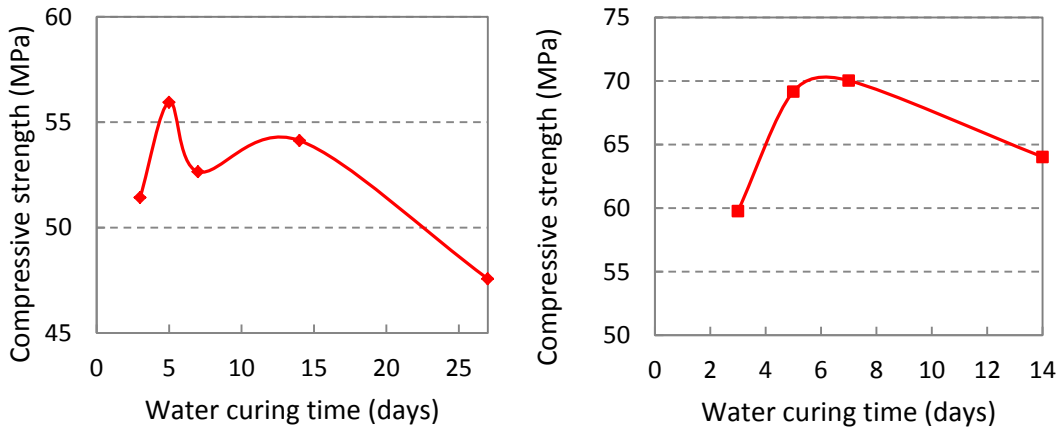

(a) (b)

Figure 4-3 Compressive strength of cubes of in various water curing time: (a) SBR-MCM; (b) PVA-MCM

It can be observed that 5-day water curing and 22-day air curing for SBR modified cement mortar (SBR-MCM), as well as 7-day water curing and 20-day air curing for PVA-MCM, are the most favourable for the two types of mixes. Thus the two curing procedures for SBR modified and PVA modified cement concrete and mortar were implemented in the following study.

Optimal Dosages of SBR and PVA

The optimum degree of SBR modification is usually achieved at 7.5 to 20% dry polymer solids by mass of cement in the mixture (ACI Committee 548 2003). The use of excess SBR is not economical, can cause excessive air entrainment, and lead to strength loss. The laboratory work conducted by the author indicated that the addition of PVA resulted in poor workability of the mix, the higher the PVA dosage the stickier the mix became. Even a low PVA dosage, such as 1% to 3%, markedly influenced the mix workability.

Based on the above, SBR modified cement paste (SBR-MCP) with dosage of 5% and 10%, and PVA modified cement paste (PVA-MCP) with dosage of 1% and 2% and 3% were tested to explore the relationship between cube compressive strength and polymer dosage. The mix proportion is shown in Tables 4-11, 4-12 and 4-13. It is noted that in the three tables C, SBR, PVA and W represent cement, SBR, PVA and water in mass, respectively. The water-cement ratio for all the mixes was 0.230, close to that used in mix SBRPMC1.5% (its water-cement ratio was 0.212) and PVAPMC1.5% (0.228). The former mix was steel fibre-reinforced roller-compacted SBR modified concrete, and the latter was steel fibre-reinforced roller-compacted PVA modified concrete. Both mixes were extensively investigated experimentally in the following chapters. The specimens were cubes with the dimensions of 50 mm x 50 mm x 50 mm. The specimen preparation and test procedure were the same as that described previously. The curing procedure for SBR-MCP was 5-day water and 22-day air curing; that for PVA-MCP was 7-day water and 20-day air curing. The cube compressive strengths tested at 28-day age are listed in Tables 4 - 11, 4 - 12 and 4 - 13, and plotted in Figure 4-4 and Figure 4-5.

Table 4-11 Mix proportion and compressive strength of SBR-MCP cubes with different SBR content

SBR conte.	Mix parameter	Mix proportion	Com. stren. (MPa)	Description
0%	W/C=0.230	C:W=1:0.230	76.19	5-day water curing, 22-day air curing. All paste behaved as glue.
5%	SBRx46%=Cx5% (SBRX54%+W)/C=0.230	C:SBR:W=1:0.109:0.171	63.74	
10%	SBRx46%=Cx10% (SBRX54%+W)/C=0.230	C:SBR:W=1:0.217:0.117	60.19	

Table 4-12 Mix proportion and compressive strength of PVA-MCP cubes with different PVA content

PVA content	Mix parameter	Mix proportion	Compressive strength (MPa)	Description
0%	W/C=0.230	C:W=1:0.230	76.19	7-day water curing, 20-day air curing. All paste behaved as glue.
1%	PVA=Cx1% W/C=0.230	C:PVA:W=1:0.01:0.230	72.5	
2%	PVA=Cx2% W/C=0.230	C:PVA:W=1:0.02:0.230	75.02	
3%	PVA=Cx3% W/C=0.230	C:PVA:W=1:0.03:0.230	60.81	

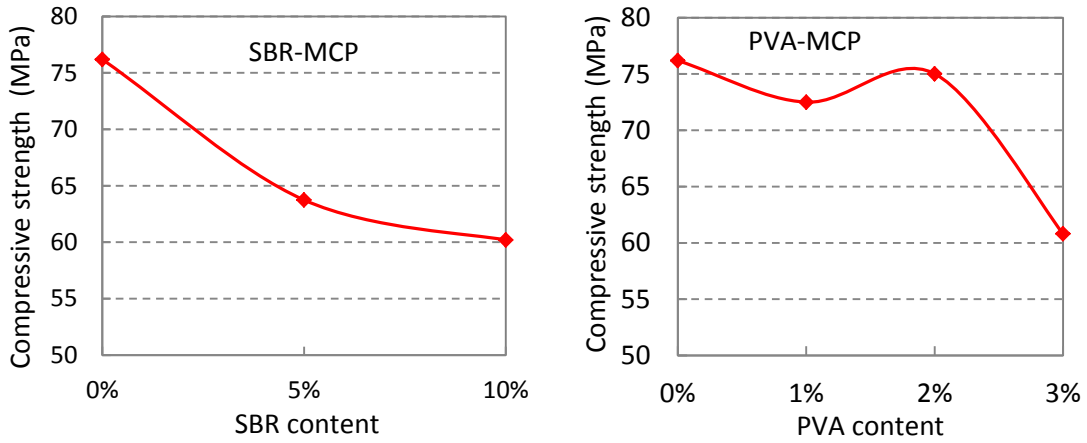

(a) (b)

Figure 4-4 (a) Compressive strength of SBR-MCP cubes with various SBR content; (b) Compressive strength of PVA-MCP cubes with various PVA content.

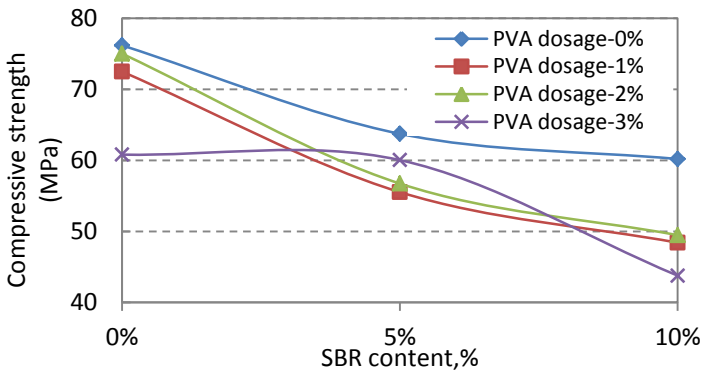

Figure 4-5 Compressive strength of SBR and PVA hybrid polymer modified cement paste cubes

Table 4-13 Mix proportion and compressive strength of cubes of SBR and PVA hybrid polymer modified cement paste

SBR conte.	PVA conte.	Mix parameter	Mix proportion	Compressive strength (MPa)
0%	0%	W/C=0.230	C:W=1:0.230	76.19
	1%	PVA=Cx1% W/C=0.230	C:PVA:W=1:0.01:0.230	72.5
	2%	PVA=Cx2% W/C=0.230	C:PVA:W=1:0.02:0.230	75.02
	3%	PVA=Cx3% W/C=0.230	C:PVA:W=1:0.03:0.230	60.81
5%	0%	SBRx46%=Cx5% (SBRX54%+W)/C=0.230	C:SBR:W=1:0.109:0.171	63.74
	1%	SBRX46%=CX5% PVA=Cx1% (SBRX54%+W)/C=0.230	C:PVA:SBR:W=1:0.01:0.109:0.171	55.53
	2%	SBRX46%=5%XC PVA=Cx2% (SBRX54%+W)/C=0.230	C:PVA:SBR:W=1:0.02:0.109:0.171	56.73
	3%	SBRX46%=5%XC PVA=Cx3% (SBRX54%+W)/C=0.230	C:PVA:SBR:W=1:0.03:0.109:0.171	60.04
10%	0%	SBRx46%=Cx10% (SBRX54%+W)/C=0.230	C:SBR:W=1:0.217:0.117	60.19
	1%	SBRX46%=CX10% PVA=Cx1% (SBRX54%+W)/C=0.230	C:PVA:SBR:W=1:0.01:0.217:0.083	48.41
	2%	SBRX46%=CX10% PVA=Cx2% (SBRX54%+W)/C=0.230	C:PVA:SBR:W=1:0.02:0.217:0.083	49.47
	3%	SBRX46%=CX10% PVA=Cx3% (SBRX54%+W)/C=0.230	C:PVA:SBR:W=1:0.03:0.217:0.0833	43.77

Analyses on the experimental results listed above led to the following conclusions:

(1) The addition of SBR markedly reduced the compressive strength of SBR-MCP. This is mainly attributed to air entrainment. Thus it seems that the dosage of 10% SBR is reasonable in this study for obtaining high bond strength.

(2) PVA-MCP appeared achieving the highest compressive strength in the PVA dosage of 2%. Meanwhile the mix with the PVA dosage of 3% became very sticky and difficult for placement and formation. Thus, the PVA dosage of 2% was adopted as optimum after considering both strength and mix workability.

(3) SBR-PVA hybrid modified cement paste was influenced by both SBR and PVA, the former mainly affected the compressive strength and the latter influenced the workability. The SBR-PVA hybrid polymer seemed unfavourable to both strength and workability. Therefore, based on the analyses above the SBR dosage of 10% and PVA dosage of 2% were adopted as optimum dosages in this study, and the concrete mixes with the optimal dosage were extensively investigated later. The SBR-PVA hybrid polymer (10%SBR+2%PVA) was only used to investigate the bond strength.

4.3 Mix Design Method

For roller compacted concrete used in pavements, optimal water content is one of main concerns for mix design. However the mix design method aiming at achieving both high bond strength and roller *compactability* is not available so far. In this section a method for determining optimal water content is proposed for steel fibre-reinforced, roller-compacted, polymer modified bonded concrete overlays. Two types of mixes suitable for asphalt paver placement and roller compaction were developed: They were the SBR and the SBR-PVA hybrid polymer modified cement concrete mixes with the optimal water contents determined by the proposed method. Both mixes achieved good bond with the old concrete substrate.

BCO can offer significant savings, since maximum use is made of the existing structural concrete pavement. However, the overlay has to provide adequate toughness, crack control, high flexural and bond strength and good resistance to fatigue. The constituents and proportion of RCC for pavements have been extensively investigated. The RCC mix designs are mainly focused on determining the optimal water content. The methods currently available for determining optimal water content are the modified Proctor (M-P) compaction method (BS 1377-4:1990 2002; ACI Committee 211 2002) and the modified Vebe (M-VB) method (ACI Committee 207 1999; ASTM C 1170-06 2006), although they relate exclusively to plain RCC (without steel fibres). Recently, Kagaya et al. (2001) carried out laboratory studies with steel fibre reinforced RCC, using the M-VB method. Neocleous et al. (2011) employed the M-P method to develop mixes containing recycled steel fibre reinforced

in RCC pavements. However, the above mentioned mix design methods were for pavements resting on a sub-base or a sub-grade but not applicable to bonded concrete overlays. In the present study a good bond between the overlay and the existing concrete pavement is the key to its success. Therefore, it is necessary to develop a new mix design method for steel fibre-reinforced, roller-compacted concrete bonded overlays. The method proposed in this study introduces an innovative approach in determining the optimal water content in RCC mixes when used as pavement overlays. Two types of mixes were developed to achieve good bond with existing concrete.

4.3.1 Mix Constituents, Workability and Design Criteria

Steel fibres and polymers, such as Styrene Butadiene Rubber (SBR) and Polyvinyl Alcohol (PVA), were selected to be included in the mixes to enhance the resistance of pavement to reflective cracking and ensure good bond with the existing concrete substrate. Hence the full name of mixes is 'steel fibre reinforced, roller-compacted, polymer modified, bonded concrete overlay'. It should be pointed out that the mix constituents of the SBR modified cement concrete (SBRPMC) used in this study were first considered by Koutselas (2011) in an earlier research programme, in which the types of aggregate, glass fibre, SBR, PFA (pulverized fuel ash) and MTK (metakaolin) were extensively investigated and carefully selected.

The physical properties of materials used are presented in Section 4.1. The focal point of the present RCC mix designs is the determination of the optimal water content. In order to simulate conventional concrete overlays on old concrete pavements in the laboratory, ordinary Portland cement concrete (OPCC) composite cylinders and blocks were first studied. They were fabricated and cured in water prior to testing. Their mechanical properties in 28-day age are listed in Table 4-14. The OPCC mix proportion in Table 4-14 was similar to that used in conventional bonded concrete overlays in successful, real pavement sites (Mokarem et al. 2007). Their tensile bond strength was reported equal to 1.65 MPa compared to our splitting tensile bond strength of 2.17 MPa. Thus, the OPCC-on-OPCC bond strengths

obtained, were selected to be the lower strength boundary for steel fibre-reinforced, roller-compacted concrete bonded overlay.

For RCC bonded overlays in construction, mixes should be dry enough to be placed by asphalt pavers and compacted by vibrating rollers. However, dry mixes may lead to poor bond with existing concrete pavements. On the other hand, good bond could be achieved by using wet mixes due to wet paste sufficiently moistening the interface. This, however, may well introduce problems while being placed by pavers due to the mix being 'lumpy'. Besides, high water content will result in high water to cement ratio and hence low strength. Therefore, the appropriate workability of a RCC bonded overlay mix is defined in terms of "*roller compactability*" and "*paver placeability*", namely a mix with the appropriate workability should be suitable for roller compaction and in the meantime, viable to be placed by asphalt pavers.

For conventional RCC, the mixes with optimal water content determined by the M-P and M-VB method are usually compacted with heavy duty vibratory rollers. However, materials such as soils, with optimum water content determined by the Standard Proctor (S-P) compaction test (BS 1377-4:1990 2002), are usually compacted with light rollers. Too wet mixes may not even be compactable by light rollers. This indicates that the mixes containing optimal water content determined by the S-P method are compactable using currently available rollers.

In addition, in practice concrete used in structural applications should be solid for durability reasons. This means that for RCC in the study, the compacted specimen with optimal water content should have no visible voids.

In general, mixes with appropriate water content for roller compacted bonded concrete overlays should satisfy the following criteria simultaneously: (1) the mix should not become lumpy during mixing and placing, rather, it should behave like a granular material for paver placeability; (2) the water content should not be higher than that determined by the S-P method for roller compactability; (3) the direct shear bond strength and splitting tensile bond

strength of PMC-on-OPCC should be at least equal to or greater than that of the OPCC-on-OPCC bond strength (4.09 MPa and 2.17 MPa, respectively); (4) the compacted specimens with optimal water content should have no visible voids.

Table 4-14 OPCC proportion and its mechanical properties

Quantities for 1 m³ concrete (kg)				Compres. Streng. of.cube (MPa)	Flexu. streng. In.4PB (MPa)	Direct shear strength (MPa)	Flexu. streng. of notch beam in 3PB (MPa)	Splitt. tensile strength (MPa)	OPCC-on-OPCC bond strength	
Cement-I	CA	FA	water						direct shear bond strength (MPa)	Split. tens.bond streng.(MPa)
402	1116	648	205	60.4	4.66	7.0	7.04	4.57	4.09	2.17

Note: (1) All cubes were: (LxWxH) ≡ (100×100×100) mm. All beams for flexural strength were: (LxWxH) ≡ (100×100×500) mm. Cylinders for direct shear and splitting tensile strengths were: (LxD) ≡ (200×100) mm. (2) Test procedures comply with the relevant British Standard. Test procedures for bond strength are presented in Section 4, in detail; (3) 4PB and 3PB are four-point bending test and three-point bending test, respectively.

4.3.2 Method for Determination of Optimal Water Content

The mixing procedure for polymer modified cement concrete is detailed in Section 4.4.1. The investigation started by utilising the following methods to explore the appropriate compaction effort: The S-P compaction method (BS 1377-4:1990 2002; 2.5 kg rammer; 300 mm dropping), the M-P compaction method (BS 1377-4:1990 2002; 4.5 kg rammer; 450 mm dropping) and the M-VB method (ASTM C 1170-06 2006; total weight of 22.7 kg of surcharge and plate). They were experimentally investigated and assessed by the abovementioned criteria. For an accurate validation of the results, the mixes employed in the study were varied in terms of steel fibre content (0% - 1.5% by volume fraction), SBR to cement ratio (solid ingredient, 3%-10% by weight), PVA to cement ratio (0% - 3% by weight) and dominant coarse aggregate size (10 mm and 14 mm). A modified method was later developed by adjusting the number of rammer drops for each layer, in order to obtain suitable compaction result, and hence the most favourable water content.

The moisture content w, wet density γ_w , dry density γ_D and air content□ were used to determine maximum dry density and optimal moisture content in the following section. The relationships used are presented below. The method of ASTM C:138/C 138M-01a 2001 was used to determine the sample density and air content.

$$w = \frac{W_T - A \times 0.5\%}{C+PFA+MTK+A+S+SBR \times 46\%+PVA+SF} \quad 4.5$$

$$\gamma_{D=\frac{\gamma_w}{1+w}} \quad 4.6$$

$$W_T = W_a + SBR \times 54\% \quad 4.7$$

$$\beta = \frac{\gamma_w}{C+PFA+MTK+A+S+SBR+PVA+Sp+W_a+F} \quad 4.8$$

$$\mathrm{V_{a1}} = \frac{C_1}{3150} + \frac{PFA_1}{2090} + \frac{MTK_1}{2507} + \frac{A_1 \times 1.005}{2770} + \frac{S_1}{2670} + \frac{SBR_1}{1040} + \frac{PVA_1}{1250} + \frac{Sp_1}{1020} + \frac{W_{a1} - A_1 \times 0.5\%}{1000} + \frac{SF_1}{7800} \quad 4.9$$

$$a = 100 \times (1 - V_{\mathrm{a1}}) \quad 4.10$$

$$\mathrm{W_e} = \mathrm{W_T}\text{-A} \times 0.5\% \quad 4.11$$

where for eqns.4.5 - 4.8: w is the moisture content (%); γ_w is the wet density (kg/m^3) determined by experiments; γ_D the dry density (kg/m^3); W_T the total mass of water (added water plus the water fraction contained in SBR) (kg); W_a is the added water mass (kg); C is mass of cement (kg); *PFA* is Pulverised fuel ash (kg); *MTK* is Metakaolin (kg); A is the Coarse aggregate (kg); S is Fine aggregate (kg); *SBR* is Styrene Butadiene Rubber (kg); *PVA* is Polyvinyl alcohol (kg), *Sp* is Super-plasticiser and *SF* is the Steel fibre (kg). Their values are listed in the Table 4-15 and Table 4-17.

For eqns.4.9 - 4.11: C_1, PFA_1, MTK_1, A_1, S_1, SBR_1, PVA_1, Sp_1 and SF_1 are the masses (kg) of cement, Pulverised fuel ash, Metakaolin, coarse aggregate, fine aggregate, Styrene Butadiene Rubber, Polyvinyl alcohol, super-plasticizer and steel fibre in 1 m^3 of concrete, respectively, which are determined by the values listed in Table 4-15 and Table 4-17 after multiplied by β. Numbers in the denominators of eqn.4.9 are densities of the corresponding materials shown in Table 4-7; a is air void content (%); V_{a1} is the total absolute volume of the component ingredients in 1 m^3 of concrete.

M-P method and M-VB method

All mixes employed in the compaction test are listed in Table 4-15. The quantities of materials in Table 4-15 should be regarded as proportions, rather than quantities for 1 m^3 concrete. Test procedures of M-P and M-VB methods complied with BS 1377-4:1990 and ASTM C 1170-06 2006, respectively.

Table 4-15 Mixes for various compaction methods

Mix ID	cement (kg)	PFA (kg)	MTK (kg)	CA (kg)	FA (kg)	SBR (kg)	total water (kg)	SF (kg)
M1	486	109	40	1053	554	31	variable	0
M2	486	109	40	1053	554	31		39
M3	486	109	40	1053	554	31		117
M4	635	0	0	964	643	138		0
M5	635	0	0	964	643	138		117

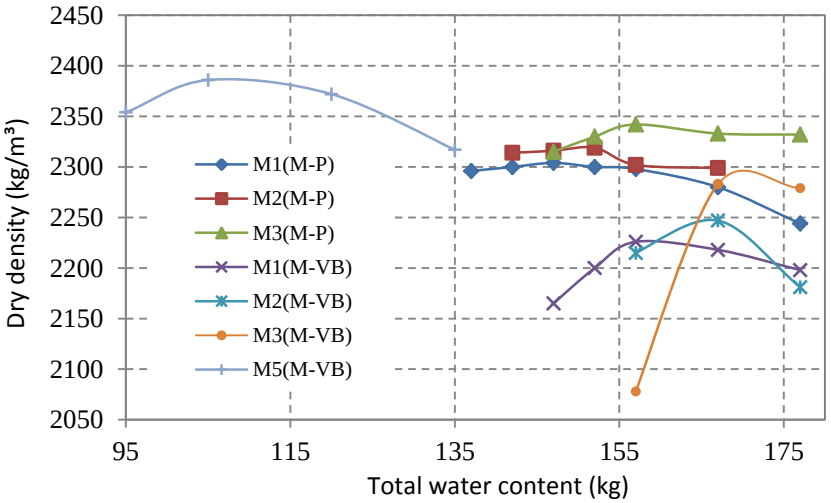

Figure 4-6 Relationship of dry density and total water by M-P and M-VB methods

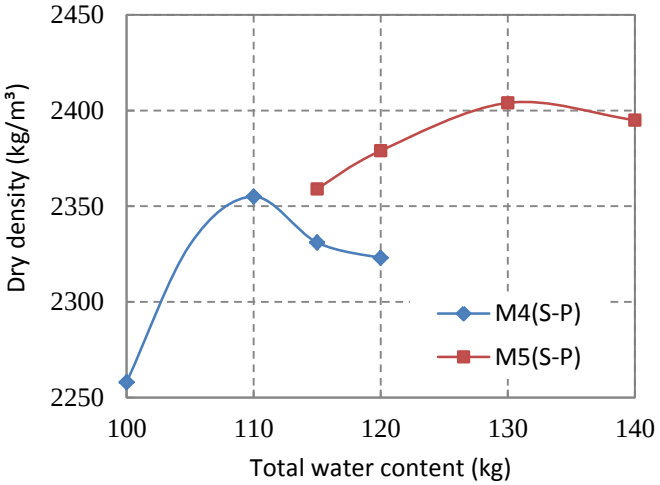

Figure 4-7 Relationship of dry density and total water content by the S-P method

The relationship between dry density and total water content by the M-P method and the M-VB method is plotted in Figure 4-6. The dry density - water content relationship follows a parabolic curve. The peak point of each curve in the figure represents a mix with the optimal water content determined by the maximum dry density using the specified method. Table 4-16 presents the maximum dry density, the corresponding wet density and air content, and the mix proportion with optimal water content. The added water contents are calculated accordingly, using eqn. 4.7. The mass of each ingredient in 1 m^3 concrete can be evaluated using the wet density and mix proportion listed in Table 4-16.

It is noted that the total water contents shown in Figures 4-6, 4-7, 4-9, 4-10 and 4-13 are not the water contents in 1 m^3 concrete.

(a) (b) (c) (d)

Figure 4-8 (a) devices for S-P(left) and M-P(right) methods, (b) compacted sample on balance, (c) M-VB tester, (d) container of M-VB and compacted sample by M-VB method

The experimental results demonstrated that for the same mixes, the M-P method results in lower optimal water content than the M-VB method. The experimental work disclosed that the mixes with the optimum water content determined by the M-P and M-VB methods were not lumpy during mixing, as expected. Hence, they met the requirements of roller compactability and paver placeability. However, for the mixes with optimal water contents determined by the M-VB method, a large number of voids were observed on the surface of the samples (see Figure 4-12(a)). This is also affirmed by the resulting air contents in Table 4-16. Obviously, the M-VB method is not an appropriate method, in terms of concrete durability.

The development of the PMC-on-OPCC composite specimen and the curing and testing methods are presented in Section 4.3.4. The direct shear bond strengths of mixes, the proportions of which (Table 4-16) were determined by the M-P and the M-VB method, are much lower than OPCC-on-OPCC bond strength (4.07MPa), as detailed in Figure 4-19, Figure 4-20 and Section 4.3.4. The laboratory work revealed that most composite cylinders of mixes determined by the M-P method developed voids at their interfaces. Nevertheless, the wet density of PMC samples, tested after the direct shear bond strength test, was close to the wet density derived in the M-P and the M-VB test, as listed in Table 4-16.

It is clear from the above that the mixes with the water contents determined by the M-P and M-VB methods are too dry, resulting in insufficient cement paste moistening the interface and hence low bond strength. Therefore, both approaches are not suitable for mix design for bonded RCC overlays.

It should be pointed out that the low bond strengths for the mixes, i.e. M1 (M-P), M2 (M-P) and M3 (M-P), M1 (M-VB), M2 (M-VB) and M3 (M-VB), were partially attributed to the low SBR content. However, the mix of M5 (M-VB), containing 10% SBR, with the optimal water content determined by the M-VB method, still produced lower direct shear bond strength and splitting strength than the corresponding strengths of OPCC-on-OPCC.

Table 4-16 Mix proportion determined by M-P and M-VB and M-L methods

Compaction method	Mix ID	Mix parameters			Mix proportion							
		max. dry density (kg/m^3)	wet density (kg/m^3)	air content (%)	cement	PFA	MTK	CA	FA	SBR	added water	SF
M-P method	M1(M-P)	2304	2446	1.62	1	0.224	0.082	2.167	1.14	0.064	0.267	0
	M2(M-P)	2319	2467	1.56	1	0.224	0.082	2.167	1.14	0.064	0.278	0.08
	M3(M-P)	2342	2492	2.34	1	0.224	0.082	2.167	1.14	0.064	0.288	0.241
M-VB method	M1(M-VB)	2226	2376	3.85	1	0.224	0.082	2.167	1.14	0.064	0.288	0
	M2(M-VB)	2247	2405	3.15	1	0.224	0.082	2.167	1.14	0.064	0.309	0.08
	M3(M-VB)	2280	2438	3.87	1	0.224	0.082	2.167	1.14	0.064	0.309	0.241
	M5(M-VB)	2386	2485	5.1	1	0	0	1.518	1.013	0.217	0.048	0.184
M-L method	M4(M-L)	2352	2454	2.92	1	0	0	1.518	1.013	0.217	0.056	0
	M5(M-L)	2424	2539	3.04	1	0	0	1.518	1.013	0.217	0.072	0.184

Standard Proctor compaction method

Since the mixes determined by the M-P and M-VB methods were deemed to be too dry, the S-P compaction method, which requires lower compaction effort, was investigated. According to British Standard (BS 1377-4:1990 2002), the S-P method requires rammer compaction in 3 layers and 27 blows for each layer. The mixes of M4 and M5 in Table 4-15, which contain solid SBR of 10% to cement by weight, were used to examine the suitability of the S-P method.

The relationship between dry density and total water content by the S-P method is illustrated in Figure 4-7. It is seen that the optimal water (total water) contents are 110 kg for mix of M4 (S-P) and 130 kg for mix of M5 (S-P), respectively. The corresponding mix of M5 (M-VB) value obtained by the M-VB method was 105kg. It is obvious that there is an increase in the optimal water content determined by the S-P method than that by the M-VB method. However, the two mixes, M4 (S-P) and M5 (S-P), with the optimal water content determined by the S-P method became lumpy during mixing, indicating that it was unsuitable for pavers. Hence this method is not an appropriate approach for mix design. The bond strengths of mixes with the optimal water content determined by the S-P method were not investigated because of the poor workability mix.

In civil engineering practice, materials with the optimal water content determined by the S-P method are usually suitable for light roller compaction. In this study the S-P method was employed and compared with the method proposed in the following section. It is envisaged that the appropriate roller compactor corresponding to the proposed method can be selected, based on the optimal water contents derived by both methods.

Modified light compaction method

Since the compaction effort of the M-P and the M-VB methods is too high, and that of the S-P too low, the optimal compaction effort should lie in the range between the M-P and the S-P compaction test. Here, the devices for the S-P compaction test with different compaction efforts were used, as follows: Five layers and twenty-seven blows per layer (5 x 27 blows), four layers and twenty-seven blows per layer (4 x 27 blows), four layers and twenty blows per layer (4 x 20 blows), three layers and twenty-seven blows per layer (3 x 27 blows, namely S-P method). The relationships of dry density and total water content for M5 (Table 4-15) by different compaction effort are illustrated in Figure 4-9. It was observed that dry densities

decrease with decreasing compaction effort. However, the optimal water contents increase with decreasing compaction effort. The compaction effort of 4 x 20 blows seemed to be appropriate because its optimal water content (120 kg) was close to that (130 kg) of 3 x 27 blows (S-P method), and the mix did not become lumpy during mixing.

M4 (Table 4-15) was used to confirm the hypothesis by employing both the compaction effort of 4 x 20 blows and the 3 x 27 blows (S-P method). The dry density versus total water content is plotted in Figure 4-10. It was found that the optimal water content (total water content) determined by 4 x 20 blows is 110 kg, the same as 3 x 27 blows (S-P method).

The above two paragraphs indicate that the mixes M4 and M5, with optimal water content determined by 4 x 20 blows, are suitable for "roller compactability" for light rollers. The laboratory observation showed that M4 with the water content of 110 kg, and M5 with the water content of 120 kg, behaved as a granular material, suggesting that they were suitable for "paver placeability".

The method with 4 x 20 compaction effort using S-P devices is named as modified light (M-L) compaction method. It had been experimentally verified for "roller compactability" and "paver placeability" by varying the mix ingredients as presented in the following section. The direct shear bond strength and splitting tensile bond strength of PMC-on-OPCC composite specimens of M5 (M-L) are illustrated in Section 4.3.5. From Figure 4-19 and Figure 4-20, the direct shear bond strength and the splitting tensile bond strength of M5 (M-L) were measured to be 5.47 MPa and 2.21 MPa, respectively, higher than the OPCC-on-OPCC bond strength.

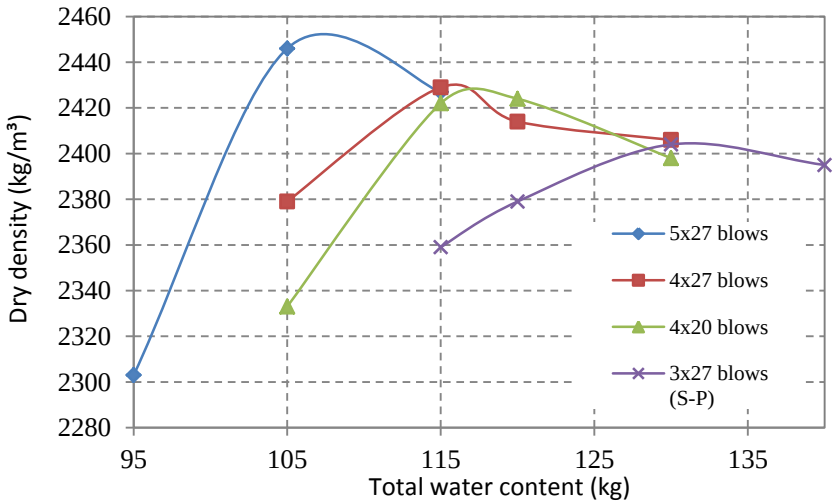

Figure 4-9 Dry density vs. total water content of M5 (Table 4-15) by different compaction efforts

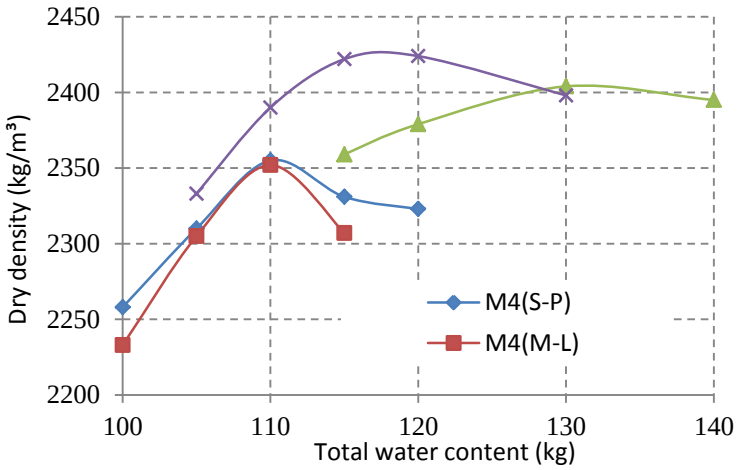

Figure 4-10 Dry density vs. total water content of M4 and M5 (Table 4-15) by the S-P and M-L methods

4.3.3 Experimental Verification for M-L Method

The M-L compaction method proposed above was experimentally verified for "roller compactability" and "paver placeability" by employing nine mixes using 4.75 mm – 14 mm size aggregate, super-plasticizer, sand ratios of 40% and 50% and different types of polymers (SBR, PVA and SBR-PVA hybrid polymer). The nine mixes are listed in Table 4-17.

In addition to the mixes listed in Table 4-17, the M-L method was first verified by using the mix of M5 (Table 4-15) but with maximum aggregate size of 14 mm. The optimal water content (total water content) was 115 kg. The behaviour of the mix was granular, not lumpy. This proved that the M-L method is suitable for mixes with maximum aggregate size 14 mm.

It should be noted that the PVA (GH-17S) and superplasticizer dosages are defined in terms of cement ratio by weight, while for SBR is defined as the solid ingredient to cement by weight. The mixes for verification contained different dosages of PVA and SBR-PVA hybrid polymer and superplasticizer, and different sand ratios, as listed in Table 4-17. The experimental results, namely the relationships between dry density and total water content are plotted in Figure 4-13. The maximum dry density, the corresponding wet density, air content and the mix proportion having optimal water content are listed in Table 4-18. The ingredient quantity for 1 m3 concrete can be evaluated easily by the wet density and mix proportion in Table 4-18.

Table 4-17 Mixes for verifying M-L compact method

Mix ID	Cement (kg)	CA (kg)	FA (kg)	SBR (kg)	PVA (kg)	Plasticizer (kg)	Total water (kg)	SF (kg)
M6	635	964	643	138	6.35	0	variable	117
M7	635	964	643	138	12.7	0		117
M8	635	964	643	138	19.05	0		117
M9	635	804	804	138	0	0		0
M10	635	804	804	138	0	0		117
M11	635	804	804	138	12.7	0		117
M12	635	804	804	0	6.35	9.53		117
M13	635	804	804	0	12.7	9.53		117
M14	635	804	804	69	12.7	0		117

The laboratory investigation showed that the mixes containing PVA were sticky. The more PVA used, the poorer the workability became. With 3% added PVA, the M8 was considered too sticky to be spread and placed by asphalt pavers, while the remaining eight mixes in Table 4-17 with the optimal water content determined by the M-L method appeared to behave as granular materials during mixing and processing and were deemed to meet the requirements of "roller compactability" and "paver placeability".

In addition, the compacted samples of the above nine mixes with optimal water content were solid, with no visible voids observed, indicating that the mixes met the durability requirements. Six compacted samples, mixes M9–M14 listed in Table 4-18, with optimal water content determined by the M-L method are illustrated in Figure 4-12(b), showing no visible voids present on the surface. As detailed in Table 4-16 and Table 4-18, the air contents of concrete with optimal water content determined by the M-L method were about 3%, slightly higher than conventional concrete (1%).

(a) (b)

Figure 4-11 Mix-5(M-L) and Mix-7(M-L) with optimal water content in mixer; (a) Mix-5(M-L), (b) Mix-7(M-L)

(a) (b)

Figure 4-12 (a) Compacted sample with optimal water content by M-VB method, visible voids are present on surface; (b) Six compacted samples of mixes M9–M14 (Table 4-18) with optimal water content by M-L method, no visible voids are present on all samples.

Table 4-18 Experimental results of mixes with optimal water content by M-L compaction method

Mix ID	Mix parameters			Mix proportion							
	Max.dry density (kg/m³)	Wet density (kg/m³)	Air cont. (%)	C.	CA	FA	SBR	PVA	Plast -icizer	Adde. water	SF
M6(M-L)	2348	2479	2.98	1	1.518	1.013	0.217	0.01	0	0.103	0.184
M7(M-L)	2334	2464	3.32	1	1.518	1.013	0.217	0.02	0	0.103	0.184
M8(M-L)	2299	2445	2.68	1	1.518	1.013	0.217	0.03	0	0.135	0.184
M9(M-L)	2343	2456	2.3	1	1.266	1.266	0.217	0	0	0.064	0
M10(M-L)	2355	2482	3.16	1	1.266	1.266	0.217	0	0	0.094	0.184
M11(M-L)	2289	2427	3.96	1	1.266	1.266	0.217	0.02	0	0.119	0.184
M12(M-L)	2380	2531	2.01	1	1.266	1.266	0	0.01	0.015	0.244	0.184
M13(M-L)	2327	2490	2.94	1	1.266	1.266	0	0.02	0.015	0.268	0.184
M14(M-L)	2296	2455	3.23	1	1.266	1.266	0.109	0.02	0	0.209	0.184

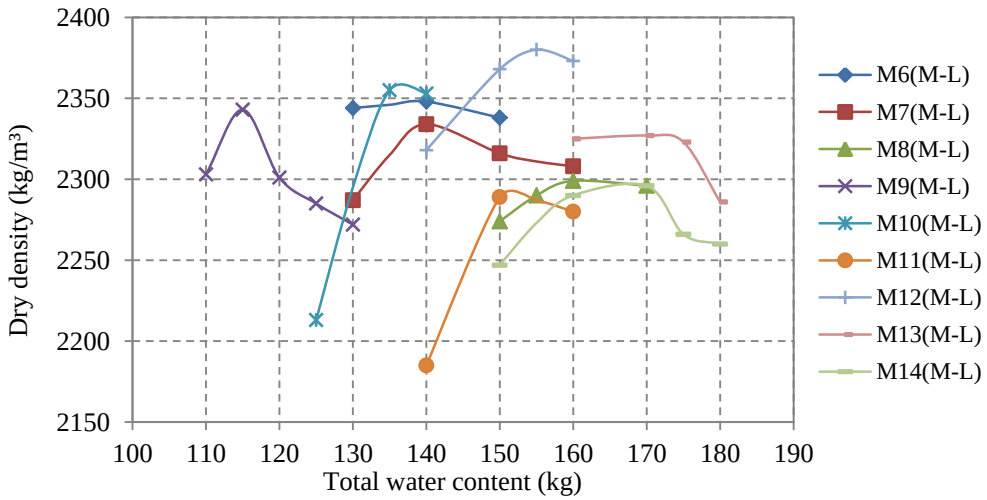

Figure 4-13 Relationship of dry density and total water content of mixes shown in Table 4-17, obtained by the M-L compaction method

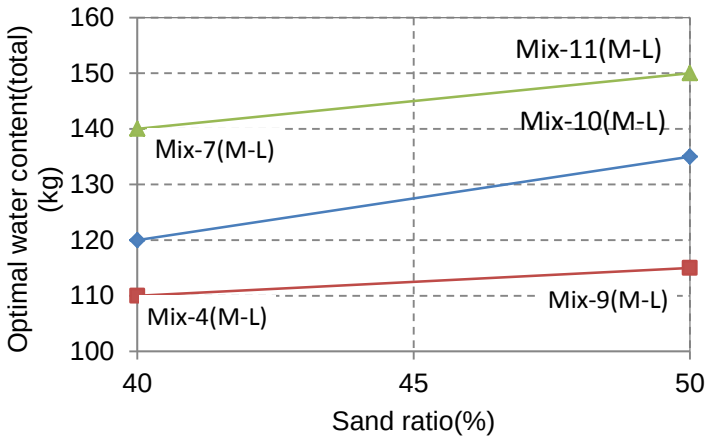

Figure 4-14 Optimal water content vs. sand ratio

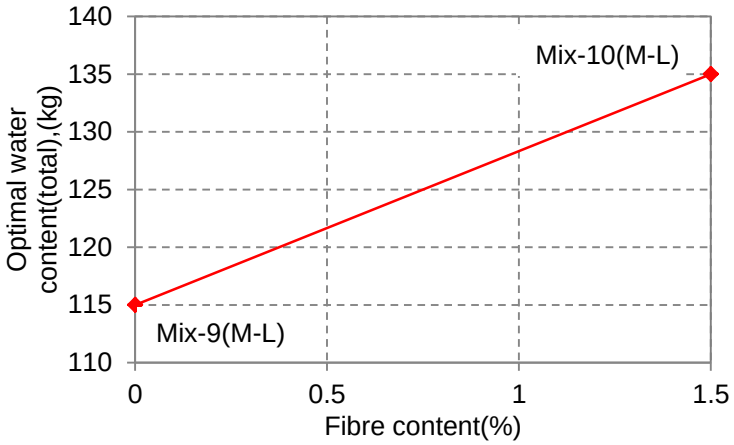

Figure 4-15 Optimal water content vs. fibre content

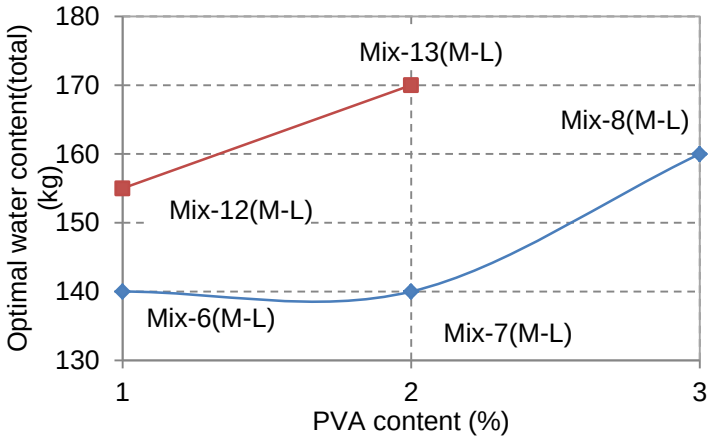

Figure 4-16 Optimal water content vs. PVA content

It is observed from Table 4-16 and Table 4-18 that the optimal water content increases with the increase of any of the following parameters: sand ratio, steel fibre content and PVA dosage (see Figures 4-14, 4-15 and 4-16, respectively).

As aforementioned, the mix M8 (M-L) containing 10% SBR and 3% PVA exhibited poor workability. However, the PVA dosage of 1% may not be sufficient to provide the adhesion required. Therefore, the PVA dosage of 2% was considered to be optimum and could potentially achieve high bond strength. Its proportion is recorded in Table 4-18 under M7 (M-L). The corresponding 28-day direct shear bond strength of PMC-on-OPCC composite specimens was later tested to be 6.07 MPa, and the 28-day splitting tensile bond strength was 2.56 MPa (see Figure 4-19 and Figure 4-20). Both are deemed to be much higher than the OPCC-on-OPCC bond strength.

In summary, the M-L method, 4-layer compaction and 20 blows for each layer with the S-P devices, is an appropriate mix design method for steel fibre reinforced roller-compacted polymer modified bonded overlays.

4.3.4 Bond Strength

Preparation of PMC-on-OPCC composite samples

The interface between overlay and old concrete pavement is undergoing shear, tension and compression under vehicular and thermal loading during its service life. Therefore, the bond performance of PMC-on-OPCC composite specimen is accordingly evaluated by both, direct shear bond strength and splitting tensile bond strength. A test composite beam with an interfacial crack and loading configuration, for simulating the existing interfacial defects of overlay pavement, was developed in this study to measure the interfacial fracture toughness, and is presented in Section 7.3.3 and Section 7.3.4. In this study, OPCC cylinders of 100 mm diameter and 100 mm height were used as a base, while the OPCC prismatic bases were 150 mm x 150 mm x 50 mm in width, length and height. The OPCC cylinders were topped up by PMC material of 100 mm diameter and 80 mm height, while the PMC part of the prismatic block was 150 mm x 150 mm x 50 mm. All the OPCC bases were at least 14 days old prior to usage. About four hours after casting, the surface of OPCC base was brush-roughened to remove surface mortar and expose coarse aggregate. The interfacial texture of OPCC cylinder and prism is shown in Figures 4-17(a) and (b) respectively. The specimen surface appeared to be similar to the treated surface of an old concrete pavement in field shown in Figure 4-17 (c). The average texture depth of OPCC cylinder and block surfaces were 1.75 mm and 1.65 mm respectively, measured by the sand patch method (BS 598-105:1990 1998).

Various methods have been developed for RCC specimen formation in the laboratory (ASTM

C 1176-05 2006; ASTM C 1435/C 1435M-06 2006; Neocleous et al. 2011). In this study, a device comprising a vibrator and steel plates designed to fit the specimen sizes was specifically manufactured for specimen formation. This is pictured in Figure 4-23. The specimen formation procedure is described in Section 4.4.4 in detail.

The PMC wet densities, tested by weighing in air and water after the bond strength test, were close to those determined by the corresponding compaction methods described earlier. The experimental set-up for direct shear bond strength and splitting tensile bond strength adopted, is illustrated in Figure 4-18 (b) and (d), and the corresponding diagrams in Figure 4-18(a) and (c). The set-up for direct shear bond strength is similar to that used in the USA (NCPTC USA 2008). The loading rates for the direct shear tests and tensile splitting tests were conducted at 0.39 kN/s and 1.4 kN/s respectively. The direct shear bond strength was evaluated by applying the maximum load divided by the area undergoing shear, while the splitting tensile strength was evaluated by eqn.4.12.

$$\sigma_c = \frac{2P}{\pi A} \qquad 4.12$$

where σ_c is the splitting tensile strength (MPa); P is the maximum load (N); A is the area of split section (mm^2). The strength for each mix was evaluated by averaging the three test readings obtained from the three specimens.

(a) (b) (c) (d) (e)

Figure 4-17 (a) Treated surface of OPCC cylinder base, (b) treated surface of OPCC block base, (c) treated surface of an old concrete pavement in use(NCPTC USA 2008), (d) PMC-on-OPCC composite cylinder, (e) PMC-on-OPCC composite block.

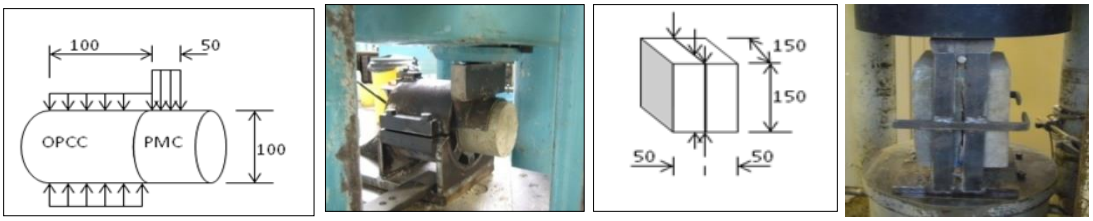

(a) (b) (c) (d)

Figure 4-18 (a) PMC-on-OPCC composite cylinder demonstrating direct shear bond strength test (unit: mm). (b) PMC-on-OPCC composite cylinder under test. (c) PMC-on-OPCC composite block for splitting tensile bond strength test (unit: mm). (d) PMC-on-OPCC composite block under test.

Bond strength

The tested direct shear bond strength and splitting tensile bond strength at the age of 28 days and 42 days are illustrated in Figure 4-19 and Figure 4-20, respectively. It is seen that M5 (M-L) in Table 4-16 and M7 (M-L) in Table 4-18 exhibited much higher bond strengths than OPCC-on-OPCC.

Careful observations during bond strength tests showed that all failed planes developed through the interfaces, both in the direct shear bond and splitting tensile bond strength tests. This indicated that both bond strength tests were appropriate to evaluate the bond strength of composite specimens. It was observed that nearly 50% of the failed section area was covered by the bonded material in the PMC-on-OPCC composite specimens made of M5 (M-L) and M7 (M-L), in which high bond strength was achieved. In contrast, when the bond strength was low, the interface did not contain traces of the bonded material.

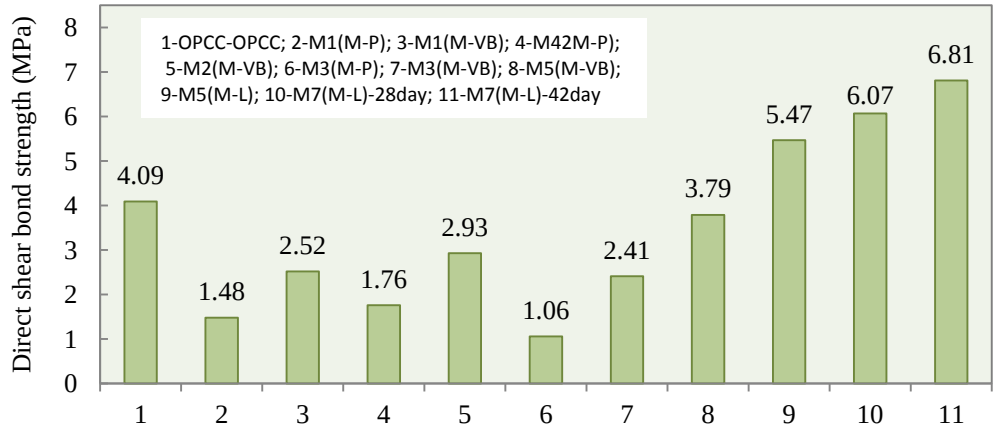

Figure 4-19 Direct shear bond strength of PMC-on-OPCC composite cylinder

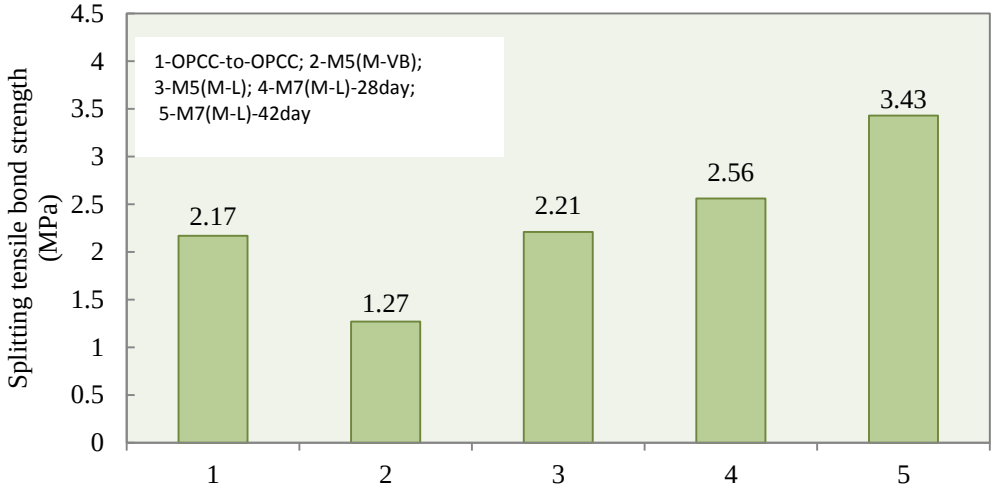

Figure 4-20 Splitting tensile bond strength of PMC -on-OPCC

The direct shear strengths of M5(M-L) and OPCC carried out using the same set-up were 9.32 MPa and 7.0 MPa respectively. The 42-day direct shear bond strength of M7 (M-L) was 6.81 MPa, very close to the OPCC direct shear strength of 7.0 MPa. This indicates that a very high bond strength was achieved with SBR-PVA hybrid polymer modified cement concrete.

4.3.5 Essentials of the M-L Compaction Method

The optimal water content determined by the maximum dry density was originally proposed in soil compaction to evaluate compactability. The philosophy is: the more the solid content in a unit volume the higher the strength. More solid content in soil means less water and air void content, which could adversely affect the soil strength. However, strength of concrete is not only dependent on air content, but also on water content and cement hydration product. This means that for the same mix proportion, concrete having maximum solid content may not guarantee the highest strength. To the author's best knowledge, the hypothesis for utilising the soil compaction method in RCC mix design is not available to date. Therefore, the M-L compaction method needs to be experimentally verified.

For this purpose six mixes, i.e. M9 – M14, as listed in Table 4-17, were tested, not only by the M-L compaction method for determining the optimal water content, but also tested at 28 days for splitting tensile strength. The container was first moistened with a concrete release agent, and then excess oil was carefully removed with a tissue. The surface of each compacted layer was roughened before accepting the next layer. After compaction, sample and container were covered with polythene sheets and de-moulded in 24 hours. Samples were cured in water for 5 days, followed by 22 days curing in air under normal laboratory conditions. The six groups of compacted samples are pictured in Figure 4-22. The experimental results indicated that four out of six mixes reached the highest strength at optimal water content, corresponding to maximum dry density. The other two mixes did not exhibit the same phenomena although only one sample was actually prepared for each strength test.

The experimental results of M9 and M11 in Table 4-17, i.e. the splitting tensile strengths and dry densities corresponding versus different water contents (total water content, W_{T1}, in 1 m^3 concrete), are plotted in Figure 4-22. It is observed that the optimal water content corresponding to the maximum dry density determined by the M-L compaction method also guarantees the highest strength. Hence the M-L method was justified.

Figure 4-21 Six groups of compacted samples by M-L method for splitting tensile strength test (mixes M9 to M14 in Table 4-17 are in the order of front to rear)

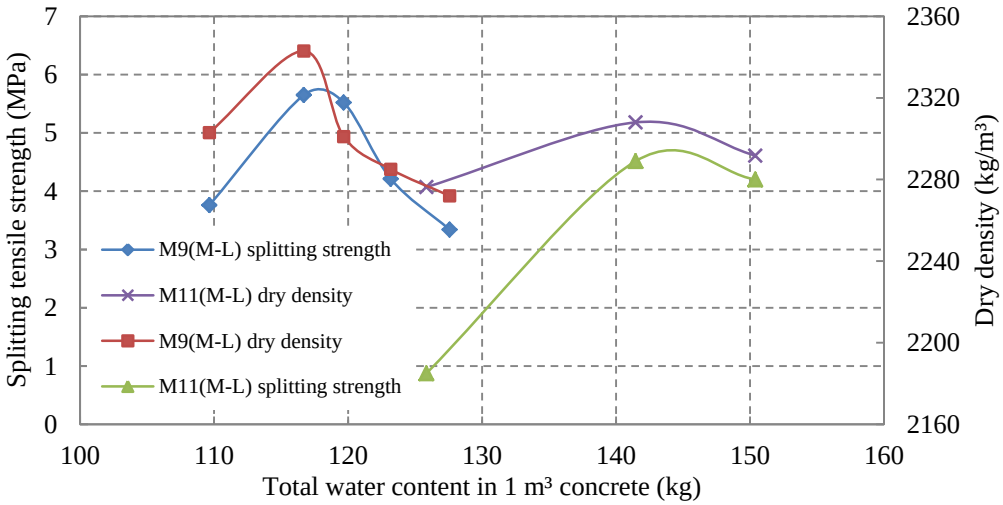

Figure 4-22 Compacted samples of M9 and M11 by the M-L method reaching highest splitting tensile strength and maximum dry density at the same water content.

Summary

Summarizing the discussion above, the following conclusions can be drawn:

(1) Mixes with optimal water content determined by the S-P method were deemed to be unsuitable for pavers, as they turned lumpy during mixing. Hence, the method itself is not recommended as a suitable method for roller compaction and paver placement of fibre-reinforced polymer modified concrete. On the contrary, mixes with optimal water content determined by the M-P and M-VB methods were found to be not-lumpy during mixing. Therefore, at first, they appeared to have met the requirements for roller ''compactability'' and paver ''placeability''. However, the bond strength was lower than the previously defined criteria. In addition, a large number of voids were detected on the surface of the samples made with the M-VB method after de-moulding. Therefore, the M-P and M-VB method was deemed to be inappropriate in terms of durability.

(2) A new mix design method for determining the optimal water content, the M-L method, is proposed for steel fibre-reinforced, roller-compacted, polymer modified, bonded concrete overlays. This was experimentally verified. This method employs devices of the Standard Proctor compaction test and a compaction effort of 4 layers and 20 hammer blows for each layer.

(3) The air contents of mixes with optimal water content determined by the M-P method are approximately 3%, slightly higher than that of the corresponding conventional concrete.

(4) Two types of mixes suitable for asphalt paver placement and roller compaction were developed: They were the SBR and the SBR–PVA hybrid polymer modified cement concrete mixes with the optimal water contents determined by the M-L method. Both mixes achieved good bond with old concrete substrate. The bond strengths were considerably higher than the conventional concrete to conventional concrete bond strength.

4.4 Mixing Procedure and Specimen Formation

In this section, special devices for specimen formation and formation method are presented respectively, and the applicability of the formation method is verified by comparison of the wet density of sample and that determined by M-L mix design method.

4.4.1 Mixing Procedure

In this study, the mixing procedure for SBR modified cement concrete conforms to ASTM C 1439-99 (1999). That is, add coarse aggregate and SBR latex and approximately half the total amount of water; rotate the mixer a few revolutions; add the fine aggregate, cement, and remaining water; mix the concrete for three minutes, followed by one minute of 'rest', followed by one minute of further mixing. For PVA modified cement concrete and hybrid SBR-PVA polymer modified cement concrete, the mixing procedure remains the same, except that the cement and PVA are mixed uniformly in a separate mixer, prior to the main mixing procedure. If a superplasticizer is to be used, the procedure will not change, other than the latter being mixed with the water prior to being added in the main mix.

4.4.2 Devices for Specimen Formation

Various methods (ASTM C 1176-05 2006; ASTM C 1435/C 1435M-06 2006; Filho et al. 2008; Neocleous et al. 2011) have been developed for RCC specimen formation in the laboratory. ASTM 1176-05 (2006) and ASTM 1435/C 1435M-06 (2006) recommend a method of using the vibrating table of the Vebe tester and vibrating hammer to fabricate cylindrical specimens in the laboratory, but formation method for beams is not available. Neocleous et al. (2011) developed a vibrating hammer with extra surcharge similar to ASTM's for formation of cylindrical and beam specimens reinforced with steel fibres. Filho et al. (2008) developed a heavy vibrating roller in laboratory to simulate vibrating roller compaction in fields.

Whatever the device is, the microstructure of specimens fabricated by the device should be similar to that of pavements compacted by vibrating roller in the field. It is obvious that the vibrating hammer is not an ideal device for fabricating beam incorporating steel fibres because the fibres in the beam would be deformed by the small compacting plate, resulting in the specimen microstructure being different from that in the fields. In this study, a device comprising a vibrator and steel plates designed to fit the specimen sizes was specifically manufactured for specimen formation. This is shown in Figure 4-23.

(a) (b) (c) (d) (e)

Figure 4-23 (a) vibrator and its components; (b) cylindrical specimen under compaction; (c) plate for blocks; (d) plate for cylinders; (e) plate for the formation of beams

The vibrating compactor shown in Figures 4-23(a) and (b), usually used in soil or pavement material compaction, was of power of 745W and frequency of 47 Hz. The compacting plates fitting specimen dimension for specimen formation are presented in Table 4-19.

Table 4-19 Technical parameters of vibrating compactor and its components

Type of plate	Plan. dimen. of plates (mm)	Total mass compactor (kg)	Static pressure (N/mm²)	Planar dime. of specimen (mm)	Description
Rectangular plate	95x495	25.6	0.00544	100x500	for beam formation
Rectangular plate	145x547	26.5	0.00334	150x550	for beam formation
Square plate	146x146	21.25	0.00997	150x150	for block formation
Circular plate	Φ95	20.2	0.02849	Φ100	for cylind. formation
Circular plate of M-Vebe	Φ236	22.7	0.00519	Φ241	M-Vebe tester

4.4.3 Curing Procedure

The specimens were de-moulded in twenty-four hours, and then cured in water five days for SMRPMC and seven days for PVAPMC, followed by air curing until testing date. The temperature in the laboratory varied between 18–23^{o}C, while the relative humidity was between 52%–60%. Specimens in curing are illustrated in Figure 4-2, and the mechanism of curing procedure of PMC specimens was presented in Section 4.2.

4.4.4 Specimen Formation

Formation of intact PMC beams

The vibrating compactor and the components are shown in Figure 4-23. In specimen formation the specimen density should be controlled to be as close as possible to those determined by the M-L compaction method proposed in Section 4.3. The intact PMC beams of 100 mm x 80 mm x 500 mm in height, width and length, were fabricated in steel moulds, while the intact PMC beams of 150 mm x 100 mm x 550 mm in height, width and length were cast in timber moulds. Compaction of PMC was carried out in two layers. Each layer was about 40 - 50 mm thick. The vibrating compaction lasted 30 - 50 seconds per layer for SBRPMC, and 60 - 90 seconds for PVAPMC until mortar formed a ring around the perimeter of the moulds. The surface of each layer was roughened before accepting the next layer of material. Three specimens were fabricated for each mix. Specimens were covered with polythene sheets to minimise the moisture evaporation after finishing compaction.

Formation of PMC-on-OPCC composite beams

All the OPCC bases were at least 14 days old prior to usage. About four hours after casting, the surface of OPCC base was brush-roughened to remove surface mortar and expose

aggregate. The average texture depth of OPCC base was 1.65 mm-1.75 mm, measured by the sand patch method (BS 598-105:1990 1998).

The planar dimension of PMC-on-OPCC composite beams used in the study was 100 mm x 500 mm in width and length, while the total typical depth of the composite beams was 125 mm, comprising of 75 mm-thick PMC and 50mm-thick OPCC base. Timber moulds were used to fabricate these composite beams. Before being placed on PMC material, the surfaces of OPCC bases were dampened, and then covered with a wet cloth for about 30 minutes to ensure surface-dry saturated condition. The compaction and curing procedure for SBPPMC and PVAPMC overlay were the same as the intact PMC beams presented earlier. The typical OPCC base with roughened surface and a PMC-on-OPCC composite beam are pictured in Figure 4-24.

(a) (b)

Figure 4-24 (a) Roughened OPCC bases for composite beams, (b) PMC-on-OPCC composite beam

Formation of cylindrical and block specimens

In this study the intact cylindrical specimens, with the dimensions of 100 mm x 180 mm in diameter and length, were used to measure the modulus of elasticity and Poisson's ratio; while the PMC-on-OPCC composite cylinders and blocks were used to measure the direct shear bond strength and splitting tensile strength, respectively. The OPCC cylinders of 100 mm diameter and 100 mm height were used as a base, while the OPCC block bases were 150 mm x 150 mm x 50 mm in width, length and height. The depths of PMC overlay of composite cylinder and composite block were 80 mm and 50 mm, respectively. The procedure of overlay formation and curing were the same as composite beam, as presented above in detail.

4.4.5 Verification of Specimen Formation Method

It is well-known that the mechanical properties of concrete are mainly dependent on the air content or the density for a given mix proportion. For the same mix the density of specimen

formed in laboratory for evaluating strength should be close to those determined by mix designs. In this study, intact beams and composite beams, intact cylinders and composite cylinders, and intact blocks and composite blocks were fabricated. Bending tests, splitting tests and compression tests were conducted for measuring flexural strength, direct shear bond strength and splitting tensile bond strength, etc. After testing, these tested intact PMC beams were saw-cut for compressive strength test, while the PMC-on-OPCC composite beams were used for splitting tensile bond strength tests. The typical dimension of PMC blocks saw-cut from tested beams was 100 mm x 100 mm x 80 mm in width, height and thickness, while the dimension of cylinders was 100 mm x 180 mm in diameter and length respectively. The densities were determined by testing the weight in air and water. The tested samples were air cured for 22 - 40 days. The proportion of mixes of Tables 4-20 and 4-21 are tabulated in Table 5-1. The mixes are extensively investigated in Chapters 5 and 6. Tables 4-20 and 4-21 demonstrate the measured mean density and the corresponding wet density determined by M-L compaction method proposed in Section 4.3. It is noted that the density ratios on Tables 4-20 and 4-21 are the tested density divided by its corresponding wet density with optimal water content determined by M-L method. The wet densities of the four mixes listed in Table 4-20, determined using M-L compaction method, are shown in Table 5-1, while the wet density of SBRPVAPMC1.5%-35 is 2464 kg/m^3, that of the mix M7 recorded in Table 4-18.

It can be observed from the experimental results listed in Tables 4-20 and 4-21 that:

(1) The density ratios range from 0.9843 through 1.0225, indicating the specimens formed by the method closely simulated the mixes determined by the M-L method, and hence the formation method was valid.

(2) The coefficients of variation (COV) for all specimen groups are in the range of 0.06% - 1.89%, indicating the specimen compaction was properly controlled.

Table 4-20 Density of PMC prisms saw-cut off from tested beams and cylinders

Mix ID	Type of specim.	Wet.densi.at opti. water cont. (kg/m³)	Measured density of specimens					Density ratio
			No. of Specim.	Mean (kg/m³)	STDEV (kg/m³)	COV (%)	Age (day)	
SBRPMC1%-35	Beam	2479	3	2462	8.28	0.34	46	0.9931
			3	2460	9.15	0.37	60	0.9923
SBRPMC1.5%-35	Beam	2482	3	2457	2.73	0.11	3	0.9899
			3	2494	8.43	0.34	7	1.0048
			3	2440	15.52	0.64	31	0.9831
	Cylinder		3	2475	3.12	0.13	40	0.9972
SBRPMC1.5%-50	Beam	2478	3	2443	10.1	0.41	28	0.9859
SBRPMC2%-35	Beam	2521	3	2499	9.15	0.37	46	0.9913
PVAPMC1.5%-35	Beam	2466	4	2474	46.78	1.89	35	1.0032
			2	2500	1.38	0.06	37	1.0032
	Cylinder		3	2459	5.82	0.24	40	1.0032

Table 4-21 Density of PMC layer separated from tested composite specimens

Mix ID	Type of specimen	Wet density in optimal water conten.(kg/m³)	Measured density of PMC				
			No. of specimen.	Average (kg/m³)	STDEV (kg/m³)	COV (%)	Age (day)
SBRPMC1.5%-35	Composite cylinder	2482	3	2538	11.59	0.46	7
	Composite block		3	2523	1.155	0.05	7
SBRPVAPMC1.5%-35	Composite cylinder	2464	2	2443	3.677	0.15	42
	Composite block		3	2453	4.961	0.2	42

4.5 Summary

The concluded remarks are presented below, while the specific summary can be found at the end of each section.

(1) The addition of SBR may be favourable to improvement of bond strength but considerably detrimental to the strength of cement paste, while PVA (GH-17S) can greatly improve bond strength but leads to poor workability. The dosage of 10% SBR and 2% PVA can be deemed as the optimal by consideration of both strength and workability.

(2) Optimal curing procedure for SBR modified concrete is 5 - day water curing and followed by airing curing to testing date; while 7 - day water curing and followed by airing curing to testing date applied to PVA modified concrete.

(3) A new mix design method for determining the optimal water content, the M-L method, is proposed for steel fibre-reinforced, roller-compacted, polymer modified, bonded concrete overlays. This was experimentally verified. This method employs devices of the Standard Proctor compaction test and a compaction effort of 4 layers and 20 hammer blows for each layer.

(4) Special devices for specimen formation were developed. With the devices and the formation method presented in Section 4.4.4, the wet density of specimen were close to that determined by M-L mix design method. This verified experimentally the formation method.

5 Flexural Strengths of SFR-RC-PMC

Flexural strengths of steel fibre reinforced concrete (SFRC) have been investigated since the 1980s (Jenq and Shah 1986; Gopalaratnam et al. 1991; Banthia and Trottier 1995; Armelin and Banthia 1997; Lok and Pei 1998; Jeng et al. 2002; Neocleous at el. 2006; Denennam et al. 2011; and so on). A vast amount of literature deals with flexural strength, residual flexural strength, toughness, toughness indexes, crack propagation, fibre bridging law, fracture energy, and so on. However, all the aforementioned SFRCs are for conventional SFRC, the mechanical properties of steel fibre-reinforced roller-compacted polymer-modified concrete (SFR-RC-PMC) have not been investigated yet.

In this study, the addition of steel fibre to concrete was intended to improve the flexural strength, especially the residual flexural strength; and the addition of polymer to improve bond strength with old concrete. Steel fibres in roller-compacted concrete (RCC) may behave differently to those in conventional concrete, due to the fact that RCC contains much less cement paste than conventional concrete, and roller compaction may result in the deformation of steel fibres. In addition, as has been presented in Chapter 4, the addition of SBR to plain cement paste and cement mortar resulted in the decrease of compressive strength. Further, the flexural performance of PVA modified concrete has rarely been investigated. Therefore, it has been necessary to investigate the flexural performance of SFR-RC-PMC for overlay pavement design, and to reveal the influence on flexural behaviour of the factors mentioned above.

For these purposes, total forty-five beams of eight mixes were tested under flexure, and accordingly the maximum flexural strength, residual flexural strength, equivalent flexural strength, fracture energy, size effect, and strength at early ages were evaluated. In addition, the experimental results, i.e. the relationship of load-CTOD and load-CMOD are further investigated in Chapter 6 to reveal the mechanism of the role played by steel fibres in steel fibre-reinforced roller-compacted polymer modified concrete.

In this study, a four-point bending test was initially used; however after assessment of the applicability of the test, a three-point bending test with notched beam was employed to explore the flexural performance. The reason for these is presented in Section 5.2.

5.1 Mix Proportion and Specimen Preparation

The workability and compressive strengths of cubes of SBR modified mortar and PVA modified mortar were experimentally investigated in Chapter 4. After considering workability and strength, mixes of SBR modified cement concrete (SBRPMC) were deemed to be optimal, and hence more SBRPMC specimens were tested.

In this chapter, the flexural strengths of beams of eight mixes, which are tabulated in Table 5-1, were tested. The ingredient materials used in beam specimens and their properties were presented in Chapter 4. Among the eight mixes, five mixes were steel fibre-reinforced roller-compacted polymer modified concrete (SFR-RC-PMC); one was conventional steel fibre-reinforced concrete; and two mixes were without fibres. Two types of polymers, i.e. SBR and PVA, and two types of steel fibre, i.e. 35mm-long fibre and 50mm-long fibre, were used. Superplasticizer was added in PVA modified concrete to reduce water content to obtain high strength, while SBR modified concrete did not incorporate any admixtures.

The five mixes of SFR-RC-PMCs varied in steel fibre content, length of fibres and type of polymers; and their optimal water contents were determined by the M-L compaction method, proposed in Chapter 4. The mix SBRPMC0%, which did not contain fibre, was the matrix of mix SBRPMC1.5%-35. The mix SBRPMC0% had the same proportion and ingredients as the mix SBRPMC1.5%-35 except for the fibre. The dimensions of the beams of the six mixes were 80 mm x 100 mm x 500 mm in width, height and length. The mixing and curing procedure and the formation method of specimens were presented in detail in Section 4.4, and the identity of beams and their dimensions and formation method are listed in Table 5-2.

The conventional steel fibre-reinforced concrete, i.e. Con.SBRPMC1.5%-35, was intended for comparison with the mix SBRPMC1.5%-35. The former had the same ingredients and mix proportion as the latter except for the water content. The mix Con.SBRPMC0% was the matrix of mix Con.SBRPMC1.5%-35, the only difference between the two mixes was that the former did not contain steel fibre. The matrix SBRPMC0% was purposely used for the evaluation of the relative toughness and for comparison with the mix SBRPMC1.5%-35 in fracture behaviour. The slump of the mix Con.SBRPMC1.5%-35 was 130 mm, and the slump of the mix Con.SBRPMC0% was much higher than 130mm (it was not measured). The mixing and curing procedures of both mixes were the same as for mix SBRPMC1.5%-35.
The dimensions of the beams of both the mixes were 100 mm x 100 mm x 500 mm in width, height and length, and fabricated in steel moulds on the vibrating table.

Table 5-1 shows the proportions of the mixes used in this study. The identities of beams are listed in Table 5-2, and their dimensions and formation methods are tabulated in the same table too. The mix ID indicates the mix proportion and fibre used, for instance, the mix ID 'SBRPMC1.5%-50' indicates the mix was roller-compacted SBR modified concrete reinforced with the 50 mm-length fibre. The beam ID indicates both mix ID and the dimension of the beam, for example, the beam ID of SBRPMC1.5%-35-H150 indicates the mix proportion and length of fibre and height of the beam, namely the mix is roller compacted SBR modified concrete reinforced with 35mm-length steel fibre, the beam was 150 mm in height.

The wet density of mix SBRPMC1.5%-35 has been presented in Section 4.3.3, recorded under M10 in Table 4-18. The wet densities of four mixes, SBRPMC1%-35, SBRPMC2%-35, PVAPMC1.5%-35 and SBRPMC1.5%-50, were determined using M-L compaction method, and listed in Table 5-1; while the densities of the three mixes Con.SBRPMC1.5%-35, Con.SBRPMC0% and SBRPMC0% were measured using the method of weighing the blocks saw-cut from tested beams in air and water, complying the British Standard (BS EN 12390-7:2009).

Table 5-1 Proportion of mixes with optimal water content determined by M-L method (C.=Cement-I, Supe.=Superplasticizer, Ad.Wat.=Added water)

Mix ID	Mix proportion							Fibre by	Wet density
	C.	Aggr.	Sand	SBR	PVA	Supe.	Ad. Wat.	volume	(Kg/m^3)
SBRPMC1%-35	1	1.266	1.266	0.217	0	0	0.072	1%	2479
SBRPMC1.5%-35	1	1.266	1.266	0.217	0	0	0.095	1.50%	2482
SBRPMC2%-35	1	1.266	1.266	0.217	0	0	0.103	2%	2521
PVAPMC1.5%-35	1	1.266	1.266	0	0.02	0.025	0.228	1.50%	2466
Con.SBRPMC1.5%-35	1	1.266	1.266	0.217	0	0	0.245	1.50%	2330
SBRPMC1.5%-50	1	1.266	1.266	0.217	0	0	0.095	1.50%	2478
Con.SBRPMC0%	1	1.266	1.266	0.217	0	0	0.245	0%	2297
SBRPMC0%	1	1.266	1.266	0.217	0	0	0.095	0%	2306

The beam dimensions recommended by BS EN 14651:2005+A1:2007 is 150 mm x 150 mm x 550 mm in width, height and length. In this study, the beam specimens were of the dimensions of 80 mm x 100mm x 500mm in width, height and length, which are also recommended by ASTM C 1609/C 1609M-06 (2006). The notches were saw-cut to the specified depth by circular saw one day prior to testing. The width of the notches was 3.5-4 mm, complying with BS EN 4651:2005+A1:2007. The ages of tested specimens were 28-40 days for most beams, while the specimens for the strengths at early ages were tested in the specified ages, such as 3-day and 7-day ages.

Table 5-2 IDs and dimension and formation method of beams tested

IDs of beams	IDs of mixes	Dimension of beams width x height x length	Formation method	Type of fibre
SBRPMC1%-35-H100	SBRPMC1%-35	80x100x500 mm^3	Vibrating compactor	35 mm-length hooked-end fibres
SBRPMC1.5%-35-H100	SBRPMC1.5%-35			
SBRPMC2.0%-35-H100	SBRPMC2.0%-35			
PVAPMC1.5%-35-H100	PVAPMC1.5%-35			
SBRPMC1.5%-35-H150	SBRPMC1.5%-35	100x150x550 mm^3	Vibrating compactor	
Conv.SBRPMC1.5%-35-H100	Conv.SBRPMC1.5%-35	100x100x500 mm^3	Vibrating table	
SBRPMC1.5% -50-H100	SBRPMC1.5%-50	80x100x500 mm^3	Vibrating compactor	50mm-length hooked-end fibres
Con.SBRPMC0%-H100	Con.SBRPMC0%	100x100x500 mm^3	Vibrating table	N/A
SBRPMC0%-H100	SBRPMC0%	80x100x500 mm^3	Vibrating compactor	N/A

5.2 Flexural Strength of SFR-RC-PMC Beams under Four-point Bend

The representative test methods for steel fibre reinforced concrete currently available are British Standard (BS) method (BS EN 14651:2005+A1:2007 2007) and ASTM method (ASTM C 1609/C 1609M-06 2006). The former is performed by testing a notched beam under a three-point bend, using crack mouth opening displacement (CMOD) control, while the latter tests an un-notched beam under a four-point bend, using mid-span deflection control. In this study, the ASTM method (ASTM C 1609/C 1609M-06 2006) was first used to evaluate the flexural strength of the mixes.

The test procedure complied with ASTM C 1609/C 1609-06 (2006). Two LVDTs were mounted on the frame shown in Figure 5-1 and Figure 5-2. The frame was for mounting the LVDTs for measuring net deflection with respect to support, and two LVDTs were mounted in both sides of the frame. This device eliminates extraneous deformation such as support settlements and specimen rotations. The test machine was hydraulic servo-closed loop with a maximum load capacity of 150 kN. The loading rate was controlled by mid-span deflection by the LVDT reading as a feedback signal. The load and vertical displacements (deflections) were continuously recorded at the frequency of 5 Hz. The representative mid-span deflection was the average of the two LVDT readings.

The loading rate was controlled by the mid-span deflection. The rate of increase of net deflection was 0.0017 mm/s until the LVDT reading reached 0.5 mm; after the 0.5 mm the rate was 0.0033 mm/s. The loading rate is within the range specified by ASTM C 1609/C 1609-06 (2006). Three mixes, i.e. SBRPMC1.5%-35, PVAPMC1.5%-35 and Con.SBRPMC1.5%-35, were tested. The proportions of the three mixes are listed in Table 5-1, and the dimensions in Table 5-2. Three beams were tested for each mix.

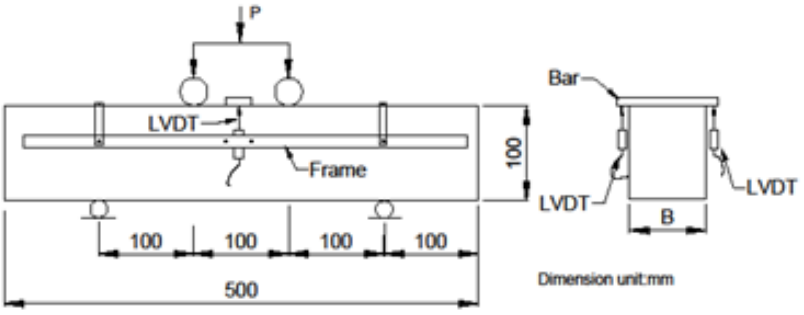

Figure 5-1 Dimensions of beams and experimental setup for four-point bending test

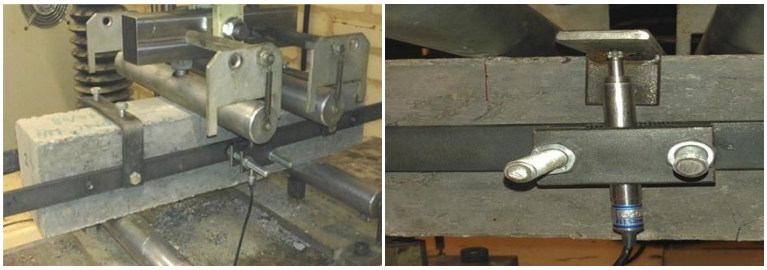

(a) (b)

Figure 5-2 (a) beam under four-point bending test; (b) close view of LVDT in frame

Although the rate of increase of net deflection was within the range recommended by ASTM (2006), the tests showed that load increments were unsuitable, resulting in abrupt failure to three beams, and hence the complete load-mid-span deflection curves for the three beams could not be made. The maximum flexural strength (f_p) and residual flexural strength ($f_{R,0.5}$ and $f_{R,2}$) calculated using eqn.5.1 in accordance with ASTM C 1609/C 1609M-06 (2006) are shown in Table 5-3 and Figure 5-4.

$$f_j = \frac{300P_j}{Bh^2} \qquad 5.1$$

Where, $j=P$ or $j=R,0.5$ or $j=R,2$; and P_p, $P_{p,0.5}$ and $P_{p,2}$, f_p, $f_{R,0.5}$ and $f_{R,2}$ are defined in Figure 5-3; B and h are the width and height of the beam, respectively.

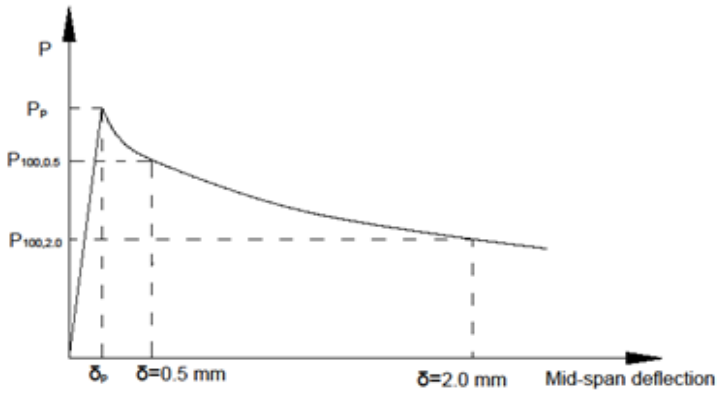

Figure 5-3 Flexural strength calculation (ASTM C 1609/C 1609M-06 2006)

Table 5-3 Flexural strengths of PMC beams under four-point bending test

Mix ID	Statistics	Num. of beams	Maximum strength		Residual strength (MPa)	
			f_p(MPa)	δ_P(mm)	$f_{R,0.5}$	$f_{R,2.0}$
SBRPMC1.5%-35	Average	3	12.53	0.3879	11.67	7.7
	STDEV		0.29	0.129	0.6	1.36
PVAPMC1.5%-35	Average	3	13.22	0.3285	7.39	6.14
	STDEV		1.52	0.033		
Con.SBRPMC1.5%-35	Average	3	9.49	0.3584	8.77	7.63
	STDEV		0.5	0.09	0.66	0.18

Note δ_P is the mean deflection at mid-span corresponding to peak load.

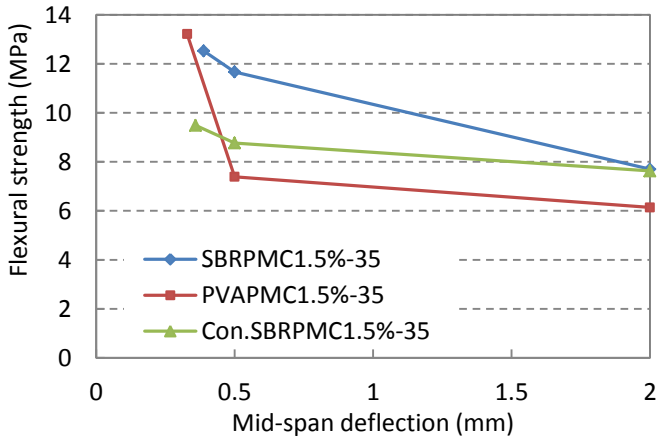

Figure 5-4 Flexural strengths of beams of three mixes under four-point bending test

The laboratory work showed that all the SBRPMC1.5%-35 and PVAPMC1.5%-35 beams failed with multiple cracking under the four-point bending test. The typical multiple cracking patterns are illustrated in Figure 5-5 (a). However, for concrete used as overlay on worn concrete pavements, a single reflective crack will initiate from the location of underlying existing cracks of worn pavements (see Figure 5-5 (b)). Therefore, the four-point bending test is not suitable for testing overlay concrete, where the overlays would fracture at the location of underlying existing cracks. Thus hereafter, three-point bending test instead of four-point bending test was used to ensure a single crack development in the beam in failure.

(a) (b)

Figure 5-5 (a) Three cracks appearance in the tested beam; (b) crack pattern in typical worn concrete pavement

Nevertheless, the maximum strengths obtained by the four-point bending test will be used in Section 5.3.3 to investigate specimen size effect on flexural strength, and consequently the equivalent flexural strength $f_{e,3}$.

5.3 Flexural Strength of SFR-RC-PMC Beams under Three-point Bend

5.3.1 Specimen Preparation and Experiment

Since the ASTM four-point bending test method is not suitable for testing the overlay concrete described above, the three-point bending test, recommended by British Standard (BS EN 14651:2005+A1:2007 2007), was employed to measure the flexural properties of SFR-RC-PMC mixes.

The beams proposed by British Standard (BS EN 14651:2005+A1:2007, 2007) are 150 mm x 150 mm x 550 mm (not less than 550 mm) in width, depth and length, and centrally notched to the depth of 25 mm, and centrally loaded under the span of 500 mm. However, due to the difficulty of uniform mix compaction in beam formation in this study, the beams used were 80 mm x 100 mm x 500 mm in width, depth and length with a central notch of 20 mm depth, and centrally loaded under the span of 400 mm. The differences of the dimensions between the specimens used in this study and those proposed by BS (BS EN 14651:2005+A1:2007, 2007) would result in slightly different flexural strength due to size effect. This is investigated in Section 5.3.3.

The experimental instrumentation and loading configuration are illustrated in Figure 5-6. The loading machine is the same as used in the four-point bending test. The frame to support LVDTs is the same as the one recommended in the ASTM code (ASTM C 1609/C 1609M-06 2006). One LVDT was fixed on the frame for measuring mid-span deflection (load-point deflection), and the other for measuring notch tip opening displacement (CTOD) was fixed by a holder glued on the beam surface, while the clip gauge was mounted on the underside for measuring the crack mouth opening displacement (CMOD) and controlling the loading rate. The testing data were automatically recorded by computer with a data acquisition frequency of 5Hz. The loading rate was controlled by CMOD by the following procedure: 0.0001 mm/s till CMOD was equal to 0.2 mm; then 0.0033 mm/s till CMOD was equal to 3 mm; then 0.005 mm/s until specimen failure. The test lasted about 1.5-2.0 hours for each beam. The rate of CMOD increase used in this study was much lower than that proposed in the BS (BS EN 14651:2005+A1:2007, 2007), which is 0.00083 mm/s till CMOD=0.1 mm; after that 0.0033 mm/s. The laboratory work showed that all the experiments were properly controlled, no abrupt failures occurred for all beam tests, and proper load-CMOD, load-CTOD and load-load point deflection curves were obtained. These results were the basis for the following analysis.

(a) (b) (c) (d)

Figure 5-6 (a) Overall view of experimental setup for three-point bending test; (b) graph of recording data; (c) overall view of instrumentation for three-point bending test, (d) close view of clip gauge for measuring CMOD, LVDTs for CTOD and load-point deflection

The typical load-CMOD, load-CTOD and load-load point deflection curves of SBRPMC1.5%-35 beam are shown in Figure 5-7. It is seen that: (1) the beam failed at the CMOD and load-point deflection being approximately equal to 18 mm, and the corresponding load reading being at around 3 kN; (2) the curve of load-CMOD is nearly coincident with that of load-load point deflection. This is due to the fact that the span was four times the depth of the beam, resulting in CMOD approximately equal to load-point deflection after hinge formation.

Based on the experimental results, the maximum flexural strength, residual flexural strength, equivalent flexural strength, relative toughness index, total fracture energy and size effects were evaluated. Furthermore, the test results were not only used to evaluate flexural strength, but also to investigate the mechanism of steel fibres in the matrix. The former is presented in this section, while the latter is discussed in Chapter 6.

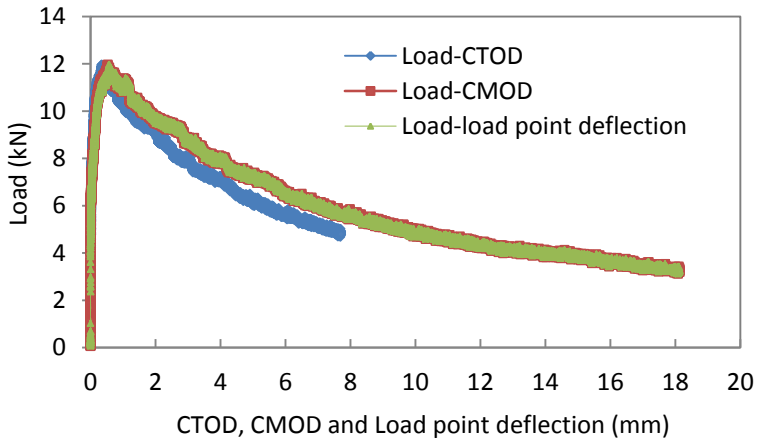

Figure 5-7 Typical load-CMOD and load-CTOD and load-load point deflection curves obtained from three-point bending test (mix SBRPMC1.5%-35, 20 mm-depth notch)

5.3.2 Maximum and Residual Flexural Strength

According to BS (BS EN 14651:2005+A1:2007, 2007), maximum flexural strength (f_p), limit of proportionality ($f_{ct,L}^{f}$), and flexural strengths ($f_{R,0.5}, f_{R,1.5}, f_{R,2.5}, f_{R,3.5}$) corresponding to $CMOD_1$=0.5 mm, $CMOD_2$=1.5 mm, $CMOD_3$=2.5 mm, $CMOD_4$=3.5 mm are evaluated to assess the flexural strengths using eqns.5.2 - 5.4. Figure 5-9 clearly demonstrates the relationship of the CMODs and the loads corresponding to flexural strength. The number of specimens, the average flexural strengths and their standard deviation (STDEV) for each group are listed in Table 5-4, and the flexural strength-CMOD curves are plotted in Figure 5-10.

The compressive strength of blocks saw-cut from the tested beams is listed in Table 5-5. The blocks were usually of the dimensions 100 mm x 80 mm x 100 mm in three sides.

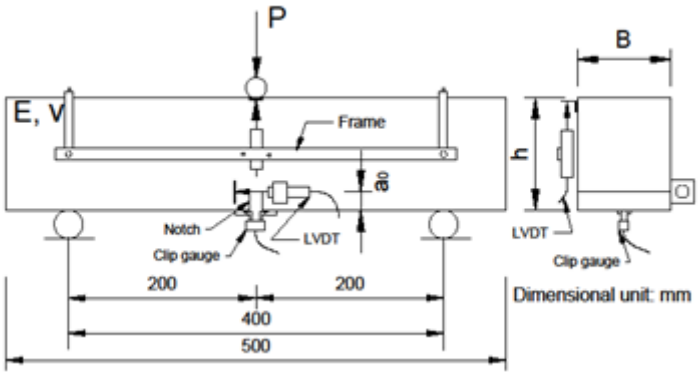

Figure 5-8 Instrumentation and dimensions of notched beam under three-point bending test

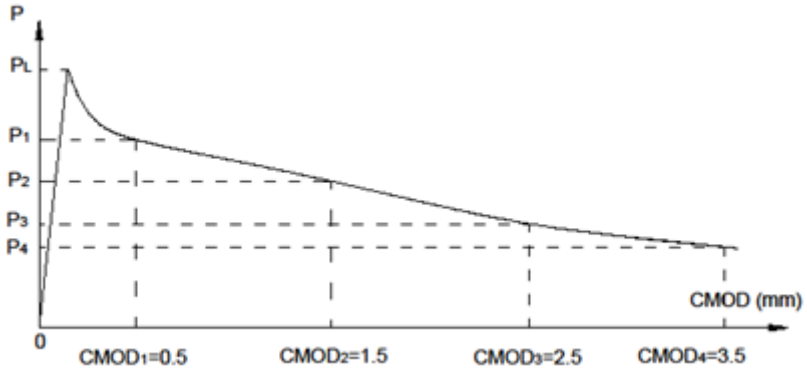

Figure 5-9 Load-CMOD diagram and P_j (j=1, 2, 3, 4) (BS EN 14651:2005+A1:2007)

$$f_{ct,L}^{f} = \frac{3SP_L}{2Bh_{sp}^2} \quad 5.2$$

$$f_{R,j} = \frac{3SP_j}{2Bh_{sp}^2} \quad 5.3$$

$$f_P = \frac{3SP_P}{2Bh_{sp}^2} \quad 5.4$$

$h_{sp} = h - a_0$

where $f^{f}_{ct,L}$ is the limit of proportionality (LOP) (MPa); P_L the load corresponding to LOP (N); *S* is the span (mm); *B* is the width of the specimen (mm); *h* is the height of the beam (mm); a_0 is the depth of notch (mm); h_{sp} is the distance between the tip of the notch and the top of the specimen (mm); $f_{R,j}$ is the residual flexural tensile strength with CMOD=j, j=0.5, 1.5, 2.5, and 3.5 mm, respectively; P_j is the load corresponding to CMOD=j, (N); f_P is the maximum flexural tensile strength (MPa); P_P is the peak load (N).

Figures 5-10 – 5-12 clearly demonstrate the maximum flexural strengths and residual flexural strengths of the beams of six mixes. From Table 5-4 and these three figures, the following conclusions can be drawn:

(1) Compared to the maximum flexural strength of 4.66 MPa of OPCC and that of 10.37 MPa of conventional SFRC (mix Con.SBRPMC1.5%-35), the steel fibre-reinforced roller-compacted polymer modified concrete (SFR-RC-PMC) (the mixes SBRPMC1.5%-35, SBRPMC2%-35, SBRPMC2%-35 and PVAPMC1.5%-35) achieved very high maximum flexural strengths. This indicates that the mixes developed by this study are suitable for the application as overlay mixes in worn concrete rehabilitation, because mixes with high flexural strength will provide longer fatigue life for overlay pavement.

(2) Mix PVAPMC1.5%-35 exhibits high maximum flexural strength, but poor toughness (residual flexural strength).

(3) With the same fibre content of 1.5% by volume, the mix SBRPMC1.5%-50, which contained the 50 mm-length fibres, exhibited the highest maximum flexural strength (see Figure 5-12 (b)).

(4) With the same mixes, i.e. mixes SBRPMC1.5%-35, PVAPMC1.5%-35 and Con.SBRPMC1.5%-35, the maximum flexural strengths of beams under the three-point bending test (Table 5-4) are significantly higher than that under the four-point bending test (Table 5-3).

(5) With the same fibre, the mix with the higher fibre content achieved higher flexural strength (see Figure 5-12 (a)).

(6) The load-CMOD curves of the four mixes SBRPMC1%-35, SBRPMC1.5%-35, SBRPMC2%-35 and SBRPMC1.5%-50 are approximately parallel to each other, indicating the four mixes had similar flexural behaviour in post-peak region.

Table 5-4 Flexural strengths of various mixes under three-point bending test (all the tested beams had the same height of 100 mm and the same ligament depth of 80mm)

ID of specimens	No. of beams	Statistics	Limit of propor		Maxim strength		Residual flexural strength			
			$f_{0.05}$ (MPa)	CMOD (mm)	f_P (MPa)	CMOD (mm)	$f_{R,0.5}$ (MPa)	$f_{R,1.5}$ (MPa)	$f_{R,2.5}$ (MPa)	$f_{R,3.5}$ (MPa)
SBRPMC 1%-35	3	Average	10.38	0.05	12.24	0.696	11.96	10.53	9.12	7.74
		STDEV	0.05	0.00	0.96	0.31	0.95	1.10	1.16	1.81
SBRPMC 1.5%-35	5	Average	9.53	0.05	15.22	0.671	14.61	13.53	11.86	10.52
		STDEV	0.85	0.00	1.49	0.33	1.22	1.71	1.63	1.48
SBRPMC 2.0%-35	3	Average	9.80	0.05	17.05	0.789	16.47	15.99	14.57	12.78
		STDEV	1.25	0.00	1.38	0.09	1.20	1.21	1.02	0.79
PVAPMC 1.5%-35	3	Average	11.41	0.05	16.60	0.436	16.17	11.77	9.56	7.39
		STDEV	0.93	0.00	1.94	0.05	1.69	1.91	1.43	1.09
Conv.SBR PMC1.5%-35	3	Average	6.68	0.05	10.37	1.056	9.51	9.88	9.24	8.48
		STDEV	0.93	0.00	0.91	0.50	1.19	0.97	0.69	0.64
SBRPMC 1.5% -50	3	Average	9.72	0.05	16.76	1.194	15.29	15.91	14.7	13.23
		STDEV	0.97	0	1.87	0.301	1.96	1.68	1.25	1.21

Table 5-5 Compressive strength of PMC blocks chopped from tested beams and flexural strength

Mix ID	Num. of blocks	Compr. strength (MPa)		Max. flexur. strength f_p (MPa)	
		Average	STDEV	Average	STDEV
SBRPMC1%-35	3	83.91	6.69	12.24	0.96
SBRPMC1.5%-35	4	79.61	1.48	15.22	1.49
SBRPMC2%-35	3	84.76	0.27	17.05	1.38
Con. SBRPMC1.5%-35	8	68.18	2.82	10.37	0.91
PVAPMC1.5%-35	6	105.87	3.78	16.6	1.94

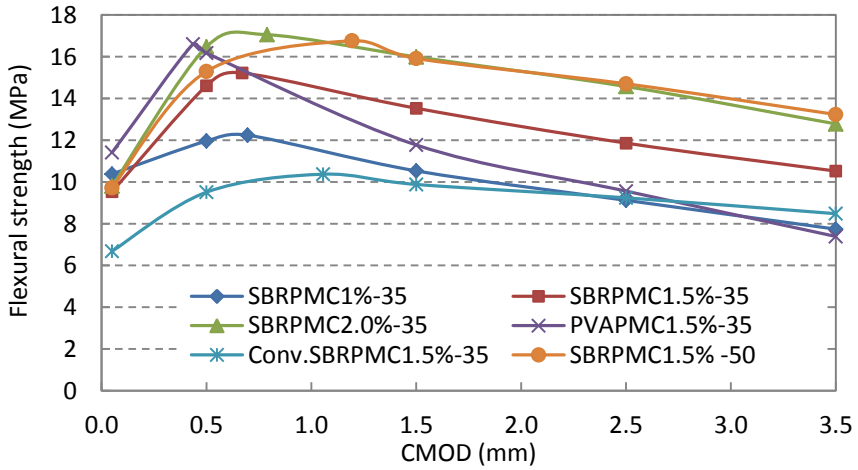

Figure 5-10 Flexural strengths of six PMC notched beams under three-point bending test.

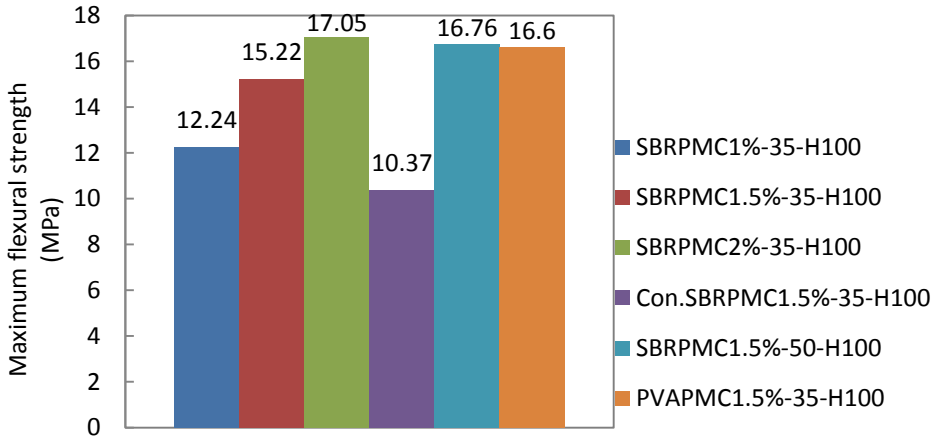

Figure 5-11 Maximum flexural strengths f_p of beams of six mixes under three-point bending test

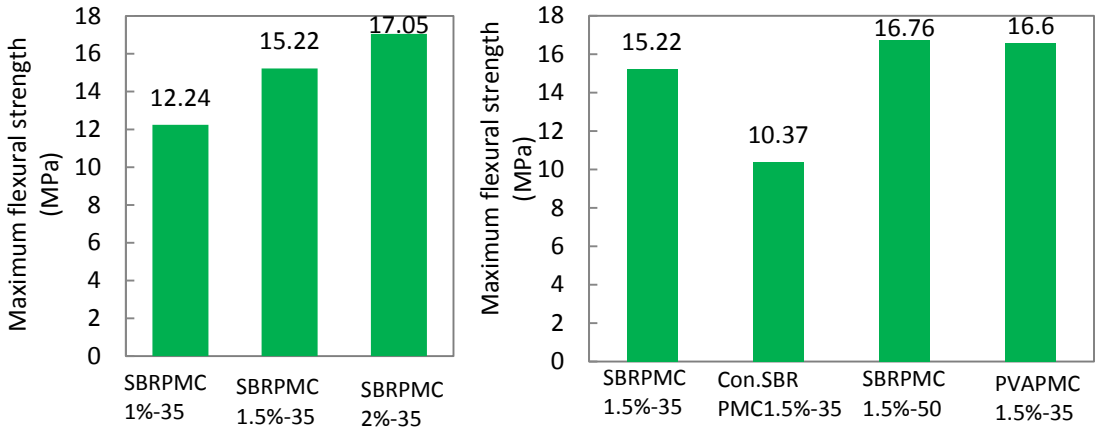

(a) (b)

Figure 5-12 (a) the relationship between maximum flexural strength and fibre content; (b) comparison of maximum flexural strengths of four mixes containing the same fibre content

5.3.3 Equivalent Flexural Strength

Maximum flexural strength is a proper mechanical parameter for assessing SFRC strength. However, it has not been taken into account in current pavement design codes. For example, ACI Committee 360R-92 (1997) recognizes the potential benefits of fibres in concrete slabs-on-ground but does not provide specific design rules for this material. Due to this, the existing design methods for slabs-on-ground are often also adopted for fibre-reinforced slabs. At the same time, design methods for conventional steel bar reinforcement are not suitable because steel fibres represent a diffused reinforcement and are not localized in defined planes.

Rodezno and Kaloush (2010) investigated polypropylene fibre-reinforced concrete for thin white-topping concrete pavements. The thin concrete overlay design is 127 mm, and a test section was constructed and successfully served for 2.5 years. A beam of 101 mm x 101 mm x 457 mm with a central notch was tested in a three-point bend by cyclic loading and

unloading. The RS, defined in Figure 5-13(a) and evaluated by eqn.5.5, was used as a correction factor added to MOR to include the toughness benefits from fibres. The δ_{post} was defined as 0.76 mm without explanation.

$$RS = \frac{A_{post} \cdot S}{(\delta_{post} - \delta_{peak}) B h_{sp}^2} \quad 5.5$$

where A_{post} is the area enveloped under the load-deflection curve from peak load to the load at deflection equal to δ_{post} (here δ_{post}=0.76 mm, defined by Rodezno and Kaloush(2010)); δ_{peak} is the mid-span deflection at peak load; S is the span; h_{sp} is the depth of ligament, i.e. the distance between the tip of the notch and the top of the specimen; B is the width of the beam.

Altoubat et al. (2008) conducted the test of full-scale SFRC slab on an elastic foundation, and related the load carrying capacity to the equivalent flexural strength proposed by the Japan Society of Civil Engineers JSCE-SF4 (1984). He then proposed a simple design method for SFRC pavement. The equivalent flexural strength, $f_{e,3}$, was measured by conducting a four-point bending test. The test beam was 150 mm x 150 mm x 450mm in width, height and span. The equivalent flexural strength is calculated using the area enveloped by load-central deflection curve. Figure 5-13(b) clearly illustrates the definition of equivalent strength, which is evaluated by eqn.5.6. Elsaigh et al. (2005) also used the same concept of equivalent flexural strength for SFRC pavement design.

$$f_{e,3} = \frac{S.A_{3mm}}{2Bh^2} \quad 5.6$$

where A_{3mm} is the area enveloped under the load-deflection curve from the origin to the load at deflection equal to 3 mm; S is the span; B and h are the width and height of beam, respectively. It is noted that eqn.5.6 is for beams with no notch under the four-point bending test.

It is seen that the method for evaluating residual strength proposed by Rodezno and Kaloush (2010) is not suitable to SFRC, because polypropylene fibres in concrete behave differently from steel fibres. Therefore, the equivalent strength, $f_{e,3,}$ which was related to the SFRC pavement design method proposed by Altoubat et al. (2008), is used to evaluate the toughness of SFR-RC-PMC.

Figure 5-13 (a) Definition of residual strength RS proposed by Rodezno and Kaloush (2010); (b) definition of equivalent flexural strength $f_{e,3}$ in JSCE-SF4 (1984)

As has been previously described, the equivalent flexural strength proposed in JSCE-SF4 (1984) is determined by testing the 150 mm (width) x 150 mm (height) x 450 mm (span) beam under the four-point bending test. However, the beams used in the present study were centrally notched, had the dimensions of 80 mm (width) x 100 mm (height) x 400 mm (span), and were tested under the three-point bend. In order to use the equivalent flexural strength concept, which is defined at the specified deflection of 3 mm, it is necessary to correlate the two different test methods via the relationship between deflection and CMOD.

In a bending test, fibres become active after cracking. In the post-peak region a hinge forms at the top of the beam, hence the residual flexural strength is only dependent on the fibre reactions. For different dimensional beams under bending test, the fibre effect can be regarded as similar if the crack lengths and crack opening displacements of the two beams are identical.

In order to compare the toughness in the post-peak region measured from different geometrical beams and loading configurations, Giaccio et al. (2007) proposed an approach to determine the deflection limits of small beams to obtain design parameters of fibre-reinforced concrete. Similar to the techniques proposed by Giaccio et al. (2007) and based on the discussion above, the deflection relationships between the two types of beams are formulated in the following.

Consider the two types of beams with different dimensions under four-point bending and three-point bending shown in Figure 5-14. Beam one is the standard un-notched beam with the dimensions S_1 and h_1 under four-point bend, while beam two is a centrally-notched beam with the dimensions S_2 and h_2 under a three-point bending. In order to obtain identical fibre effect, $CMOD_1$ should be equal to $CTOD_2$.

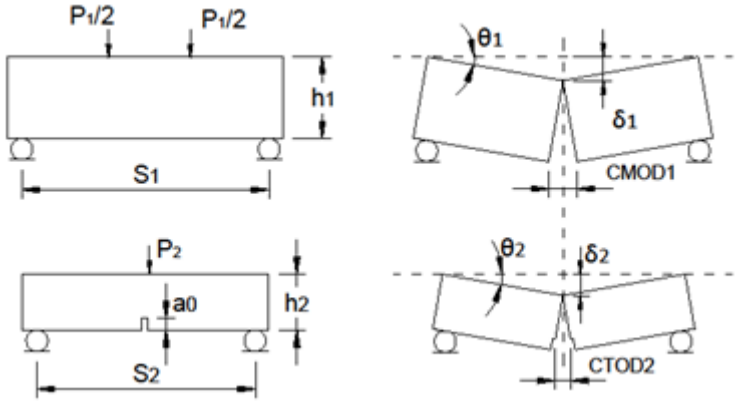

Figure 5-14 Correlation of δ_1 and δ_2 of two beams with different dimensions

In the post-peak region, the relationship between deflection and the rotation angle and crack opening is as follows,

$$\delta_1 = \theta_1 s_1/2 \quad (5.7)$$

$$\delta_2 = \theta_2 s_2/2 \quad (5.8)$$

$$CMOD_1 = 2h_1\theta_1 \quad (5.9)$$

$$CTOD_2 = 2(h_2 - a_0)\theta_2 \quad (5.10)$$

From the equations above and the condition of $\mathrm{CMOD}_1 = \mathrm{CTOD}_2$, the following equation is obtained:

$$\frac{\delta_1}{\delta_2} = \frac{s_1(h_2 - a_0)}{s_2 h_1} \quad (5.11)$$

The standard beam for testing equivalent flexural strength is 150 mm x 150mm x 450 mm, and the specified deflection δ_1 is 3mm. The beams used in the present study were 80 mm x 100 mm x 400mm with an initial notch of 20 mm. Hence, substitution of the dimensions into eqn.5.11 results in:

$$\delta_2 = 1.67\delta_1 \quad (5.12)$$

Thus the corresponding deflection limit δ_2 determined using eqn.5.12 is 5.0 mm. Hereafter, the equivalent strength for the deflection limit of 5 mm is denoted as $f_{e,5}$.

The equivalent flexural strength and maximum flexural strength of the six mixes are listed in Table 5-6 and illustrated in Figure 5-15. The equivalent flexural strengths ($f_{e,5}$) listed in Table 5-6, is used to determine the standard equivalent flexural ($f_{e,3}$) later.

Table 5-6 Equivalent flexural strengths $f_{e,5}$ of PMC beams with the same ligament of 80 mm under three-point bending test

Mix ID	Number of specimens	Loading mode	Statistics	f_P (MPa)	$f_{e,5}$ (MPa)
SBRPMC1%-35	3	3PB	Average	12.24	8.87
			STDEV	0.96	1.42
SBRPMC1.5%-35	3	3PB	Average	15.22	10.86
			STDEV	1.49	0.64
SBRPMC2%-35	3	3PB	Average	17.05	14.05
			STDEV	1.38	1.01
Con.SBRPMC1.5%-35	3	3PB	Average	10.37	9.13
			STDEV	0.91	0.18
SBRPMC1.5%-50	3	3PB	Average	16.76	14.24
			STDEV	1.87	1.16
PVAPMC1.5%-35	3	3PB	Average	16.6	10.05
			STDEV	1.94	0.75

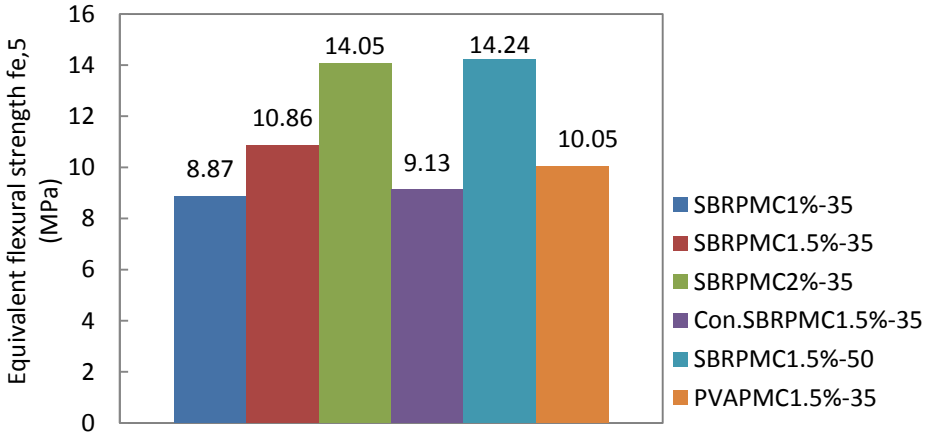

Figure 5-15 Equivalent flexural strengths ($f_{e,5}$) of PMC beams with the same ligament of 80 mm under three-point bending test

Standard Equivalent Flexural Strength $f_{e,3}$

However, the equivalent flexural strength $f_{e,5}$ listed in Table 5-6 and shown on Figure 5-15 cannot be directly used for the design of the steel fibre-reinforced PMC overlay pavement proposed by Altoubat et al. (2008), because specimen sizes remarkably affect flexural strength, which will be studied in Section 5.3.6. As has been presented earlier, the tested beams in this study were of the dimensions 80 mm x 100 mm x 400 mm in width, height and span with a central notch of 20 mm, quite different from the standard beam for testing

equivalent flexural strength proposed by JSCE-SF4 (1984), which is of the dimensions 150 mm x 150 mm x 450 mm in width, height and span. Therefore, the $f_{e,5}$ above needs to be converted using the size effect law for maximum flexural strength developed in Section 5.3.6.

It is seen from Figure 5-10 that the flexural strength-CMOD curves for all mixes are basically parallel to each other except for the mix PVAPMC1.5%-35. It indicates that all mixes have the same scale factor for equivalent strength conversion. The equivalent flexural strengths above were obtained by testing centrally notched beams under the three-point bending test, in order to use the SFRC pavement design method proposed by Altoubat et al.(2008), the $f_{e,5}$ has to be converted twice to obtain the standard equivalent flexural strength $f_{e,3}$: First, it has to be converted from the three-point bending (3PB) to the four-point bending (4PB), its conversion factor (β_1) can be taken as the ratio of maximum flexural strength under 3PB to that under 4PB. Second, it has to be converted from 4PB tested with the beam of 100 mm height to 4PB tested with the standard beam of 150 mm height, with conversion factor (β_2) that can be determined using the size effect equation 5.22 for mix SBRPMC1.5%-35. Both conversion factors are attributed to the size effect, the first factor β_1 is for converting the strength of the small volume to the large volume, which can be explained by Weibull's theory (Quinn 2003) and the factor β_2 is for converting the strength of the small ligament to the large ligament, which is explained by Bazant's theory (Bazant 1989).

The maximum flexural strengths tested under the four-point bend, listed in Table 5-3 are shifted to Table 5-7, for convenience. The conversion factor (β_1) can be easily obtained by simply comparing the f_p in the four-point bend to the three-point bend. The second conversion factor β_2 is calculated in the following way:

$$\beta_1 = \frac{f_P \quad (in\ 4PB)}{f_P \quad (in\ 3PB)} \tag{5.13}$$

$$\beta_2 = \frac{f_P \quad (in\ 150mm-height\ beam)}{f_P \quad (in\ 100mm-height\ beam)} = \frac{\sqrt{\frac{100}{2.7}-1}}{\sqrt{\frac{150}{2.7}-1}} = 0.813 \tag{5.14}$$

$$\beta = \beta_1 \cdot \beta_2 \tag{5.15}$$

The process of calculating the total conversion factor β is listed in Table 5-7, and the standard equivalent flexural strength $f_{e,3,}$ determined by the double conversion, is tabulated in Table 5-8 and plotted in Figure 5-18. The standard equivalent flexural strength $f_{e,3}$ can be regarded as the maximum flexural strength of OPCC and can be used for SFRC pavement design, which was proposed by Altoubat et al.(2008).

It should be pointed out that this equivalent flexural strength $f_{e,3}$ will leads to conservative design for SFRC pavement, due to the fact that SFRC exhibits much higher fatigue life than OPCC with the same maximum flexural strength (Johnston and Zemp 1991; Sun et al. 1996; Paskova and Meyer 1997; Zhang and Stang 1998; Singh and Kaushik 2001).

Table 5-7 Calculation of conversion factors for converting $f_{e,5}$ to $f_{e,3}$

Mix ID	f_p in 3PB (MPa)	f_p in 4PB (MPa)	First conv. factor β_1	Second conv. factor β_2	Total conv. factor β
SBRPMC1%-35	12.24	N/A	0.823	0.813	0.669
SBRPMC1.5%-35	15.22	12.53	0.823	0.813	0.669
SBRPMC2%-35	17.05	N/A	0.823	0.813	0.669
Con.SBRPMC1.5%-35	10.37	9.49	0.915	0.813	0.744
SBRPMC1.5%-50-35	16.76	N/A	0.823	0.813	0.669
PVAPMC1.5%-35	16.6	13.2	0.795	0.813	0.646

Table 5-8 Standard equivalent flexural strengths fe,3 of six mixes converted from fe,5

Mix ID	$f_{e,5}$ (MPa)	Total conversion factor β	$f_{e,3}$ (MPa)
SBRPMC1%-35	8.87	0.669	5.93
SBRPMC1.5%-35	10.86	0.669	7.27
SBRPMC2%-35	14.05	0.669	9.4
Con.SBRPMC1.5%-35	9.13	0.744	6.79
SBRPMC1.5%-50	14.24	0.669	9.53
PVAPMC1.5%-35	10.05	0.646	6.49

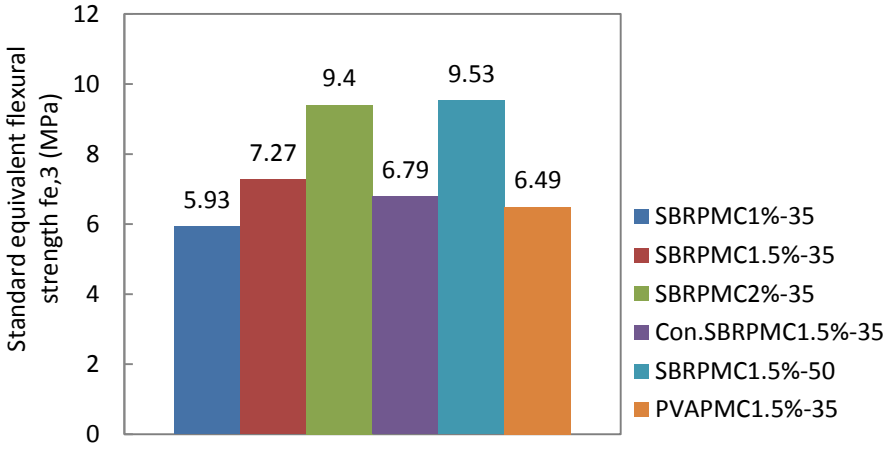

Figure 5-16 Standard equivalent flexural strengths $f_{e,3}$ of six mixes

Verification

The experimental results of SBRPMC1.5%-35 beams with different notch lengths and beam depths, which are used for establishing the size effect law presented in Section 5.3.6, are analysed to verify the method for calculating the equivalent flexural strength, $f_{e,3,}$ which

should be theoretically identical. Two types of beams, i.e. three 80 (width) x 100 (height) x 400 (span) mm with 40 mm-long notch and two 100 (W) x 150 (H) x 500 (S) mm beams with 25 mm-long notch are analysed. The deflection limit for the former, determined using eqn. 5.11, was 6.8 mm, while that of the latter was 4 mm. The equivalent flexural strengths $f_{e,5}$, $f_{e,6.8}$ and $f_{e,4}$ corresponding to the deflection limits of 5, 6.8 and 4 mm, and their conversion factors are tabulated in Table 5-9. It is seen that the standard equivalent flexural strengths, $f_{e,3}$, determined using the method proposed earlier are approximately identical. This validates the method for calculating the standard equivalent flexural strength, $f_{e,3}$ for overlay pavement design.

Table 5-9 Standard equivalent flexural strength determined using the experimental results of beams with different notch length and beam depth (a_0=notch length, h=height of beam)

Mix ID	a_0/h (mm/mm)	$f_{e,5}$ /$f_{e,6.8}$/$f_{e,4}$ (MPa)	f_P in 3PB (MPa)	f_p in 4PB (MPa)	β_1	β_2	$f_{e,3}$ (MPa)
SBRPMC1.5%-35	20/100	10.86	15.22	12.53	0.823	0.813	7.27
	40/100	13.31	16.85	12.53	0.743	0.813	8.04
	25/150	8.89	11.94	N/A	0.823	1.00	7.32

From Table 5-8 and Figure 5-16, the conclusions can be summarised as follows:

(1) For the same fibre content of 1.5%, the mix SBRPMC1.5%-50, which contained 50 mm-length fibres, exhibited much higher standard equivalent flexural strength than the mixes containing 35 mm-length fibres.

(2) The mix SBRPMC1.5%-35 had higher standard equivalent flexural strength than the mix Con.SBRPMC1.5%-35, although they had the same fibre content.

(3) The maximum flexural strength of mix PVAPMC1.5%-35 is higher than that of mix SBRPMC1.5%-35. However, the standard flexural strength of the former is lower than that of the latter, indicating the toughness of the latter is higher than that of the former.

5.3.4 Relative Toughness Index of Two Mixes

ACI Committee 544 (1988, reapproved in 2009) recommends three toughness indexes to assess the toughness of SFRC, shown in Figure 5-17. However, laboratory work indicated that it was difficult to identify the first crack during test; and it is also not easy to identify the first crack deflection δ using load-deflection curves. This resulted in significant scatter in calculated values of toughness indexes. Thus, the indexes are not used to assess the toughness in this study.

Figure 5-17 Definition of toughness of ACI Committee 544 (1988, reapproved in 2009) based on un-notched beam under four-point bending test

In addition to the indexes I_5, I_{10} and I_{30} described earlier, ACI (544.2R-89 1988, reapproved in 2009) also defines the non-dimensional index I_t (see Figure 5-18) representing the relative improvement in the energy absorption capacity due to the inclusion of fibres. The relative index I_t is also a parameter to assess the fibre efficiency in SFRC. It is evaluated by the ratio of the areas enveloped by the load-deflection curve of fibre-reinforced concrete to that by unreinforced concrete.

In this study, five mixes, i.e. mix SBRPMC1.5%-35 and its matrix SBRPMC0%, mix Con.SBRPMC1.5%-35 and its matrix Con.SBRPMC0%, and mix SBRPMC1.5%-50 were used to study the fibre efficiency in roller-compacted concrete and conventional concrete, respectively. The mix proportions of the four mixes are listed in Table 5-1. The beams of mixes SBRPMC1.5%-35 and SBRPMC0% were fabricated by the vibrating compactor, whereas Con.SBRPMC1.5% and Con.SBRPMC0% were fabricated on the vibrating table.

The test procedure for the beams of mixes SBRPMC1.5%-35 and Con.SBRPMC1.5% has been presented in Section 5.3.1. The beams of mixes SBRPMC0% and Con.SBRPMC0% had centrally saw-cut notches to the depth of 33 mm made prior to the test. The three-point bending test was conducted to measure fracture parameters, such as fracture toughness and fracture energy. The specimen dimensions and test procedure complied with the code of RILEM Report 5 1991, but the CMOD- control loading rate was 0.0001 mm/s to obtain stable load-deflection curves, much lower than that recommended by the test code. In addition, the loading-unloading procedure, which is suggested by the RILEM code (1991),

was not performed in the test. The present test for each beam lasted about 30 minutes, much longer than that recommended by the RILEM code.

However, even loaded in the low loading rate of 0.0001 mm/s, the beam of SBRPMC0% failed abruptly at approximate 4 kN, while Con.SBRPMC0% failed at approximate 2.3 kN. As a result, the complete load-midspan deflection curves were not available; consequently the fracture energy determined using these curves are actually the specific fracture energy. Nevertheless, these facture energies will be used for comparison of mixes.

The reason for the abrupt failure of beam during tests is unclear. This phenomenon in the flexural tests also occurred in other steel fibre reinforced PMC beams, at which the load reading was around 2.5-3 kN. The author believes this may be attributed to the software used for controlling the loading rate and the brittleness of the unreinforced material. The relative toughness index, I_t, is evaluated by eqn.5.16 or eqn.5.17, and listed in Table 5-11.

Table 5-10 Mix IDs and dimensions of specimens for testing relative toughness indexes

ID of beams	Mix ID	Dimension (mm) W x H x Span	Depth of notch (mm)
SBRPMC1.5%-35-H100	SBRPMC1.5%-35	80x100x400	20
SBRPMC0%-H100	SBRPMC0%	80x100x400	33
Con.SBRPMC1.5%-35-H100	Con.SBRPMC1.5%-35	100x100x400	20
Con.SBRPMC0%	Con.SBRPMC0%	100x100x400	33

Figure 5-18 Definition of relative toughness index of SFRC and unreinforced concrete by ACI (544.2R-89 1988; Reapproved in 2009)

$$I_t = \frac{Area_{OCD}}{Area_{OAB}} \quad 5.16$$

$$\mathrm{I_t} = \frac{\mathrm{G_{F,SFRC}}}{\mathrm{G_{F,unrein.}}} \quad 5.17$$

where I_t is the relative toughness index, $Area_{OCD}$ and $Area_{OAB}$ are the area enveloped by curve *OCD* and *OAB*, respectively; $G_{F,SFRC}$ and $G_{F,unrein.}$ are the total fracture energy of SFRC and unreinforced concrete, respectively.

Figure 5-19 shows clearly the typical experimental load-deflection at load point curves. The load point deflections of mixes SBRPMC1.5% and SBRPMC0% at failure were 0.178 mm and 18.95 mm, respectively; and Con.SBRPMC1.5%-35 and Con.SBRPMC0% were 19.55 mm and 0.339 mm, respectively. This indicates that the addition of steel fibre greatly enhances the flexural toughness of concrete. The fracture energy of SBRPMC1.5%-35 was 221 times that of SBRPMC0%, while Con.SBRPMC1.5%-35 was 102 times that of Con.SBRPMC0%, indicating that steel fibres in roller-compacted PMC exhibit higher efficiency than in conventional concrete.

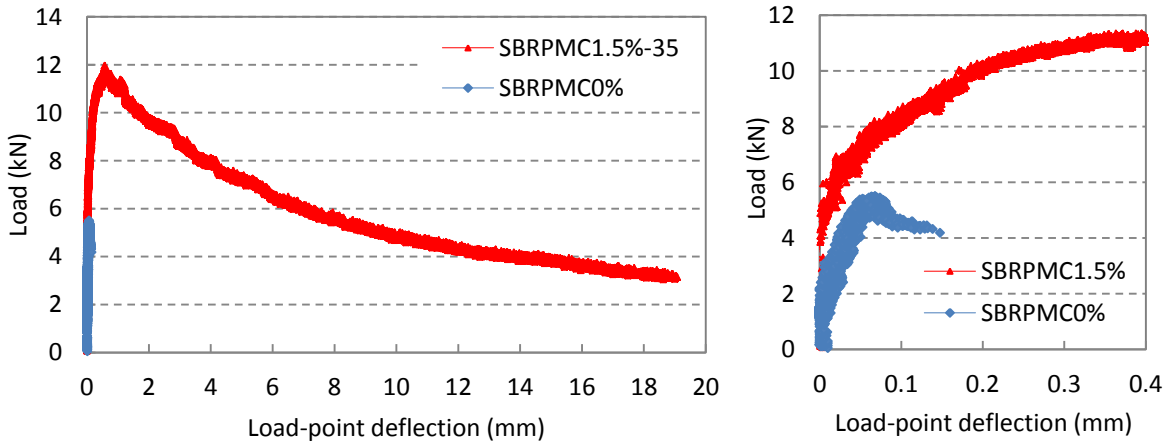

(a) (b)

Figure 5-19 Typical experimental load-load point deflection of mixes SBRPMC1.5%-35 and SBRPMC0%: (a) complete curves, (b) initial parts of load-deflection curves

Table 5-11 Relative toughness indexes I_t of mixes SBRPMC1.5%-35 and SBRPMC1.5%-50 and Con.SBRPMC1.5%-35

Mix ID	Fracture energy G_F (J/m^2)	Relative toughness indexes I_t
SBRPMC1.5%-35	18580	221
SBRPMC0%	84	
SBRPMC1.5%-50	28300	337
SBRPMC0%	84	
Con.SBRPMC1.5%-35	15650	103
Con.SBRPMC0%	152	

5.3.5 Fracture Energy

Griffith (1920) proposed the concept of fracture energy to characterize the material failure process. In 1985, RILEM (1985) proposed a method for measuring the fracture energy of concrete by using a three-point bending test. The fracture energy is defined as the energy absorbed by the unit area of fracture section. In the three-point bending test of a notched beam, work done by the applied load is regarded as equal to the energy absorbed by the

fracture section. Hence, the fracture energy is evaluated by the area enveloped by the load-load point deflection divided by the area of the fractured section.

In this study, the centrally-notched beams of various mixes were tested under three-point bending. The test procedure has been presented in Section 5.3.1. In this section, the fracture energy of beams of six mixes with the same ligament height of 80 mm is evaluated and used to assess the fibre efficiency. The typical load-load point deflection curves have been shown in Figure 5-19. As mentioned earlier, all the tests automatically terminated at the load reading of 2.5-3 kN, other than zero; and the deflections were typically of 18-21 mm for the mixes containing 35 mm-long fibres, while they were 28-29 mm for the mix containing 50 mm-long fibres. This may be attributed to the software used. Thus, the fracture energy should be regarded as specific fracture energy. Nevertheless, the fracture energy obtained by this study can be reasonably used to compare the fracture toughness of different mixes, since their load-deflection curves terminated at the similar load and deflection readings.

The experimental results are tabulated in Table 5-12 and demonstrated in Figure 5-20. It is seen from the values of standard deviation that the fracture energy under flexure is greatly scattered. The following conclusions can be drawn by summarizing the experimental results:

(1) The mix SBRPMC1.5%-50, which contained 50mm-long fibres, exhibited the highest fracture energy, even higher than the mix SBRPMC2%-35, indicating that longer fibres are much more efficient than shorter ones.

(2) The fracture energy of mix SBRPMC1.5%-35 is 1.19 times that of mix Con.SBRPMC1.5%-35, indicating that steel fibres in roller-compacted concrete were more efficient than in conventional concrete (see Figure 5-21).

(3) The fracture energy of mix SBRPMC1.5%-35 is 1.18 times that of mix PVAPMC1.5%-35, although the maximum flexural strength of the former was only 0.92 times that of the latter. Therefore, mix SBRPMC1.5%-35 is better than mix PVAPMC1.5% -35 from the fracture mechanics point of view.

Table 5-12 Total flexural fracture energy of beams of six mixes with the same ligament height of 80 mm under three-point bending test

Mix ID	Heights of ligament (mm)	Num. of beams	Total fracture energy G_F Average (J/m^2)	STDEV (J/m^2)
SBRPMC1%-35	80	3	11620	3160
SBRPMC1.5%-35		2	18580	810
SBRPMC2%-35		3	21590	1160
SBRPMC1.5%-50		3	28300	3330
Con.SBRPMC1.5%-35		2	15650	890
PVAPMC1.5%-35		3	15710	4200

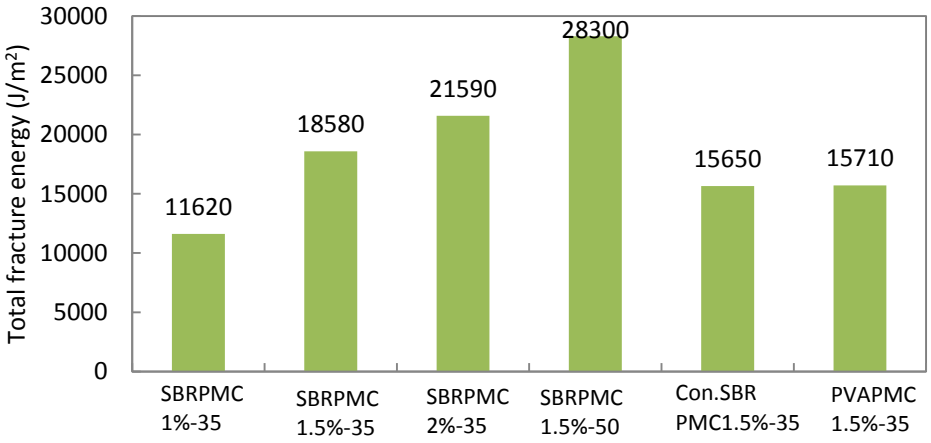

Figure 5-20 Total flexural fracture energy of beams of six mixes with the same ligament height under three-point bending test

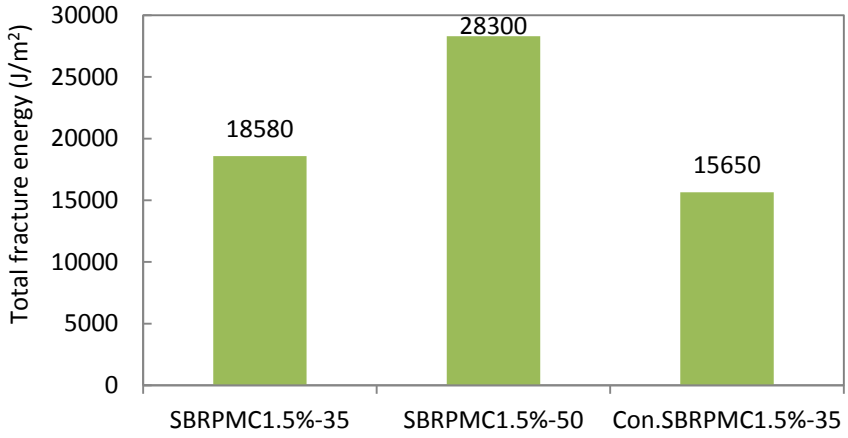

Figure 5-21 Comparison of total flexural fracture energy of different mixes with the same fibre content

5.3.6 Size Effect on Flexural Strength

The fracture mechanics size effect of plain concrete structures has been investigated for more than three decades (Bazant 1984; Bazant and Kazemi 1990; Carpinteri and Ferro 1994; Bazant and Chen 1997; Karihaloo 1999). Most of the literature involves the size effect on

flexural strengths and toughness. Recently Abdalla and Karihaloo (2003), Karihaloo et al. (2003) and Kwon et al. (2008) studied the size effect on fracture energy of plain concrete beams in mode-I loading. However, little literature has been devoted to the size effect on flexural strength of steel fibre-reinforced concrete (Nguyen et al. 2013; Giaccio et al. 2008; Bryars et al.1994).

There are two major approaches to explaining the size effect on the strength of material: the statistical and deterministic approaches. The representative statistical approach is Weibull's theory (Quinn 2003), while the representative deterministic approach is Bazant's(1984) theory based on fracture mechanics. According to Weibull's theory, a larger specimen has a weaker strength because it has a higher probability of having larger and more severe flaws or defects in specimens.

It was not intended for this study to probe the mechanisms of the size effect of SFRC, but to reveal the size effect on flexural strength for further applications. For this purpose, the beams of mix SBRPMC1%-35 and mix SBRPMC1.5%-35 and SBRPMC2%-35 with different ligament heights were tested under the three-point bend. The dimensions of beams and mix ID are listed in Table 5-13. The test procedure was the same as presented in Section 5.3.1.

Table 5-13 IDs of tested beams with different ligament heights under three-point bending test

ID of beams	ID of mixes	Num.of beams	Dim. of beam (mm) W x H x Span	Ligam./notch (mm)
SBRPMC1.5%-35-L40	SBRPMC1.5%-35	2	80x100x400	40/60
SBRPMC1.5%-35-L60	SBRPMC1.5%-35	3	80x100x400	60/40
SBRPMC1.5%-35-L80	SBRPMC1.5%-35	5	80x100x400	80/20
SBRPMC1.5%-35-L125	SBRPMC1.5%-35	2	100x150x500	125/25
SBRPMC1%-35-L50	SBRPMC1%-35	3	80x100x400	50/50
SBRPMC1%-35-L80	SBRPMC1%-35	3	80x100x400	80/20
SBRPMC2%-35-L60	SBRPMC2%-35	3	80x100x400	60/40
SBRPMC2%-35-L60	SBRPMC2%-35	3	80x100x400	80/20

The experimental results are listed in Table 5-14 and Table 5-15, and plotted in Figure 5-22 and Figure 5-23. It is seen that the beam size greatly affects the flexural strength. The maximum flexural strengths and residual strengths significantly decrease with the increase of ligament heights. Therefore, it is necessary to consider the size effect on flexural strength in simulating flexural behaviour and overlay pavement design.

Table 5-14 Flexural strengths of beams of mix SBRPMC1.5%-35 with different ligament heights

Height of ligament mm	Num.of beams	Statistics	Limit of propor.		Maxim. strength		Residual flexural strength			
			$f_{0.05}$ (MPa)	CMOD (mm)	f_p (MPa)	CMOD (mm)	$f_{R,0.5}$ (MPa)	$f_{R,1.5}$ (MPa)	$f_{R,2.5}$ (MPa)	$f_{R,3.5}$ (MPa)
40	2	Average	16.35	0.05	22.24	0.7807	19.15	21.11	19.81	19.33
		STDEV	0.23	0	1.48	0.49	2.27	1.2	2.47	3.9
60	3	Average	10.83	0.05	16.85	0.967	15.41	15.63	14.63	13.53
		STDEV	0.86	0	0.98	0.56	0.71	1.39	1.55	1.06
80	5	Average	9.53	0.05	15.22	0.6709	14.61	13.53	11.86	10.52
		STDEV	0.85	0	1.49	0.33	1.22	1.71	1.63	1.48
125	2	Average	6.44	0.05	11.94	0.561	10.97	10.4	9.36	8.18
		STDEV	1.19	0	0.2	0.42	0.19	0.63	0.4	0.44

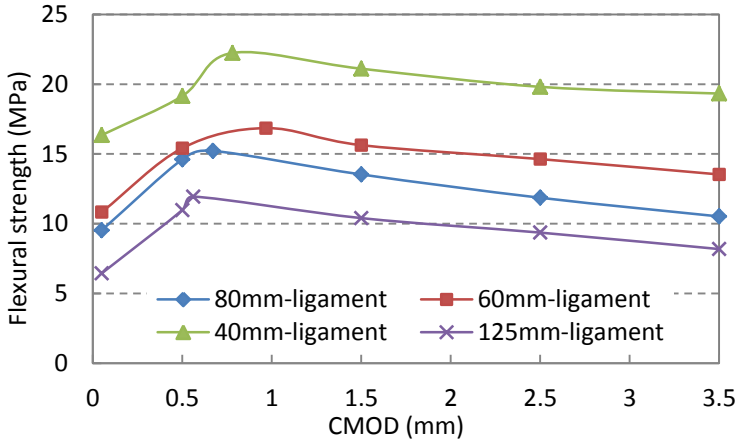

Figure 5-22 Flexural strengths with different ligament heights of mix SBRPMC1.5%-35

Table 5-15 Flexural strengths of mixes SBRPMC1%-35 and SBRPMC2%-35 with various ligament heights

Mix ID	Ligam. heights mm	Statistics	Limit of proport.		Maxi strength		Residual flexural strength			
			$f_{0.05}$ (MPa)	CMOD (mm)	f_p (MPa)	CMOD (mm)	$f_{R,0.5}$ (MPa)	$f_{R,1.5}$ (MPa)	$f_{R,2.5}$ (MPa)	$f_{R,3.5}$ (MPa)
SBRPMC 1%-35	50	Average	14.23	0.05	19.67	0.872	18.72	17.12	14.94	13.74
		STDEV	0.66	0	3.12	0.2	2.37	3.81	3.47	3.16
	80	Average	10.38	0.05	12.24	0.696	11.96	10.53	9.13	7.74
		STDEV	0.05	0	0.96	0.31	0.95	1.1	1.16	1.81
SBRPMC 2%-35	60	Average	11.47	0.05	20.88	1.153	19.02	20.17	19.32	18.33
		STDEV	1.69	0	5.05	0.23	4.55	4.75	4.85	4.76
	80	Average	9.8	0.05	17.05	0.807	16.47	15.99	14.57	12.78
		STDEV	1.25	0	1.38	0.082	1.2	1.21	1.02	0.79

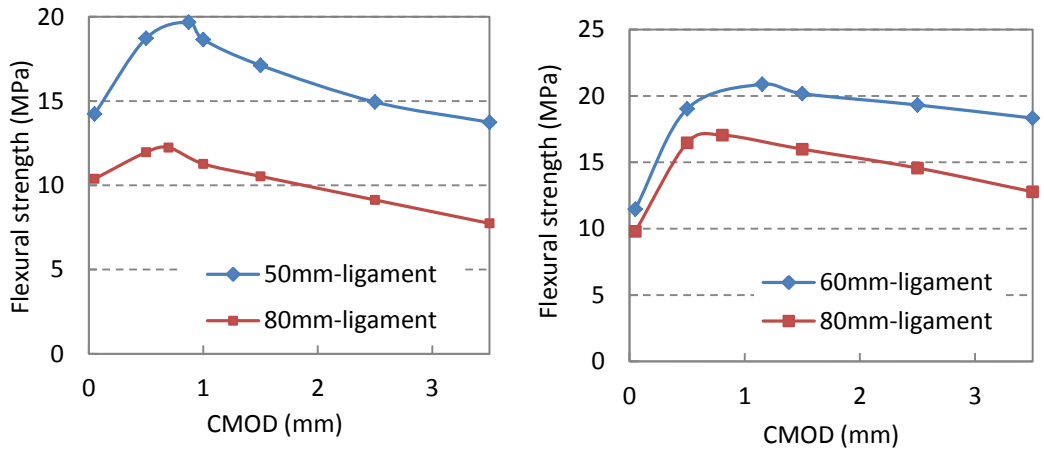

(a) (b)

Figure 5-23 Flexural strengths with different ligament heights: (a) SBRPMC1%-35; (b) SBRPMC2%-35

The size effect on maximum flexural strengths of mix SBRPMC1.5%-35 is further studied by regression analysis for further usage in Section 5.3.3 and Chapter 6. The size effect law for plain concrete proposed by Bazant (1989) describes the relationship between strength and specimen size. It is of the form:

$$\sigma_N = \frac{Bf_t'}{\sqrt{1+\frac{D}{D_0}}} \qquad 5.18$$

where σ_N is nominal stress at failure (MPa); B and D_0 are dimensionless constants; D is the characteristic dimension of structure(mm); f_t' is the tensile strength of the material (MPa). For the notched beam under flexure test, D is the height of ligament. Replacement of σ_N by f_p results in

$$f_p = \frac{Bf_t'}{\sqrt{1+\frac{D}{D_0}}} \qquad 5.19$$

Rearrangement of the above equation results in

$$(\frac{f_t'}{f_p})^2 = \frac{1}{B^2 D_0} D + \frac{1}{B^2} \qquad 5.20$$

If $y = (\frac{f_t'}{f_p})^2$, substituting y into the above equation:

$$y = \frac{1}{B^2 D_0} D + \frac{1}{B^2} \qquad 5.21$$

In this study, the splitting tensile strength of mix SBRPMC1.5%-35 by testing three cylinders with the dimensions Φ100 mm x 170 mm was 9.88 MPa. Plotting the y against D using the experimental results of maximum flexural strengths f_p and the corresponding ligament heights

D (Table 5-14 and Figure 5-24(a)), the linear equation by regression was obtained (Figure 5-24(b)). Thus the following two equations were obtained:

$$\frac{1}{B^2} = -0.0151$$

$$\frac{1}{B^2 D_0} = 0.0056$$

Solving the two equations gives B=-8.14i, D_0=-2.70. Note B is a complex number. Substitution of B and D_0 into eqn.5.19 results in:

$$f_p = \frac{-8.14\text{i}\times 9.88}{\sqrt{1-\frac{D}{2.7}}}$$

Simplification and noting $i = \sqrt{-1}$ leads to:

$$f_p = \frac{80.42}{\sqrt{\frac{D}{2.7}-1}} \qquad 5.22$$

where f_p is the maximum flexural strength (MPa); D is the depth of ligament of the beam (mm).

Equation 5.22 is the size effect law for maximum flexural strength of mix SBRPMC1.5%-35. The experimental maximum flexural strengths and that predicted by eqn.5.22 are plotted in Figure 5-25. It is seen that the size effect of eqn.5.22 predicts the experimental results very well.

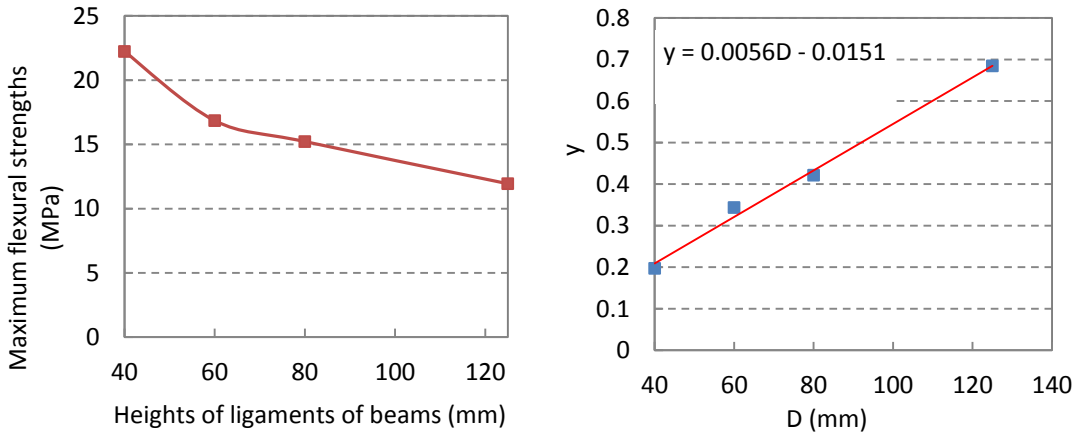

Figure 5-24 Mix SBRPMC1.5%-35 under tree-point bending test: (a) Maximum flexural strengths vs. different ligament heights of beams; (b) y-D diagram for regression

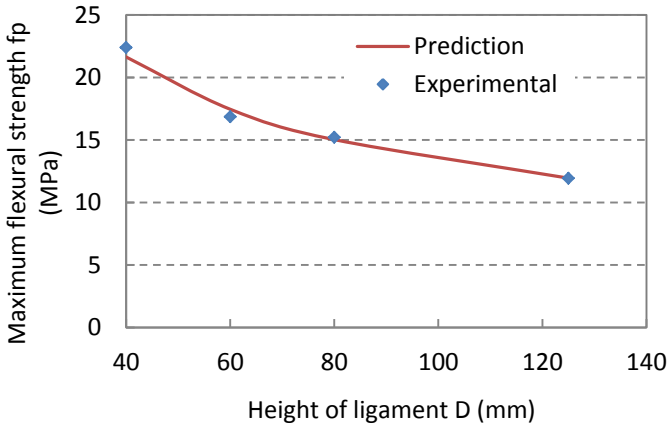

Figure 5-25 Measured maximum flexural strength and that predicted by eqn.5.22

5.4 Flexural Strength of SFR-RC-SBRPMC at Early Ages

During rehabilitation of a worn concrete pavement, traffic disruption is expected. Therefore, high strength at early ages, such as 3 or 7-day ages is desired. In this study, the mix with 10% SBR and the steel fibre content of 1.5% (i.e. mix SBRPMC 1.5%-35) seemed to be the optimum due to both its strength and workability. In order to reveal the flexural strength at early ages, three beams of mix SBRPMC 1.5% -35 for 3-day age and three beams for 7-day age were tested. The beam dimensions, notch depth and test method were all kept the same as described in Section 5.3.1. After de-moulding, the specimens for testing at 3-day age were cured in water until the testing date, whereas the specimens for testing at 7-day age were cured in water for five days, followed by one day of air curing. All beams had saw-cut 20mm-depth notches made in the middle two hours prior to testing.

The experimental results are listed in Table 5-16 and plotted in Figure 5-26, and 28-day strength is illustrated in the same figure as well for comparison. Note the STDEV in Table 5-16 is the standard deviation of the tested strengths of the three beams. It can be seen that the flexural strength of 3-day and 7-day age are much more scattered than that of 28-day age, and the average flexural strength at 3-day, 7-day and 28-day ages are similar. The compressive strength of blocks saw cut from tested SBRPMC1.5%-35 beams at different ages is listed in Table 5-17.

It is not reliable to use the average value to characterize the widely-scattered strength. Therefore, representative strength is necessarily employed to represent the strength. The representative flexural strengths, f_R, calculated by using eqn.5.23 with the confidence level of 90%, are tabulated in Table 5-17 and plotted in Figure 5-27.

$$f_R = f_A - 1.64\,\sigma \qquad 5.23$$

where, f_A is the average strength; σ is the standard deviation (STDEV in Table 5-15) of the tested strengths of the three specimens.

The plot indicates that the representative strength of 3-day age is lower than those of 28-day strength, i.e. the former is 76 percent of the latter. Nevertheless, the representative flexural strength at peak load for 3-day age is 10.10 MPa, much higher than OPCC, whose flexural strength is 4.66 MPa (listed in Table 4-14 under 4PB). The high strength at early-age is the most desirable advantage of the mix of SBRPMC1.5%-35, demonstrating that the mix is very suitable to concrete pavement rehabilitation.

Table 5-16 Flexural strength of mix SBRPMC1.5%-35 at 3-day, 7-day and 28-day ages

Curing age	Statistics	Limit of proport.		Max. strength		Residual flexural strength			
		$f_{ct,L}$ (MPa)	CMOD (mm)	f_p (MPa)	CMOD (mm)	$f_{R,0.5}$ (MPa)	$f_{R,1.5}$ (MPa)	$f_{R,2.5}$ (MPa)	$f_{R,3.5}$ (MPa)
3-day	Average	9.94	0.05	14.4	0.394	13.95	12.83	11.65	10.4
	STDEV	1.03	0	2.62	0.15	2.7	3.34	3.1	2.85
7-day	Average	10.58	0.05	14.27	0.977	13.55	13.44	11.58	10.31
	STDEV	0.77	0	2.68	0.06	2.43	2.63	2.57	2.04
28-day	Average	9.53	0.05	15.22	0.671	14.61	13.53	11.86	10.52
	STDEV	0.85	0	1.49	0.33	1.22	1.71	1.63	1.48

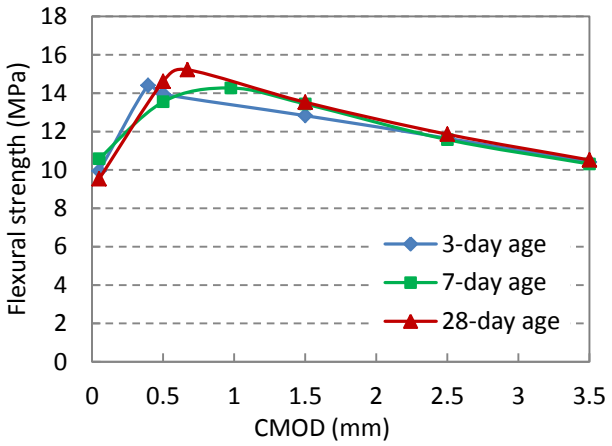

Figure 5-26 Average flexural strength of the mix of SBRPMC1.5%-35 at 3-day and 7-day and 28-day ages

Table 5-17 Representative flexural strengths of SBRPMC1.5%-35 at three ages at the confidence level of 90%

Specimen ID	Limit of proport.	Maximum strength	Residual flexural strength			
	$f_{ct,L}$ (MPa)	f_p (MPa)	$f_{R,0.5}$ (MPa)	$f_{R,1.5}$ (MPa)	$f_{R,2.5}$ (MPa)	$f_{R,3.5}$ (MPa)
3-day age	8.25	10.10	9.52	7.35	6.57	5.73
7-day age	9.32	9.87	9.56	9.13	7.37	6.96
28-day age	8.14	12.78	12.61	10.73	9.19	8.09

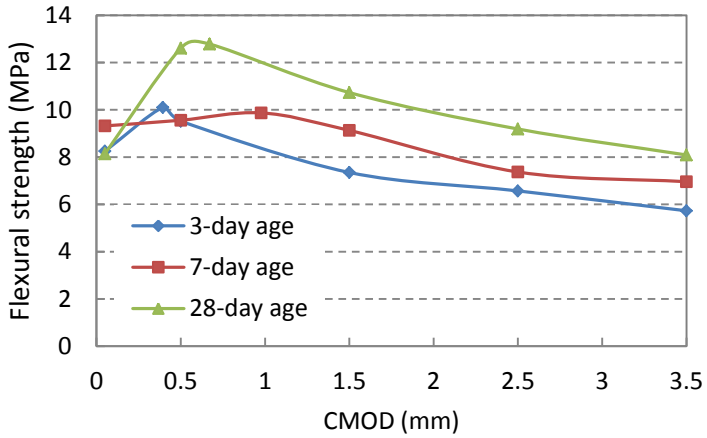

Figure 5-27 Representative flexural strength of SBRPMC1.5%-35 at different ages at confidence level of 90%

Table 5-18 Maximum flexural strength and compressive strength of mix SBRPMC1.5%-35 at different ages

Mix ID	Age (day)	MOR (MPa) Average	STDEV	Compressive strength (MPa) Average	STDEV
SBRPMC1.5%-35	3	14.4	2.62	62.06	0.84
	7	14.27	2.68	67.6	3.64
	28	15.22	1.49	79.61	1.48

5.5 Comparison of Mixes

It is necessary to select the optimal mix for engineering application by comparing both mechanical properties and workability. The flexural properties of six mixes were revealed by the three-point bending test and have been presented in preceding sections, while the workability of the six mixes was assessed by careful judgment from laboratory work. The workability for the mixes suitable for placement by asphalt pavers and compaction by rollers was already defined in Section 4.3.1. The mix SBRPMC1%-35 exhibited low $f_{e,3,}$ which was 0.82 times that of mix SBRPMC1.5%-35; while, the mix SBRPMC2%-35 behaved poor in placement and compaction during specimen formation in laboratory; therefore, the two mixes were regarded as being not suitable for overlay pavements. For this reason the mechanical properties of the four mixes listed in Table 5-1 are rearranged and tabulated in Table 5-19 and Table 5-19, where f_p is maximum flexural strength, $f_{e,3}$ is standard equivalent flexural strength, and G_F is total fracture energy.

The four mixes listed in Table 5-19 contained the same fibre content. It is seen that the mix SBRPMC1.5%-50 is the best from the mechanics point of view. However difficulty in placement and compaction arose due to long fibres. Mix SBRPMC1.5%-35 exhibited proper strength and good workability, and thus seemed to be the optimal. Mix PVAPMC1.5%-35,

which incorporated PVA, exhibited poor toughness and workability; and thus is not a suitable material, although the mix had high bond strength with old existing concrete. Table 5-20 also shows that mix SBBPMC1.5%-35 exhibited appropriate mechanical properties compared with the other two mixes.

The difference between mix SBRPMC1.5%-35 and Con.SBRPMC1.5%-35 in mix proportion is that the former contains less water than the latter. However, the maximum flexural and standard equivalent flexural strengths of mix SBRPMC1.5%-35 are 1.47 and 1.07 times that of Con.SBRPMC1.5%-35. Compared to OPCC used in this study, mix SBRPMC1.5%-35 developed 3.3 times the maximum flexural strength and 1.56 times the equivalent flexural strength than the OPCC (MOR=4.66MPa, listed in Table 4-14).

Table 5-19 Comparison of mechanical properties of four mixes with the same fibre content

ID of mix	f_p (MPa)	$f_{e,3}$ (MPa)	G_F (J/m^2)
SBRPMC1.5%-35	15.22	7.27	18580
SBRPMC1.5%-50	16.76	9.53	28300
PVAPMC1.5%-35	16.6	6.49	15710
Con.SBRPMC1.5%-35	10.37	6.79	15650

Table 5-20 Mechanical properties of three mixes with different fibre contents

ID of mix	f_p (MPa)	$f_{e,3}$ (MPa)	G_F (J/m^2)
SBRPMC1%-35	12.24	5.93	11620
SBRPMC1.5%-35	15.22	7.27	18580
SBRPMC2%-35	17.05	9.4	21590

5.6 Summary

The conclusions from this chapter are presented below, while the specific summaries can be found in each sub-section:

(1) The flexural strength of six mixes, of steel fibre-reinforced roller compacted polymer modified concrete, were tested under a three-point bend, and listed in Table 5-4. The maximum flexural strength for mix SBRPMC1.5%-35 and SBRPMC1.5%-50 were 15.22 MPa and 16.76 MPa, respectively; which are much higher than OPCC; the flexural strength of the latter is usually around 5.0 MPa.

(2) The standard equivalent flexural strength of six mixes, i.e. $f_{e,3}$ listed in Table 5-8, can be regarded as the OPCC with flexural strength identical to the equivalent strength, and

can be used in the overlay design method (thickness design) proposed by Altoubat et al. (2008).

(3) Flexural strength of steel fibre-reinforced roller compacted polymer modified concrete is greatly affected by specimen size. Equation 5.22 describes the relationship between the maximum flexural strength of beam under three-point bending and the depth of ligament of beam for mix SBRPMC1.5%-35.

(4) Mix SBRPMC1.5%-35 can be regarded as the optimal mix considering both strength and workability. Its flexural strength at early ages is very high, and hence it is a suitable mix for worn concrete pavement rehabilitation. Mix PVAPMC1.5%-35 is not the best from the toughness and workability point of view, however it exhibited high bond strength with the old concrete and that influenced its choice. The mix proportion is listed in Table 5-1.

(5) The maximum flexural and standard equivalent flexural strengths of mix SBRPMC1.5%-35 are 1.47 and 1.07 times that of Con.SBRPMC1.5%-35. Compared to OPCC used in this study, mix SBRPMC1.5%-35 developed 3.3 times the maximum flexural strength and 1.56 times the equivalent flexural strength than the OPCC.

6 Mechanism of Flexural Behaviour of SFR-RC-PMC Beams

The mechanical properties of steel fibre-reinforced roller-compacted polymer modified concrete (SFR-RC-PMC) in flexure, including maximum flexural strengths, residual strengths, equivalent flexural strengths, fracture energy and relevant toughness indexes, were extensively studied in Chapter 5. This chapter focuses on the internal mechanism of flexural performance of SFR-RC-PMC beams. For these purposes, this chapter starts with a literature review, and continues with establishment of the relationship of fibre tensile stress and crack face opening displacement. Finally, the fibre efficiency in roller-compacted PMC and conventional SFRC is investigated.

6.1 Introduction

Fibres become active after cracking. SFRC used for structural strengthening is usually in cracked state during normal service life. The addition of steel fibre to OPCC is intended to improve the flexural behaviour of the mixture. After cracking, additional tensile stress acting on the crack face (see Figures 6-1 and 6-5) induced by fibres make a contribution to resisting further opening of the crack and further extension. Therefore, the relationship between the tensile stress developing in the fibre and the crack opening displacement should fully characterize the contribution made by the fibre-matrix interaction. It is thus important to set up the relationship of tensile stress and the crack face opening displacement.

Simulation of crack propagation in SFRC beams in flexure

The main objectives of the simulation of a structure in the test are to establish the relationships of load-CMOD or load-load point deflection to reveal the mechanical behaviour of structures. Three-point bending tests were usually used to avoid multiple-cracking occurrence. The simulation of load-CMOD of SFRC beam in flexure can be roughly classified into two categories: one is the material mechanics-based method, the other is fracture mechanics-based method. For the mechanics of materials approach, three assumptions were usually adopted (Maalej and Li 1994; Zhang and Stang 1998; Nour et al. 2011), such as: linear distribution of stress at the un-cracked section; the tensile stress at the crack tip being equal to the tensile strength of the material; and hinge formation after cracking. Based on these assumptions, the relationships of load-CMOD and load-deflection

were established by applying global equilibrium condition. Figure 6-1 illustrates the three assumptions and the definition of Mode-I loading in fracture mechanics.

Recently, Zhang et al. (2010) proposed the cracking strength of SFRC using three-point bending test, and then simulated the load-CMOD relationships of SFRC beam based on the cracking strength concept (Zhang and Ju 2011). The simulation method using cracking strength concept is essentially a material mechanics based method.

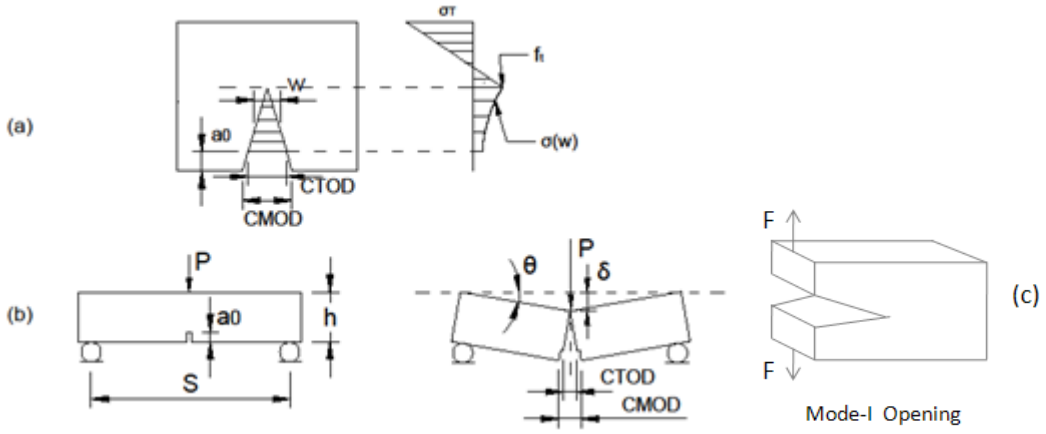

Figure 6-1 In material mechanics based simulation method: (a) assumed linear stress distribution in un-cracked section and the tensile stress at crack tip equal to tensile strength, (b) assumed hinge formed in cracked section. (c) Opening mode (mode-I) in fracture mechanics

Whereas, the fracture mechanics based method was based on the crack propagation criterion, described by eqn.6.1. Crack initiates and extends when the total stress intensity factor is equal to the matrix material toughness

$$K_{Ia} - K_{Ib} = K_{IC,M} \qquad 6.1$$

Where, K_{Ia} and K_{Ib} are the stress intensity factors (SIF) induced by applied load and fibre bridging traction under mode-I loading, respectively; $K_{IC,M}$ is the fracture toughness of the matrix.

The three assumptions adopted in material mechanics-based simulation are obviously debatable, the reasons for these are: (1) the crack tip behaves differently from hinge before crack reaches the top of beam, (2) the tensile stress at crack tip does not exist after the crack reaching the top of the beam. However, the fracture mechanics-based method did not incorporate any assumption, indicating that the latter appears more reasonable than the former.

Fracture mechanics approach used to simulate the crack propagation has been studied since

1980's. Visalvanich and Naaman (1982) used the fracture energy concept to study the extension of cracks. Ballarini et al. (1984) and Foote et al. (1986) employed the stress intensity factor to study the crack growth length and fracture resistance of a SFRC beam. Jenq and Shah (1986) combined materials mechanics and fracture mechanics to simulate crack propagation of SFRC beam under the three-point bending regimes with the aid of several assumptions. Recently, Zhang and Li (2004) simulated the crack propagation of SFRC beams under three-point bend by employing fracture mechanics, based on the criterion of eqn.6.1.

The relationship of tensile stress and crack opening displacement

It seems that whatever the choice of the method, both methods resort to the same relationship of fibre tensile stress and crack opening displacement, usually named fibre bridging law, or σ(w)-w law for convenience (Lindhagen et al.2000; Zhang and Li 2004).

The fibre bridging law of SFRC has been investigated since the 1980s (Stroeven et al. 1978; Li et al 1992; Baggottet and Abdel-monem1992; Li and Chan1994; Zhang and Stang 1998; Guo et al. 1999; Kazemi et al. 2007). These studies can be categorized into two groups, i.e. fibre pullout test and inverse analysis. The former resorts to pulling out individual fibre or aligned fibres to obtain a relationship of the tensile force, versus fibre slip. Fibre pull-out test, including normal fibre and inclined fibre pull-out, provides precise insight into the behaviour of the relationship of tensile stress and fibre slip displacement (Stroeven et al. 1978, Li and Chan 1994, Armelin and Banthia 1997, and Laranjeira et al. 2010). However, the fibre bridging law cannot be obtained directly from these tests because fibres randomly distributed in the matrix behave differently to that in single fibre or aligned fibres tests. Several factors, such as the global orientation factor and the volumetric fraction of fibre, have to be taken into account in establishing the σ(w)-w law. Among these factors considered, the global orientation factor and effective volumetric fraction cannot be tested, and thus their values would be an empirical guess (Jenq and Shah 1986; Armelin and Banthia1997). Therefore, it seems ideal to establish σ(w)-w laws by directly analysing load-CMOD or load-deflection since it is often used to simulate the load-deformation response.

Figure 6-2 (a) experimental tensile stress versus slip displacement carried out by Jenq and Shah (1986), and σ(w)-w law used in simulation using fracture mechanics-based method; (b) experimental tensile stress versus slip displacement carried out by Armelin and Banthia (1997), and σ(w)-w law used to simulate using material mechanics based method.

The shape of σ(w)-w law

Several shapes of σ(w)-w laws have been proposed for material mechanics-based methods to simulate flexural performance. For example, the four models were used by Sousa and Gettu (2006) for establishing σ(w)-w laws by inverse analysis, although the shapes of the four models are quite different from each other; Armelin and Banthia (1997) used a complicated expression derived from fibre pull-out test; Zhang and Li (2004) used the multi-linear lines. Jenq and Shah (1986), and Footeet al. (1986) used the exponential function described by eqn. 6.2.

$$\sigma(w) = f_t \left(1 - \frac{w}{w_c}\right)^m \qquad 6.2$$

where f_t is the maximum stress; w is the crack opening displacement; w and w_c are defined in Figure 6-3, and w_c is usually taken as a half of the fibre length; m is the material constant.

Figure 6-3 σ (w)-w law in exponential form used by Jenq and Shah (1986) and Foote et al. (1986)

The shape of σ(w)-w law under uni-axial tension test

The σ(w)-w laws obtained by direct tensile test are rare to date, the only two σ(w)-w laws available were carried out by Zhang and Stang (1998) for SFRC, and Visalvanich and Naaman (1983) for SFR mortar. Both the fibre bridging laws are illustrated in Figure 6-4.

Zhang and Stang (1998) conducted a direct tensile test of notched SFRC bar, and then established a σ(w)-w law using the regression fitting technique. It was a multi-linear lines, consisting of ascending segment at the initial and descending segments in post-peak region. The multi-linear lines bridging law, which was directly derived from a uniaxial test, was successfully used to simulate the load-CMOD relationship of SFRC beam in flexure by Zhang and Li (2004). The bridging law shown in Figure 6-4(a) can be regarded as the real shape of bridging law for SFRC, since it was established from direct uniaxial test.

It is seen that the bridging laws, such as an exponential function used by Foote et al. (1986) and Jenq and Shah (1986), and the complicated expression used by Armelin and Banthia (1997) are quite different from the real shape, shown in Figure 6-4(a).

Therefore, linear function was used to establish the fibre bridging law by inverse analysis using experimental data from the three-point bending test in this study, since the real shape of the σ(w)-w law of SRFC, experimentally established by Zhang and Stang (1998), shown in Figure 6-4 (a), is consisted of multi-linear lines.

(a) (b)

Figure 6-4 Typical relationship of tensile stress and crack width under direct tensile test: (a) σ(w)-w law obtained using SFRC double-notch strip under direct tensile test; (b) σ(w)-w law obtained using steel fibre-reinforced mortar under direct tensile test

Fibre bridging law by inverse analysis

It is not viable to plant fibers in roller-compacted concrete (RCC) for pull-out tests, and also it is even more difficult to fabricate SFR - RCC (Steel Fibre-Reinforced – Roller -Compacted Concrete) dog-bone-shape specimens for direct tensile tests using a vibrating compactor, due to the mixes being very dry. Thus, the fibre bridging law for steel fibre-reinforced RCC may only be determined by an indirect method. The inverse analysis method, also known as back

analysis technique, has been employed to establish the σ(w)-w law by the following researchers: Guo et al.(1999) proposed a method for determining σ(w)-w laws for the tail of load-deflection curve utilising mechanics of materials. Sousa and Gettu (2006) employed an analytical solution based on the hinged concept proposed by Stang and Oleson (1998, 2000) to establish σ(w)-w laws of concrete and SFRC. Slowik et al. (2006) developed a specialized software for obtaining the σ(w)-w laws of concrete and SFRC from experimental results through an inverse analysis method, which contained an optimization procedure and finite element analysis (FEA) programme. Kwon et al.(2008) also developed a FEA program for analysing experimental results to obtain the σ(w)-w laws of concrete and SFRC. Recently, Zhang and Ju (2011) derived σ(w)-w laws of SFRC by inverse analysis using the concept of cracking strength. All the methods above were based on the materials mechanics-based method. To the authors' best knowledge no researcher has established the σ(w)-w laws by using inverse analysis and fracture mechanics yet.

6.2 Fibre Bridging Law in Flexure Established by Inverse Analysis

Observation on SFRC beam under three-point bending test indicated that the crack initiated from the notch tip, and extended monotonically with load increments. The crack continued to extend but the applied load started falling after the peak load was reached and a hinge formed beneath the top of the beam. The hinge was located at about 0.1h beneath the top (where h is the height of the beam). The complete process of the failure of SFRC beam in flexure consisted of two stages: The stage prior to hinge formation (stage-I) and the stage after the hinge formation (stage-II). In the former, the crack propagates monotonically, and thus it can be considered by fracture mechanics. In the latter, the crack no longer extends, and thus fracture mechanics is no longer valid and material mechanics should take over. Therefore, two expressions are needed to characterize the stress vs. crack-face-opening-width. They are established separately by employing fracture mechanics and material mechanics, respectively.

Crack face profile

The real crack profile can be determined by using the self-consistency concept proposed by Cox and Marshall (1991). Zhang and Stang (2004) employed the concept to determine the crack profile for predicting load-CMOD curves of SFRC beams under a three-point bending test. However, the computation was a complicated iterative procedure and time-consuming. Fortunately, Foote et al. (1986) verified that the straight-line crack profile assumption was

sufficiently accurate for calculating fracture parameters by comparing the exact and the approximate solution. Since then, linear crack profiles have been successfully used in many studies (Jenq and Shah 1986; Maalej and Li 1994; Armelin and Banthia1997; Zhang and Stang 1998; Song et al. 1999; Denneman et al. 2011; Nour et al. 2011).

6.2.1 Formulation of Load-CMOD Relation for Stage-I

Load-CMOD relationships for the stages before and after hinge formation are separately formulated. In stage-I, the crack propagates monotonically, and thus it can be considered by fracture mechanics. Consider the beam under a three point bending shown in Figure 6-15, which shows the specimen dimensions used in this study. Figure 6-5 shows the fibre tensile stress acting on the crack face. The total stress intensity factor (SIF) at the crack tip is the sum of that induced by the applied load P and fibre bridging stress $\sigma(w(x))$, respectively. The crack initiates from the tip of the initial notch when the SIF is equal to fracture toughness of matrix $K_{IC,M}$; and the crack continues advancing as the load increases. After the peak load is reached, the load decreases with crack growth in a displacement control mode. The criterion described by eqn.6.1 is always satisfied during crack propagation in stage-I. The typical experimental load-CMOD curve is illustrated in Figure 6-17.

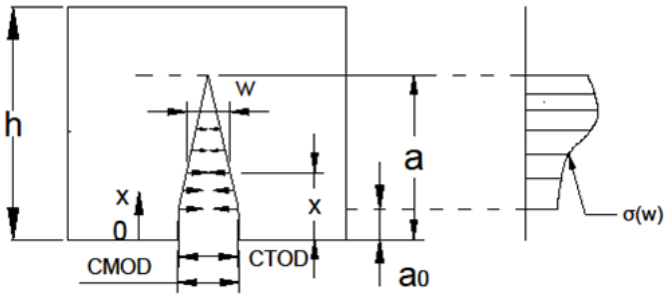

Figure 6-5 Tensile stress of fibres at cracked section of SFRC beam

Verification of Paris' method

In the following, the relationship of load and CMOD is established using Paris' Equation (Tada et al. 2000). The beam without fibres is firstly considered to formulate the load-CMOD relationship, and then load-CMOD relationship is compared with the available analytical solution (Tada et al. 2000). Consider an unreinforced notched beam under the three-point bending test shown in Figure 6-6. Tada et al 2000 provides the following equations to evaluate SIF and CMOD.

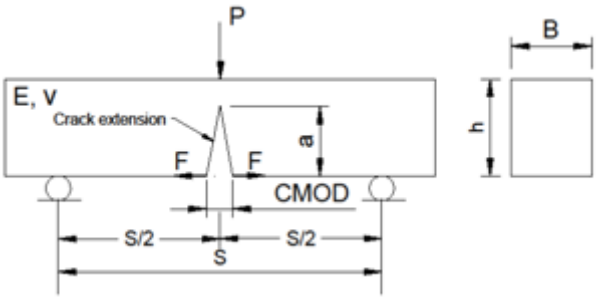

Figure 6-6 Unreinforced beam under 3PB for verification of load-CMOD relationship by Paris' Equation

$$K_{Ia} = \sigma\sqrt{\pi a}F(\frac{a}{h}) \quad 6.3$$

$$CMOD_a = \frac{4\sigma a}{E}V_1(\frac{a}{h}) \quad 6.4$$

$$\sigma = \frac{3PS}{2Bh^2} \quad 6.5$$

$$F\left(\frac{a}{h}\right) = \frac{1.99-\frac{a}{h}\left(1-\frac{a}{h}\right)(2.15-3.93\frac{a}{h}+2.7(\frac{a}{h})^2)}{\sqrt{\pi}\left(1+2\frac{a}{h}\right)(1-\frac{a}{h})^{1.5}} \quad 6.6$$

$$V_1 = 0.76 - 2.28\frac{a}{h} + 3.87(\frac{a}{h})^2 - 2.04(\frac{a}{h})^3 + \frac{0.66}{(1-\frac{a}{h})^2} \quad 6.7$$

where K_{Ia} is the stress intensity factor induced by applied load, $CMOD_a$ is the crack mouth opening displacement induced by applied load, σ is the stress evaluated by eqn.6.5, a and h are the length of crack and depth of beam, respectively.

In the following, the relationship for evaluating *CMOD* is formulated by Paris' Equation (Tada et al. 2000), and then compared with the relationship of eqn.6.7. Referring to Figure 6-6, a virtual pair of forces F acting at crack mouth is exerted. According to Green's function method (Tada et al. 2000) the stress intensity factor K_{IF} induced by the pair of forces is:

$$K_{IF} = \frac{2F}{\sqrt{\pi a}} \cdot \frac{G\left(\frac{0}{a},\frac{a}{h}\right)}{(1-\frac{a}{h})^{1.5}\sqrt{1-(\frac{0}{a})^2}} \quad 6.8$$

where $G\left(\frac{x}{a},\frac{a}{h}\right)$ is Green's function, and evaluated by the following equations

$$G\left(\frac{x}{a},\frac{a}{h}\right) = g_1\left(\frac{a}{h}\right) + g_2\left(\frac{a}{h}\right)\cdot\frac{x}{a} + g_3\left(\frac{a}{h}\right)\cdot\left(\frac{x}{a}\right)^2 + g_4\left(\frac{a}{h}\right)\cdot\left(\frac{x}{a}\right)^3 \quad 6.9$$

$$g_1\left(\frac{a}{h}\right) = 0.46 + 3.06\frac{a}{h} + 0.84\left(1-\frac{a}{h}\right)^5 + 0.66\left(\frac{a}{h}\right)^2\left(1-\frac{a}{h}\right)^2 \quad 6.10$$

$$g_2\left(\frac{a}{h}\right) = -3.52(\frac{a}{h})^2 \quad 6.11$$

$$g_3\left(\frac{a}{h}\right) = 6.17 - 28.22\frac{a}{h} + 34.54(\frac{a}{h})^2 - 14.39(\frac{a}{h})^3 - (1-\frac{a}{h})^{1.5} - 5.88(1-\frac{a}{h})^5 - 2.64(\frac{a}{h})^2(1-\frac{a}{h})^2 \quad 6.12$$

$$g_4\left(\frac{a}{h}\right) = -6.63 + 25.16\frac{a}{h} - 31.04(\frac{a}{h})^2 + 14.14(\frac{a}{h})^3 + 2(1-\frac{a}{h})^{1.5} + 5.04(1-\frac{a}{h})^5 + 1.98(\frac{a}{h})^2(1-\frac{a}{h})^2 \quad 6.13$$

Differentiation of eqn.6.8 with respect to *F* results in

$$\frac{\partial K_{IF}}{\partial F} = \frac{2}{\sqrt{\pi a}} \cdot \frac{G\left(\frac{0}{a'},\frac{a}{h}\right)}{(1-\frac{a}{h})^{1.5}} \quad 6.14$$

Paris' Equation (Tada et al. 2000) for plane stress condition is

$$CMOD = \frac{2}{E}\int_0^a K_{Ia}\frac{\partial K_{IF}}{\partial F}da \quad 6.15$$

Substitution of K_{Ia} and $\frac{\partial K_{IF}}{\partial F}$ into eqn.6.15 results in

$$CMOD = \frac{4\sigma}{E}\int_0^a \frac{F\left(\frac{a}{h}\right)G\left(\frac{0}{a'},\frac{a}{h}\right)}{(1-\frac{a}{h})^{1.5}}da \quad 6.16$$

Replacing *a* with a' in the integrand above to avoid confusion, the following is obtained:

$$CMOD = \frac{4\sigma a}{E}\frac{1}{a}\int_0^a \frac{F\left(\frac{a'}{h}\right)G\left(\frac{0}{a'},\frac{a'}{h}\right)}{(1-\frac{a'}{h})^{1.5}}da' \quad 6.17$$

Let $V_P(\frac{a}{h}) = \frac{1}{a}\int_0^a \frac{F\left(\frac{a'}{h}\right)G\left(\frac{0}{a'},\frac{a'}{h}\right)}{(1-\frac{a'}{h})^{1.5}}da'$, then CMOD derived by Paris' Equation is

$$CMOD = \frac{4\sigma a}{E}V_P \quad 6.18$$

In order to verify the *CMOD* determined by the Paris' Equation, the loading configuration of the unreinforced concrete beam in Figure 6-14 is taken as an example, with the following parameters: S=400 mm, P=100 N, B=1 mm, h=100 mm, E=32365 MPa. The dimensions of the beam were the same as the PMC beams used in this study and the Young's modulus was taken as the elasticity modulus of mix SBRPMC1.5%-35. The comparison of $V_1(\frac{a}{h})$ and $V_P\left(\frac{a}{h}\right)$ is listed in Table 6-1 and illustrated in Figure 6-7. It can be observed that the CMOD evaluated by Paris' method is in excellent agreement with that found by analytical solution.

Table 6-1 Comparison of CMOD factors of Vp (Paris' method) and theoretical V_1

a	10	20	30	40	50	60	70	80	90
V_P	1.4490	1.5532	1.7924	2.2303	3.0140	4.5009	7.7315	16.8908	64.4818
V_1	1.3835	1.4737	1.7162	2.1700	2.9725	4.4696	7.6939	16.8683	66.3555
V_P/V_1	1.0474	1.0539	1.0444	1.0278	1.0140	1.0070	1.0049	1.0013	0.9718

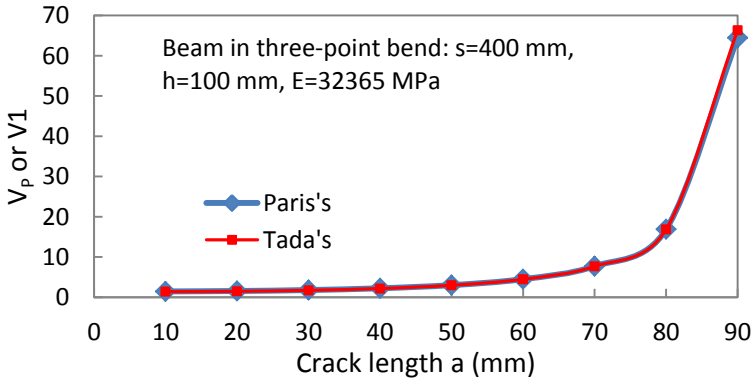

Figure 6-7 Comparison of CMOD factors of Paris' method V_p and theoretical V_1

SIF and CMOD induced by fibre bridging traction

The Paris' Equation method for calculating CMOD induced by applied load has been verified above. It will now be used to formulate the relationships for computing SIF and CMOD of the SFRC beam under three-point bend. Consider the SFRC beam under the three-point bending test shown in Figure 6-8. With the assumption of a straight line crack face, the crack face opening displacement w at x is

$$w = \frac{CTOD}{a-a_0} \cdot (a - x) \qquad 6.19$$

where w is the crack face opening displacement at x, $CTOD$ is the notch tip opening displacement, a_0 is depth of notch, a is crack length.

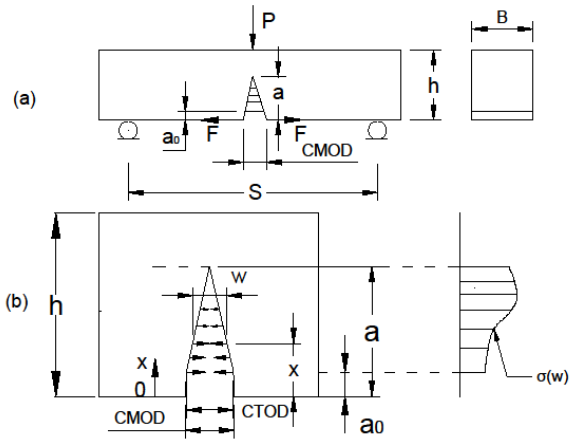

Figure 6-8 (a) notched SFRC beam in three-point bend; (b) fibre tensile stress in cracked section

SIF induced by fibre bridging traction

For a given crack length a, the stress intensity factor K_b induced by fibre tensile stress is evaluated by using Green's function method (Tada et al. 2000):

$$K_{Ib} = \frac{2}{\sqrt{\pi a}} \int_{a_0}^{a} \frac{G\left(\frac{x}{a'}\frac{a}{h}\right)\sigma(w(x))}{(1-\frac{a}{h})^{1.5}\sqrt{1-(\frac{x}{a})^2}} dx \quad 6.20$$

Where, $\sigma(w(x))$ is the fibre bridging law, a and h are defined in Figure 6-8.

$CMOD_b$ induced by fibre bridging traction

The $CMOD_b$ induced by fibre tensile stress is formulated by using Paris' Equation in the following. In order to apply Paris' Equation (Tada et al. 2000) to obtain CMOD induced by fibres, one has to exert a virtual pair of forces F acting at the crack mouth(see Figure 6-8(a)), the stress intensity factor K_{IF} induced by the pair forces is then:

$$K_{IF} = \frac{2F}{\sqrt{\pi a}} \cdot \frac{G\left(\frac{0}{a'}\frac{a}{h}\right)}{(1-\frac{a}{h})^{1.5}\sqrt{1-(\frac{0}{a})^2}} \quad 6.21$$

$$\frac{\partial K_{IF}}{\partial F} = \frac{2}{\sqrt{\pi a}} \cdot \frac{G\left(\frac{0}{a'}\frac{a}{h}\right)}{(1-\frac{a}{h})^{1.5}} \quad 6.22$$

$$CMOD_b = \frac{2}{E}\int_0^a K_{Ib} \cdot \frac{\partial K_{IF}}{\partial F} da = \int_0^a [\frac{2}{\sqrt{\pi a}} \int_{a_0}^{a} \frac{G\left(\frac{x}{a'}\frac{a}{h}\right)\sigma(w(x))}{(1-\frac{a}{h})^{1.5}\sqrt{1-(\frac{x}{a})^2}} dx] \frac{2}{\sqrt{\pi a}} \cdot \frac{G\left(\frac{0}{a'}\frac{a}{h}\right)}{(1-\frac{a}{h})^{1.5}} da \quad 6.23$$

Simplification of eqn.6.23 results in

$$CMOD_b = \frac{8}{\pi E}\int_0^a [\int_{a_0}^{a} \frac{G\left(\frac{x}{a'}\frac{a}{h}\right)G\left(\frac{0}{a'}\frac{a}{h}\right)}{(1-\frac{a}{h})^{3}\sqrt{1-(\frac{x}{a})^2}} \frac{\sigma(w(x))}{a} dx] da \quad 6.24$$

The a in the integrand being replaced with a' to avoid confusion results in

$$CMOD_b = \frac{8}{\pi E}\int_0^a [\int_{a_0}^{a} \frac{G\left(\frac{x}{a'}\frac{a'}{h}\right)G\left(\frac{0}{a'}\frac{a'}{h}\right)}{(1-\frac{a'}{h})^{3}\sqrt{1-(\frac{x}{a'})^2}} \frac{\sigma(w(x))}{a'} dx] da' \quad 6.25$$

Therefore, for the SFRC beam the total CMOD is evaluated by the equation below

$$CMOD = CMOD_a - CMOD_b \quad 6.26$$

Where, $CMOD_a$ and $CMOD_b$ are the crack mouth opening displacement induced by applied load and fibre tensile stress, respectively; and evaluated by eqn.6.4 and eqn.6.25, respectively.

As has been discussed in Section 6.1, the condition for crack extension is $K_{Ia} - K_{Ib} = K_{IC,M}$. It is noted that in eqn.6.25 the expression $1 - \left(\frac{x}{a'}\right)^2$ may take a negative value due to the fact that variables a' and x are integrated over the intervals [0, a] and [a_0, a], resulting in x being larger than a', and consequently leading to the radical $\sqrt{1 - (\frac{x}{a'})^2}$ being a complex number. The applicable value for $CMOD_b$ is the real part of the complex quantity for engineering applications. This was discussed by Xiao and Karihaloo (2002). The right hand side of eqn.6.25 is singular at the integral lower bound for variable a', thus Gaussian quadrature (Richard et al. 2005) was employed to avoid singularity problem. Numerical computation is needed.

6.2.2 Formulation of Load-CMOD for Stage-II

After a hinge formation beneath the top of the beam, the concept of SIF at the crack tip is no longer valid; while the tensile stress on crack face can be characterised by the mechanics of materials approach. In fact, the criteria for crack extension defined by eqn.6.1 would not be satisfied after the hinge formation. Figure 6-9 shows a half of SFRC beam under three-point bending test, in which the crack reaches the top of the beam, and a hinge forms. The fibre tensile stress distributed on the crack face consists of $\sigma_I(w)$ and $\sigma_{II}(w)$. The bending moments caused by applied load and fibre tensile stress with respect to the hinge are:

$$M_P = \frac{PS}{4} \tag{6.27}$$

$$M_f = B\int_{a_0}^{h} \sigma(w(x))(h-x)dx \tag{6.28}$$

where M_P and M_f are the bending moments induced by applied load and fibre traction, respectively. Application of global equilibrium condition with respect to the bending moments results in:

$$\frac{PS}{4} = B\int_{a_0}^{h} \sigma(w(x))(h-x)dx \tag{6.29}$$

where $\sigma(w(x))$ is the fibre bridging law, consisted of $\sigma_I(w) - w$ and $\sigma_{II}(w) - w$; Applying the assumption of straight crack face, the relationships of CTOD and CMOD and crack width at x are:

$$w(x) = \frac{h-x}{h} \cdot CMOD \tag{6.30}$$

$$CTOD = \frac{h-a_0}{h} \cdot CMOD \tag{6.31}$$

where *CTOD* and *CMOD* are the notch tip opening displacement and crack mouth opening displacement, respectively, defined in Figure 6-9.

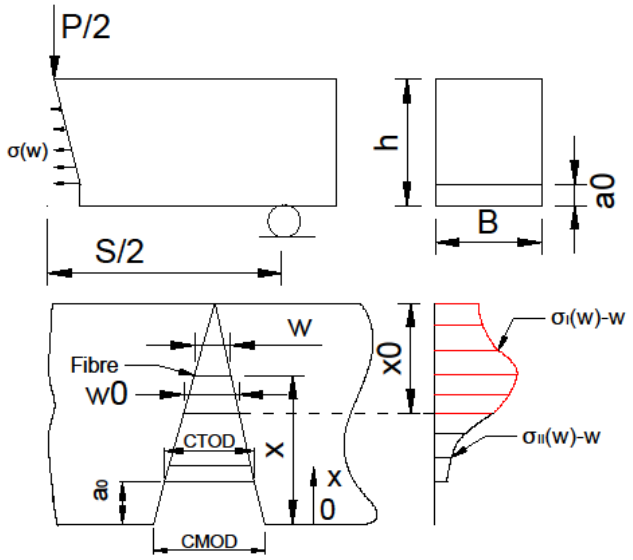

Figure 6-9 Crack reaching top in SFRC beam under three-point bend

Assuming that a hinge form at $w = w_0$, namely fracture mechanics based method is valid in the interval [0, w_0], thus the corresponding length x_0, over which the bridging law $\sigma_I(w) - w$ has been previously established and is still valid, is (see Figure 6-9):

$$x_0 = \frac{w_0(h-a_0)}{CTOD} \tag{6.32}$$

Thus, bending moment with respect to the hinge induced by fibres is evaluated by

$$M_f = B\int_{h-x_0}^{h} \sigma_I\big(w(x)\big)(h-x)dx + B\int_{a_0}^{h-x_0} \sigma_{II}\big(w(x)\big)(h-x)dx \tag{6.33}$$

6.2.3 Fundamentals of Establishment of σ(w)-w Law

The fundamentals of establishing the bridging law

Consider the SFRC notched beam under a three-point bending test shown in Figure 6-10. The x'-axis system is introduced for convenience; x' axis and x-axis system can be easily converted by the following equations. The latter was used to formulate the relationship of stress intensity factor K_{Ib} and $CMOD_b$, as described previously.

$$w = \frac{CTOD}{a-a_0} \cdot x' \tag{6.34}$$

$$x = a - x' \tag{6.35}$$

$$\Delta a = a - a_0 \qquad 6.36$$

It is reasonable to assume that the fibres are evenly distributed in the cracked section. The crack extends when the criterion of eqn.6.1 is satisfied. For crack lengths of $a_1$and a_2 and a_3, the fibre tensile stress distributions are illustrated in Figure 6-10. Consider a layer of fibres near the notch tip. For a small crack extension $\Delta a_1 = a_1 - a_0$, the stress $\sigma(x)$ on the crack face is equal to the tensile stress σ_1 induced by the layer of fibres, as Δa_1 approaches zero. On the crack extension of $\Delta a_2 = a_2 - a_0$, the fibre tensile stress at the crack tip remains invariant, equal to σ_1 with the assumption of uniform fibre distribution, while the stress distribution over a_2 changes. Figure 6-10 clearly shows the variation of stress distribution at the three crack length of a_1 and a_2 and a_3. The $\sigma(w) - w$ can be related to $\sigma(x')$ through the eqns.6.34 and 6.35.

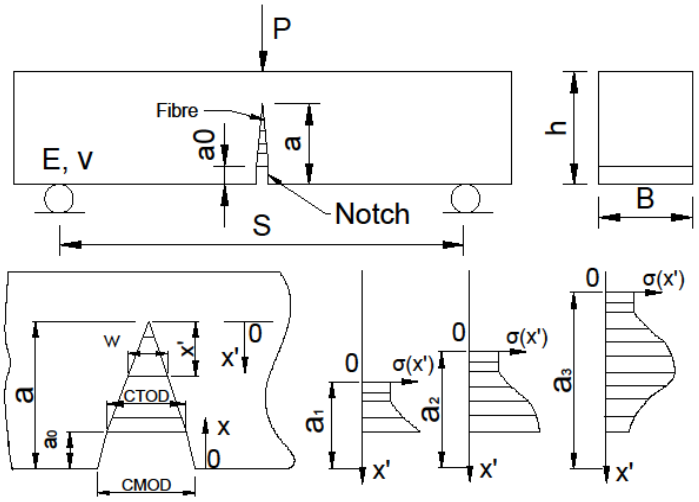

Figure 6-10 SFRC beam under three-point bend and the fibre stress distributions at crack length of a_1 and a_2 and a_3, respectively.

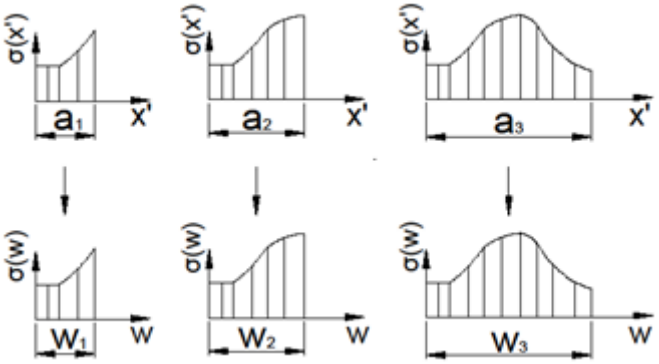

Figure 6-11 Transformation of $\sigma(x')$ to $\sigma(w)$ at three crack lengths of a_1 and a_2 and a_3

Calculation procedure

It has been previously described that the real shape of graph of fibre bridging law, established by Zhang and Stang (1998) using the results of the uniaxial tension test of SFRC bar, was consisted of multi-linear lines. Therefore, the linear function is used to establish $\sigma(w) - w$ law by inverse analysis in this study. Figure 6-12 shows the multi-linear lines, which constitute the bridging law. The calculation procedure is illustrated in Figure 6-13.

$$\left|K_{Ia} - K_b - K_{IC,M}\right| \leq \varepsilon_1 \quad 6.37$$

$$|CMOD - CMOD_i| \leq \varepsilon_2 \quad 6.38$$

$$\left|\frac{M_P - M_f}{M_P}\right| \leq \varepsilon_3 \quad 6.39$$

$$\sigma_i(w) = \sigma_i + \frac{\sigma_{i+1} - \sigma_i}{w_{i+1} - w_i}(w - w_i) \quad 6.40$$

where ε_1, ε_2 and ε_3 are allowable tolerance; *CMOD* is the sum of calculated crack mouth opening displacement determined by eqn.6.26, $CMOD_i$ is the experimental results; i=1, 2, 3, ……, σ_i,σ_{i+1},, w_i, and $w_{i+1}$are defined in Figure 6-12.

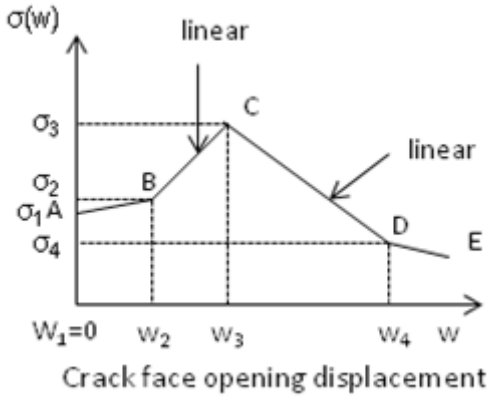

Figure 6-12 Fibre bridging law consisting of multi-linear lines

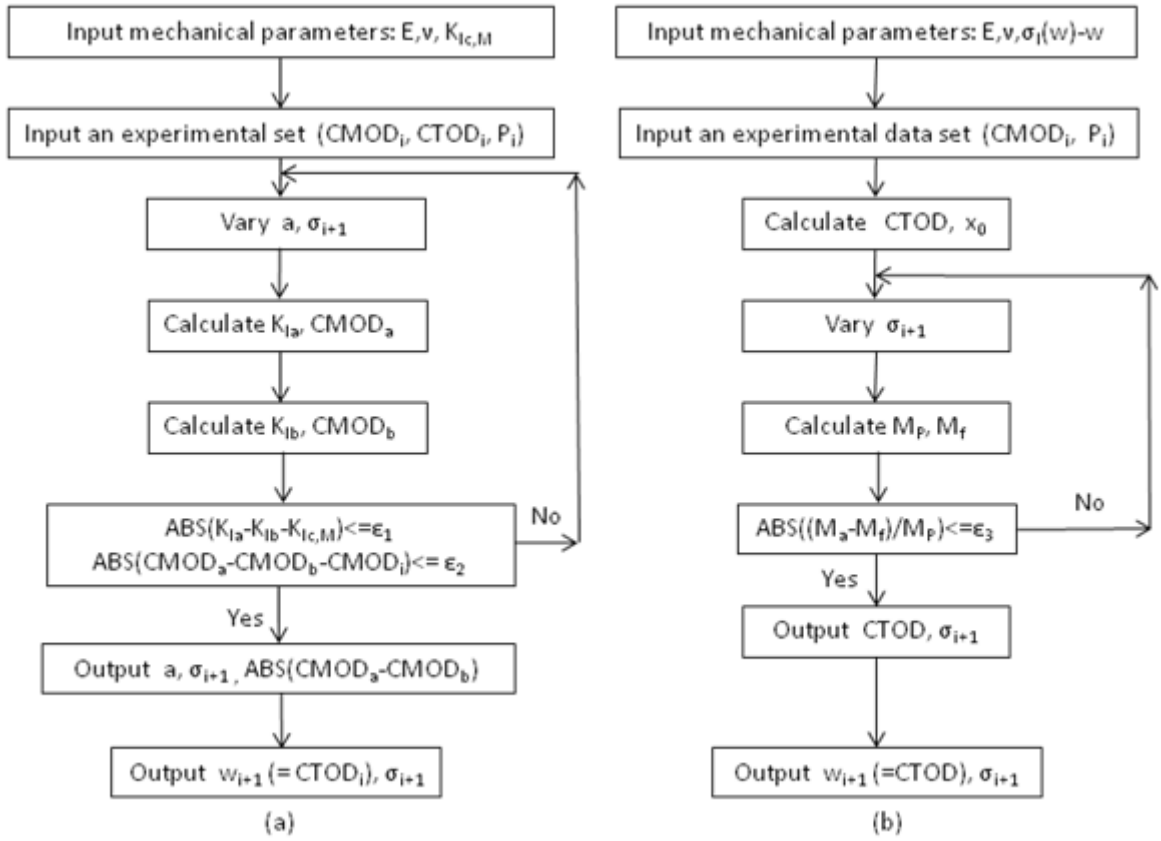

Figure 6-13 Calculation procedures for establishing fibre bridging laws: (a) for stage-I, (b) for stage-II

More detailed explanations for the calculation procedure are as follows (see Figure 6-12):

(1) For the segment AB and its corresponding experimental data set ($CMOD_1$, $CTOD_1$, P_1), it is in stage-I. At the beginning, w_1=0, and setting $\sigma_{1=}\sigma_2$, a and σ_2 are varied to calculate K_{Ia}, K_{Ib}, $CMOD_a$ and $CMOD_b$. The a_1 and σ_2 satisfying the criteria of eqns.6.37 and 6.38 are the solution, and the w_2 is equal to $CTOD_1$. Then, the calculated data sets $(0, \sigma_1)$ and (w_2, σ_2) is obtained.

(2) For the segment BC and its corresponding experimental data set ($CMOD_2$, $CTOD_2$, P_2), the σ_2 has been determined previously. a ($a>a_1$) and σ_3 are varied to calculate K_{Ia}, K_{Ib}, $CMOD_a$ and $CMOD_b$. The a_2 and σ_3 satisfying the criteria of eqns.6.37 and 6.38 are the solution, and the w_3 is equal to $CTOD_2$. Then, the calculated data set (w_3, σ_3) is obtained.

(3) For the segment CD and its corresponding experimental data set ($CMOD_3$, $CTOD_3$, P_3), the σ_3 has been determined previously, The a ($a>a_2$) and σ_4 are varied to calculate K_{Ia}, K_{Ib}, $CMOD_a$ and $CMOD_b$. If the calculation of CMOD or the total sum of SIFs does not converge, it indicates that fracture mechanics based method is no longer valid, and thus the material mechanics based method is needed.

(4) For the same segment CD and its corresponding experimental data set ($CMOD_3$,

P_3) (it is noted that the *CTOD* determined by eqn.6.30 is theoretically more accurate than that measured by LVDT after a hinge formation), it is currently in stage-II. σ_4 is varied to calculate M_P and M_f using eqns.6.27 and 6.28. The σ_4 satisfying the criterion of eqns.6.39 is the solution, and the w_4 is equal to $CTOD_3$. Then, the calculated data set (w_4, σ_4) is obtained.

To now, the calculated data sets (0, σ_1), (w_2, σ_2), (w_3, σ_3) and (w_4, σ_4) are obtained. Repeating the procedure described above, the $\sigma(w) - w$ law can be established.

6.2.4 Experiment

Mix proportion and specimen formation

In this study, eight groups of beams with five types of mixes were prepared. The mix ID and beam ID are shown in Tables 6-2 and 6-3, respectively. The mixes, previously presented in Table 5-1, are listed in Table 6-2, for convenience. The ingredient materials have been presented in detail in Chapter 4. The dimensions of the beams are shown in Table 6-3. The ID of beam indicates both the mix ID and the height of ligament of the beam. For example, beam SBRPMC1.5%-35-L125 indicates that the mix ID is SBRPMC1.5%-35, and the height of the beam is 125 mm. All the specimens listed in Table 6-3 were centrally notched and tested under three-point bend.

Beams of the three mixes SBRPMC1.5%-35-L80, SBRPMC1.5%-50-L80 and Con.SBRPMC1.5%-35-L80 were used to establish fibre bridging laws, while the SBRPMC1.5%-35-L40 and SBRPMC1.5%-35-L60 beams were tested to investigate the size effect on fibre bridging law. The beam SBRPMC1.5%-35-L125 was tested under three-point bend, to compare the load-CMOD relationship with that predicted using the fibre bridging law, established by the beam SBRPMC1.5%-35-L80 beam.

The mix SBRPMC0% was the matrix of the mixes SBRPMC1.5%-35 and SBRPMC1.5%-50. The SBRPMC0%-L67 beams were used to measure the mechanical properties. The experimental results will be used to establish the fibre bridging laws of SBRPMC1.5%-35-L80 and SBRPMC1.5%-50-L80 beams.

All the beams mentioned in the above paragraphs were roller-compacted concrete, thus they were formed with a vibrating compactor. The mixing procedure, curing procedure and specimen formation have been presented in detail in Section 4.4.

Both mixes Con.SBRPMC1.5%-35 and Con.SBRPMC0% were conventional concrete. Mix Con.SBRPMC0% was the matrix of mix Con.SBRPMC1.5%-35. The mix proportion of both

the mixes was the same except that the matrix did not contain fibres. The fresh mix of Con.SBRPMC1.5%-35 exhibited 130 mm slump. The beams of Con.SBRPMC1.5%-35-L80 and Con.SBRPMC0%-L67 were consolidated on the vibrating table. The mixing and curing procedures for the two types of beams were the same as the SBRPMC1.5%-35 beams.

Table 6-2 Mix proportion of mixesSBRPMC1.5%-35, SBRPMC1.5%-50, Con.SBRPMC1.5%-35, matrixes SBRPMC0% and Con.SBRPMC0%

Mix ID	Mix proportion						Mix wet density (MPa)
	Cem.	Coarse aggre.	Sand	SBR	Added water	Fibre by volume	
SBRPMC1.5%-35	1	1.266	1.266	0.217	0.095	1.50%	2482
SBRPMC1.5%-50	1	1.266	1.266	0.217	0.095	1.50%	2478
Con.SBRPMC1.5%-35	1	1.266	1.266	0.217	0.244	1.50%	2330
SBRPMC0%	1	1.266	1.266	0.217	0.095	0%	2306
Con.SBRPMC0%	1	1.266	1.266	0.217	0.244	0%	2297

Table 6-3 Dimensions of tested beams for establishing σ(w)-w by inverse analysis

ID of beams	Num.of beams	Fibre leng. (mm)	Dimen.of beam (mm) width x height x span	Ligament/notch (mm)
SBRPMC1.5%-35-L40	2	35	80x100x400	40/60
SBRPMC1.5%-35-L60	3	35	80x100x400	60/40
SBRPMC1.5%-35-L80	2	35	80x100x400	80/20
SBRPMC1.5%-35-L125	2	35	100x150x500	125/25
SBRPMC1.5%-50-L80	2	50	80x100x400	80/20
Con.SBRPMC1.5%-35-L80	3	35	100x100x400	80/20
SBRPMC0%-L67	3	0	80X100X400	33/67
Con.SBRPMC0%-L67	3	0	100X100X400	33/67

Toughness of Matrixes

The two groups of matrix beams, SBRPMC0%-L67 and Con.SBRPMC0%-L67, were tested under three-point bend. The experimental setup for measuring fracture toughness in mode-I loading is shown in Figure 6-14. The span to depth ratio and notch to depth ratio were 4 and 0.33, respectively. The test procedure complied with RILEM (International union of laboratories and experts in construction materials, systems and structures) code (1991), except for the loading rate. The unloading process required by the RILEM code was not conducted. The loading rate was controlled by COMD at the incremental rate of 0.0001 mm/s. The loading rate was much lower than that recommended by the RILM code (1991). The loading rate was the same as that used in the corresponding mixes in flexural test. CMOD and CTOD and load-point deflection were measured and recorded automatically during the test. The measurement of CTOD at maximum load was taken as the critical crack tip opening

displacement ($CTOD_C$). The Two-parameter model proposed by Jenq and Shah (1985) and adopted by the RILEM code (1991) was employed. The critical stress intensity factor ($K_{IC,M}$,) was determined based on the RILEM code. In the meantime, the stress intensity factor corresponding to crack initiation at the notch tip ($K_{IC,M}^{ini}$), modulus of rupture (MOR) and compressive strength (f_c) were determined from the same test data and listed in the same Table 6-4. The determination method for $K_{IC,M}^{ini}$ was the same as that proposed in Double-K model by Xu and Reinhardt (1999); and the load corresponding to crack initiation at notch tip was obtained by identifying the point of load-CMOD curve from linearity to nonlinearity. The compressive strength was measured by the blocks sawn off the tested beams. All the measured mechanical parameters of the two matrixes are presented in Table 6-4.

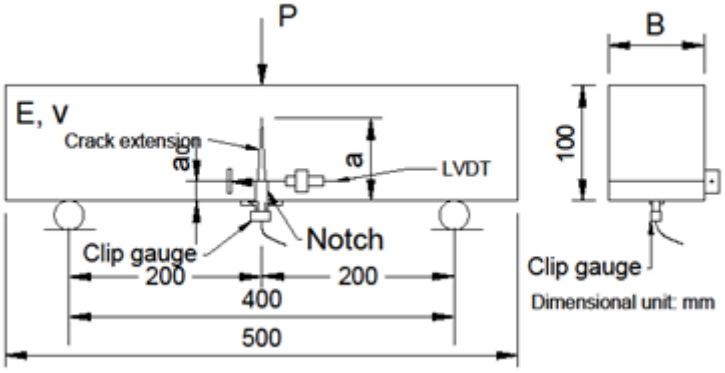

Figure 6-14 Dimensions and instrumentation of unreinforced PMC beam under three-point bend

Table 6-4 Mechanical properties of matrixes SBRPMC0% and Con.SBRPMC0%

Mix ID	Num.of beams	$K_{IC,M}$ (MPamm$^{0.5}$)	$CTOD_C$ (mm)	$K^{ini}_{Ic,M}$ (MPamm$^{0.5}$)	G_F (J/m^2)	MOR(3PB) (MPa)	f_c (MPa)
SBRPMC0%	3	48.76	0.0104	24.63	84	7.93	75.5
Con.SBRPMC0%	3	41.36	0.0182	15.2	152	6.52	65.9

Test procedure and experimental results

The beams of SBRPMC1.5%-35-L40, SBRPMC1.5%-35-L60, SBRPMC1.5%-35-L80, SBRPMC1.5%-35-L125, SBRPMC1.5%-50-L80 and Con.SBRPMC1.5%-35-L80 were tested under three-point bend.

The test machine was a hydraulic servo-closed loop with a maximum load capacity of 150 kN. The beam instrumentation and the experimental setup are pictured in Figures 6-15 and Figure 6-16. The testing data were automatically recorded at a frequency of 5 Hz. The loading rate was controlled by CMOD by the following procedure: 0.0001 mm/s till CMOD was equal to

0.2 mm; and then 0.0033 mm/s till CMOD was equal to 3 mm; and then 0.005 mm/s until the specimen failed. This above has been presented in Section 5.3.1 in detail.

The experimental data of beams of SBRPMC1.5%-35-L40, SBRPMC1.5%-35-L60, SBRPMC1.5%-35-L80, SBRPMC1.5%-50-L80 and Con.SBRPMC1.5%-35-L80 are used to establish fibre bridging laws; while that of SBRPMC1.5%-35-L125 are used to compare with the prediction by the fibre bridging law established by SBRPMC1.5%-35-L80 beam. These will be presented later.

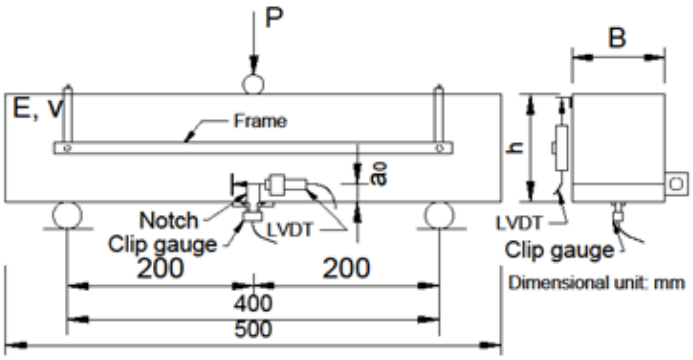

Figure 6-15 Instrumentations and dimension of notched SFRC beam under three-point bending test

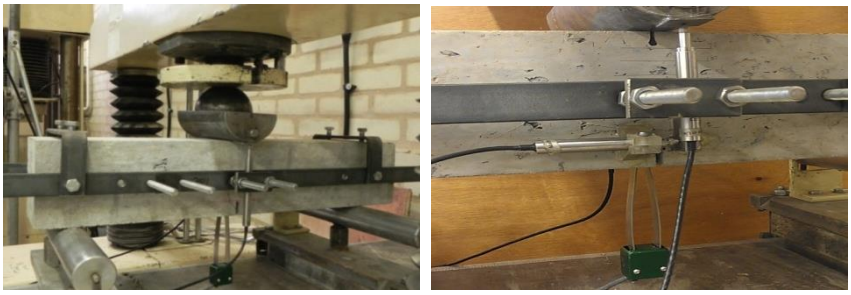

(a) (b)

Figure 6-16 (a) notched SFR-RC-PMC beam in three-point bend; (b) close view of LVDTs for measuring CTOD and load-point deflection, and clip gauge for measuring CMOD

Mechanical properties of SFR-RC-PMC

The mechanical properties of four SFR-RC-PMC mixes, i.e. elasticity modulus *E*, Poisson's ratio *v*, maximum flexural strength f_p, splitting tensile strength f_t and compressive strength f_c are summarized in Table 6-5. The elasticity modulus of mixes SBRPMC1.5%-35 and PVAPMC1.5%-35 were measured using cylinders in compression, of 100 mm x 170 mm in diameter and length. The elasticity modulus of mix Con.SBRPMC1.5%-35 was determined using the experimental load-CMOD relationship. That of mix SBRPMC1.5%-50 was taken as the value of mix SBRPMC1.5%-35 since the only difference between the two mixes was the

fibre length. The compressive strength was measured using blocks saw-cut from the tested beams.

Table 6-5 Mechanical properties of four SFR-RC-PMC mixes

Mix ID	E (MPa)	ν	f_p (MPa)	f_t (MPa)	f_c (MPa)
SBRPMC1.5%-35	32365	0.187	15.22	9.88	79.86
SBRPMC1.5%-50	32365	0.187	16.76		
Con.SBRPMC1.5%-35	31000	0.19	10.37		68.18
PVAPMC1.5%-35	37357	0.239	16.6	9.83	105.87

6.2.5 Establishment of Bridging Laws for SFR-RC-PMC Beams

In this section, the fibre bridging law is established by an inverse analysis approach for mixes of steel fibre-reinforced roller-compacted polymer modified concrete **(**SFR-RC-PMC**)**.

The computational procedure was programmed with MATLAB (Valentine and Hanhn 2007). 6 x 6 Gaussian integrating points (Richard et al. 2005) were used to evaluate the integration for $CMOD_b$, and six Gaussian integrating points were used to evaluate the integration for K_{Ib} and M_f. During the iterative procedure, the crack length a_i at i-iterative step was always bigger than the previous one a_{i-1}, to ensure a monotonically increasing crack length for the crack propagation in stage-I. The allowable tolerance of ε_1 was usually taken to be in the range of 2-6 MPamm$^{0.5}$, that of ε_2 was in the range of 0.008-0.02 mm; and of ε_3 was less than 0.01. The variable allowable tolerance for ε_1 and ε_2 was set for the computational convergence and the obtainment of unique solution.

SBRPMC1.5%-35-L80 beams

In order to clearly demonstrate the method proposed previously, the SBRPMC1.5%-35-L80 beam with 20 mm-depth notch under three-point bend is taken as an example for the establishment of the fibre bridging law. The experimental load-CMOD curves of the two beams are plotted in Figure 6-17; and the averages of CMOD and CTOD and P of the two beams at specified CMOD values are listed in Table 6-6. The calculated σ(w) and corresponding *w* are tabulated in Table 6-6 as well. The fracture mechanics based method was applicable until the crack face opening was equal to 0.958 mm, i.e.w_0=0.958 mm. After that a hinge formed beneath the load point, and thus the mechanics of materials theory was utilised. The interval for calculation in stage-I was in the range of 0.1 – 0.2 mm, while that in stage-II was in the range of 2 – 4 mm. The established fibre bridging law for SBRPMC1.5%-

35 beam is plotted in Figure 6-18. Figure 6-19 illustrates more clearly the enlarged σ(w)-w relationship in stage-I, where fracture mechanics theory is used.

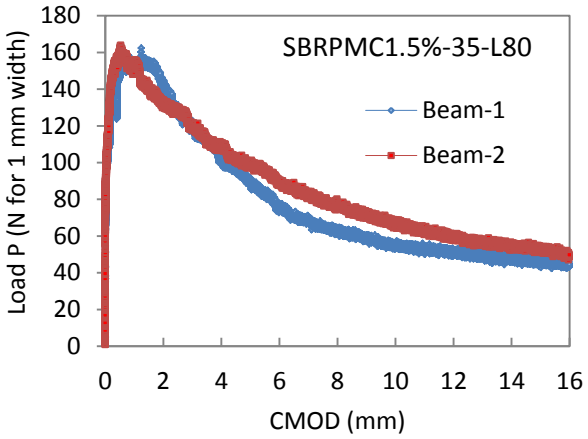

Figure 6-17 Experimental load-CMOD curves of two beams of mix SBRPMC1.5%-35 under 3PB

Table 6-6 Experimental data of beams of SBRPMC1.5%-35-L80 under three-point bend and calculated σ(w) for a given w by inverse analysis (average: h=99.3 mm, a_0=22 mm)

Type of theory	Average of experimental results			Calculated values for σ(w)-w	
	CMOD (mm)	CTOD (mm)	P (1mm width) (N)	w (mm)	σ(w) (MPa)
Fracture mechanics	0	0	0	0.000	5.2
	0.2	0.1206	137.4	0.121	5.2
	0.4	0.2495	147.6	0.250	5.5
	0.6	0.3676	154.6	0.368	5.5
	0.8	0.522	153.5	0.522	5.12
	1	0.663	151.8	0.663	4.93
	1.4	0.958	147	0.958	4.56
Material mechanics	1.6	1.103	146.7	1.103	4.54
	2	1.407	138.4	1.407	4.22
	4	2.945	105.7	2.945	2.5
	6	4.497	82.7	4.497	1.94
	8	6.078	70.2	6.078	1.84
	10	7.646	60.2	7.646	1.06
	12	9.34	54.1	9.340	1.42
	14	10.9	50.5	10.900	1.42
	16	12.45	47.8	12.450	1.38

It is seen that the bridging law for SBRPMC1.5%-35-L80 beams in bending consists of multi-linear lines. It is quite similar to the experimental one under direct tensile tests, illustrated in Figure 6-4(a). This validates the method for establishing σ(w)-w proposed above. The regression fittings with polynomial for the calculated stress σ(w) and crack face opening *w* basically represent its general tendency. The fibre bridging laws will be used to simulate and predict the load-CMOD relationships in Section 6.3 and Chapter 8.

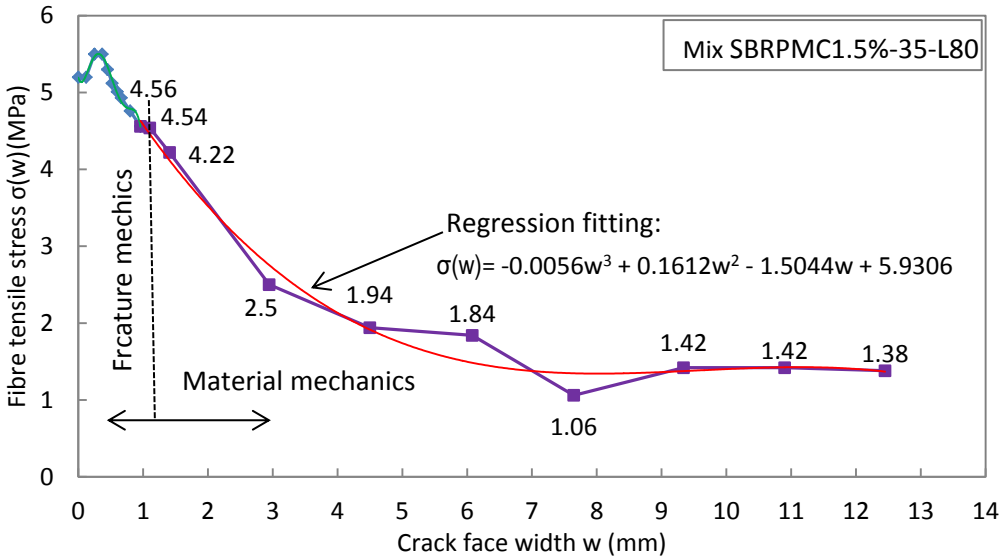

Figure 6-18 Calculated tensile stress σ(w) for given crack face opening w and regression fitting equations for the beams of mix SBRPMC1.5%-35-L80 under 3PB by inverse analysis

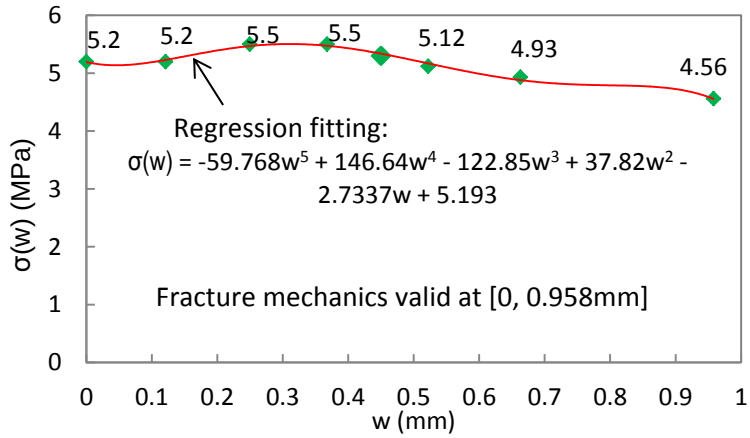

Figure 6-19 Calculated tensile stress σ(w) for given crack face opening w and regression fitting equations for the beams of mix SBRPMC1.5%-35-L80 under 3PB by inverse analysis using fracture mechanics, $w \leq 0.958$mm

Con.SBRPMC1.5%-35-L80 and SBRPMC1.5%-50-L80 beams

The procedure for establishing fibre bridging laws for the Con.SBRPMC1.5%-35-L80 and SBRPMC1.5%-50 beams are the same as that described above. The results are illustrated in Figure 6-20 to Figure 6-23. The fitted polynomials for the fibre bridging laws are shown in the same figures and listed in Table 6-7.

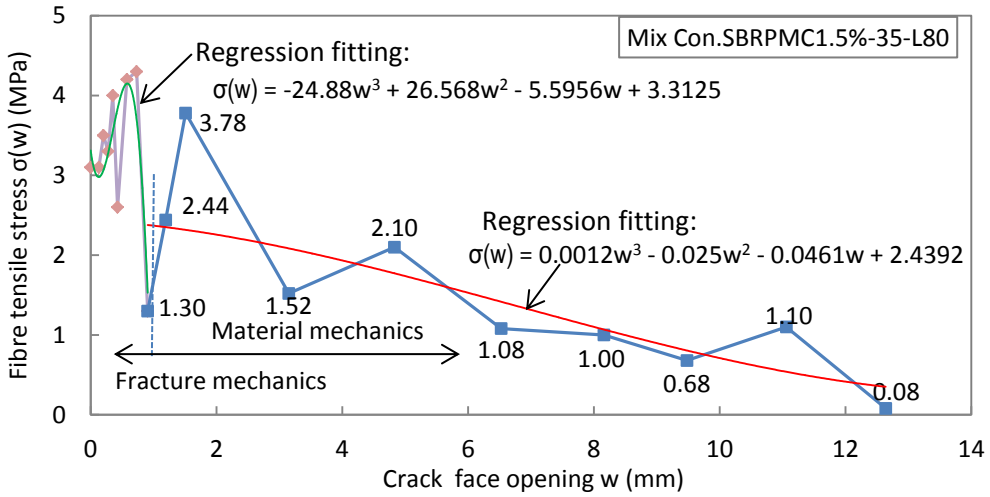

Figure 6-20 Calculated σ(w) and w and regression fitting equations of beam Con.SBRPMC1.5%-35-L80

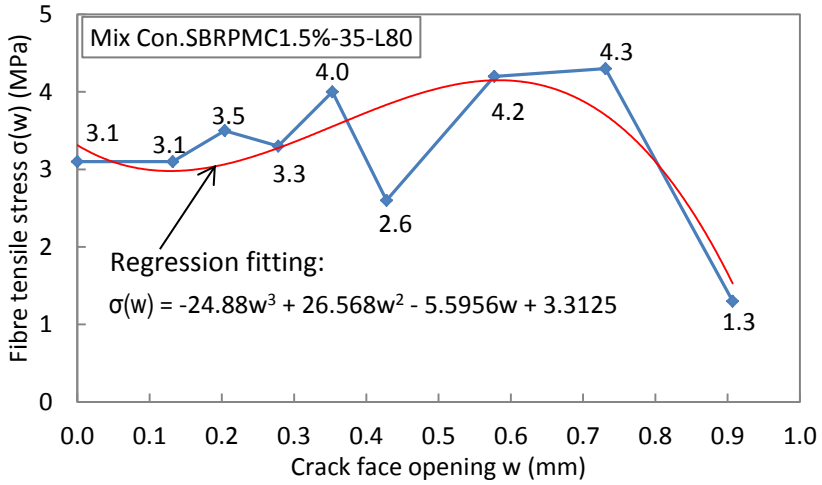

Figure 6-21 Enlarged calculated σ(w) and *w* and regression fitting equations of beam Con.SBRPMC1.5%-35-L80 under 3PB by inverse analysis using fracture mechanics, $w \leq 0.907$mm

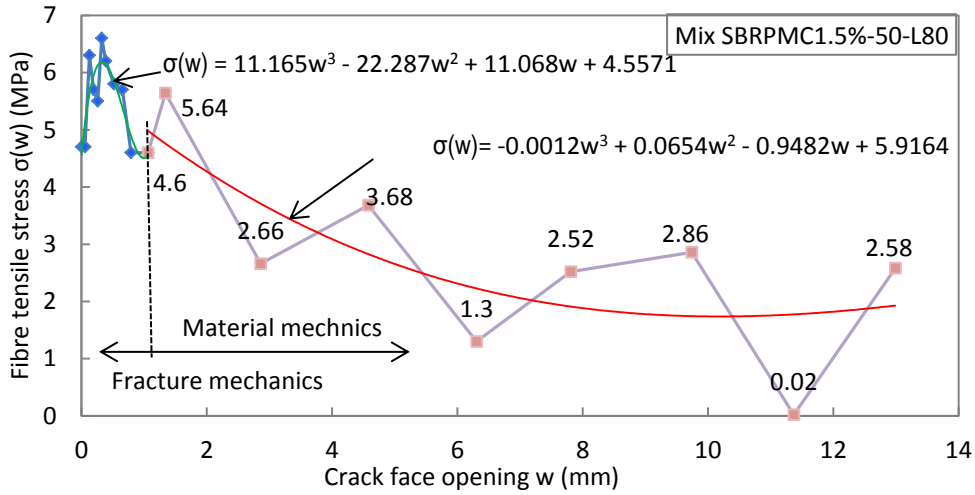

Figure 6-22 Calculated σ(w) and w and regression fitting equations of beam SBRPMC1.5%-50-L80

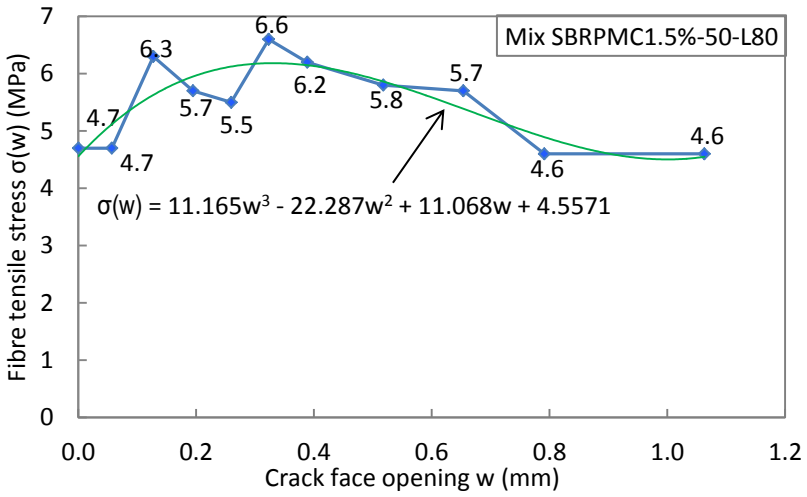

Figure 6-23 Enlarged calculated σ(w) and w and regression fitting equations of beam SBRPMC1.5%-50-L80 under 3PB by inverse analysis using fracture mechanics, w ≤ 1.063mm

The three fibre bridging laws of the three types of beams, i.e. SBRPMC1.5%-35-L80, SBRPMC1.5%-50-L80 and Con.SBRPMC1.5%-35-L80 are demonstrated in Figure 6-24. It is seen that the three fibre bridging laws consist of multi-linear lines, forming ascending and descending segments. The general tendency of the fibre bridging law in stage-I includes an ascending and descending segment, very similar to that experimentally established by Zhang and Stang (1998) (Figure 6-4 (a)). After the hinge formation, the general tendency exhibits descending trend until beam failure. The profile of the σ(w)-w curve of mix SBRPMC1.5%-50 is basically higher than that of mix SBRPMC1.5%-35, indicating that the long fibre provides higher resistance to crack opening than the short fibre.

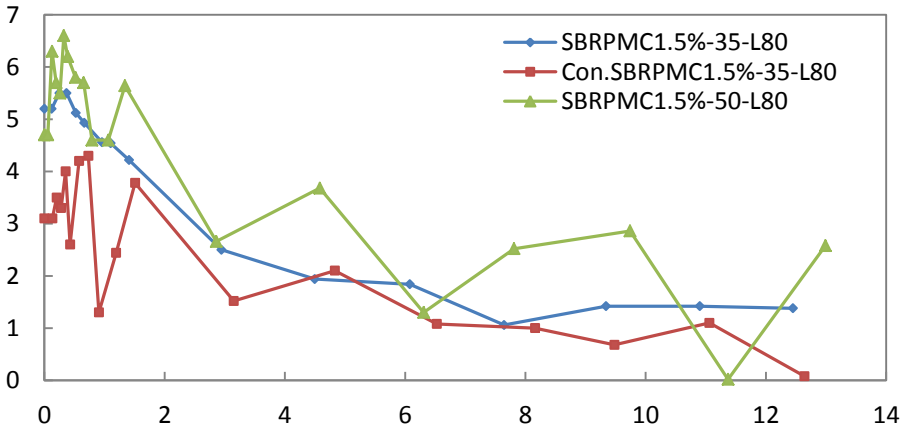

Figure 6-24 Calculated bridging laws of three mixes in poly-linear line form

Table 6-7 Fibre bridging laws of SBRPMC1.5%-35-L80, Con.SBRPMC1.5%-35-L80 and SBRPMC1.5%-50-L80 beams (the unit for σ is MPa, and for w is mm)

Mix ID	Fibre bridging laws under flexure	
SBRPMC1.5%-35-L80	$\sigma(w) = -59.768w^5+146.64w^4-122.85w^3+37.82w^2-2.7337w+5.193$	$0 \le w \le 0.958$
	$\sigma(w) = -0.0056w^3+0.1612w^2-1.5044w+5.9306$	$0.958 \le w \le 12.45$
Con.SBRPMC1.5%-35-L80	$\sigma(w) = -24.88w^3 + 26.568w^2 - 5.5956w + 3.3125$	$0 \le w \le 0.907$
	$\sigma(w) = 0.0012w^3 - 0.025w^2 - 0.0461w + 2.4392$	$0.907 \le w \le 12.64$
SBRPMC1.5%-50-L80	$\sigma(w) = 11.165w^3 - 22.287w^2 + 11.068w + 4.5571$	$0 \le w \le 1.063$
	$\sigma(w) = -0.0012w^3 + 0.0654w^2 - 0.9482w + 5.9164$	$1.063 \le w \le 12.99$

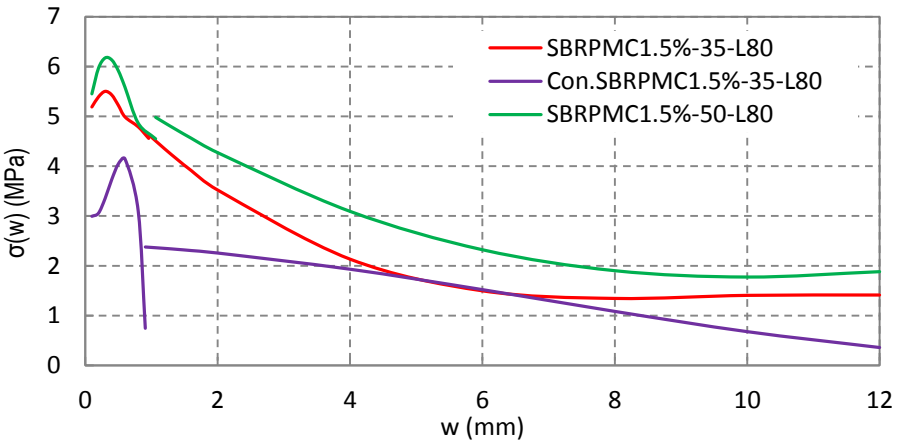

Figure 6-25 Plots of fibre bridging laws in polynomial form listed in Table 6-7

The plots of the fibre bridging law expressed by polynomial expression listed in Table 6-7 are illustrated in Figure 6-25. The polynomial expressions are separately fitted for stage-I and stage-II, due to the fact that they were set up by different mechanics concepts. It is seen that the functions of the bridging law are not continuous at the interface. This causes a slight jump in simulation and prediction of the load-CMOD relationship (Figures 6-28(a) and 6-29).

6.2.6 Fibre Bridging Law Affected by Specimen Size

In this study, three groups of mix SBRPMC1.5%-35 notched beams with different ligament of 80 mm and 60mm and 40mm were tested under a three-point bend to explore the size effect on flexural strength. The beams were denoted as SBRPMC1.5%-35-L80, SBRPMC1.5%-35-L60 and SBRPMC1.5%-35-L40, respectively. The beams were saw-cut to specified depth to obtain different ligaments. The three σ(w)-w relationships for stage-I for the three different ligament beams are shown in Figure 6-26. It shows that the bridging law is affected by specimen size.

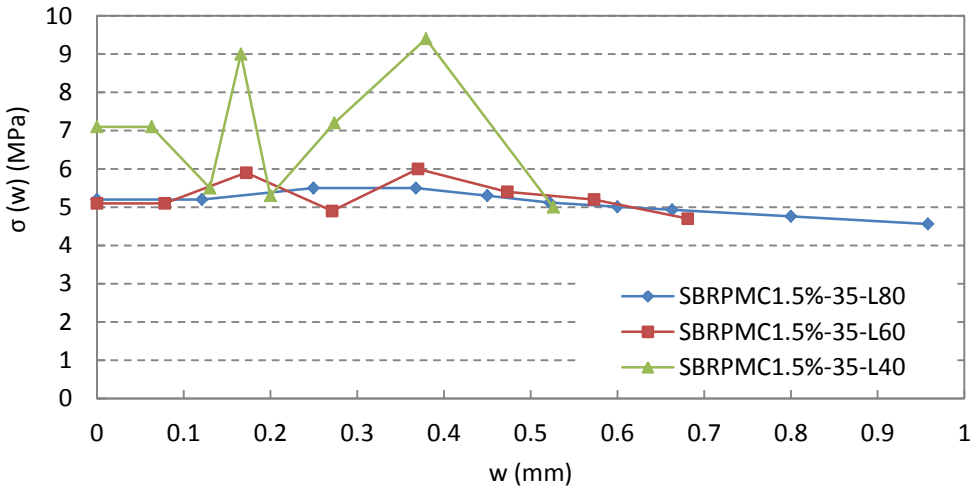

Figure 6-26 *σ(w)* – *w* relationships of beams of SBRPMC1.5% -35-L80, SBRPMC1.5% -35-L60 and SBRPMC1.5%-35-L40

Studying the *σ(w)*–*w* relationships established above, the conclusions can be summarized as follows:

(1) All the profiles of *σ(w)*-*w* laws above are similar to the shape of the *σ(w)*–*w* law established from direct tensile test by Zhang and Stang (1998) (see Figure 6-4(a)), indicating that the method proposed is validated.

(2) The fibre bridging laws are obviously influenced by the size effect. It is thus not a constant material property. The size effect must be taken into account in analysis of flexural performance using fibre bridging law.

(3) Fibre bridging law is greatly affected by fibre aspect ratio (see Figure 6-24 and Figure 6-25); the fibres of higher aspect ratio provide higher tensile stress to resist crack opening.

6.3 Simulation and Prediction of Load-CMOD Relationship

It has been previously pointed out that the bridging law defined by a polynomial, only approximately represented the general tendency of experimental load-CMOD. Thus it is necessary to verify the polynomial bridging law by simulating the load-CMOD relationship. The fibre bridging laws previously established and listed in Table 6-7 are used to simulate the relationship of load-CMOD in the following.

In addition, the fibre bridging laws listed in Table 6-7 will be used to predict the flexural performance of beams with different dimensions, and will be compared with experimental results under three-point bending test conducted independently.

6.3.1 Simulation of Load-CMOD Relationship

The simulation of the complete load-CMOD relationship consists of three stages, i.e. the load and CMOD at cracking initiation at notch tip, in stage-I and stage-II.

Crack initiation at notch tip

Before cracking of the matrix takes place the fibres are inactive, thus the first crack initiation is only dependent on the matrix. The load causing crack initiation at notch tip can be evaluated using eqn.6.3 by setting a=a_0 and $K_{Ia} = K_{IC,M}^{ini}$. The CMOD is calculated using eqn.6.4 with a known load. The critical stress intensity factor of the matrix for crack initiation at notch tip is listed in Table 6-4.

Crack propagation in stage-I

In stage-I, when the notch tip opening displacement (CTOD) is less than w_0, the fracture mechanics method is used. The establishment of the load-CMOD relationship is to calculate the load *P* for a given *CMOD* using the fibre bridging laws established previously. Therefore, for a given *CMOD*, load *P* and crack length *a* are varied to calculate K_{Ia}, K_{Ib}, $CMOD_a$ and $CMOD_b$. The *P* and *a* are the solutions when the criteria of eqns.6.37 and 6.38 are satisfied. In the computation, CTOD is calculated by

$$CTOD = \frac{a-a_0}{a} \cdot CMOD \qquad 6.41$$

where *a* is crack length, a_0 is the depth of notch.

Simulation for stage-II

In stage-II, when the notch tip opening displacement (CTOD) is larger than w_0, the material mechanics-based method is used. The establishment of the load-CMOD relationship is to calculate the load *P* for a given *CMOD* using the fibre bridging law established previously. Therefore, for a given *CMOD*, *P* is varied to calculate x_0 and M_P and M_f. The *P* is the solution when the criterion of eqn. 6.39 is satisfied. The calculation procedure is illustrated in Figure 6-27.

The numerical simulation results are plotted and compared with experimental results in Figures 6-28 and 6-29. It is seen that the simulation of load-CMOD curves are in good agreement with the experimental results, with a slight deviation at interface between fracture and material mechanics.

This validates the fibre bridging laws in polynomial form listed in Table 6-7. It indicates that the complicated multi-linear lines of the *σ(w)-w* relationship can be simply fitted with one polynomial, and the latter can be used to simulate the load-CMOD relationships.

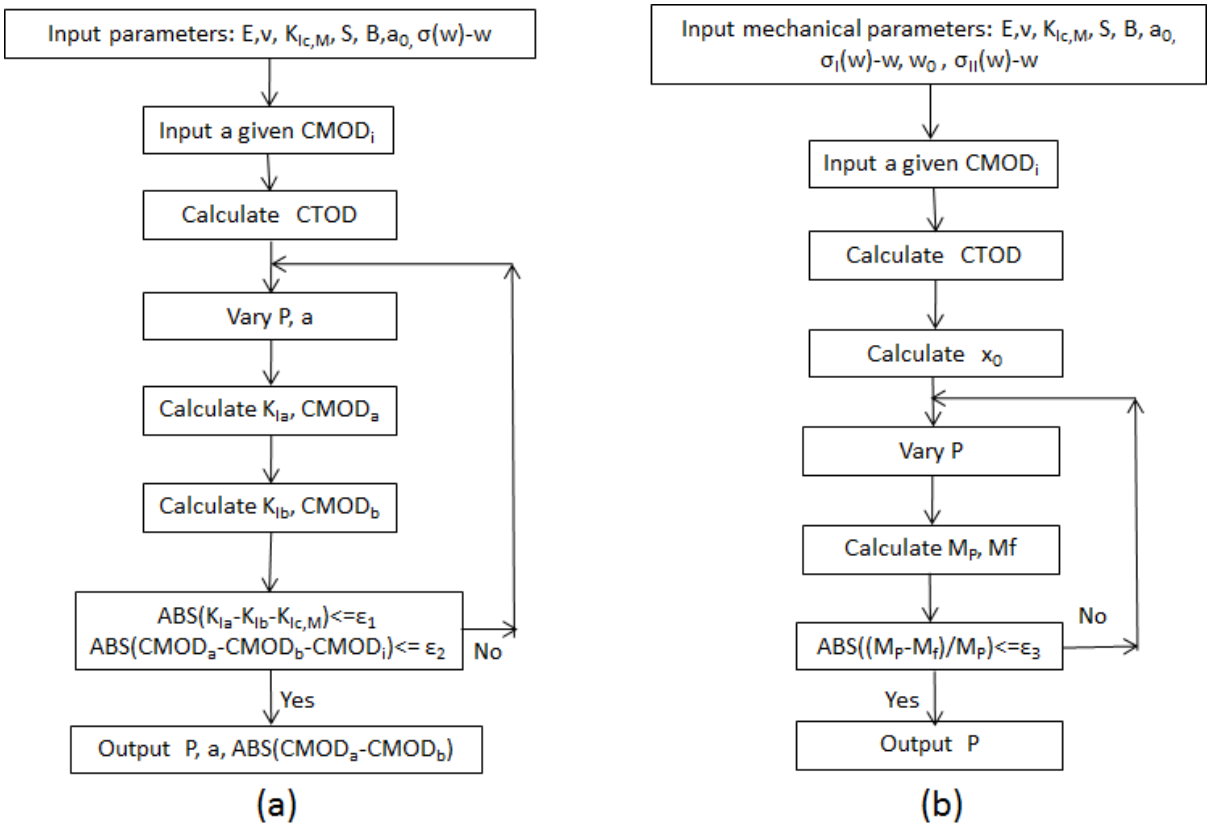

Figure 6-27 Flowchart of calculation procedure for the simulation of load-CMOD relationships: (a) for stage-I, (b) for stage-II

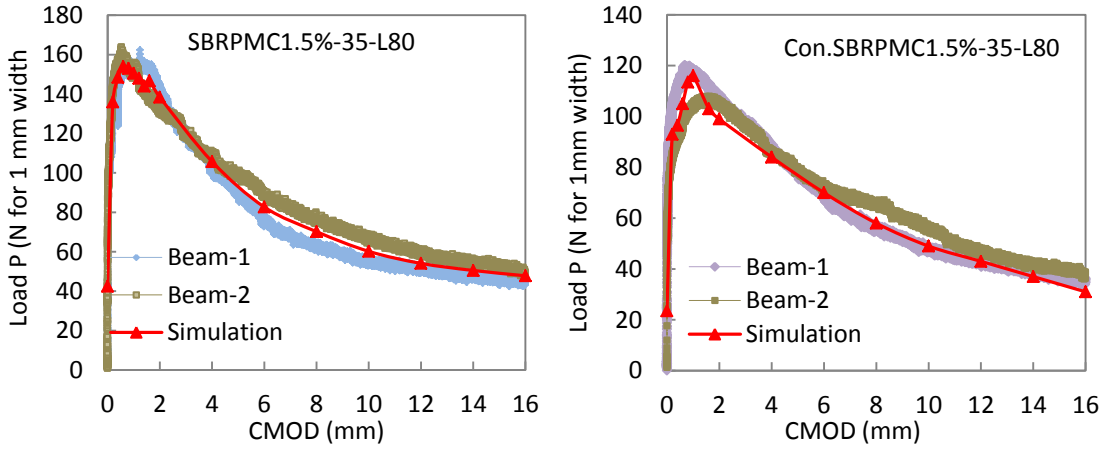

(a) (b)

Figure 6-28 Comparison of experimental load-CMOD curves and simulation curves: (a) SBRPMC1.5%-35-L80 beam; (b) Con.SBRPMC1.5%-35-L80 beam

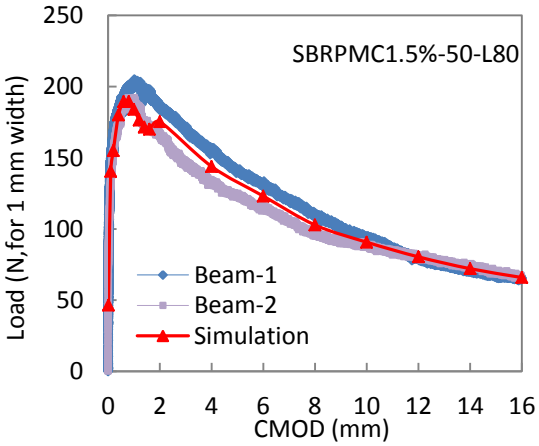

Figure 6-29 Comparison of tested load-CMOD curves and simulated curves of SBRPMC1.5%-50-L80 beam (The transition from fracture mechanics to mechanics of materials approach is visible at the simulation curve)

6.3.2 Prediction of Load-CMOD Relationship

In this study, two beams of mix SBRPMC1.5%-35 with the dimensions 100 mm x 150 mm x 500 mm in width, height and span were tested with the same procedure for other mix beams, such as the SBRPMC1.5%-35-L80 beam described previously. These beams were obviously bigger in size than the beams used for establishing the fibre bridging law, listed in Table 6-7. The relationship of load-CMOD of the bigger beam is predicted using both the fibre bridging law and the calculation procedure proposed earlier.

It has been experimentally affirmed that the fibre bridging law is markedly affected by specimen size. Moreover, the profiles of experimental flexural strength-CMOD curves of beams with different heights of ligament obtained by this study were basically parallel to each other (Figure 6-30), implying that the $\sigma(w) - w$ relationship for different specimen size may be related by a constant factor.

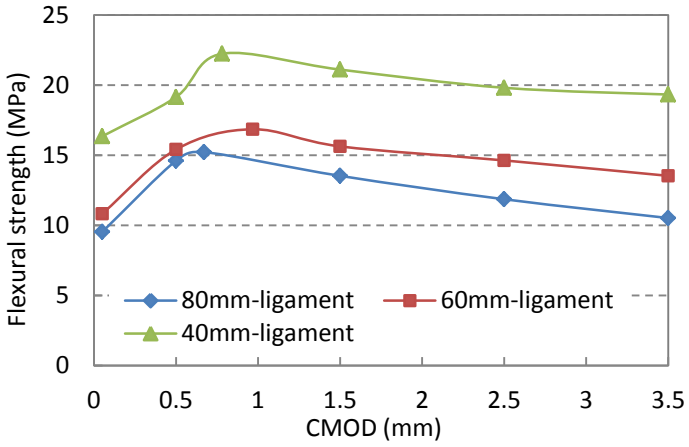

Figure 6-30 Flexural strengths of beams with different ligament heights of mix SBRPMC1.5%-35

In the study, the specimen size effect on maximum flexural strength was experimentally investigated in Section 5.3.6. Equation 5.22 describes the relationship of maximum flexural strength and specimen size for mix SBRPMC1.5%-35. The size effect law is listed here as eqn.6.42, for convenience.

$$f_p = \frac{80.42}{\sqrt{\frac{D}{2.7}-1}} \qquad 6.42$$

where f_p is maximum flexural strength, and D is height of ligament.

The ligament height of the beam for establishing bridging law was 77.3 mm (Table 6-6), and the average height of ligaments of the beams for prediction was 123 mm. Thus, their ratio of maximum flexural strength is 0.787, which is determined using eqn. 6.42. According to the previous discussion, the bridging law for the beam with the 123 mm-height ligament is then:

$$\sigma(w) = 0.787 \times [-59.768w^5 + 146.64w^4 - 122.85w^3 + 37.82w^2 - 2.7337w + 5.193]$$

$$0 \le w \le 0.958\text{mm} \qquad 6.43$$

$$\sigma(w) = 0.787 \times [-0.0056w^3 + 0.1612w^2 - 1.5044w + 5.9306$$

$$0.958 \le w \le 12.45\text{mm} \qquad 6.44$$

where σ(w) is fibre tensile stress, (MPa); *w* is crack face opening displacement, (mm).

The procedure for the prediction of load-CMOD relationship is the same as that described in Section 6.3.1. The prediction of load-CMOD using the bridging law above is illustrated and compared with experimental load-CMOD curves in Figure 6-31. It is reported that the clip gauge of beam-2 disengaged itself from the specimen at a CMOD reading equal to 4 mm, thus the complete experimental load-CMOD curve was not available. It is observed that the prediction is in good agreement with the experimental results; the predicted maximum load is only 8% higher than the average of measured readings of the two beams.

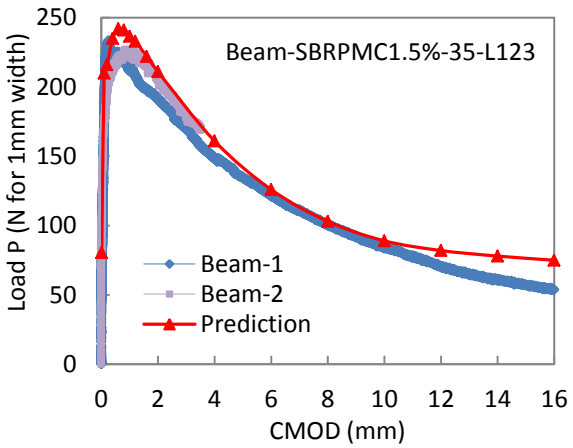

Figure 6-31 Comparison of experimental load-CMOD and predicted curves of beam of SBRPMC1.5%-35-L123

Remarks and conclusion

Summarizing the above, the following conclusions can be drawn:

(1) A method for establishment of SFRC in flexure by inverse analysis was proposed, and verified by simulation and prediction of the load-CMOD relationships of beams. The proposed method consists of two stages: before hinge formation the bridging law was set up by using the fracture mechanics method, and after hinge formation the fibre bridging law was established by using the material mechanics method.

(2) The calculated relationship of stress and crack face width can be regarded as the real stress distribution on the crack face, and shapes of the established bridging laws for the mixes used in the study are similar to those obtained by direct tension tests conducted by previous researchers.

(3) Fibre bridging law is affected by the specimen size. The combination of fibre bridging law and size effect law can be regarded as a material property, and can be used to predict the flexural performance of SFRC beams.

Although the specimens used in the study were steel fibre-reinforced roller compacted SBR modified concrete, the proposed method for the establishment of fibre bridging law is suitable to any fibre reinforced concrete, even plain concrete.

6.4 Efficiency of Steel Fibre

The flexural behaviour of steel fibre-reinforced roller-compacted SBR-modified concrete (SFR-RC-SBRPMC) is mainly dependent on the interaction between the matrix and the steel fibres. Compared to conventional concrete, the roller-compacted concrete has more air voids

and relatively less cement paste, hence this may lead to: (1) the steel fibres may not be fully bonded by cement paste; (2) the steel fibres may be deformed during specimen formation by compaction by the vibrating compactor. The two factors may consequently lead to poor steel fibre efficiency. In addition, the efficiency of 50mm-length fibres also need to be quantitatively investigated by comparison with 35mm-length fibres. So, it is necessary to investigate the fibre efficiency in roller-compacted concrete. Steel fibres have been successfully used in conventional concrete to improve the performance of concrete for several decades. The conventional concrete containing the same steel fibre type and fibre content may be a good benchmark for the investigation of the fibre efficiency in SFR-RC-SBRPMC.

Table 6-8 shows the main physical parameters of mixes SBRPMC1.5%-35, SBRPMC1.5%-50 and Con.SBRPMC1.5%-35. The three mixes contained the same fibre content; and the beams of the three mixes were of similar dimension to avoid any size effect. Table 6-8 clearly indicates that the water to cement ratios and cement paste contents of mixes SBRPMC1.5%-35 and SBRPMC1.5%-50 are much lower than that of the conventional Con.SBRPMC1.5%-35. Also, the former have higher air content than the latter. The mix Con.SBRPMC1.5%-35 was conventional concrete, its slump of fresh mix was measured to be 130 mm.

Table 6-8 Comparison of physical properties of mixes SBRPMC1.5%-35, SBRPMC1.5%-50 and Con.SBRPMC1.5%-35 and their corresponding matrixes SBRPMC0% and Con.SBRPMC0%

Mix ID	Workability of fresh mixes	W/C	Cem. paste by volume (%)	Air content (%)	Comp. streng. (MPa)
SBRPMC1.5%-35	Dry, non-slump	0.206	37.94	2.94	80.08
SBRPMC1.5%-50	Dry, non-slump	0.206	37.94	2.94	78.37
Con.SBRPMC1.5%-35	High slump of 130mm	0.355	42.3	1.2	65.22
SBRPMC0%	Dry, non-slump	0.206	N/A	N/A	65.99
Con.SBRPMC0%	High slump, > 130mm	0.355	N/A	N/A	65.87

Note: the water for determining water to cement ratio and cement paste fraction included the water contained in SBR but excluded the water absorbed by coarse aggregate

The three mixes were tested under three-point bend, and the experimental data have been analysed to obtain maximum flexural strength f_p, equivalent flexural strength $f_{e,3,}$ relative toughness index $I_{t,}$ and total fracture energy G_F. These mechanical parameters are rearranged to study the fibre efficiency in the following:

Flexural strength

Flexural strengths, including maximum strength and residual flexural strength of the three mixes, are plotted in Figures 6-32 and 6-33. It is seen that mix SBRPMC1.5%-50 exhibited the highest maximum flexural strength and residual flexural strength, and mix Con.SBRPMC1.5%-35 exhibited the lowest.

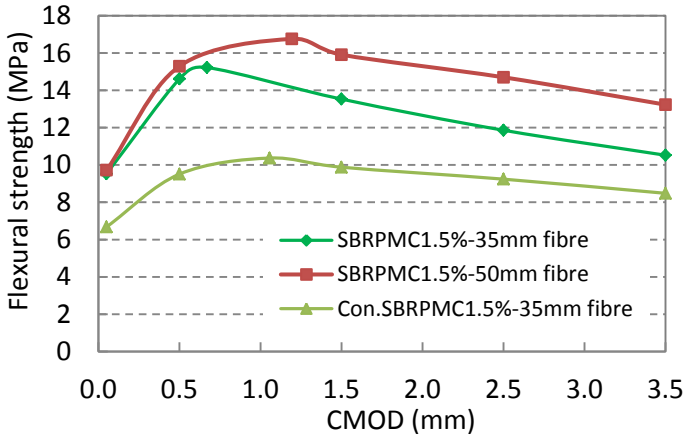

Figure 6-32 Flexural strengths of mixes SBRPMC1.5%-35, SBRPMC1.5%-50 and Con.SBRPMC1.5%-35

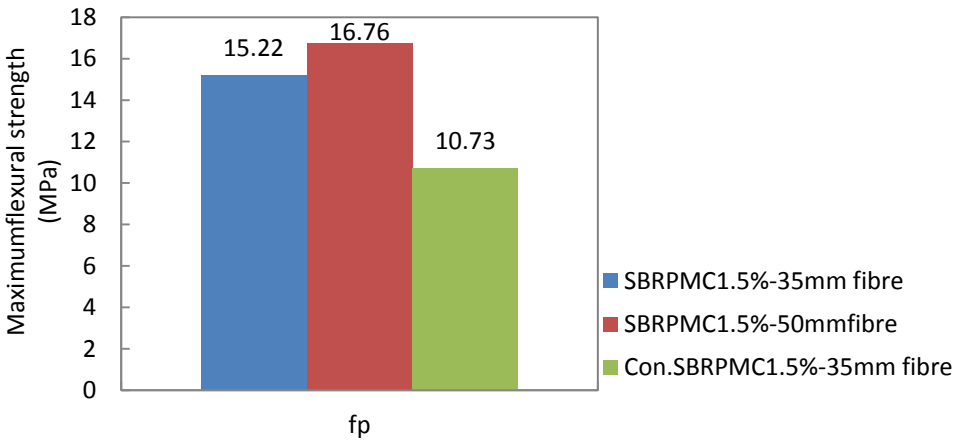

Figure 6-33 Maximum flexural strengths of mixes SBRPMC1.5%-35. SBRPMC1.5%-50 and Con.SBRPMC1.5%-35

Standard equivalent flexural strength $f_{e,3}$

The standard equivalent flexural strengths of the three mixes, determined in Section 5.3.3, are listed in Table 6-9. The strength $f_{e,3}$ can be regarded as the flexural strength of equivalent OPCC, and can be directly used in pavement design (Altoubat et al.2008). The size effect on the flexural strength has been taken into account in the determination of $f_{e,3}$.

Table 6-9 Standard equivalent flexural strengths of mixes SBRPMC1.5%-35, SBRPMC1.5%-50 and Con.SBRPMC1.5%-35

Mix ID	Maximum strength f_p (MPa)	Standard equivalent strength $f_{e,3}$ (MPa)
SBRPMC1.5%-35	15.22	7.27
SBRPMC1.5%-50	16.76	9.53
Con.SBRPMC1.5%-35	10.73	6.79
SBRPMC0%	7.93	N/A
Con.SBRPMC0%	6.52	N/A

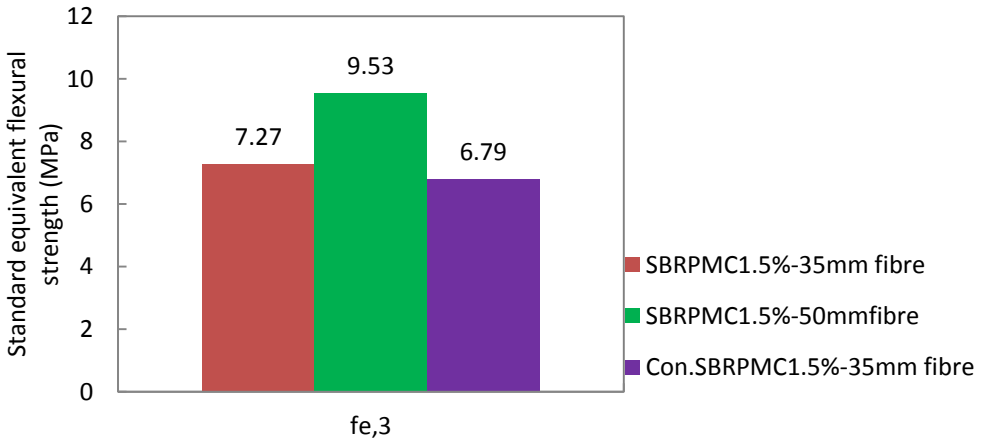

Figure 6-34 Standard equivalent flexural strengths of mixes SBRPMC1.5%-35, SBRPMC1.5%-50 and Con.SBRPMC1.5%-35

Relative toughness index

The relative toughness index indicates the improvement of toughness by adding fibres. The relative flexural toughness of mixes SBRPMC1.5%-35 and Con.SBRPMC1.5%-35 has been presented in Section 5.3.4. The matrix of mix SBRPMC1.5%-50 was the same as mix SBRPMC1.5%-35 except that the former incorporated 50 mm-long fibre, and latter 35 mm-long fibres. Thus, the relative flexural toughness index of mix SBRPMC1.5%-50 can be determined using the fracture energy of mix SBRPMC0%. It can be seen from Table 6-10 by comparing mixes SBRPMC1.5%-35 and Con.SBRPMC1.5%-35 that both mixes contained the same fibres and the same fibre content, however, the I_t of the former is two times that of the latter, and mix SBRPMC1.5%-50 had the highest relative toughness.

Table 6-10 Relative toughness indexes of three mixes

Mix ID	Fracture energy G_F (J/m^2)	Relative toughness indexes I_t
SBRPMC1.5%-35	18580	221
SBRPMC0%	84	
SBRPMC1.5%-50	28300	337
SBRPMC0%	84	
Con.SBRPMC1.5%-35	15650	103
Con.SBRPMC0%	152	

Total fracture energy G_F

Figure 6-35 shows the total fracture energy of mixes SBRPMC1.5%-35, SBRPMC1.5%-50 and Con.SBRPMC1.5%-35, which were presented in Section 5.3.5. It is seen that mix SBRPMC1.5%-50 developed the highest fracture energy, while mix Con.SBRPMC1.5%-35 exhibited the lowest. Total fracture energy is a reliable parameter to assess the toughness of materials; higher fracture energy indicates better the energy absorption in the structure fracture process.

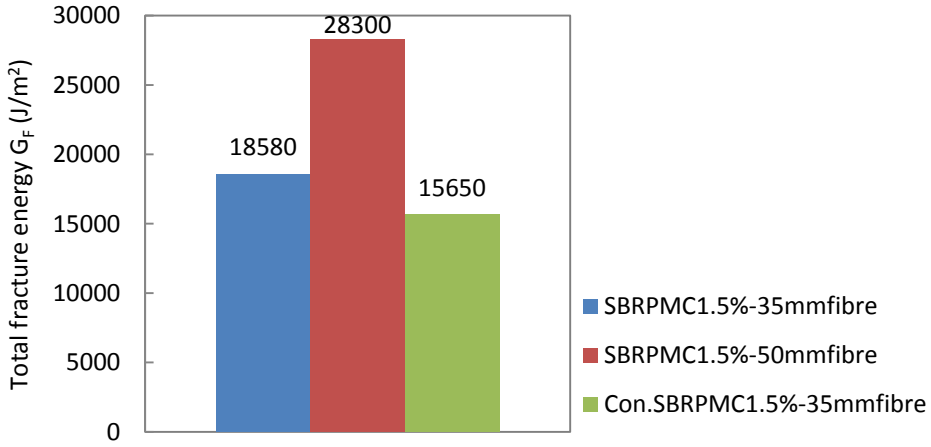

Figure 6-35 Total flexural fracture energy G_F of mixes SBRPMC1.5%-35, SBRPMC1.5%-50 and Con.SBRPMC1.5%-35

The fibre bridging laws

Fibre bridging law provides deeper insight into the mechanism of mechanical response. However, it is affected by the size effect. The fibre bridging laws shown in Table 6-7 were established using the experimental data of beams with the same height of 80 mm. Figure 6-24 and Figure 6-25 demonstrate the $\sigma(w) - w$ laws of the three mixes. It is seen that for a given crack face opening, steel fibres in roller-compacted PMC provides higher tensile stress. The traction force induced by fibres enhances the resistance to cracking.

Discussion and summary

The mechanical parameters described above are rearranged and listed in Table 6-11 for convenient comparison. The mechanical parameters of mix SBRPMC1.5%-35 are taken as one, and then the relative ratios of mixes SBRPMC1.5%-50 and Con.SBRPMC1.5%-35 are normalized on the basis of the parameters of the former. The relative ratios listed in Table 6-11 clearly demonstrates that the steel fibres in roller-compacted concrete are much more efficient than in conventional concrete.

Table 6-11 Comparison of mechanical parameters of beams of mixes SBRPMC1.5%-35, SBRPMC1.5%-50 and Con.SBRPMC1.5%-35 with the same ligament of 80 mm

Mechanical parameters	SBRPMC1.5%-35	SBRPMC1.5%-50	Con.SBRPMC1.5%-35
Maximum flexural strength f_p	1	1.10	0.70
Equivalent flexural strength $f_{e,3}$	1	1.31	0.93
Fracture energy G_F	1	1.52	0.84
Relative toughness index I_t	1	1.52	0.47

The main mechanism for the fibre higher efficiency of roller-compacted concrete may be due to a lower water to cement ratio, resulting in higher friction between fibre and mortar.

6.5 Summary

The main points of this chapter are presented below, while the specific conclusions can be found at the end of each sub-section.

(1) A method for establishing fibre bridging law of SFRC in flexure by inverse analysis was proposed and verified by successful simulation and prediction of the load-CMOD relationships of beams. The proposed method consists of two stages: before hinge formation the bridging law was set up by using the fracture mechanics method, and after hinge formation the fibre bridging law was established by using the material mechanics method.

(2) Fibre bridging law is greatly affected by specimen size. The combination of fibre bridging law and size effect law can be regarded as a material property, and can be used to predict the flexural performance of SFRC beams.

(3) Steel fibre in roller compacted polymer modified concrete exhibits much higher efficiency than in conventional polymer modified concrete. The improvement of efficiency is mainly attributed to the lower water-cement ratio compared to conventional concrete.

7 Flexural Behaviour of SFRPMC-on-OPCC Composite Beam

The interface of the overlay pavement system experiences both tension and shear under the action of vehicular loading and environmental loading in normal service life. The overlay being fully bonded with the existing concrete pavement is the key to success. It should be pointed out that the bond strength criteria defined in Section 4.3.1 for steel fibre-reinforced roller-compacted polymer modified concrete (SFR-RC-PMC) bonded overlays were derived from OPCC-on-OPCC bond strength, which were 4.09 MPa for direct shear bond strength and 2.17 MPa for splitting tensile bond strength. For the SFR-RC-PMC overlay composite system, it is clearly not theoretically rigorous because the criteria measured from bonded OPCC-on-OPCC composite specimens cannot guarantee the PMC-on-OPCC composite beam behaves as a single solid beam under flexure loading. Therefore, the flexural performance of PMC-on-OPCC composite beams, especially the interfacial delamination was investigated in this study to verify experimentally the bond criteria. In addition, the interfacial toughness of PMC-on-OPCC composite specimens under flexure was measured for PMC overlay pavement design.

For these purposes, three types of experiments using PMC-on-OPCC composite beams were conducted, i.e. composite beams under four-point bending test; composite beams with interfacial notch under three-point bending test; and composite beam with notch through OPCC under shear loading test. The first of these tests was to investigate the flexural behaviour of the composite beam, and the last two tests were to measure the interfacial toughness.

In the following sections, fully-bonded composite beam theory and interface fracture mechanics are employed to formulate the relationship of mechanical parameters and experimental results. The specimen dimensions, experimental setup and loading configuration are presented in detail in the following sections.

7.1 Flexural Behaviour of Composite Beams under Four-point Bending Test

Interfacial stiffness greatly influences the behaviour of composite beams under flexure. Fully-bonded composite beams should act as a single solid beam. The theoretical relationships of load-strain, load-stress and slope of load-deflection are easily formulated based on the existing theory for fully-bonded composite beams. If the experimental results are in good

agreement with the theoretical relationship for fully-bonded beams, the SFRPMC-on-OPCC composite beams are verified as being fully-bonded beams. Therefore, in order to properly evaluate the bond performance, the experimental setup used should produce tensile stress along the interface after loading. Thus, the experimental method should be carefully selected. Hence the 4PB test.

Figure 7-1 (a) shows a typical concrete overlay pavement system with an existing crack through the existing concrete base, subjected to a vehicular load. The Figures 7-1(b) and (c) present the composite beam with a crack through the OPCC base under four-point bend and three-point bend, to simulate the overlay pavement under the action of vehicular loading. The composite beams shown in Figure 7-1(b) and (c), with the mechanical properties listed in Table 7-3, and with the dimensions presented in Table 7-1, were analysed using FE code ANSYS 12.0. The calculated results showed that the interface near point A and B was in tension for four-point bend shown in Figure 7-1 (b). However, the interface near point A and B was in compression for three-point bend shown in Figure 7-1 (c). It is clear that the four-point bending test illustrated in Figure 7-1(b) is an appropriate experimental setup to investigate the interfacial bond of composite beams.

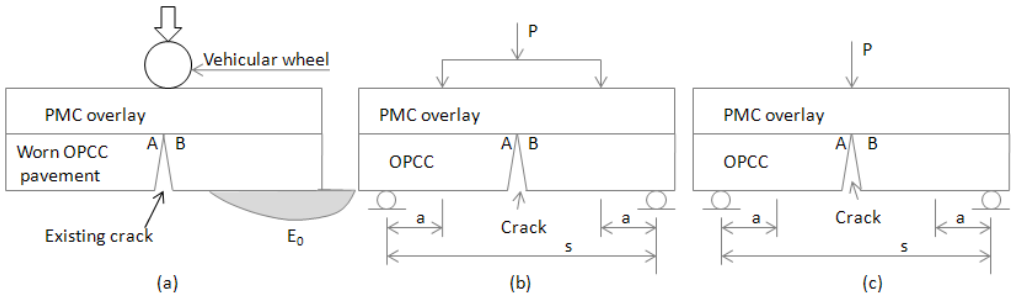

Figure 7-1 (a) overlaid pavement with an interfacial defect subjected to vehicular load, (b) composite beam with a crack impinging interface under 4PB, (c) composite beam with a crack impinging interface under 3PB

In this study, two types of PMC-on-OPCC composite beams, i.e. composite beams with rough interface and smooth interface, were tested under a four-point bend to reveal the interfacial behaviour of composite beams.

7.1.1 Formulation

Relationship of strains at top and bottom layers

The classic theory for fully-bonded composite beams is employed to relate the strains at top and bottom. Consider the PMC-on-OPCC composite beam in flexure. This beam consists of two parts, shown in Figure 7-2: the top part material is of the elasticity modulus of E_1 and

thickness of h_1, while the bottom part is E_2 and h_2. Axis z is the neutral axis, and y_1 and y_2 are the distances from the top to neutral axis and from the bottom to neutral axis, respectively. Gere and Timoshenko (1999) analysed the fully-bonded composite beam using classic beam theory (plane assumption) and provided the equations below (eqns.7.1-7.3) for locating the neutral axis Z, the compressive stress σ_T at top and tensile stress σ_B at bottom.

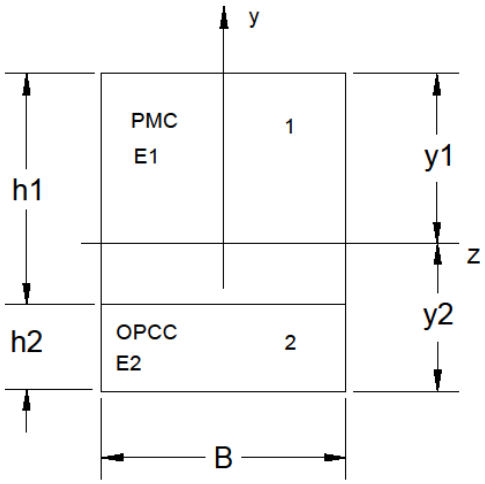

Figure 7-2 Cross-section of SFRPMC-on-OPCC composite beam

The generalized form equations are:

$$E_1\int_1 ydA + E_2\int_2 ydA = 0 \qquad 7.1$$

$$\sigma_T = \frac{ME_1y_1}{E_1I_1+E_2I_2} \qquad 7.2$$

$$\sigma_B = \frac{ME_2y_2}{E_1I_1+E_2I_2} \qquad 7.3$$

where M is the bending moment; $E_1$and E_2 are elasticity modulus of the top layer and the bottom layer materials, respectively; I_1 and I_2 are moments of inertia of the top layer and bottom layer materials with respect to the neutral axis, respectively.

Substitution of the geometrical parameters of the composite section into eqn.7.1 results in:

$$E_1Bh_1\left(y_1-\frac{h_1}{2}\right) - E_2h_2B\left(y_2-\frac{h_2}{2}\right) = 0 \qquad 7.4$$

$$y_1 + y_2 = h_1 + h_2 \qquad 7.5$$

Solving the two equations above, y_1 and y_2 are obtained as

$$y_1 = \frac{E_2h_2(h_1+\frac{h_2}{2})+\frac{E_1h_1^2}{2}}{E_1h_1+E_2h_2} \qquad 7.6$$

$$y_2 = \frac{E_1 h_1 (\frac{h_1}{2} + h_2) + \frac{E_2 h_2^2}{2}}{E_1 h_1 + E_2 h_2} \quad 7.7$$

Eqn.7.2 divided by eqn.7.3 results in:

$$\frac{\sigma_T}{\sigma_B} = \frac{E_1 y_1}{E_2 y_2} \quad 7.8$$

Thus, the following relationships are obtained:

$$\frac{\epsilon_T}{\epsilon_B} = \frac{y_1}{y_2} \quad 7.9$$

$$\frac{\varepsilon_T}{\varepsilon_B} = \frac{E_2 h_2 (h_1 + \frac{h_2}{2}) + \frac{E_1 h_1^2}{2}}{E_1 h_1 (\frac{h_1}{2} + h_2) + \frac{E_2 h_2^2}{2}} \quad 7.10$$

where ε_T and ε_B are the strains at top and bottom of the beam, respectively.

Slope of relationship of load-deflection

For the fully-bonded composite beam under four-point bending test, the mid-span deflection δ_c before the base cracking (see Figure 7-1(b)) is evaluated by the following relationship (Gere and Timoshenko 1999):

$$\delta_c = \frac{Pa(3S^2 - 4a^2)}{48(E_1 I_1 + E_2 I_2)} \quad 7.11$$

where δ_c is mid-span deflection (mm); P is total load (N); S is span (mm); a is defined in Figure 7-1(b) (mm); E_1 and E_2, I_1 and I_2 have been defined previously, and are in MPa and mm^4, respectively. Eqn.7.11 is converted in the following form for comparison with experimental results of load-deflection curves.

$$P = \frac{48(E_1 I_1 + E_2 I_2)}{a(3S^2 - 4a^2)} \delta_C \quad 7.12$$

Maximum bending moments

Before OPCC cracking, the maximum bending moment carried by OPCC base, theoretically predicted by the fully-bonded composite beam is an indicator for identifying the interfacial delamination. The maximum bending moment, $M_{OPCC,}$ carried by the whole composite beam is determined by letting the stress at the bottom of the OPCC base be equal to its maximum flexural strength $f_{OPCC.}$ After beam OPCC has cracked, the maximum moment (load carrying capacity), M_{PMC}, carried by the PMC overlay is determined by letting the stress at the bottom

of the PMC overlay be equal to its maximum flexural strength $f_{PMC.}$ Based on the discussion and eqn. 7.3, the following two equations are obtained:

$$M_{OPCC} = \frac{f_{OPCC}(E_1 I_1 + E_2 I_2)}{E_2 y_2} \quad 7.13$$

$$M_{PMC} = \frac{f_{PMC} B h_1^2}{6} \quad 7.14$$

where M_{OPCC} is the bending moment carried by the whole composite beam, M_{PMC} is the bending moment carried by the PMC overlay alone after OPCC base cracking. With the given OPCC flexural strength f_{OPCC} and the maximum flexural strength of the SFRPMC overlay f_{PMC}, the first peak load P_1 can be determined through M_{OPCC} by eqn.7-13. After OPCC base failure, the SFRPMC overlay carries the load alone, thus the second peak load P_2 is evaluated through M_{PMC} by eqn.7-14.

Up to now, the three parameters, i.e. the ratio of top strain to bottom strain, the slope of the load-mid-span deflection relationship, and the first peak load P_1 have been formulated to verify the fully-bonded PMC-on-OPCC composite beam. The three theoretical parameters are compared with the corresponding experimental results in the following sections.

7.1.2 Experiment

7.1.2.1 Specimen Preparation

The mix proportion of OPCC and its mechanical properties are listed in Table 4-14. The interfacial treatment method for roughened OPCC bases and the texture depth are presented in Section 4.3.4. The smooth-interface OPCC bases were not roughened.

The mixing and curing procedures, specimen formation method for SFRPMC overlay are presented in Section 4.4. The PMC mix proportions are listed in Table 5-1. Three groups of SFRPMC-on-OPCC composite beams were prepared, (i.e. SBRPMC1.5%-on-OPCC-R, SBRPMC1.5%-on-OPCC-S and PVAPMC1.5%-on-OPCC-R composite beams respectively), and tested under four-point bend. The details of the composite beams are tabulated in Table 7-1. Note that the thickness of PMC overlay and OPCC base shown in the table were the averages; the actual thicknesses of h_1 and h_2 for individual beam are listed in Table 7-4.

Table 7-1 SFRPMC-on-OPCC composite beams for four-point bending test

ID of beams	Num. of beams	Mix ID of PMC overlay	OPCC Interface	Dimension width x height x Length	Loading mode
SBRPMC1.5% -on-OPCC-R	3	SBRPMC1.5%-35	Rough	PMC overlay: 100 x75x500 mm^3	Four-point bend
SBRPMC1.5% -on-OPCC-S	3	SBRPMC1.5%-35	Smooth	OPCC base: 100x48x500 mm^3	
PVAPMC1.5% -on-OPCC-R	3	PVAPMC1.5%-35	Rough		

(a) (b)

Figure 7-3 (a) OPCC bases with roughened interfaces; (b) OPCC bases with smooth interfaces

7.1.2.2 Test Procedure and Experimental Results

Two strain gauges were glued on top and bottom, to measure the strains; and two LVDTs were fixed on both sides of the frame to measure the load-point deflection and to control the loading rate. The instrumentation and experimental setup is shown in Figure 7-4 and Figure 7-5. The strains and displacements were automatically recorded by computer at a frequency of 5 Hz. The loading rate was displacement-controlled.

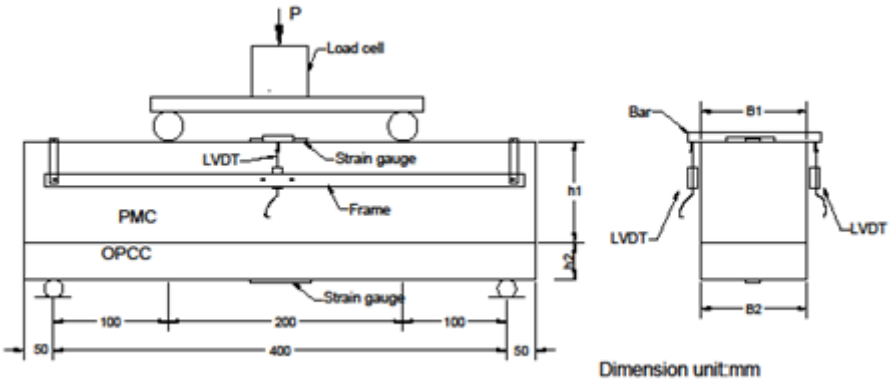

Figure 7-4 Experimental configuration of composite beam under four-point bending test

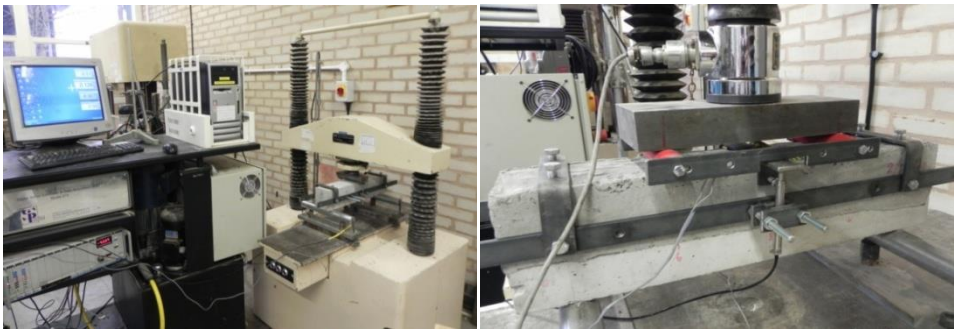

(a) (b)

Figure 7-5 (a) general view of experimental setup; (b) composite beam under four-point bending test

Composite beam with roughened interface

For the three SBRPMC1.5%-35-on-OPCC-R composite beams (rough interface), two beams, which are recorded under beam-1 and beam-2 in Table 7-2, were loaded at the mid-span deflection of the rate of 0.0017 mm/s conforming to the ASTM method for SFRC testing (ASTM C 1609/C 1609M-06, 2006). They failed abruptly and thus complete load-displacement curves were not obtained. The third beam, which is denoted as beam-3 in Table 7-2, was loaded at the mid-span deflection of rate of 0.0001 mm/s; the beam fractured gradually until failure. Interfacial cracking did not occur in any of the three beams. The beam-3 will be further analysed in Section 7.3.3 to investigate the competition of crack penetration and deflection into interface.

The three PVAPMC1.5%-35-on-OPCC-R composite (roughened interface) beams were tested at the mid-span deflection of the rate of 0.0001 mm/s. All three beams slowly cracked from the OPCC bases to the top layers of PVAPMC1.5% until failure. No interfacial cracking was observed in the three beams. A typical pattern of vertical cracking path without interfacial delamination is shown in Figure 7-6(a).

Composite beam with smooth interface

For the three SBRPMC1.5%-on-OPCC-S composite beams (smooth interface), the increase rate of mid-span displacement was 0.0017 mm/s, in compliance with the ASTM method for SFRC test (ASTM C 1609/C 1609M-06 2006). Two beams failed abruptly and thus complete load-displacement curves were not obtained. Close observation of the two composite beams revealed that cracking did not extend into the interface. However, the third beam (beam-6 in Tables 7-2, 7-4 and 7-5) fractured gradually during test, and the crack firstly initiated from the bottom of the OPCC base and extended to the interface, and finally vertically penetrated into the SFRPMC overlay until the beam failed. Figure 7-6 (b) and (c) clearly shows the

paths of crack propagation. The interfacial delamination behaviour of beam-6 in Table 7-2 will be further investigated in Section 7.3.3.

The results of careful observation during the test, the first peak load P_1 (corresponding to OPCC cracking), and the second peak load P_2 (corresponding to load carried by PMC overlay alone) are tabulated in Table 7-2. The typical relationships of load-midspan deflection, load-top strain and load-bottom strain, obtained from experimental results, are given in Figure 7-7.

The transformation points of linearity to nonlinearity of the load-strain relationship, and the load-midspan deflection relationship (see Figure 7-7) indicated that the OPCCs were cracking and the first peak load P_1 corresponded to the points. Note that the top and bottom strains are meaningless after the OPCC base has cracked.

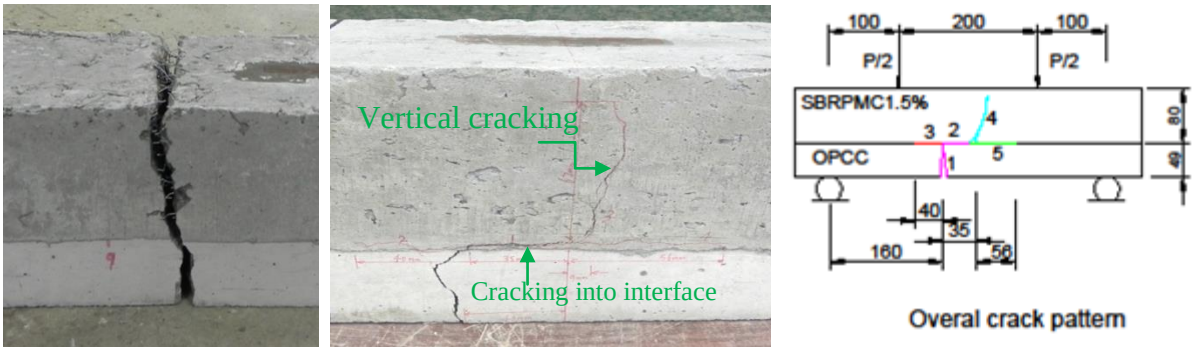

(a) (b) (c)

Figure 7-6 Crack propagation of composite beam under 4PB test: (a) beam vertical cracking without interfacial delamination (beam PVAPMC1.5%-on-OPCC-R), (b) crack propagation into interface due to poor bond (beam-6 in Table 7-2); (c) crack propagation trajectory of beam-6 in Table 7-2,

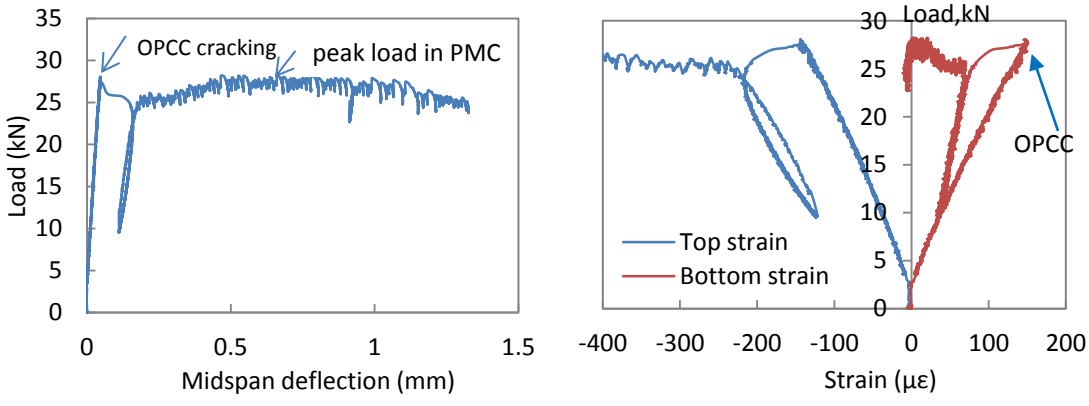

(a) (b)

Figure 7-7 SBRPMC1.5%-35-on-OPCC-R composite beam under four-point bending test: (a) relationship of load-midspan deflection; (b) relationships of load- top strains and bottom strain

Table 7-2 Experimental results of SFRPMC-on-OPCC composite beams under four-point bend test (Note Beam-1 and Beam-2 failed abruptly during test)

No.	ID of beams	Interface	Description of test results	P_1 (kN)	P_2 (kN)
1	SBRPMC1.5% -on-OPCC-R	Rough	Loading rate 0.0017mm/s, failed abruptly, no interface cracking	N/A	N/A
2				N/A	N/A
3			Loading rate 0.0001mm/s, no interfacial delamination, complete P-D was obtained	28.09	28.23
4	SBRPMC1.5% -on-OPCC-S	Smooth	0.0017mm/s, failed abruptly, no interface cracking.	32.02	N/A
5			0.0017mm/s, nice P-D obtained no interface cracking.	21.78	31.13
6			0.0017mm/s, complete P-D was obtained, crack started from OPCC base deflected into interface.	27.08	27.99
7	PVAPMC1.5% -on-OPCC-R	Rough	Loading rate 0.0001 mm/s, nice P-D curves were obtained.	24.30	26.88
8				24.34	26.02
9				25.54	N/A

7.1.3 Comparison of Theoretical and Experimental Results

As has been presented previously, observation during testing showed that no interfacial de-bonding occurred in SFRPMC-on-OPCC composite beams with rough interface under 4PB test, but at least one composite beam with smooth interface delaminated at the interface under the four-point bending test. However, in order to verify theoretically and rigorously that the SFRPMC-on-OPCC composite beams with rough interface behaved as a single solid structure, the three parameters defined and formulated previously (i.e. ratio of top strain to bottom strain, slope of the relationship of load-midspan deflection and first peak load P_1) are calculated and compared with the experimental results. The mechanical properties of mixes SBRPMC1.5%-35, PVAPMC1.5%-35 and OPCC are presented in Table 7-3.

Table 7-3 Mechanical properties of mixes SBRPMC1.5%-35 and PVAPMC1.5%-35 and OPCC

Mix ID	Elasticity modulus (MPa)	Poisson's ratio	Maximum flexural strength f_p (MPa)
SBRPMC1.5%-35	32365	0.187	15.22
PVAPMC1.5%-35	37357	0.239	16.6
OPCC	25200	0.21	4.66 (under 4PB)

The ratios of top strain to bottom strain

With the mechanical properties of SFRPMC and OPCC listed in Table 7-3 and the geometric dimensions listed in Table 7-4, the theoretical ratios of top strain to bottom strain are evaluated using eqn.7.10, and tabulated in Table 7-4. The experimental ratios are evaluated by fitting the testing data with linear straight lines. Figure 7-8(b) is taken as an example to

show the method for determining the experimental ratio of top strain to bottom strain. Ignoring the minus sign (which only indicates the compressive strain), the top and bottom strains can be expressed as:

$$\varepsilon_T = \frac{P-2.5}{0.2037} \quad 7.15$$

$$\varepsilon_B = \frac{P-2.5}{0.1664} \quad 7.16$$

And thus the ratio of top to bottom strains is

$$\frac{\varepsilon_T}{\varepsilon_B} = \frac{0.1664}{0.2037} = 0.817$$

Similarly to the above method, the experimental ratios can be evaluated for all beams and are tabulated in Table 7-4. It is seen that the theoretical ratios of top strain to bottom strain for fully-bonded composite beams are in good agreement with those of the experimental results. Note that the theoretical ratio was evaluated by eqn.7.10.

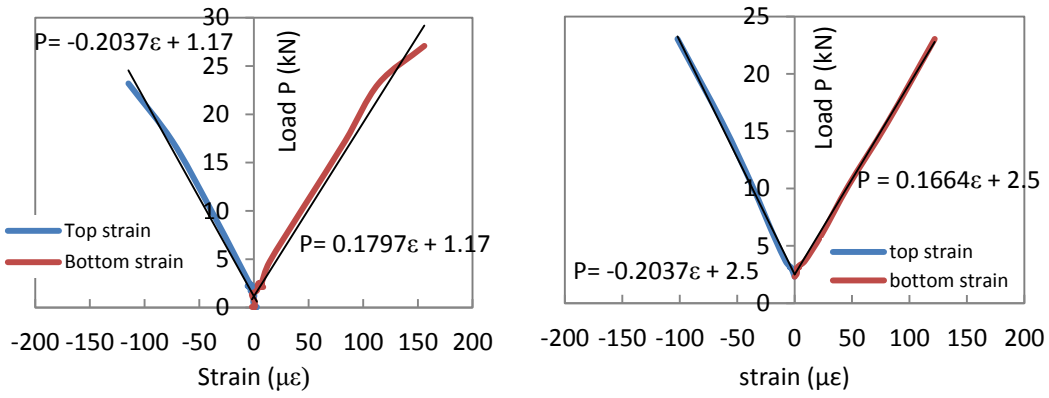

Figure 7-8 Typical relationships of load-strains: (a) the beam of SBRPMC1.5%-on-OPCC-S (Beam 6 in Table 7-4); (b) the beam of PVAPMC1.5%-on-OPCC-R (Beam 9 in Table 7-4)

Table 7-4 Comparison of the theoretical ratios of top strain to bottom strain of composite beams with those obtained from experimental results under 4PB test (Beam-1 and Beam-2 failed abruptly during test)

No.	ID of beams	Interface	P_1 (kN)	B (mm)	h_1 (mm)	h_2 (mm)	Top to bottom strain ratio, $\varepsilon_T/\varepsilon_B$ Theoretical	Experimental
1	SBRPMC1.5% -on-OPCC-R	Rough	N/A	N/A	N/A	N/A		
2			N/A	N/A	N/A	N/A		
3			28.093	100	78	48	0.892	0.882
4	SBRPMC1.5% -on-OPCC-S	Smooth	32.028	100	79.5	48.5	0.892	0.899
5			21.78	100	78.5	49.5	0.891	0.864
6			27.081	100	79.5	48.5	0.892	0.882
7	PVAPMC1.5% -on-OPCC-R	Rough	24.303	100	75	50	0.835	0.756
8			24.34	100	74	48	0.836	0.798
9			25.548	100	71	50	0.833	0.817

The slopes of relationship of load-midspan deflection

With the mechanical properties of PMC and OPCC listed in Table 7-3, and the geometrical dimensions listed in Table 7-5, the theoretical slopes of the relationship of load-midspan deflection before OPCC base cracking are evaluated using eqn.7.12, and tabulated in Table 7-5. The experimental slope of load-midspan deflection was evaluated by fitting the testing data with a straight line. The typical experimental load-midspan deflection prior to OPCC base cracking are pictured in Figure 7-9. Both theoretical and experimental slopes are listed in Table 7-5. It is seen that the experimental slopes of load-midspan deflection relationships are basically in agreement with that predicted, and the slight difference from each other may be attributed to the accuracy of the displacement measurement. It is well known that much higher accuracy can be obtained in measuring strain than displacement in flexural tests.

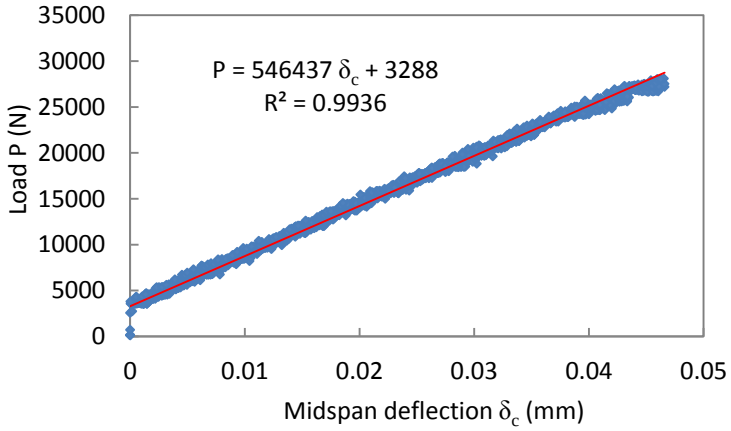

Figure 7-9 Typical relationship of load-midspan deflection prior to OPCC base cracking (beam of No.3, SBRPMC1.5%-on-OPCC-R in Table 7-5)

Table 7-5 Comparison of the slopes of load - midspan deflection theoretically predicted and experimental results (Beam-1 and Beam-2 failed abruptly during test)

No.	ID of beams	Interface	P_1 (kN)	B (mm)	h_1 (mm)	h_2 (mm)	Slope of P-δ_c, (N/mm) Theoretical	Experimental
1	SBRPMC1.5% -OPCC-R	Rough	N/A	N/A	N/A	N/A	N/A	N/A
2			N/A	N/A	N/A	N/A	N/A	N/A
3			28.093	100	78	47.5	$5.13X10^5$	$5.46X10^5$
4	SBRPMC1.5% -OPCC-S	Smooth	32.028	100	79.5	48.5	$5.44X10^5$	N/A
5			21.78	100	78.5	49.5	$5.44X10^5$	$4.88X10^5$
6			27.081	100	79.5	48.5	$5.44X10^5$	$4.83X10^5$
7	PVAPMC1.5% -OPCC-R	Rough	24.303	100	75	50	$5.42X10^5$	$6.29X10^5$
8			24.34	100	74	48	$5.05X10^5$	$5.14X10^5$
9			25.548	100	71	50	$4.91X10^5$	N/A

First peak load P_1

As has been discussed earlier, the first peak load P_1 is one of indicators for verifying fully-bonded composite behaviour. The first peak load is dependent on both the flexural strength of the OPCC base and the bond quality at interface. The first peak load for the fully bonded composite beam can be evaluated using eqn.7.13. The theoretical prediction and experimental results are listed in Table 7-6. It can be seen that the theoretical prediction for P_1 is in good agreement with experimental results.

Table 7-6 Theoretical predicted average peak load and test results of composite beams under 4PB test

No.	ID of beams	Interface	B (mm)	h_1 (mm)	h_2 (mm)	Theoretical predict. P_1 (kN)	Theoretical predict. P_2 (kN)	Experim. results P_1 (kN)	Experim. results P_2 (kN)
1	SBRPMC1.5%	Rough	N/A	N/A	N/A				
2	-on-OPCC-R		N/A	N/A	N/A				
3			100	78	47.5	24.224	30.866	28.093	28.235
4	SBRPMC1.5%	Smooth	100	79.5	48.5	27.268	31.798	26.963	30.387
5	-on-OPCC-S		100	78.5	49.5				
6			100	79.5	48.5				
7	PVAPMC1.5%	Rough	100	75	50	25.989	29.773	24.73	26.153
8	-on-OPCC-R		100	74	48				
9			100	71	50				

Splitting tensile bond strength

After the flexure test, the PMC-on-OPCC composite beams were saw-cut to prisms for testing the splitting tensile bond strength. Figure 7-10 shows the typical prism saw-cut from the tested composite beam and the typical dimensions. The test procedure complied with BS EN 12390-6:2009, and the loading rate was 1.4 kN/s. The splitting tensile bond strength was evaluated using the eqn. 4.12.

The experimental results are listed in Table 7-7 and illustrated in Figure 7-12. It is seen that the strength of prisms of SBRPMC1.5%-on-OPCC-R (rough interface) is much higher than that of SBRPMC1.5%-on-OPCC-S (smooth interface). This explains why the latter exhibited debonding under four-point bending test but the former did not.

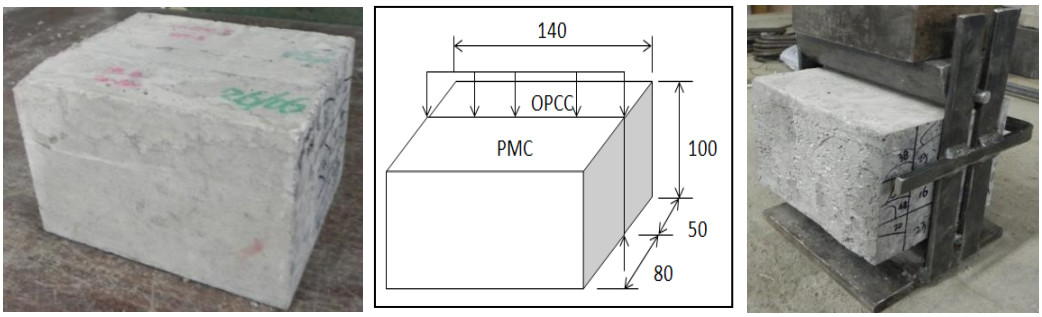

(a) (b) (c)

Figure 7-10 (a) typical prism saw-cut from tested composite beam; (b) typical dimensions of composite prism saw-cut from tested beam; (c) composite prism under splitting test

Table 7-7 Splitting tensile bond strength of prisms saw-cut from tested SFRPMC-on-OPCC composite beams

ID of composite beams	OPCC interface	Number of specimens	Average (MPa)	STDEV (MPa)
SBRPMC1.5%-on-OPCC-R	Rough	10	2.96	0.472
SBRPMC1.5%-on-OPCC-S	Smooth	6	1.80	0.192
PVAPMC1.5%-on-OPCC-R	Rough	7	3.70	1.336
OPCC-on-OPCC-R	Rough	7	2.68	0.282

Figure 7-11 Tested prism saw-cut from tested composite beam of roughened OPCC interface: PMC patch bonded on OPCC interface

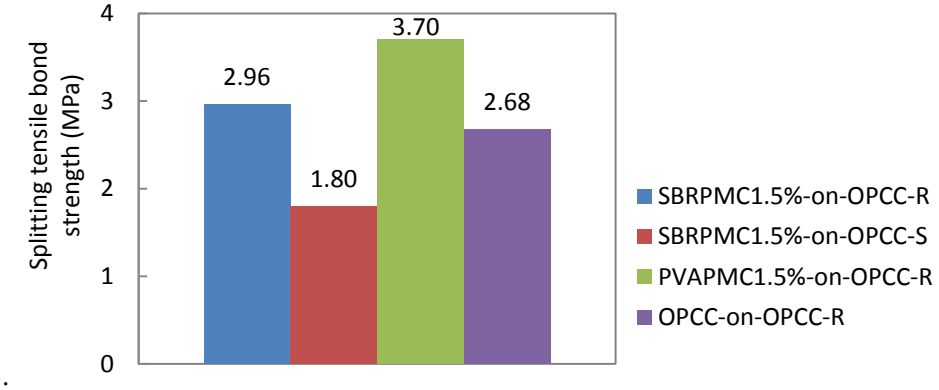

Figure 7-12 Splitting tensile bond strengths of PMC-on-OPCC prisms saw-cut from tested composite beams

7.1.4 Discussion and Summary

It has been confirmed by both laboratory tests and theoretical analysis that no delamination occurred in all SFRPMC-on-OPCC composite beams with roughened interface under four-point bending test, while at least one out of three composite beams with smooth interface experienced debonding at the interface. It is seen from Table 7-7 that the average splitting tensile bond strength of composite blocks of SBRPMC1.5%-on-OPCC with roughened interface is 2.96 MPa, higher than the criterion of 2.17 MPa, which was previously defined for mix design in Section 4.3.1. The bond strength of SBRPMC1.5%-on-OPCC beams with smooth interface is 1.80 MPa, lower than the criterion of 2.17 MPa. This indicates that the criterion of splitting tensile bond strength of 2.17 MPa for bonded overlay mix design was experimentally verified.

This demonstrated how crucial a good bond is for the composite beam; a poor bond results in interfacial delamination under bending. For bonded concrete overlay on worn concrete pavements, interfacial delamination in all loading modes should be avoided. Further investigation of interfacial bond quality is performed in Section 7.3.2, where a special experiment is conducted to measure the interfacial fracture toughness.

7.2 Load Carrying Capacity of Composite Beams under Four-Point Bend

As has been experimentally illustrated in Section 7.1, for SBRPMC1.5%-on-OPCC and PVAPMC1.5%-on-OPCC composite beams with roughened interfaces under the four-point bending test, the crack firstly developed at the bottom of the OPCC base and the first peak load P_1 was reached. Then the crack continued extending through interface, and finally penetrated into the SFRPMC overlay. The second peak load P_2 was achieved during crack propagation in the SFRPMC. However, the composite beams with smooth interface behaved differently. Cracking started from the bottom of the OPCC and propagated into interface. Both types of beam exhibited two peak loads: the first peak load occurred at OPCC cracking, while the second was achieved when the SFRPMC overlay reached its peak flexural strength f_p. It is clear that for the bonded composite beams, the first peak load is dependent on both OPCC flexural strength and the cross-sectional stiffness constituents of the composite beam, while the second peak load only depends on the flexural resistance of the SFRPMC overlay. In this section, classic composite beam theory (Gere and Timoshenko 1999) is employed to evaluate both load carrying capacities.

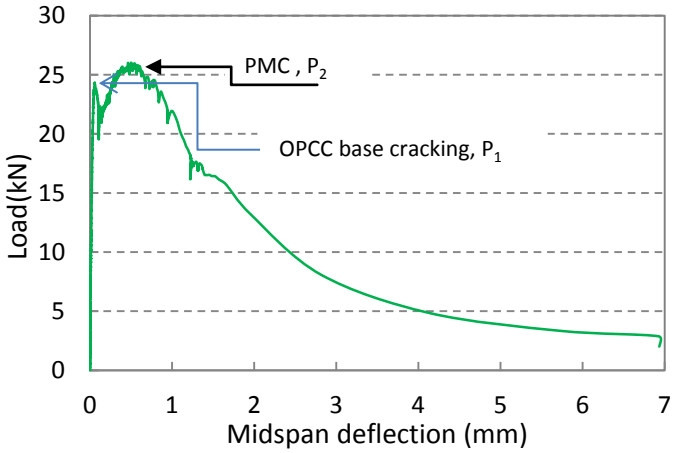

Figure 7-13 Typical load-midspan deflection curve exhibiting first peak load and second peak load

Both the peak bending moments, i.e. M_{OPCC} and M_{PMC}, which correspond to the two peak loads, are evaluated using eqn.7.13 and eqn.7.14 for the known mechanical parameters listed

in Table 7-3 and the geometrical dimensions. The first peak load (P_1) and second (P_2) can be readily determined with the knowledge of M_{OPCC} and M_{PMC}. The two theoretically-predicted peak loads and experimental results are listed in Table 7-6. It is seen that the theoretical predictions for the two peak loads are in good agreement with the experimental results.

Since the SBRPMC1.5%-on-OPCC and PVAPMC1.5%-on-OPCC composite beams with rough interface were experimentally verified as being fully-bonded, the efficiency of overlays of mix OPCC, SBRPMC1.5%-35 and PVAPMC1.5%-35 can be evaluated. For a given OPCC base with the typical thickness of 200 mm, the first maximum bending moment (M_{OPCC}) is evaluated using eqn.7.13 with the knowledge of the mechanical parameters listed in Table 7-3. The increased ratios of the first peak moment of composite beams for various overlay thicknesses, on the basis of a 200 mm-thickness OPCC base, are tabulated in Table 7 -8 and plotted in Figure 7-14.

Table 7-8 Increased ratios of maximum bending moments of OPCC beams strengthened with different overlays in various thicknesses (for the given thickness of OPCC base of 200 mm)

Type of overlays	Thickness of overlays (mm)						
	0	50	100	150	200	252	266
OPCC	1	1.56	2.25	3.06	4	5.11	5.43
SBRPMC1.5%	1	1.66	2.4	3.25	4.25	5.44	5.79
PVAPMC1.5%	1	1.71	2.48	3.36	4.4	5.64	6.3

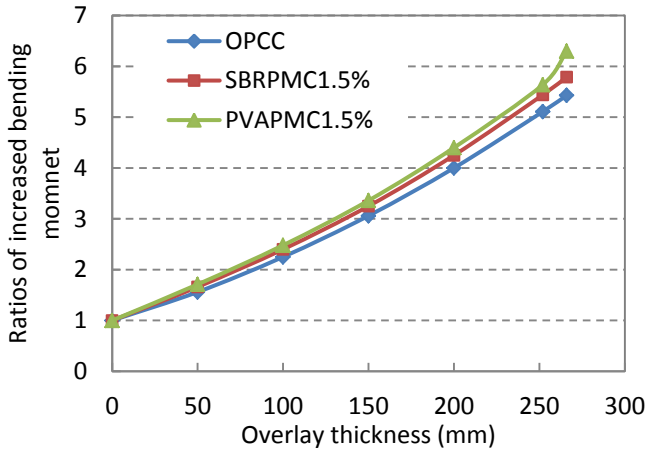

Figure 7-14 Increased ratios of maximum bending moments of OPCC beams strengthened with different overlays in various thicknesses (for the given OPCC base thickness of 200 mm)

It is seen from the Table 7-8 and Figure 7-14 that overlays of mixes OPCC, SBRPMC1.5%-35 and PVAPMC1.5%-35 have similar increasing ratios of maximum bending moments for the same thickness. It seems that the load carrying capacity improvement of SBRPMC1.5%-35 and PVAPMC1.5%-35 overlays is not efficient due to the higher cost of materials used.

However, experiments later carried out in Chapter 8 show that SBRPMC1.5%-35-on-OPCC and PVAPMC1.5%-35-on-OPCC composite beams on elastic foundation behaved completely differently from OPCC-on-OPCC overlay pavement systems.

7.3 Interface Fracture and Interfacial Fracture Toughness

Since numerous cracks exist in a worn concrete pavement, it is natural to employ fracture mechanics to investigate the overlay pavement system. In this section, the method for calculating the strain energy release rate (ERR) of the interface is first investigated. Then, a test specimen is set up for simulating overlay pavement system. Measurement of interfacial fracture toughness of polymer modified concrete – on – concrete under three-point bend is followed. Finally the prediction of the behaviour of crack propagation in the interface of composite beam under four-point bend is presented.

Eight composite beams with interfacial notches were tested to measure the interfacial fracture toughness (G_{ic}), i.e. the critical energy release rate of the interface. The measured interfacial fracture toughness is used in this section to predict the interfacial delamination performance of composite beam under four-point bending, and will be further used to compare with the energy release rate of the PMC overlay pavement system in Chapter 9.

7.3.1 Interface Fracture of Bi-material

For the fracture process in homogeneous material under mixed mode loading, the criterion for fracture is dependent on the combination and the ratio of stress intensity factors K_I and K_{II}, and thus the strain energy release rate (ERR) has attracted relatively little attention. In an interfacial fracture, the crack propagation is usually constrained in the interface due to the fact that the bond strength is normally much lower than that of the bonded materials. Since stress distribution in the crack line at the vicinity of the crack tip varies greatly due to the stress singularity and stress oscillation in the crack tip, the strength-based criterion (tensile and shear bond strengths) method for evaluating interface delamination is no longer the appropriate approach, thus interface mechanics is necessarily employed.

7.3.1.1 Stress Intensity Factor

Unlike the fracture mechanics of homogeneous materials, several definitions of stress intensity factors have been introduced depending on the solution selected. Sun and Qian (1997) compared the definitions and pointed out that most of them differ by either a phase

factor or a constant. Eqns.7.17 and 7.18 describe the definitions proposed by Malysev and Salganik (1965), and Sun and Jih (1987), respectively.

$$\left(\sigma_y + i\tau_{xy}\right)_{\theta=0} = \frac{K_m}{\sqrt{2\pi r}}\left(\frac{r}{2a}\right)^{i\varepsilon} \quad 7.17$$

$$\left(\sigma_y + i\tau_{xy}\right)_{\theta=0} = \frac{K_s}{\cosh(\pi\varepsilon)\sqrt{2\pi r}}\left(\frac{r}{2a}\right)^{i\varepsilon} \quad 7.18$$

where K_m and K_s are the definitions proposed by Malysev and Salganik (1965), and Sun and Jih (1987), respectively; $2a$ is crack length, ε is a material constant; σ_y, τ_{xy}, r and θ are defined in Figure 7-15(a).

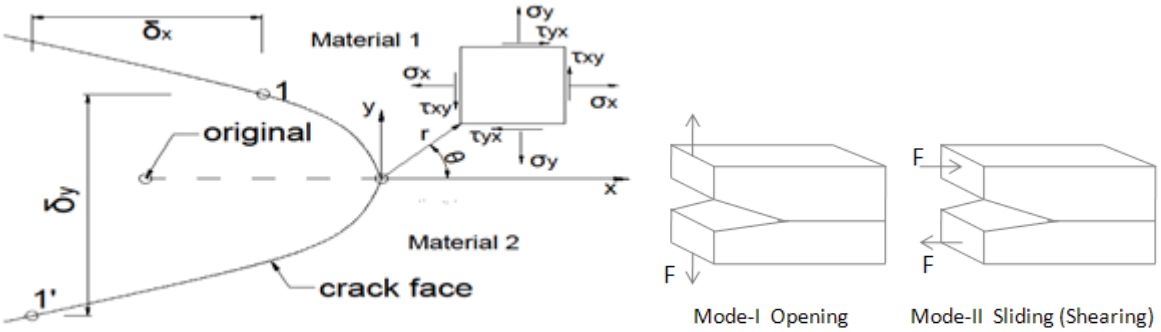

(a) (b) (c)

Figure 7-15 (a) stress field and displacement at vicinity of crack tip of bi-material; (b) mode-I loading; (c) mode-II loading

Shi et al. (2006) adopted the definition introduced by Malysev and Salganik (1965), and proposed an extrapolation method for calculating SIFs using crack face displacement, and correlated the total ERR with SIFs as follows for the plane strain condition.

$$K_I = (AcosQ + BsinQ)/D \quad 7.19$$

$$K_{II} = (BcosQ - AsinQ)/D \quad 7.20$$

$$G_i = \frac{1}{cosh^2(\pi\varepsilon)}\frac{K_I^2 + K_{II}^2}{E^*} \quad 7.21$$

$$\psi_K = \tan^{-1}\left(\frac{K_{II}}{K_I}\right) \quad 7.22$$

$$\beta = \frac{\mu_2(k_1-1) - \mu_1(k_2-1)}{\mu_2(k_1+1) + \mu_1(k_2-1)} \quad 7.23$$

$$k_1 = 3 - 4\nu_1 \quad 7.24$$

$$k_2 = 3 - 4\nu_2 \quad 7.25$$

$$\mu_j = \frac{E_i}{2(1+\nu_j)} \quad 7.26$$

$$\varepsilon = \frac{1}{2\pi}\ln(\frac{1-\beta}{1+\beta}) \quad 7.27$$

$$\frac{2}{E^*} = \frac{1-\nu_1}{E_1} + \frac{1-\nu_2}{E_2} \quad 7.28$$

$$Q = \varepsilon \ln(\frac{r}{l}) \quad 7.29$$

$$A = \delta_y - 2\varepsilon\delta_x \quad 7.30$$

$$B = \delta_x + 2\varepsilon\delta_y \quad 7.31$$

$$D = \frac{8}{E^*\cosh(\pi\varepsilon)}\sqrt{\frac{r}{2\pi}} \quad 7.32$$

where K_I and K_{II} are SIFs corresponding to mode-I and mode-II loading, respectively; G_i is the total ERR, Ψ_K is phase angle for SIF, β is one of Dunder's parameters, ε is material constant; j=1, 2; μ_j is the shear modulus, ν_j is the Poisson's ratio, E_j is the elastic modulus of the two materials, δ_y and δ_x are the relative opening displacements and relative sliding displacement, respectively. The method described above is to extract crack face displacement data from FEA, and then plot K_I-r/a and K_{II}-r/a relationships using eqns.7.19 and 7.20, and then obtain K_I and K_{II} by the linear extrapolation method; and the ERR is evaluated using eqn.7.21.

However, verification by the author, presented later, indicates that the K_I determined by the extrapolation method described above is in good agreement with the analytical solution, but K_{II} is not. This leads to an erroneous G_i evaluated by eqn.7.21. It has been discussed earlier that ERR (energy release rate) may play a more important role than SIFs in interface delamination. Therefore, in this study interfacial ERR is directly determined using Irwin's crack closure integral to avoid ambiguity. Meanwhile K_I is evaluated by the crack face displacement extrapolation method presented above and finally K_{II} is calculated using eqn.7.21 with the known G_i and K_I.

7.3.1.2 Strain Energy Release Rate

For most cases, the numerical method, such as finite element analysis (FEA) and boundary element analysis, is needed to extract fracture parameters due to the lack of analytical solutions. The three methods, i.e. J-integral method (Matos et al. 1989, Soares and Tang 1998, Tong et al. 2007), the crack faces displacement-based method (Sun and Qian 1997, Shi et al. 2006) and the nodal force-based method (Bjerkén and Persson 2001, Xie and Biggers 2006),

were usually employed to calculate interfacial fracture parameters. The J-integral method is to calculate a contour integration surrounding the crack tip, which is usually computed within the FE code. The crack face displacement-based method is easily handled. However, verification by the author indicates (that is presented later) the SIF K_{II} by the method is not accurate. Among the three methods, the nodal force-based method seems to be the simplest and easily implemented. Rybicki and Kanninen (1977) firstly proposed a nodal force-based method for calculating SIFs of homogeneous materials based on Irwin's crack closure integral (Irwin 1958). Sun and Qian (1997) extended the method to interfacial cracks. However, the details are not available in the literature. Bjerkén and Persson (2001) employed an ABAQUS FE code, the decoupling concept and nodal force technique to calculate the interfacial SIFs. Xie and Biggers Jr. (2006) developed a special interfacial element and embedded it in the ABAQUS FE code to compute ERR using the nodal force technique. It is seen that these methods mentioned above appear complicated and not easily implemented for engineers. The method for calculating ERR proposed in the following sections is based on the nodal force and relative nodal displacements and offers a deeper insight into the ERR concept and is quite simple to use.

Irwin's contention (Irwin 1958) states that if a crack extends by a small amount (Δa), the energy absorbed in the process is equal to the work required to close the crack to its original length. The ERR (energy release rate) is evaluated by (Sun and Qian 1997):

$$G_i = \frac{1}{2\Delta a}\int_0^{\Delta a} \sigma_y \delta_y dx + \frac{1}{2\Delta a}\int_0^{\Delta a} \tau_{xy}\delta_{xy} dx \qquad 7.33$$

where G_i is the total ERR, the first and the second integral are the ERRs corresponding to opening and sliding mode (mode-I and mode-II), respectively; σ_y and τ_{xy} are the normal stress and shear stress, respectively; δ_y and δ_{xy} are the relative opening displacement and sliding displacement, respectively; and Δa is the length of the crack extension. These parameters are defined in Figure 7-15(a).

However, accurate results cannot be obtained using the stress along the crack line, due to the great variation of stress distribution along the interface caused by stress singularity and stress oscillation at crack tip. Rybicki and Kanninen (1977) proposed a nodal force-based method for calculating SIFs of homogeneous materials based on Irwin's crack closure integral.

Figure 7-17 shows the relative positions of the node 1 and $1'$ and 2 after the crack extension Δa. The essential of Irwin's crack closure integral, the strain energy dissipated for the crack

extension Δa, is equal to the work required to close the crack of amount Δa. Assuming that the relative displacements of a node in x and y direction are δ_x and δ_y (see Figure 7-16), respectively, and the nodal forces in x and y direction are F_x and F_y, respectively, the total work *w* required for bringing the node to its original position is given by

$$w = \sqrt{(F_x\delta_x)^2 + (F_y\delta_y)^2} \qquad 7.34$$

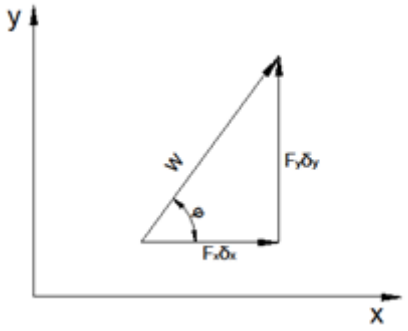

Figure 7-16 Illustration of work required to bring the node to the original position

In most cases, the relative position of the two nodes 1 and 1′after crack extension, which are originally coincident shown in the same figure as *original* before crack extension, is located between the original shown in Figure 7-17(a), i.e. $abs(u_{1y}^{(b)} - u_{1'y}^{(b)}) \geq abs(u_{1y}^{(b)} - u_{1y}^{(a)})$, where $u_{1y}^{(b)}$, $u_{1'y}^{(b)}$ and $u_{1y}^{(a)}$ are defined in Figure 7-18 (a) and (b) as follows: $u_{1y}^{(b)}$ refers to Figure 7-18(b) and it is the displacement of node 1 in the y-direction, and so on. According to eqn. 7.34 and the definition, the ERR is equal to the work required to bring both nodes to the original position divided by 2Δa, and thus is determined by:

$$G_1 = \frac{1}{2\Delta a}\sqrt{(F_{1x} \times \delta_{1x})^2 + (F_{1y} \times \delta_{1y})^2} \qquad 7.35$$

$$G_{1'} = \frac{1}{2\Delta a}\sqrt{(F_{1'x} \times \delta_{1'x})^2 + (F_{1'y} \times \delta_{1'y})^2} \qquad 7.36$$

$$G_i = G_1 + G_{1'} \qquad 7.37$$

$$F_{1y} = F_{1'y} \qquad 7.38$$

where G_1 and $G_{1'}$ are the work required to bring node 1 and $1'$ back to the original position, respectively; G_i is the total work; F_{1x} and F_{1y}, δ_{1x} and δ_{1y} are the nodal forces and relative displacements for node 1 respectively; $F_{1'x}$ and $F_{1'y}$, $\delta_{1'x}$ and $\delta_{1'y}$ are the nodal forces and relative displacements for node $1'$ respectively. These components are clearly illustrated in Figure 7-17(a).

Phase angle Ψ_G for ERRs, which characterises the ratio of opening mode and sliding mode, is defined by:

$$\psi_G = \tan^{-1}\left(\frac{G_{II}}{G_I}\right) \quad 7.39$$

where G_I and G_{II} are the energy dissipated for opening and sliding, respectively. The two quantities can be obtained by decomposing the total ERR G_i, and is analysed in the following. Refers to Figures 7-16 and 7-17 (a), the energy release rate G_I for opening consists of the ERR for bringing node 1 and $1'$ to the original position in *y* direction; similarly, G_{II} is the ERR required for bringing node 1 and $1'$ to the original position in *x* direction:

$$G_I = \frac{1}{2\Delta a}\left(F_{1x}\delta_{1x}\cos\varphi_1 + F_{1'x}\delta_{1'x}\cos\varphi_{1'}\right) \quad 7.40$$

$$G_{II} = \frac{1}{2\Delta a}\left(F_{1y}\delta_{1y}\sin\varphi_1 + F_{1'y}\delta_{1'y}\sin\varphi_{1'}\right) \quad 7.41$$

$$\varphi_1 = \tan^{-1}\left(\frac{F_{1y}\times\delta_{1y}}{F_{1x}\times\delta_{1x}}\right) \quad 7.42$$

$$\varphi_{1'} = \tan^{-1}\left(\frac{F_{1'y}\times\delta_{1'y}}{F_{1'x}\times\delta_{1'x}}\right) \quad 7.43$$

where, F_{1x}, F_{1y}, $F_{1'x}$ and $F_{1'y}$ are the nodal forces of node 1 and $1'$, in *x* and *y* direction respectively; δ_{1x}, δ_{1y}, $\delta_{1'x}$ and $\delta_{1'y}$ are the nodal relative displacements of node 1 and $1'$, in *x* and *y* direction respectively, and are determined by eqns.7.47 – 7.50.

Figure 7-17(b) shows the other case in which both nodes after crack extension are located at the same side with respect to the original, i.e. $abs(u_{1y}^{(b)} - u_{1'y}^{(b)}) \leq abs(u_{1y}^{(b)} - u_{1y}^{(b)})$, where $u_{1y}^{(b)}$, $u_{1'y}^{(b)}$ and $u_{1y}^{(a)}$ are defined in Figure 7-18. This implies the crack experienced a rigid motion during crack extension. In this case, the ERR is determined by eqn. 7.44, and the phase angle is defined by eqn. 7.45.

$$G_i = \frac{1}{2\Delta a}\left(F_y\delta_y + F_x\delta_x\right) \quad 7.44$$

$$\psi_G = \tan^{-1}\left(\frac{G_{II}}{G_I}\right) = \tan^{-1}\left(\frac{F_x\delta_x}{F_y\delta_y}\right) \quad 7.45$$

It is noted that: in Figure 7-17(b), $F_{1y} = F_{1'y}$, while F_{1x} is usually not equal but very close to $F_{1'x}$, the bigger one should be chosen to substitute F_x in eqn. 7.44 to calculate G_i.

Alternatively, the rigid motion can be circumvented by applying an additional constraint to the structure (this will be presented later). The relative position of both nodes will be located between the original after being imposed the additional constraint, like the one shown in Figure 7-17 (a); and thus eqns. 7.35 – 7.37 can be used to calculate the ERR.

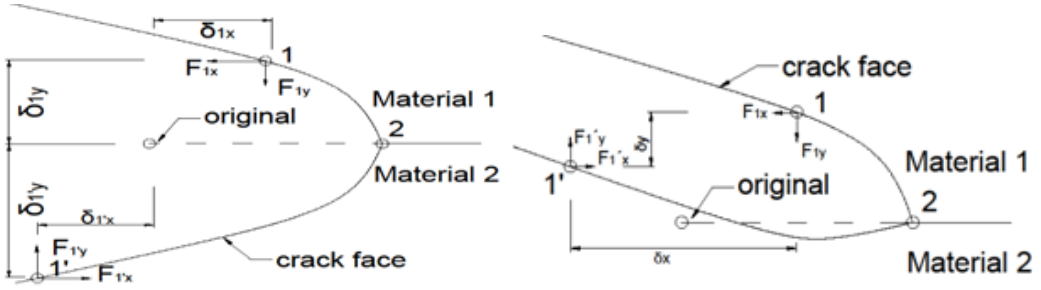

Figure 7-17 The nodal relative position after crack extension: (a) the both nodes located between the original; (b) the both nodes located at the same side with respect to the original

7.3.1.3 Calculation Procedure for Interfacial ERR

The calculation procedure consists of three analyses on three models shown in Figure 7-18, namely: model-a, which is the original model; model-b, when the crack extends a length of Δa; and model-c, when three very stiff spring elements are imposed to connect the nodes at the vicinity of the tip. The areas surrounding the crack tip in the three models are meshed with square elements of identical length L_0. It is noted that node 1 and 1′ in Figure 7-18(b) and (c) are originally at the same position before crack extension.

The procedure is as follows:

(1) First, apply load and analyse the original model-a (Figure 7-18(a)), then obtain the nodal displacements of both crack faces, $(u_{1x}^{(a)}, u_{1y}^{(a)})$, $(u_{2x}^{(a)}, u_{2y}^{(a)})$, $(u_{4x}^{(a)}, u_{4y}^{(a)})$, $(u_{4'x}^{(a)}, u_{4'y}^{(a)})$, $(u_{5x}^{(a)}, u_{5y}^{(a)})$, $(u_{5'x}^{(a)}, u_{5'y}^{(a)})$, and so on. Thus, K_I is calculated using eqn.7.19 and the crack face displacement extrapolation method proposed by Shi et al. (2006), and the 'initial length' is determined by eqn. 7.46;

$$L_{ini} = L_0 + (u_{2x}^{(a)} - u_{1x}^{(a)}) \qquad 7.46$$

(2) Second, analyse the model-b (Figure 7-18(b)). Allow the crack extension a small amount Δa, which is equal to the element length L_0, then apply load and analyse the model. The displacements of node 1 and 1′ are then obtained, i.e. $(u_{1x}^{(b)}, u_{1y}^{(b)})$, $(u_{1'x}^{(b)}, u_{1'y}^{(b)})$;

(3) Third, referring to Figure 7-18(c), generate three very stiff spring elements connecting nodes 1 and $1'$, 1 and 2, and $1'$and 2; meanwhile 'initial lengths' of node 1 - 2 and node $1'$ - 2 are set to be equal to the one determined by eqn. 7.46 during the spring element creation in ANSYS code. This ensures the deformations of nodes 1, $1'$ and 2 in model-c be close to model-a, which was the original. Analyse the loaded model - c to obtain the nodal forces $F_{y1-1'}$, F_{x1-2} and $\mathrm{F_{x1'-2}}$ (note: $\mathrm{F_{1y}} = \mathrm{F_{1'y}} = \mathrm{F_{y1-1'}}, and\ \mathrm{F_{1x}} = \mathrm{F_{x1-2}}, \mathrm{F_{1'x}} = \mathrm{F_{x1'-2}}$, in Figure 7-18 (c)).

(4) Fourth, check the relative positions of the three nodes using the displacements of nodes 1, $1'$ of Figure 7-18(b) and the original node 1 of Figure 7-18(a); ERR is calculated using eqns. 7.35 – 7.37 for the case in which the relative position of both nodes are located between the original (like the one shown in Figure 7-17(a)); otherwise ERR is calculated using eqn. 7.44.

$$\delta_{1x} = \left|u_{1x}^{(a)} - u_{1x}^{(b)}\right| \qquad 7.47$$

$$\delta_{1y} = \left|u_{1y}^{(a)} - u_{1y}^{(b)}\right| \qquad 7.48$$

$$\delta_{1'x} = \left|u_{1x}^{(a)} - u_{1'x}^{(b)}\right| \qquad 7.49$$

$$\delta_{1'y} = \left|u_{1y}^{(a)} - u_{1'y}^{(b)}\right| \qquad 7.50$$

where the relative nodal sliding displacements δ_{x1} and $\delta_{x1'}$ take positive values, because the energy required to close the crack is positive wherever the nodes are. This is illustrated in Figure 7-18 in more detail.

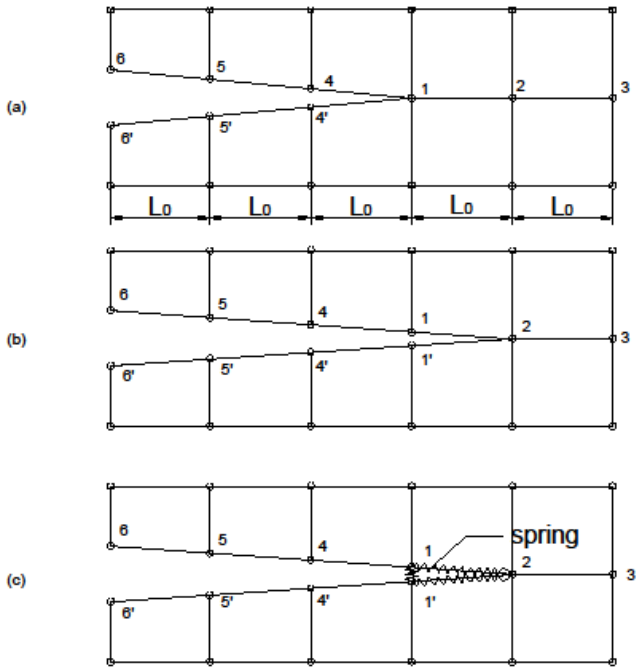

Figure 7-18 (a) original meshed model-a: square elements with identical size; (b) meshed model-b: square elements with identical size with crack extension ($\Delta a = L_0$); (c) meshed model-c: square elements with identical size, imposed stiff spring.

7.3.1.4 Verification of the Method for Calculating Interfacial ERR

In order to verify the applicability and accuracy of both the ERRs determined by the method proposed earlier and SIFs proposed by Shi et al. (2006), two examples, which have been presented by previous researchers, are used to calculate the ERR and SIF using the proposed method, and compared with the theoretical solutions.

Example I: An infinite bi-material panel with a central crack

The first example is shown in Figure 7-19(a). The system consists of two semi-infinite dissimilar materials and a central crack of length *2a*. It is loaded by a uniform pressure P_0 on the crack face. The analytical, exact solution of SIF at crack tip (Shi et al. 2006) is:

$$K = K_I + iK_{II} = (1 + 2i\varepsilon)P_0\sqrt{\pi a} \qquad 7.51$$

Table 7-9 Mechanical properties and dimension of the bi-material system

Bi-material	Elasticity modulus (MPa)	Poisson's ratio	Width (mm)
Material 1	71000	0.33	14
Material 2	3300	0.34	14
2a=1.4mm, β=-0.22, ε=0.071, P_0=10 N/mm			

The mechanical parameters of the system are listed in Table 7-9. The width of square panel is 14 mm, and the uniform pressure is 10 N/mm, plane strain conditions are considered. The analytical K_I and K_{II} evaluated by eqns.7.51, and G_i evaluated by eqn. 7.21 are listed below:

$K_I = 14.83 MPamm^{0.5}$

$K_{II} = 2.11 MPamm^{0.5}$

$G_i = 0.0229 N/mm$

The FE code ANSYS12.0 was employed. Only the right half of the panel was analysed due to symmetry. Similar to the analysis by Shi et al. (2006), the 4-node-Plane 42 element was used and the area surrounding the crack tip was fine meshed with an element length of 0.01 mm, while the length of the global elements beyond the fine meshed zone was about 0.2 mm. The total number of nodes was approximately 14000. The crack extension Δa was 0.01 mm, equal to the crack length in the zone. The meshed panel and the elements in the fine meshed zone are shown in Figure 7-19(b) - (c).

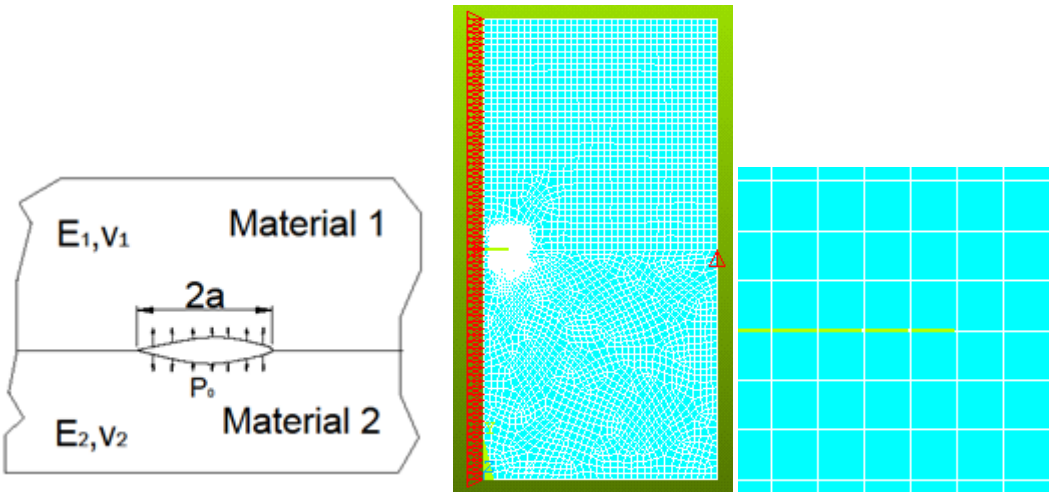

(a) (b) (c)

Figure 7-19 (a) Infinite bi-material system with a central crack loaded by pressure P_0, (b) right half of the meshed system, (c) square element at crack tip in fine - meshed zone.

The total energy release rate, calculated using the procedure proposed earlier, is 0.0224 N/mm, with 2% error compared to the analytical solution of 0.0229 N/mm. Thus the calculation method for determining G_i is verified.

Figure 7-20 shows the K_I-r/2a relationship and the linear fitting. The K_I was calculated using eqn. 7.19. The linear fitting equation in Figure 7-20 indicates that the K_I is $13.90 MPamm^{0.5}$, which is close to the analytical solution of $14.83 MPamm^{0.5}$. However, the $K_{II,}$ determined using the same method, greatly deviates from the theoretical value of 2.11 $MPamm^{0.5}$.

Therefore, in the present study, the strain energy release rate is evaluated using the method presented earlier with the aid of FE code ANSYS, and K_I is calculated by using the method proposed by Shi et al. (2006), while K_{II} is determined by eqn.7.21.

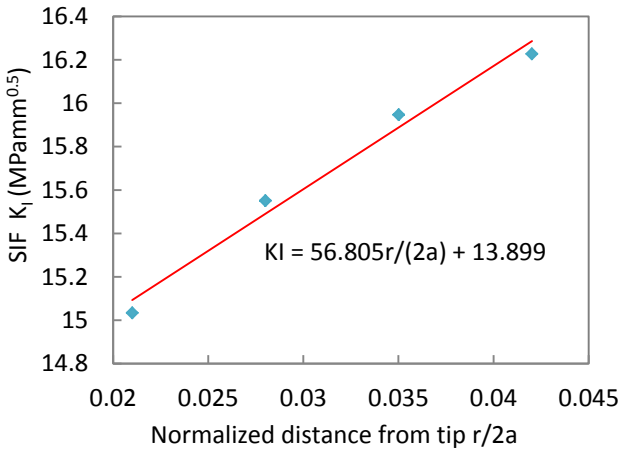

Figure 7-20 K_I and normalized distance with linear-fitting for Figure 7-19

Example II: A bi-material beam with symmetrical interfacial crack under 4PB

The second example is a bi-material beam with the symmetrical interfacial cracks under four-point bend shown in Figure 7-21(a). The specimen and its loading configuration was purposely designed for measuring the interfacial fracture toughness of bi-material by Charalambides et al. (1989) and Matos et al.(1989). Charalambides et al. (1989) offered an analytical solution shown by the eqn. 7.52, for the crack length *a* being much bigger than the height of the beam.

$$G_i = G^* \frac{P^2 L^2 (1-\nu_2^2)}{b^2 h^3 E_2} \qquad 7.52$$

$$G^* = \frac{3}{2}\{1/(h_2/h)^3 - \lambda/[(h_1/h)^3 + \lambda(h_2/h)^3 + 3\lambda(h_1 h_2/h^2)(h_1/h + \lambda\, h_2/h)^{-1}]\} \qquad 7.53$$

$$\lambda = \frac{E_2(1-\nu_1^2)}{E_1(1-\nu_2^2)} \qquad 7.54$$

where G_i is the total ERR; G^* is the dimensionless factor, b and h is the width and total height of the beam, respectively, h_1 and h_2 are the height of the layers of material 1 and material 2, respectively; P is the total load, E_1 and ν_1 are the elastic modulus and Poisson's ratio of material 1, respectively; E_2 and ν_2 are the elastic modulus and Poisson's ratio of material 2, respectively; L is the spacing between the inner and the outer load points. According to the analysis by Charalambides et al. (1989), the dimensions of the bi-material beam shown in

Figure 7-21(a) are taken as those listed in Table 7-10. Consequently, the value of G^* determined by eqn. 7.53 is 6.52, thus the ERR G_i calculated using eqn. 7.52 is 0.0371N/mm.

Table 7-10 Dimensions and mechanical parameters of biomaterial beam illustrated in Figure 7-21 (a)

a=10mm, $h_1=h_2$=2 mm, L=10 mm, C=20 mm, b=1 mm, P=2 N, E_1=100MPa, E_2=1000MPa, $v_1=v_2$=0.3

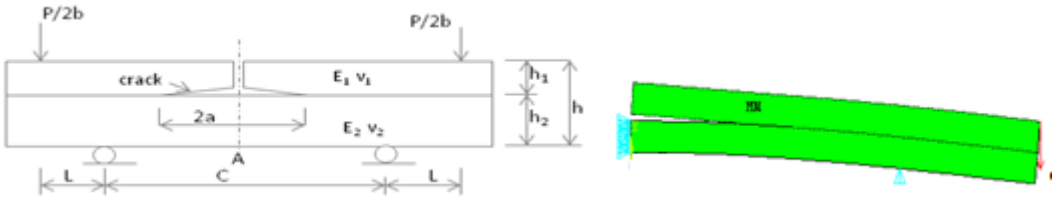

(a) (b)

Figure 7-21 (a) a bi-material beam with symmetrical interfacial cracks under four-point bend; (b) the deformed right half of the biomaterial beam in (a)

The bi-material beam with the dimensions, mechanical parameters and the applied load listed in Table 7-10 was analysed. The analysis procedure was the same one presented previously. Similar to the modelling of first example, the 4-node-Plane 42 element was used and the area surrounding the crack tip was fine meshed with the element of the length of 0. 1 mm. Only the right half of the beam was analysed due to symmetry. The deformed beam under loading is shown in Figure 7-21(b). The calculated results indicated that the first two nodes of upper and lower crack faces behind the crack tip (see Figure 7-17(b)) after crack extension were located at the same side with respect to the original, i.e. the interfacial crack experienced a rigid motion during the crack extension Δa. Therefore, the ERR G_i was determined using eqn.7.44, the value was 0.0364N/mm, that is 1.8% error compared to the analytical solution 0.0371N/mm.

Alternatively, in order to circumvent the rigid motion of the interfacial crack, an additional boundary condition was imposed, namely: the vertical displacement at the beam bottom at middle (point A in Figure 7.21(a)) after crack extension was set to be equal to that before crack extension, and consequently the value of G_i was determined using eqn. 7.35 – 7.37 was 0.0357N/mm, that is 3.8% error compared to the analytical solution.

It is seen from the numerical calculation results of the two examples that the method proposed by this study for calculating the total interfacial energy release rate is verified. In addition, it is also verified that evaluation of SIF K_I using the method proposed by Shi et al. (2006) is accurate enough, but K_{II} is not.

7.3.2 Measurement of Interfacial Fracture Toughness of SBRPMC1.5%-on-OPCC Composite Beams

7.3.2.1 Test Specimen and Specimen Preparation

In an interfacial fracture, the crack propagation along the interface is usually constrained in the interface due to the fact that the bond strength is normally much lower than that of both materials. Because stress distribution in the crack line at the vicinity of the crack tip varies greatly due to the stress singularity at the crack tip and the stress oscillation in the vicinity, the strength-based criterion (tensile and shear bond strengths) method for assessing interface delamination is no longer the appropriate approach. In fact, interface fracture mechanics has been used to evaluate the interfacial fracture toughness since the 1990's. For example, Klingbeil and Beuth (1997), and Huang et al. (2005) employed the experimental setup shown in Figure 7-22(a) to measure the interfacial toughness of two metal layers. Watanabe (2009) investigated the interfacial delamination of mortar and ceramic tiles under shear loading. Wang and Suo (1990), and Shi et al. (2006) tested interfacial toughness of adhesive joints using Brazil-nut-sandwiches specimens; Büyüköztürk and Lee (1993) studied the interfacial fracture toughness of a mortar-granite interface. Satoh et al. (2010), Shah and Kishen (2010) conducted the experiment shown in Figure 7-22(b) to measure interfacial fracture toughness of concrete-to-concrete. Chabot et al. (2013) investigated the interfacial fracture behaviour of cement concrete and asphalt concrete using the experiment illustrated in Figure 7-22(c), for investigation of interfacial performance of asphalt concrete overlay on old cement pavements.

For concrete composite beams, the experiment shown in Figure 7-22(a) may not be an appropriate one, due to the fact that the cracking may not symmetrically propagate along left and right interfaces. The specimen shown in Figure 7-22(b) is not viable for roller-compacted concrete, because the mix is very dry, and the vertical interface is different from the actual one in fields. Therefore, it is necessary to develop a new test specimen and loading configuration for testing the interfacial fracture toughness of concrete – on – concrete, for the design of concrete overly on worn concrete pavements.

The specimen and loading configuration for testing interfacial toughness should properly simulate the mechanical behaviour of the actual structures. The present research is to develop a new mix used as bonded overlay on worn concrete pavements, which is shown in Figure 7-23(a). The inherent interfacial crack shown in Figure 7-23(a) will open under the vehicular loading (it will be presented in Chapter 9). The loading configuration shown in Figure 7-23(b)

appears to be an appropriate test setup for simulating the pavement system, as it forces the crack to propagate along the interface and minimise the probability for the crack to deflect upwards. Moreover, the advantage of this loading configuration is that it is much more easily to handle the test process due to the single crack propagation along the interface on the right hand side. Therefore, the experiment illustrated in Figure 7-23(b) was adopted to measure the interfacial toughness in the present study.

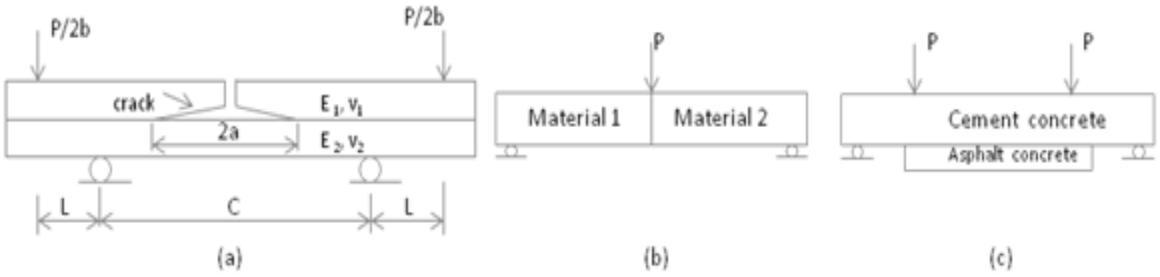

Figure 7-22 (a) bi-material beam with symmetrical interfacial cracks under four-point bend; (b) bi-material beam with vertical interface under 3PB; (c) bi-material beam with horizontal interface under 4PB.

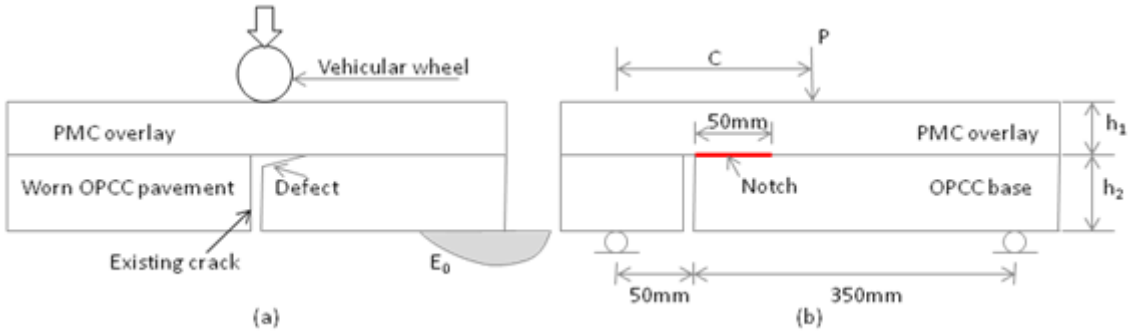

Figure 7-23 (a) concrete overlay bonded on worn concrete pavement system, (b) composite beam with interfacial crack under three-point bend for measuring the interfacial fracture toughness

In this study, for the composite beams used for the three-point bending test, the interfacial notch was 50 mm long, and was created by gluing a tape on the OPCC base prior to casting the PMC mix (see Figure 7-23 (b) and Figure 7-25(a)). A vertical notch saw-cut through the OPCC base was 50 mm away from the left support. Two groups of composite beams were prepared: one was fabricated with OPCC bases with a roughened interface, and the other with a smooth interface.

More explanation of the composite beams is presented in Table 7-11. The mix proportion of SBRPMC1.5%-35 can be found in Table 5-1 and that of the OPCC in Table 4-14. The formation of the composite beam and its curing procedure were detailed in Section 4.4.

All spans of the beams for the three-point bending test were 400 mm, and the distances between the loading point and the left support were 150 mm and 200 mm for the roughened

interface composite beam and the smooth interface composite beam, respectively. This is to obtain interfacial debonding for both types of specimens. The experiments conducted by this study, presented later, showed that interfacial delamination really developed in all composite beams. The loading rate was controlled by the clip gauge mounting at the mouth of the interfacial notch. The following loading procedure was applied: the loading rate was 0.0001 mm/s until CMOD was equal to 0.2 mm, then 0.0002 mm/s until CMOD was equal to 0.5 mm, and then 0.001 mm/s until CMOD was equal to 2 mm, and finally 0.003 mm/s until beam failure. Due to the very low loading rate, the crack extended slowly along the interface, and thus the load reading and the corresponding crack length were easily recorded by observation. The experimental results are tabulated in Table 7-12.

The composite beams for the shear test were without interfacial notch, and the OPCC bases were centrally saw-cut to the interface to form a notch through OPCC base. The shear test aimed at measuring the shear strength of PMC. This constituted a research by a colleague. Unfortunately, two of the three composite beams exhibited interfacial delamination before the cracks penetrated vertically into the PMC layer. This was due to the segment of 23mm-length beam being under bending, resulting in fracture at the interface. The loading rate was controlled by the vertical displacement measured at the position of the top roller (see Figure 7-24(b) and Figure 7-25(b)), and the incremental rate was 0.00001 mm/s. The crack length and corresponding load reading were made available, and recorded in Table 7-12. They are also illustrated in Figure 7-29.

The width of all the composite beams was 100 mm, and the height of the PMC overlay and OPCC bases are listed in Table 7-12.

Table 7-11 Description of composite beams used for measurement of interfacial fracture toughness

ID of beams	Num. of beams	Mix ID of PMC overlay	OPCC interface	Dimensions W x H x Length	Loading mode
SBRPMC1.5% -on-OPCC-R	3	SBRPMC1.5%	Rough	PMC overlay: 100x72x500mm^3	Three-point bend C=150 mm
SBRPMC1.5% -on-OPCC-S	3	SBRPMC1.5%	Smooth	OPCC base: 100x48x500mm^3	Three-point bend C=200 mm
SBRPMC1.5% -on-OPCC-R	2	SBRPMC1.5%	Rough		Shear test

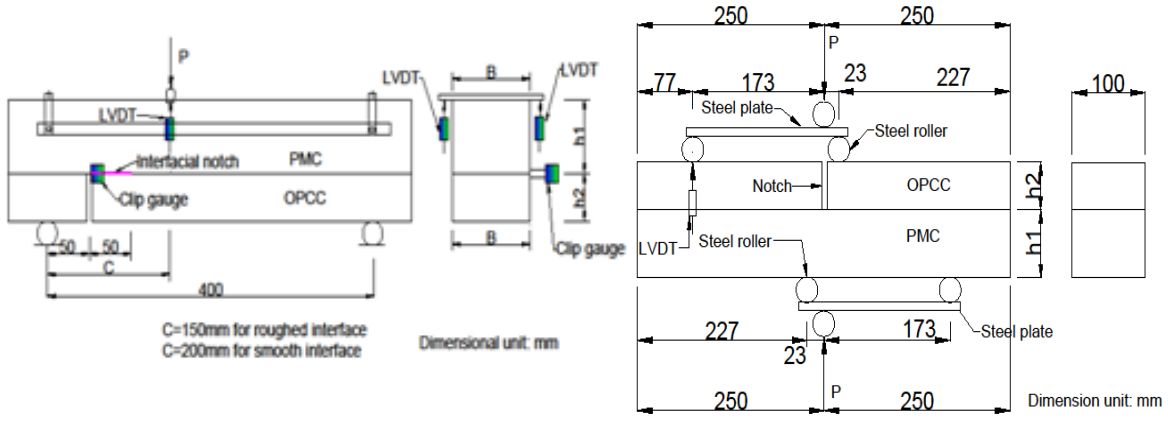

(a) (b)

Figure 7-24 (a) SFRPMC-on-OPCC composite beam with interfacial notch under three-point bend, (b) PMC-on-OPCC composite beam with through OPCC base notch under shear test

(a) (b)

Figure 7-25 (a) experimental setup for SFRPMC-on-OPCC composite beam with interfacial notch under 3PB, (b)experimental setup for SFRPMC-on-OPCC composite beam with a notch through OPCC under shear test

7.3.2.2 Experimental Results

Interfacial delamination and experimental results

During the propagation of the crack along the interface, the stress field ahead of the crack tip was always at critical state because the crack extended very slowly, implying that the SIF and ERR determined under the condition were critical SIF or critical ERR.

Careful observation during testing indicated that all composite beams made of OPCC bases with smooth and roughened interface exhibited interfacial delamination during testing under the present loading configuration. Figure 7-26 illustrates the typical trajectories of crack propagation. Figure 7-27 pictures the interfacial debonding of composite beams under three-point bending and shear test. Figure 7-28 shows the typical load – CMOD curves of SBRPMC1.5%-on-OPCC composite beam with interfacial notch under three-point bending;

and Figure 7-29 illustrates the crack lengths of interfacial delamination and the corresponding load readings of beam 1 and beam 2 under shear test.

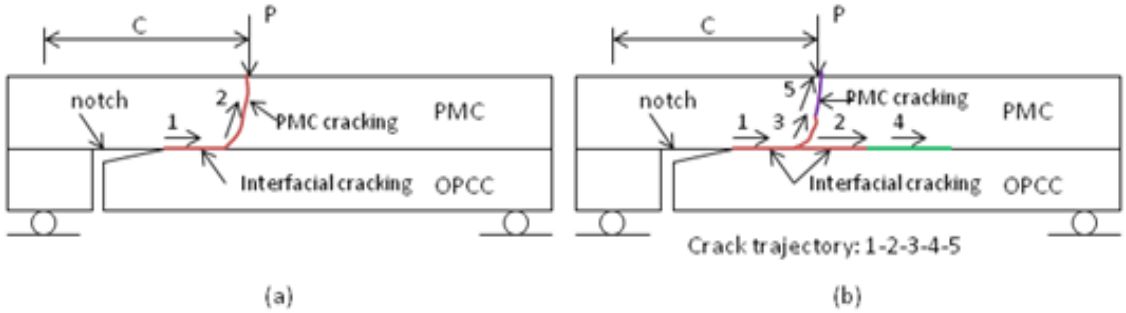

Figure 7-26 Cracking trajectories: (a) type-1: cracking initiated at notch tip and extended along interface, and then obliquely penetrated into PMC; (b) type-2: cracking initiated at notch tip and extended in interface and then obliquely penetrated into PMC, and then propagated along interface again.

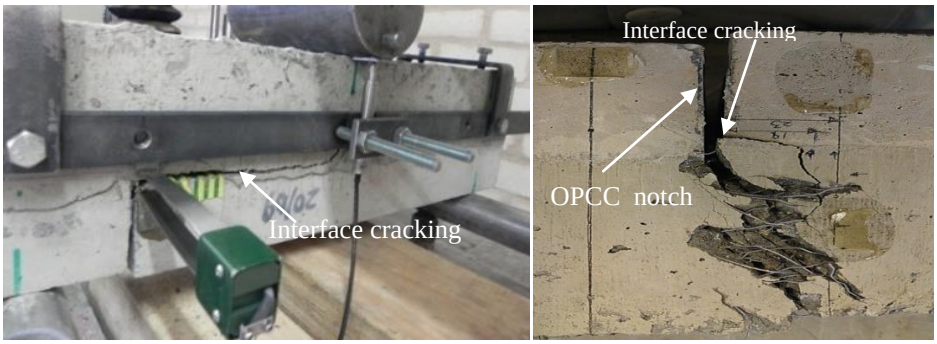

(a) (b)

Figure 7-27 Interfacial debonding of composite beams: (a) under three-point bending test, (b) under shear test.

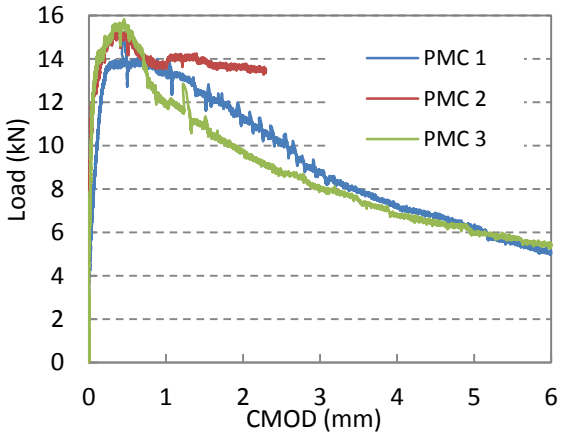

Figure 7-28 Typical load vs. CMOD of SBRPMC1.5%-on-OPCC composite beam with horizontal interface notch under three-point bending test

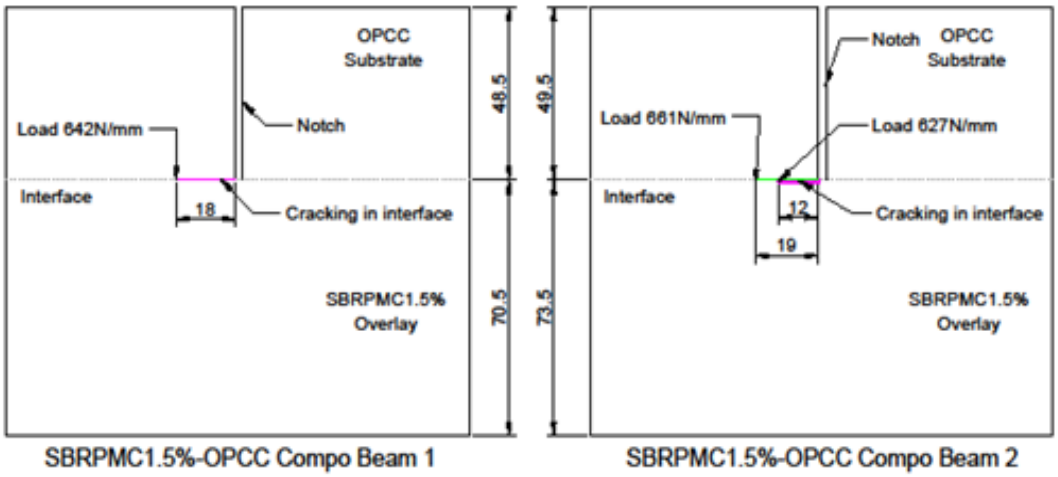

Figure 7-29 Crack lengths of interfacial delamination and the corresponding load readings of beam 1 and beam 2 under shear test

Determination of interfacial fracture toughness

With the knowledge of the load reading and the corresponding crack length, the critical interfacial ERR (interfacial fracture toughness) G_{ic} was calculated using the method proposed previously. The mechanical properties of the two materials, i.e. SBRPMC1.5% and OPCC, are shown in Table 7-3. The characteristic length was taken as 120 mm for all beams; consequently Dunder's bi-material parameter β (Sun and Qian 1997) and material constant ε are determined by eqns.7.23 and 7.27 for the SBRPMC1.5%-on-OPCC composite beam as:

β=-0.0361

ε=0.01149

The characteristic length of 120 mm is similar to the average of the height of composite beams. Matos et al. (1989) ever used the beam height as characteristic length in the analysis of a bi-material specimen shown in Figure 7-22(a). The value of characteristic length may be arbitrarily taken as it has little effect on calculation results. The FE code ANSYS12.0 (2009 SAS *IP* Inc) was employed to analyse the loaded specimens. The fine mesh zone around the crack tip was meshed with square element with lengths of 0.1 mm, and accordingly the ratio of element size to crack length was less than 0.01. The four-node constant strain element, i.e. 4-node Plane 42 in ANSYS code was employed in the fine mesh zone, and the element Spring14 was used to connect the three nodes at the crack tip. Plane strain conditions were assumed. The number of nodes for a typical model was around 30000. The typical general meshed model for the three-point bending test is illustrated in Figure 7-30(a); that for the

shear test is shown in Figure 7-31(a); and the square elements in the fine mesh zone, with the same size of 0.1 mm in the two models, are shown in Figure 7-31(b).

As described earlier, the complete solution in obtaining the strain energy release rate consisted of three analyses: (1) The model was first analysed with the knowledge of load and crack length. The K_I was calculated with the nodal displacements (from the third node away from the tip) of both upper face and lower face in the vicinity of the crack tip extracted from the FEA results. The initial length of tip node and the next node ahead of the crack tip was determined. (2) Crack extension of 0.1 mm, i.e. Δa=0.1 mm, was allowed and the model was analysed to obtain the displacement of the node at the original crack tip. (3) Three stiff spring elements were imposed to connect the three nodes at the crack tip to obtain nodal forces, and then the strain energy release rate (G_{ic}) was calculated with the knowledge of the nodal forces and the relative opening and sliding displacements. (4) K_{II} was calculated using eqn.7.21. The typical relationships of calculated K_I and normalized distance r/a is plotted in Figure 7-32, and the linear fitting shows that the K_I is equal to 42.62 MPamm$^{0.5}$.

The critical interfacial strain energy release rate G_{ic}, the critical SIFs K_{Ic} and K_{IIc}, phase angle ψ_G is listed in Table 7-12.

It is worth pointing out that the calculated results using all testing data listed in Table 7-12 showed that the relative position of the two nodes 1 and 1′ after crack extension (see Figure 7-18(b)), which are originally at the same position before crack extension, is located between the original position, like the one shown in Figure 7-17(a). Accordingly, the critical interfacial ERRs (interfacial fracture toughness) and phase angles were determined using eqns. 7.35 -7.37 and 7.39.respectively.

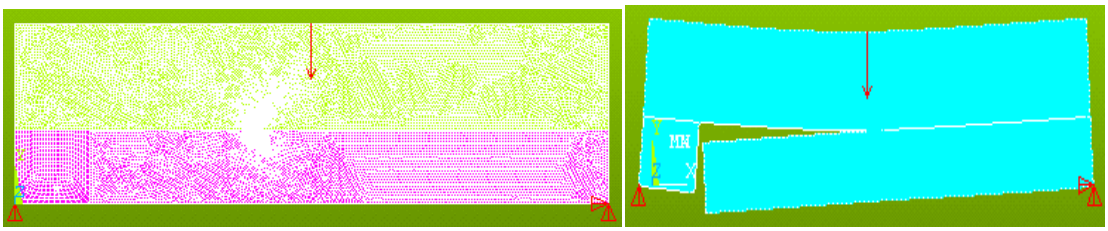

(a) (b)

Figure 7-30 (a) meshed composite beam under three-point bend modelled by ANSYS code, (b) deformed composite beam under loading modelled by ANSYS code.

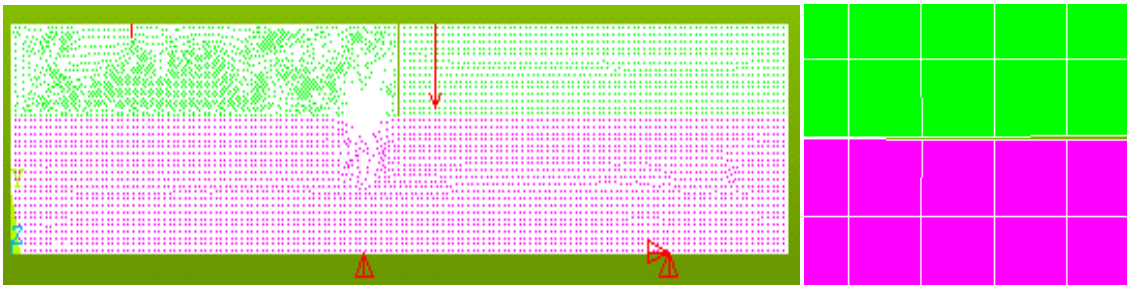

(a) (b)

Figure 7-31 (a) meshed composite beam under shear test modelled by ANSYS code, (b) square element in fine mesh zone modelled by ANSYS code.

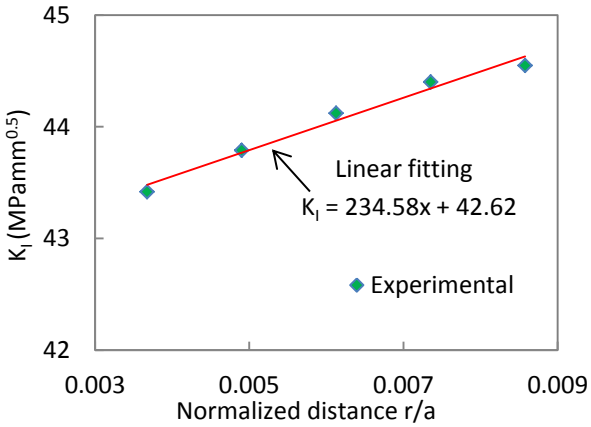

Figure 7-32 Typical K_I-r/a relationship and linear fitting by extrapolation method using crack face displacement

Table 7-12 Dimensions of composite beams, load reading and its corresponding crack length and calculated interfacial fracture toughness of SBRPMC1.5%-35-on-OPCC composite beams

Interface condition	Loading mode	Geomet. of beams			Experimental		Calculation results				
		h_1 mm	h_2 mm	a_0 mm	p N/mm	a mm	K_{IC} (MPamm$^{0.5}$)	K_{IIC}	G_{ic} (J/m^2)	ψ_G (Deg.)	Average G_{iC} (J/m^2)
Roughe.	3PB	71	47	50	152	56	36.83	16.82	46.2	11.86	52.0
		70	47	50	150	87	35.17	32.14	64	33.67	
		68	48	50	143	50	37.97	19.43	51.3	17.20	
				50	155	80	42.62	21.78	64.6	19.68	
Roughe.	Shear	49	71	0	654	18	38.02	19.88	51.9	16.99	
	loading	50	74	0	627	12	39.63	7.80	46	3.06	
				0	661	19	35.63	12.35	40.1	8.27	
Smooth	3PB	70	50	50	115	155	26.3	17.96	28.6	30.19	22.6
		72	48	50	124	200	18.29	5.55	10.3	79.01	
		71	50	50	126	70	29.79	11.72	28.9	10.80	

Note: the load p shown in the table is for 1 mm width beam, not the total load.

According to the definition of the phase angle for ERR, the tangent value of phase angle characterises the ratio of ERR dissipated by sliding mode to that dissipated by opening mode. Figure 7-33 demonstrates the relationship of G_{ic} and phase angles for both the rough and smooth interface beams. It appears that the interfacial toughness G_{ic} is insensitive to phase angle for these bi-materials, i.e. SBRPMC1.5%-35-on-OPCC.

This interfacial fracture toughness and phase angle corresponding to the critical ERR will be used to compare with those of SBRPMC1.5%-35 overlay pavement system subjected to vehicular loading in Chapter 9.

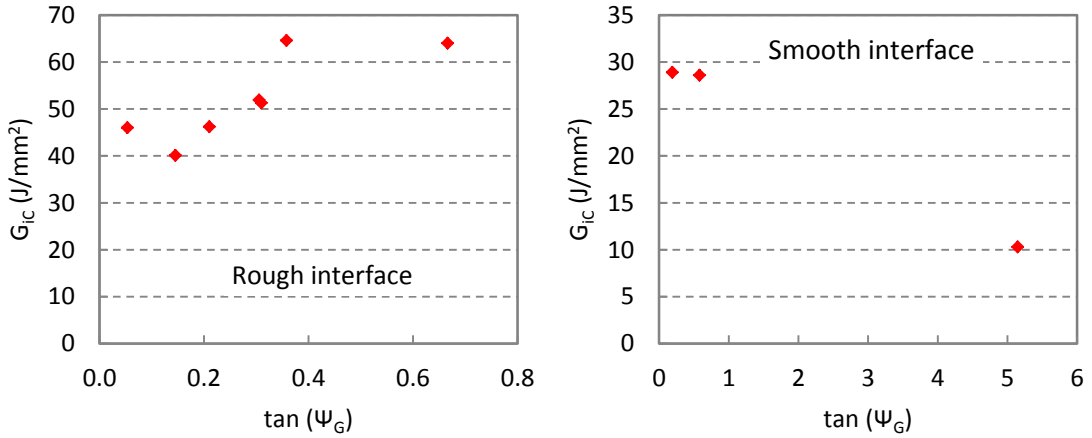

Figure 7-33 G_{ic} vs. tan (Ψ_G) relationship for SBRPMC1.5%-on-OPCC composite beams under three-point bend and shear test: (a) beam with roughened interface, (b) beams with smooth interface

It is seen from Table 7-12 that the critical strain energy release rate (G_{ic}) of the interface of the SBRPMC1.5%-35-on-OPCC composite beam with roughened and smooth interfaces are 52 J/m^2 and 22.6 J/m^2, respectively; the former is about 2.3 times the latter. The splitting tensile bond strengths of blocks, saw-cut from the tested composite beams were 2.96 MPa and 1.80 MPa for roughened interface beam and smooth interface beam respectively, listed in Table 7-7; the former is 1.64 times the latter.

Tschegg et al. (1993) investigated the interfacial fracture energy of OPCC-on-OPCC, whose 28-day compressive cube strength was 41.4 MPa, by splitting notched interfaces of old concrete-on-new concrete composite blocks, and by recording the work-done by the externally applied load. The average of fracture energy (G_F) at the age of 28 days for new concrete for smooth and rough interface was 10 J/m^2 and 15 J/m^2, respectively. This interfacial fracture toughness is much lower than those listed in Table 7-12, which are measured using SBRPMC1.5%-35-on-OPCC composite beams. It indicates from the fracture mechanics point of view that high bond strength between the mix SBRPMC1.5%-35 and OPCC was achieved.

7.3.3 Applications

The interfacial toughness of the SBRPMC1.5%-on-OPCC composite beams was measured and is listed in Table 7-12, and the procedure for calculating the energy release rate of the

interface was proposed and verified. In order to gain more confidence in the utilization of the calculation procedure and to explore the interfacial delamination behaviour, two composite beams under the four-point bending test, which have been presented in Section 7.1, are analysed using interface fracture mechanics, and compared with the experimental results.

7.3.3.1 Interfacial Behaviour of Composite Beam under Four-Point Bend

In the SFRPMC-on-OPCC composite beam, cracking initiates from the bottom of the OPCC base. When the crack reaches the interface, it will penetrate into the top layer without debonding if the specimen has a good bond, while the crack will deflect into the interface for a poor bond. He and Hutchinson (1989) proposed a competition criterion for the crack impinging interface, shown in Figure 7-34. The impinging crack is likely to be deflected into the interface if the inequality 7.55 is satisfied; conversely, the crack will tend to penetrate the interface when the inequality is reversed:

$$\frac{G_{ic}}{G_c} \leq \frac{G_d}{G_p} \qquad 7.55$$

where, G_{ic} and G_c are the toughness of the interface and the toughness of the top layer material in mode-I loading, respectively. G_d and G_p are the strain energy release rate for deflection into the interface and penetration into the top material, respectively. Both G_d and G_p are computed by assuming crack extension of a small amount (Δa). For the computation of G_p, the crack tip is in the top layer, and thus the stress field at the crack tip is dominated by the homogeneous material.

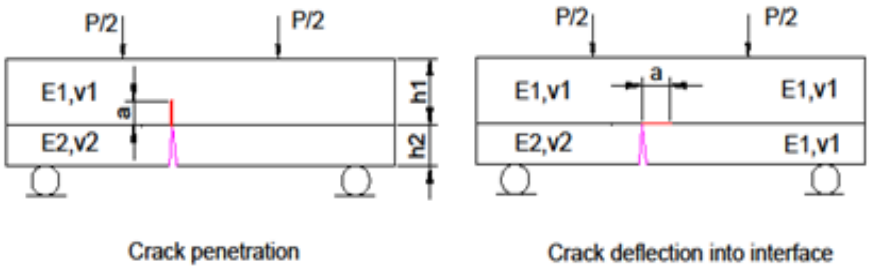

Figure 7-34 Competition of cracking penetration or deflection in composite beam under four-point bend

For a crack in single material, crack fracture is traditionally characterized by stress intensity factors, i.e. K_I and K_{II}, instead of the energy release rate, although both can be correlated. For a crack in a homogeneous material under mixed mode loading, Broek (1986) proposed a general criterion for crack extension given by:

$$\left(\frac{K_I}{K_{IC}}\right)^{\alpha} + \left(\frac{K_{II}}{K_{IIC}}\right)^{\beta} = 1 \qquad 7.56$$

where K_I and K_{II} are stress intensity factors (SIF) for mode-I and mode-II loading, respectively; K_{IC} and K_{IIC} are the critical stress intensity factors for mode-I and mode-II loading, respectively; α and β are material constants. In the present composite beam under four-point bend, the K_{II} is small and can be ignored, thus a simple criterion for vertical penetration into top material is given by:

$$K_I \geq K_{IC,M}^{ini} \qquad 7.57$$

where K_I is SIF in mode-I loading, and $K_{IC,M}^{ini}$ is the critical fracture toughness of matrix at cracking initiation at notch tip in mode-I loading. It is noted that $K_{IC,M}^{ini}$ is the critical SIF of the matrix (mix without fibres) because the fibres in the matrix are inactive before cracking. The $K_{IC,M}^{ini}$ of matrix SBRPMC0% is 24.63 MPamm$^{0.5}$, listed in Table 6-4, and the matrix corresponds to the mix SBRPMC1.5%-35.

For crack deflection into the interface or crack propagation in the interface, the single mechanical parameter, i.e. strain energy release rate $G_{i,}$ may properly characterize the interfacial delamination behaviour, because interfacial bonds are usually much weaker than the strength of both materials, and thus the crack propagation may be constrained in the interface. This is more or less verified by the experimental results of K_I and K_{II} and G_{ic} listed in Table 7-12, which indicates that G_{ic} is almost independent of the constituents of K_I and K_{II}. Based on this discussion, the single parameter G_i is used to assess crack propagation at interface; namely the crack is likely to be deflected into the interface or to extend in the interface if the inequality expression 7.58 is satisfied:

$$G_i \geq G_{ic} \qquad 7.58$$

where G_i is the energy release rate of the interface, and G_{ic} is the interfacial toughness.

7.3.3.2 Interfacial Behaviour of Composite Beam with Roughened Interface

It has been presented in Section 7.1.2.2 that the composite beam-3, recorded in Tables 7-2, 7-4 and 7-5 fractured vertically without interfacial delamination under four-point bending test. The beam consisted of SBRPMC1.5% overlay and OPCC base, with roughened interface. The beam dimensions and loading configuration are shown in Figure 7-35, and the test procedure has been described in Section 7.1.2. The crack initiated from the bottom at a position 140 mm from the left support.

Now, the fracture behaviour of the composite beam will be analysed by comparison of the calculated K_I and G_i and the criteria proposed above. It can be observed from Figure 7-36 that OPCC started cracking at a load of 281 N (for 1 mm width of beam), and then the load dropped down to 102 N in displacement-controlled loading mode. So, the load corresponding to crack impinging the interface might lie in the range of 281 N to 102 N. Let it be assumed to be 102 N (1 mm width of beam). At the crack impinging interface, the SIF K_I for vertical penetration and G_i for left deflection in the crack length of 2 mm, 5 mm and 10 mm are analysed, and listed in Table 7-13. The crack length chosen is mainly dependent on the maximum size of coarse aggregate, which was 10 mm for both mixes SBRPMC1.5%-35 and OPCC, and the possible defect may thus be in the range of 0 - 10 mm. The calculation procedure for G_i has been presented in Section 7.3.1.2.

It should be pointed out that the calculated G_i for right deflection is similar to that for left deflection. It can be observed that at the crack with possible length of 2 mm, 5 mm and 10 mm, the K_I for penetration achieved the cracking initiation toughness of matrix SBRPMC0% at the crack length of 2 mm, which is 24.63 MPamm$^{0.5}$ listed in Table 6-4, while the G_i for interfacial delamination was much lower than the interfacial toughness, which was measured at 52 J/m^2, listed in Table 7-12. This predicts that the beam fails in the top layer fracture without interfacial delamination. It is obvious that the analytical prediction is in agreement with the experimental results.

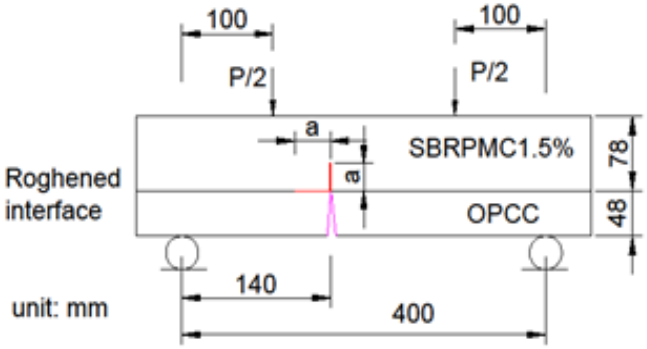

Figure 7-35 Dimension and cracking configuration of beam-3 in Table 7-4

Table 7-13 SIF K_I for penetration into top layer and G_i for deflection into left interface SBRPMC1.5%-on-OPCC beam with roughened interface under four-point bending test (P=2 x 51 N, beam-3 in Table 7-4)

Crack length a (mm)		2	5	10
Penetration into top material	K_I (MPamm$^{0.5}$)	29.6	30.8	34.8
Deflection into interface	G_i (J/m^2)	5.0	4.4	4.0

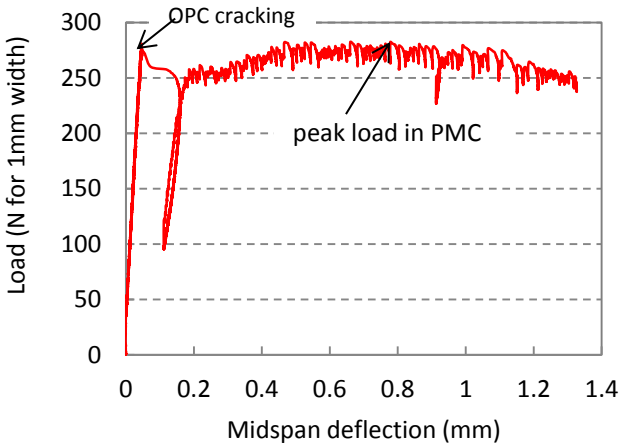

Figure 7-36 Experimental load vs. midspan deflection of SBRPMC1.5%-on-OPCC composite beam with roughened interface under four-point bending test (beam-3 in Table 7-4)

7.3.3.3 Interfacial Behaviour of Composite Beam with Smooth Interface

It has been presented in Section 7.1.2.2 in detail that the composite beam-6, recorded in Tables 7-2, 7-4 and 7-5 was delaminated in the interface under the four-point bending test. The beam consisted of SBRPMC1.5% overlay and OPCC base, with smooth interface. These crack propagation trajectories have been illustrated in Figure 7-6(b) and (c), are shown in Figure 7-37(a) for convenience. The figure indicates that the crack deflected into right interface, propagating in the interface for 35 mm, and after that the left interface debonded. The experimental load-midspan deflection is pictured in Figure 7-38(a). The load reading at crack reaching interface was 244 N (for 1 mm width of beam). The two models shown in Figure 7-37 is analysed in the following. Model-1 corresponds to the crack impinging the interface, and penetration or deflection are analysed, while as for Model-2, the G_i at point A and point B are investigated in the process of crack propagation in the interface from point A to C (see Model-2 in Figure 7-37).

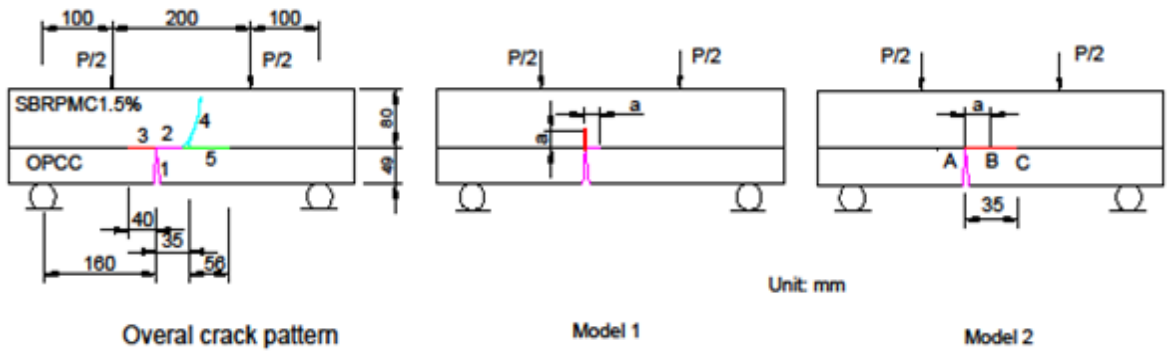

Figure 7-37 Overall cracking trajectory of SBRPMC1.5-on-OPCC composite beam with smooth interface (beam number 6 in Table 7 -3), and Model-1 illustrates crack reaching interface, and Model-2 illustrates crack propagation in right interface

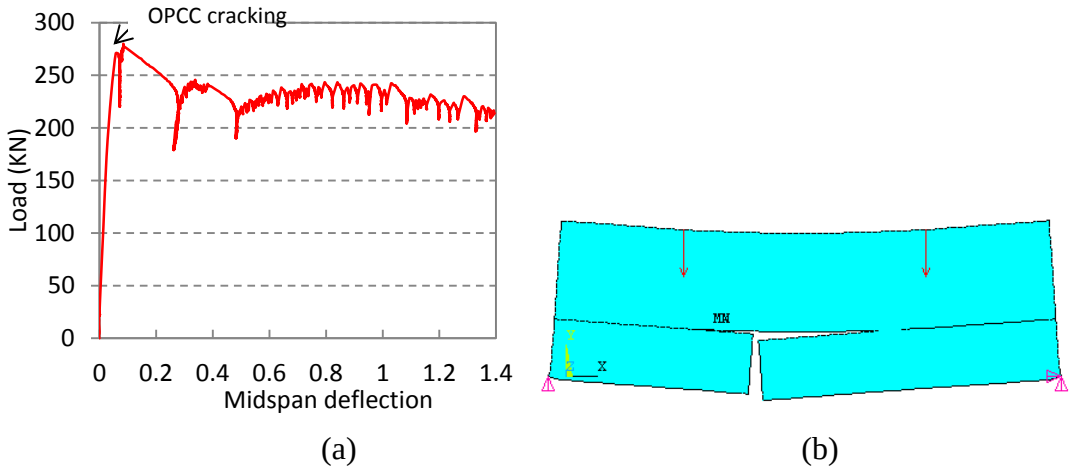

(a) (b)

Figure 7-38 (a) experimental load-midspan deflection of composite beam with smooth interface of number 6 in Table 7-3, (b) simulation of loaded composite beam with interfacial debonding

Model-1

For Model-1, the K_I for penetration and G_i for deflection are calculated using the method presented previously. The calculation results with the crack lengths of 2 mm, 5 mm and 10 mm are listed in Table 7-14. It can be seen that both K_I and G_i exceed their critical values under the load of 244 N, these values being 24.63 MPamm$^{0.5}$ for the former, and 22.6 J/m^2 for the latter. The experimental result indicated that crack deflected into the right interface and propagated 35 mm in it. This might be attributed to the scatter of bond quality.

Table 7-14 K_I for penetration into top layer and G_i for deflection into interface of Model-1 in Figure 7-37 (load p=244N for 1 mm width of beam)

Crack length a (mm)		2	5	10
Penetration into top material	K_I (MPamm$^{0.5}$)	66.8	72.6	81.1
Deflection into interface (right)	G_i (J/m^2)	25.9	26.2	25.7

Model-2

For Model-2, after the crack impinging the interface, the crack deflection into right or left interfaces depend on the competition of the G_{iA} and G_{iB} (see Figure 7-37). The calculation results for normalized G_i of points A and B as the crack propagated in the right interface in normalized form are listed in Table 7-15. It is seen that the energy release rate at both point A and point B increased during crack propagation in the right interface from point A to point C, but the incremental rate of the former was slightly higher than that of the latter. G_i at point A was bigger than that at point B after the crack length was longer than 20 mm. Consequently, the analytical result predicted the left interface starting debonding at point A to left interface after the crack propagated 20 mm at the right interface. This prediction is basically in

agreement with the experimental results. The experimental results showed that the left interface starts debonding at point A when the crack propagated 35 mm at right interface.

Table 7-15 Normalized energy release rate of point A and B in the process of crack propagation in right interface from point A to C (see Figure 7-35 model 2)

a (mm)	0	2	5	10	20	35
G_{iA} (J/m^2)	1	1.01	1.02	1.05	1.10	1.13
G_{iB} (J/m^2)	-	1.01	1.02	1.05	1.09	1.1

Summarising the analysis above, it can be concluded that the single parameter G_i is able to properly characterize the crack propagation in the interface, and the calculated G_i using the method proposed by the research is suitable.

7.4 Summary

The main conclusions drawn from the above are presented below, while the specific conclusions can found at the end of each sub-sections.

(1) The bond strength criteria (splitting tensile bond strength of 2.17 MPa) previously used in Chapter 4.3.1 in the investigation of mix design was experimentally verified, i.e. the interface of composite beams with roughened interface did not delaminate under four-point bending test, while interfacial debonding occurred when the bond strength is lower than 2.17MPa.

(2) A calculation procedure for interfacial energy release rate and its phase angle using crack closure with nodal force technique, and FE technique is proposed. It was also verified that the interfacial SIF K_I can be accurately determined using crack face displacement extrapolation method proposed by Shi et al. (2006). With known G_i and K_I, the K_{II} can be calculated using eqn. 7.21 without ambiguity. This method was verified by comparing the results obtained with the analytical solutions available. The method for calculating ERR is much simpler than those currently available and can easily be handled by engineers.

(3) A test specimen for measuring interfacial fracture toughness of bi-material interface was developed. The interfacial fracture toughness of SBRPMC1.5%-35-on-OPCC was measured. The experimental setup can be used to test the interfacial fracture parameters for concrete overlays on worn concrete pavements. The measured interfacial fracture toughness of SBRPMC1.5%-35-on-OPCC was 52.0 J/m^2 for roughened interface composite

beams, and is 22.6 J/m^2 for smooth interface composite beams. They can be used to assess the interfacial fracture behaviour of SBRPMC1.5% overlay pavement system.

(4) The energy release rate of interface is an appropriate parameter to characterise interface fracture performance (crack deflection and propagation into the interface) of SBRPMC1.5%-on-OPCC composite beam in flexure. It seems that the two parameters K_I and K_{II} were not necessary in the analysis procedure for the behaviour of interfacial delamination of composite beams.

8 Flexural Behaviour of Beams on Elastic Foundation

It is ideal to test full-scale concrete slabs on an elastic foundation to simulate the pavement system. However, the large scale test needs a complicated experimental setup, is expensive and time - consuming. The beam on an elastic foundation may be regarded as an approximate system for simulating a slab on an elastic foundation, and the experiment may offer deeper insight into the mechanism of the SFRC beam. In reality, SFRC beams are widely used in soil foundation engineering. Therefore, an experimental investigation with beams on an elastic foundation instead of slabs was conducted to study its flexural behaviour. SBRPMC1.5%-35 notched beams, OPCC notched beams, SBRPMC1.5%-on-OPCC and PVAPMC1.5%-on-OPCC composite beams on rubber foundation (RF) and cement stabilized aggregate foundation (CF) were tested in this study. The formation procedure of intact SFRPMC beam and SFRPMC-on-OPCC composite beam has been presented in detail in Chapter 4.

8.1 Introduction

The addition of steel fibres can greatly enhance the mechanical properties of concrete, e.g. reduction of crack width and shrinkage. Fibres in the concrete matrix are inactive before cracking. In most cases, SFRC structures are in cracked state in normal service life. Falkner et al. (1995) tested SFRC slabs on cork subbase and rubber subbase to simulate an SFRC slab on soil in order to evaluate the load bearing capacity using yield line theory, and employed ANSYS code to simulate the load-deflection process; Belletti et al. (2008) performed SFRC slab experiments, in which the slabs were laid on springs to simulate subgrade, and simulated the experimental results with the nonlinear fracture mechanics method using ABAQUS code. Meda et al. (2004) proposed a design method for SFRC slabs on the ground. Altoubat et al. (2008) conducted a test of full-scale SFRC slabs on subgrade to validate a design method for SFRC pavement.

The SFRC-on-OPCC composite slab has hardly been experimentally investigated to date, and thus the experiment with SFRC beam on an elastic foundation may be applicable to approximately simulate SFRC slabs, and moreover the deeper mechanism may be revealed from the beam test. Olesen (2001) gave a closed-form solution to infinitely long SFRC beam on Winkler foundations by using the crack-hinge model and bilinear fibre-bridging law, but this has not been experimentally verified.

In this section, the load-CMOD relationship for SFRC beam and OPCC beam was firstly investigated, and then the relationships were used to simulate the flexural behaviour, and consequently the load carrying capacity of SFRC beams was predicted by using the verified simulation method. The flexural performance of PMC-on-OPCC composite beams, which consists of OPCC base and PMC overlay, was experimentally finally investigated.

Conversion of COD_{13} to CMOD

In this study, the crack opening displacement at the position 13 mm above the bottom of beams (COD_{13}) was recorded during test. The COD_{13} is approximately converted to crack mouth opening displacement CMOD by eqn.8.1 for convenient usage. The relationship expressed by eqn.8.1 is derived from British Standard (BS EN 14651:2005+A1:2007), which is used for taking knife thickness effect on CMOD into account.

$$CMOD = \frac{h}{h+y} \cdot COD_{13} \qquad 8.1$$

where h is height of beam, it was 100 mm in this study; y is depth of knife, in here y=-13 mm. The relationship $CMOD=1.149COD_{13}$ is obtained by substitution of the dimensions into eqn.8.1. Hereafter, the CMOD instead of COD_{13} is used.

The modulus of foundation

In this study, two types of foundation were used to investigate the beams on elastic foundation. One was cement stabilized aggregate foundation (hereafter called CF in brief); the other was rubber foundation (RF). The former was similar to the subbase used in real highways, whereas the latter simulates the soil subgrade. The CF consisted of three layers, which were (top to bottom): 70 mm cement stabilized aggregate layer; 220 mm of graded aggregate layer and concrete floor. The RF was a rectangular piece of rubber with the thickness of 25 mm resting on the CF. The CF was constrained by a timber box with the dimensions: 300 mm depth, 700 mm width and 1100 mm length. The dimensions of the foundation were purposely designed to avoid wall influence. Both the graded aggregate layer and the cement stabilized aggregate layer were compacted by vibrating compactor, shown in Figure 8-1(a).

(a) (b)

Figure 8-1 (a) cement stabilized aggregate foundation in construction; (b) overall view of loading frame

(a) (b) (c)

Figure 8-2 (a) close view of CF under test, (b) close view of RF under test, (c) dimension of steel cylinder for foundation modulus test

Two elastic foundation models are widely used to characterize the foundation stiffness in engineering applications, i.e. the Winkler foundation (Hetenyi 1946) and the elastic solid foundation (Highway Agency, UK, 2013). The Winkler foundation postulates a foundation in which the reaction at each point is proportional to the beam deflection at that point and independent of the deflection of neighbouring points (Hetenyi 1946). A single parameter, the coefficient of reaction K_0, is needed to characterize the mechanical response; whereas, the elastic solid foundation behaves as an elastic solid, and is characteristic of Young's modulus and the Poisson's ratio as with other elastic solids.

The two types of foundations were tested to evaluate the stiffness. The loading frame and the instruments are shown in Figure 8-2. A steel cylinder with the diameter of 85 mm served as loading plate, a load cell on the top of the cylinder was for measuring applied load, and two LVDTs were used to measure the deflection. The experimental load vs. deflection relationships are plotted in Figure 8-3. It is seen that the experimental load-deflection relationship exhibits a linear behaviour within the deflection range of the real beam tested, which was 0.2 mm in CF and 4 mm in RF. The experimental results are used to calculate the coefficient of reaction and Young's modulus in accordance with the British Standard (SS EN 1997-2:2007), respectively.

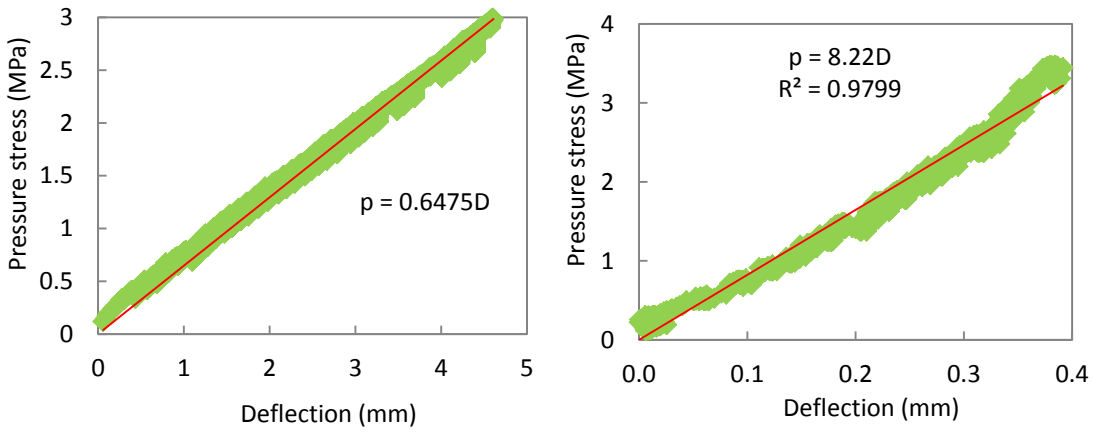

(a) (b)

Figure 8-3 The relationship of pressure and deflection and linear fitting of two types of foundations: (a) rubber foundation; (b) cement stabilized aggregate foundation

The relationships given by British Standard (BS EN 1997-2: 2007) for evaluating K_0 and E_0 are:

$$K_0 = \frac{\Delta p}{\Delta s} \quad 8.2$$

$$E_0 = \frac{\Delta p}{\Delta s} \times \frac{\pi b}{4}(1 - \nu_0^2) \quad 8.3$$

where K_0 is the reaction coefficient of the Winkler foundation; E_0 is the elasticity modulus of the elastic solid foundation; Δp is the selected range of applied contact pressure considered; Δs is the deflection corresponding to the Δp selected; b is the diameter of the plate; ν_0 is the Poisson's ratio of the foundation, taken as 0.3 here. So, the K_0 and E_0 for RF and CF are determined using eqns.8.2 and 8.3, and listed in Table 8-1.

Table 8-1 Stiffness of rubber foundation and cement stabilized aggregate foundation

Type of foundation	Winkler foundation model	Elastic solid foundation model	
	K_0 (N/mm^3)	E_0 (MPa)	ν_0
RF	0.648	37	0.3
CF	8.22	498	0.3

It should be pointed out that the values of the reaction coefficient of Winkler foundation listed in Table 8-1 are higher than that recommended in the pavement design manual (Highway Agency, UK 2013). This may be attributed to the smaller loading plate used. The diameter of the standard loading plate is 760 mm (Croney 1998).

8.2 Formulations of Beam on Winkler Foundation

To the author's best knowledge, the relationship of load-CMOD for beams on elastic foundation is not available so far. In this section, the load-CMOD relationships for beams on

Winkler foundation and elastic solid foundations are established, and then used to simulate flexural performance in Sections 8.3 – 8.5.

8.2.1 Flexure of Un-notched OPCC Beam on Winkler Foundation

The flexural performance of unreinforced beams without notch on Winkler foundations has been extensively studied (Hetenyi 1946). For an unreinforced beam with no notch on Winkler foundations subjected to a centrally placed point load P (see Figure 8-4), the bending moment M_0 at the section through the load-line is given by:

$$M_0 = \frac{P}{4\lambda}\frac{cosh\lambda L - cos\lambda L}{sinh\lambda L + sin\lambda L} \quad 8.4$$

$$K = BK_0 \quad 8.5$$

$$\lambda = \sqrt[4]{\frac{k}{4EI}} \quad 8.6$$

$$I = \frac{1}{12}Bh^3 \quad 8.7$$

where M_0 is the bending moment at the load-line section (N·mm); K_0 is the reaction coefficient of the foundations (N/mm^3); E is the elasticity modulus of beam material (MPa); $1/\lambda$ is the characteristic length of the system (mm); I is the moment of inertia of the cross-section (mm^4); L, B and h are defined in Figure 8-4 (mm). In the following, only 1 mm width of beam is considered for convenience, i.e. B=1 mm.

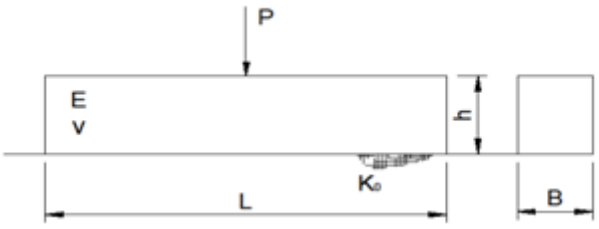

Figure 8-4 OPCC beam with no notch on Winkler's foundation subjected to a central point load

Based on classic simple beam theory, the maximum stress σ_0 at the bottom of the beam is:

$$\sigma_0 = \frac{6M_0}{h^2} \quad 8.8$$

For a given dimension of beam and the material mechanical property, the load carrying capacity can easily be evaluated by using the equations above.

8.2.2 Flexure of Notched (or Cracked) OPCC Beam on Winkler Foundation

For a notched beam on Winkler foundation subjected to centrally place point load P (see Figure 8-5), the bending moment at the notched section decreases due to the presence of the notch; the deeper the notch, the more the moment reduction is (Parmerter 1976; Parmerter and Mukherji 1975). The bending moment M_c at notch section was given by:

$$M_C = \beta M_0 \tag{8.9}$$

$$\beta = \frac{1}{1+\varphi} \tag{8.10}$$

$$\varphi = \frac{\lambda h C(a/h)[\cosh\lambda L+\cos\lambda L-2]}{2(\sinh\lambda L+\sin\lambda L)} \tag{8.11}$$

$$C\left(a/h\right) = (\frac{a}{h})^2\left[12.0 - 19.5\frac{a}{h} + 70.1(\frac{a}{h})^2 - 97.6(\frac{a}{h})^3 + 142(\frac{a}{h})^4 - 138(\frac{a}{h})^5 + 128(\frac{a}{h})^6 - 132(\frac{a}{h})^7 + 379(\frac{a}{h})^8 - 417(\frac{a}{h})^9 + 131(\frac{a}{h})^{10} + 313(\frac{a}{h})^{12} - 357(\frac{a}{h})^{13} + 102(\frac{a}{h})^{14}\right]$$

$$0 \le a \le 0.45h \tag{8.12}$$

$$C\left(a/h\right) = \frac{1.32}{(1-\frac{a}{h})^2} - 1.78 \qquad 0.45h \le a \le h \tag{8.13}$$

where M_C is the bending moment at notch section; M_0 is the bending moment of non-notch beam in load line section, evaluated by eqn.8.4; β is the bending moment reduction factor; $C\left(a/h\right)$ is the compliance function; a and h are the depth of notch (here $a=a_0$) and the height of the beam, respectively; λ has been previously defined, and evaluated by eqn.8.6.

With the knowledge of bending moment M_c at notch section, the maximum tensile stress at notch tip can be readily evaluated by eqn.8.8, but here M_0 and h should be replaced by M_c and $(h-a_0)$, respectively. In this study, the equations presented above are used to analyse the flexural performance of PMC-on-OPCC composite beams on a Winkler foundation.

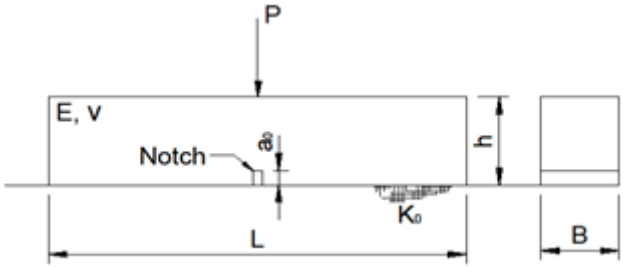

Figure 8-5 Notched beam on Winkler foundation subjected to a central point load

It has been mentioned above that the load-CMOD relationship on a Winkler foundation is not available so far. In the present study, the load and CMOD is related with eqn.8.15, which was previously used to evaluate the CMOD of beam under pure bending (Tada et al. 2000). This load-CMOD relationship will be verified later by finite element analysis in Section 8.2.4. In addition, eqn.8.14, previously used for the beam under pure bend, is used to evaluate the SIF.

It is pointed out that Parmerter (1976) offered an equation for evaluating SIF at crack tip in the same literature. The comparison of SIFs of unreinforced cracked beam on Winkler foundation, evaluated by Parmerter's method and by eqn.8.14 showed that both the calculated values of SIFs were very close, i.e. the relative difference was less than 3%. Thus, the author prefers to use eqn.8.14 for calculating SIF.

$$K_{Ia} = \sigma\sqrt{\pi a}F(\frac{a}{h}) \quad 8.14$$

$$CMOD_a = \frac{4\sigma a}{E}V(\frac{a}{h}) \quad 8.15$$

$$\sigma = \frac{6M_c}{h^2} \quad 8.16$$

$$F\left(\frac{a}{h}\right) = \sqrt{\frac{2h}{\pi a}\tan(\frac{\pi a}{2h})}\,\frac{0.923+0.199(1-sin\frac{\pi a}{2h})^4}{cos\frac{\pi a}{2h}} \quad 8.17$$

$$V\left(\frac{a}{h}\right) = 0.8 - 1.7\frac{a}{h} + 2.4(\frac{a}{h})^2 + \frac{0.66}{(1-\frac{a}{h})^2} \quad 8.18$$

where K_{Ia} is the stress intensity factor induced by applied load (MPamm$^{0.5}$); $CMOD_a$ is the crack mouth opening displacement induced by applied load (mm); *Mc* is the bending moment at the cracked (notch) section (N·mm), evaluated by eqn.8.9; *a* and *h* are defined in Figure 8-5, in mm; σ is the tensile stress (MPa), evaluated by eqn.8.16.

8.2.3 Flexure of Notched SFRC Beam

It has been mentioned previously that, to the author's best knowledge, the load-CMOD or load-deflection relationships for SFRC beams on elastic foundations has not been established

to date. In the following fracture mechanics is employed to simulate the flexural behaviour of SFRC beams on Winkler foundation.

Consider a notched SFRC beam on a Winkler foundation subjected to central pointed load P shown in Figure 8-6. The whole system consists of a beam without fibres subjected to the load P, plus a beam reinforced with fibres subjected to fibre tensile stress only (without external applied load), and thus a superposition scheme is employed. With the knowledge of bending moment M_c at the notch section, the stress intensity factor K_{Ia} and the $CMOD_a$ induced by the applied load can be evaluated by eqns.8.14 and 8.15, respectively.

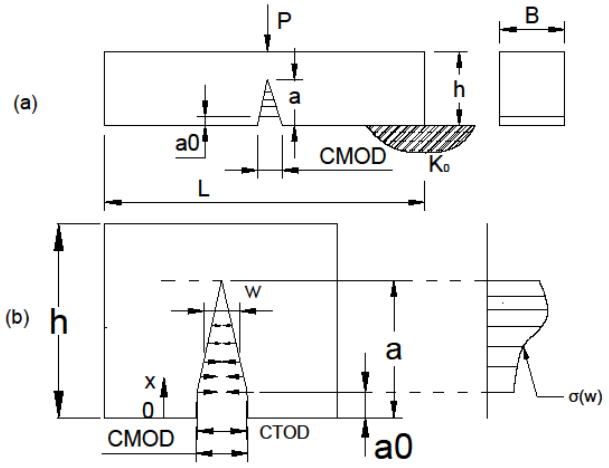

Figure 8-6 (a) steel fibre-reinforced PMC beam on elastic foundation; (b) fibre tensile stress distribution

For the effect of fibre tensile stress, the stress intensity factor K_{Ib} and crack mouth opening displacement $CMOD_b$ induced by fibre tensile stress $\sigma(w)$ have been formulated in Chapter 6; and the former was derived based on Green's function, while the latter was derived based on Paris' equation. Both are listed below for convenience (see Figure 8-6):

$$K_{Ib} = \frac{2}{\sqrt{\pi a}} \int_{a_0}^{a} \frac{G\left(\frac{x}{a'}\frac{a}{h}\right)\sigma(w(x))}{(1-\frac{a}{h})^{1.5}\sqrt{1-(\frac{x}{a})^2}} dx \qquad 8.19$$

$$CMOD_b = \frac{8}{\pi E} \int_0^a \left[\int_{a_0}^{a} \frac{G\left(\frac{x}{a'}\frac{a'}{h}\right)G\left(\frac{0}{a'}\frac{a'}{h}\right)}{(1-\frac{a'}{h})^{3}\sqrt{1-(\frac{x}{a'})^2}} \frac{\sigma(w(x))}{a'} dx\right] da' \qquad 8.20$$

$$w = \frac{CTOD}{a-a_0} \cdot (a-x) \qquad 8.21$$

$$CTOD = CMOD \cdot \frac{a-a_0}{a} \qquad 8.22$$

where $G\left(\frac{x}{a}, \frac{a}{h}\right)$ is Green's function, evaluated by eqns.6.9 - 6.13 listed in Section 6.2; $\sigma(w(x))$ is the stress-crack opening relationship (fibre bridging law); w is crack face opening

displacement at *x*; *CTOD* is the notch tip opening displacement; *a* is crack length; *h* is the height of the beam. It should be pointed out again that the calculated values of eqn.8.20 may take complex form, and the applicable value for $CMOD_b$ is the real part of the complex quantity for engineering applications (This has been discussed in Chapter 6). It is noted that a straight line for the crack face is assumed for the formulation of eqns.8.21 and 8.22. Therefore, for the SFRC beam on elastic foundation (including Winkler and elastic solid foundation) the net stress intensity factor K_{Inet} and total *CMOD* are evaluated by the following relationships:

$$K_{Inet} = K_{Ia} - K_{Ib} \tag{8.23}$$

$$CMOD = CMOD_a - CMOD_b \tag{8.24}$$

where K_{Ia} and K_{Ib} are the SIFs evaluated by eqn.8.14 and 8.19, respectively; $CMOD_a$ and $CMOD_b$ are the crack mouth opening displacement induced by the applied load and the fibre tensile stress, respectively, and evaluated by eqns. 8.15 and 8.20, respectively.

8.2.4 Verification of Parmerter's and Irwin's Method

Parmerter's method for evaluating the SIF of a beam on a Winkler foundation has been described above. However, the values of λh required by Parmerter (1976) were bigger than 5, i.e. λh>5. This requirement is not satisfied by the beams used in this study, for which the values of λh for beams on RF and CF were 0.28 and 0.53, respectively, much smaller than the limit required by Parmerter's theory (Parmerter 1976). Moreover, Irwin's crack closure method seems applicable, and has been successfully employed by Cox and Marshall (1991) to study crack profile, and Zhang and Li (2004) to simulate the load-CMOD relationship of SFRC beams under three-point bending test. Irwin's method states that the SIF can be evaluated using the stress of the uncracked body on the crack line.

For the unreinforced beam on Winkler foundation shown in Figure 8-7, the application of both the Irwin method combined with Green's function method results in:

$$\sigma_x = \sigma_0(1 - \frac{2x}{h}) \tag{8.25}$$

$$\sigma_0 = \frac{6M_0}{h^2} \tag{8.26}$$

$$K_{Ia} = \int_0^a \frac{2\sigma_x}{\sqrt{\pi a}} \frac{G(\frac{x}{a},\frac{a}{h})}{(1-\frac{a}{h})^{1.5}\sqrt{1-(\frac{x}{a})^2}} dx \tag{8.27}$$

$$CMOD_a = \frac{8}{\pi E}\int_0^a [\int_0^a \frac{G\left(\frac{x}{a'},\frac{a'}{h}\right)G\left(\frac{0}{a'},\frac{a'}{h}\right)}{(1-\frac{a'}{h})^3\sqrt{1-(\frac{x}{a'})^2}} \cdot \frac{\sigma_x}{a'} dx]\, da' \qquad 8.28$$

where M_0 is the bending moment of a beam with no crack, evaluated by eqn.8.4; $G(\frac{x}{a},\frac{a}{h})$ is Green's function; a and h are the crack length and height of the beam, respectively.

In order to verify the applicability of the two methods, the unreinforced beam with 1 mm width on the Winkler foundation is considered. The beam is of the dimensions 100 mm x 500 mm in height and length, and of modulus of elasticity of 32365 MPa, and is subjected to central pointed load of 100 N. The SIFs and CMODs of beams on RF and CF are calculated by Parmerter's, Irwin's and FEA methods, respectively. Both the RF and CR were assumed to be Winkler foundations. The loading configuration and beam dimensions are the same as those of steel fibre-reinforced roller-compacted PMC beams used in this study. ANSYS code 12.0 was employed to evaluate the SIFs and CMOD. 8-node Plane183 element was used as the singular element surrounding crack tip, 4-node Plane 42 was used as global element; and Combin14 served as the spring for simulating the Winkler foundation. 100 springs were evenly located along the bottom of the beam; the length of singular elements surrounding the crack tip was 0.1 for all models. The typical meshed model is shown in Figure 8-8. The calculated results are listed in Tables 8-2 and 8-3, and shown in Figures 8-9 and 8-10, respectively.

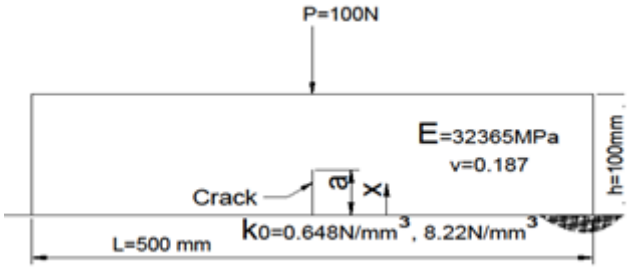

Figure 8-7 Unreinforced beam on RF or CF subjected to central pointed load

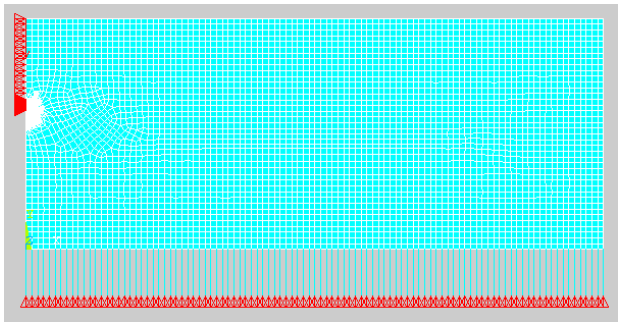

Figure 8-8 Typical meshed ANSYS' model of beam on elastic foundation (right half system) for evaluating SIFs and CMODs.

Table 8-2 Comparison of SIFs of unreinforced beam on Winkler foundation model, evaluated using Parmerter's, Irwin's and FEA methods under the same conditions as shown in Figure 8-7

a	K_0=0.648N/mm^3			K_0=8.22N/mm^3		
	Parmerter's	Irwin's	FEA	Parmerter's	Irwin's	FEA
(mm)	(MPamm$^{0.5}$)	(MPamm$^{0.5}$)	(MPamm$^{0.5}$)	(MPamm$^{0.5}$)	(MPamm$^{0.5}$)	(MPamm$^{0.5}$)
20	29.97	30.07	26.71	23.45	24.8	19.71
50	64.5	70.25	58.86	37.12	57.93	32.87
60	87.17	99.64	80.82	40.68	82.16	37.49
70	123.75	153.33	116.65	42.46	126.43	41.34
80	184.64	277.26	177.51	40.52	228.62	43.22
90	258.54	763.99	256.18	31.86	629.97	41.89

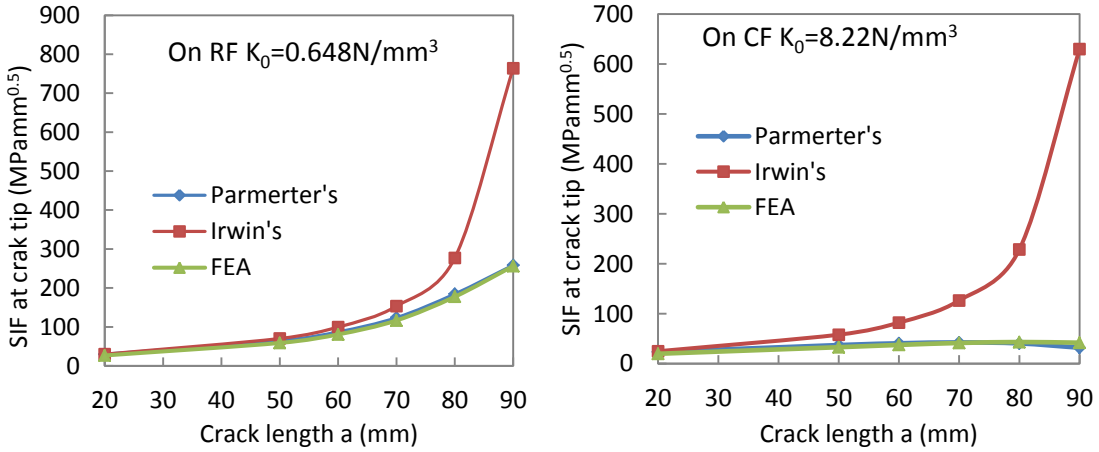

(a) (b)

Figure 8-9 Comparison of SIFs of beams on RF and CF at different crack lengths (in Figure 8-7): (a) on rubber foundation; (b) on cement foundation

Table 8-3 Comparison of CMODs of unreinforced beam on Winkler foundation model, evaluated using Parmerter's. Irwin's and FEA methods under the same conditions as shown in Figure 8-7

a	K_0=0.648N/mm^3			K_0=8.22N/mm^3		
	Parmerter's	Irwin's	FEA	Parmerter's	Irwin's	FEA
(mm)	(mm)	(mm)	(mm)	(mm)	(mm)	(mm)
20	0.0143	0.0067	0.0126	0.0112	0.0055	0.00928
50	0.0688	0.0506	0.0606	0.0396	0.0417	0.033
60	0.1183	0.1022	0.1048	0.0522	0.0843	0.0466
70	0.2158	0.2242	0.1946	0.074	0.1849	0.0644
80	0.4305	0.5816	0.3991	0.0945	0.4796	0.0859
90	0.9219	2.221	0.8773	0.1136	1.8323	0.1093

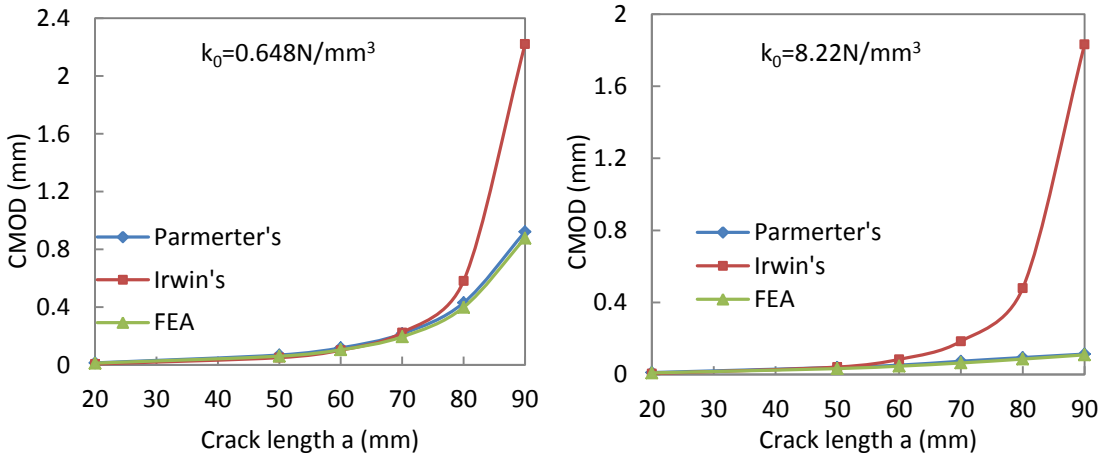

Figure 8-10 Comparison of CMODs of beam on RF and CF determined by Parmerters', Irwin's and FEA methods in different crack lengths: (a) on RF, (b) on CF

It is seen from Table 8-2 and Figure 8-9, and Table 8-3 and Figure 8-10 that the SIFs and CMODs evaluated by Parmerter's method are in good agreement with those found by FEA, while the SIFs by Irwin's method are greatly different from those found by FEA. It is clear that Parmerter's method can be reliably used to simulate the flexural behaviour of cracked unreinforced beams on Winkler foundations, although the values of λh in this study did not satisfy the requirement proposed by Parmerter (1976).

8.2.5 Cracked Unreinforced Beam on Elastic Solid Foundation

It has been mentioned earlier that two foundation models, i.e. Winkler foundation and elastic solid foundation, are extensively used to characterize subgrade and subbase in civil engineering. The former behaves as a dense liquid or springs and is thus depicted by a single parameter (usually called K foundation); whereas the latter is an elastic solid and thus characteristic for Young's modulus and Poisson's ratio. The elastic solid foundation (usually called E foundation) may better characterize the rubber foundation and the cement foundation used in this study. Unfortunately, no analytical solution is available to date to evaluate SIF and CMOD of cracked beam on E foundations. Gallagher (1983) analysed an intact finite-length beam on E foundation, and proposed a numerical analysis approach to evaluate the solution; however, the solution to the cracked beam on E foundation is not available.

To the author's best knowledge, solutions to the fracture of a cracked beam on E foundation are not available to date. In this study, the general finite element code ANSYS 12.0 was employed to analyse the beam used in the study, and both the relationships between SIF and crack length and load, and between CMOD and crack length and load are established, by

fitting the calculated SIFs and CMODs and crack lengths and loads. For this purpose, a beam with the dimension of 1-mm width, 100 mm-height and 500 mm-length was analysed. Plane stress conditions were assumed. A fine mesh zone was around the crack tip, and the singularity element Plane183 with the length of 0.1 mm was used surrounding the crack tip. Contact elements (Contact172 and Target169) were employed to simulate the contact condition along the interface between the beam and the foundation. The normal stiffness of the contact element was set very high to avoid the beam end curling up from the interface; different friction coefficients at the interface were considered. The load P was set to be 100 N; and the foundation modulus E_0 was 37 MPa for RF and 498 MPa for CF, respectively. The Poisson's ratio is 0.3 for both types of the foundations. The model is illustrated in Figure 8-11.

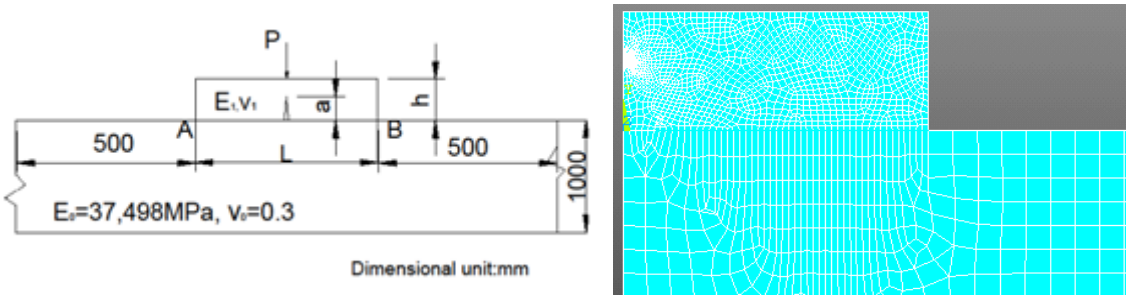

(a) (b)

Figure 8-11 (a) the model of a cracked beam subjected to central pointed load on E foundation, (b) meshed model of right half in ANSYS code.

It is seen from Table 8.4 and Figure 8.12 that both SIFs and CMODs are greatly affected by interface friction. The relationships between K_{Ia} and load P and crack length a, between $CMOD_a$ and load P and crack length a, can be easily established with the calculated data listed in Table 8-4 and by noting that the SIF and CMOD have a linear relationship with load P. As an example, the data listed in Table 8-4 for the beam under the condition of E_0=37 MPa and f=0 are plotted in Figure 8-13, and fitted by exponential function. Eqns. 8.29 - 8.32 show the relationships between K_{Ia} and load P and crack length a, and $CMOD_a$ and load P and crack length a. These relationships will be used to simulate the flexural fracture performance of steel fibre-reinforced PMC beams on E foundation, and are later presented in Sections 8.4 and 8.5.

The experimental study, presented later in Section 8.4, indicated that the Winkler foundation model is not suitable to simulate the flexural performance of the SFRC beam, but the elastic solid foundation model is suitable to characterize the system.

Table 8-4 SIFs and CMODs of unreinforced beam on elastic solid foundations in different crack lengths and friction coefficients (see Figure 8-11: P=100N in 1 mm width, L=500mm, h=100mm, E_1=32365MPa, ν_1=0.187)

a	E_0=37MPa, ν_0=0.3					
	f=0		f=0.2		f=0.4	
(mm)	K_I (MPamm$^{0.5}$)	CMOD (mm)	K_I (MPamm$^{0.5}$)	CMOD (mm)	K_I (MPamm$^{0.5}$)	CMOD (mm)
20	34.92	0.0166	31.7	0.0151	31.07	0.0148
40	59.14	0.0484	53.64	0.0442	51.51	0.0425
60	109.66	0.1435	97.52	0.128	91.08	0.1198
70	164.37	0.277	146.67	0.2479	128.65	0.2181
80	272.72	0.6232	238.78	0.5474	204.42	0.4706
90	512.74	1.793	412.08	1.4498	359.38	1.2693
a	E_0=498MPa, ν_0=0.3					
	f=0		f=0.2		f=0.4	
(mm)	K_I (MPamm$^{0.5}$)	CMOD (mm)	K_I (MPamm$^{0.5}$)	CMOD (mm)	K_I (MPamm$^{0.5}$)	CMOD (mm)
20	29.46	0.0139	25.88	0.01223	24.2	0.0115
40	45.51	0.0371	38.89	0.0317	34.49	0.0282
60	67.75	0.0872	58.79	0.0757	46.8	0.0606
70	81	0.1327	67.75	0.1115	54.84	0.09088
80	99.44	0.2175	77.51	0.1704	59.65	0.1327
90	143.48	0.4726	93.09	0.3044	63.04	0.2014

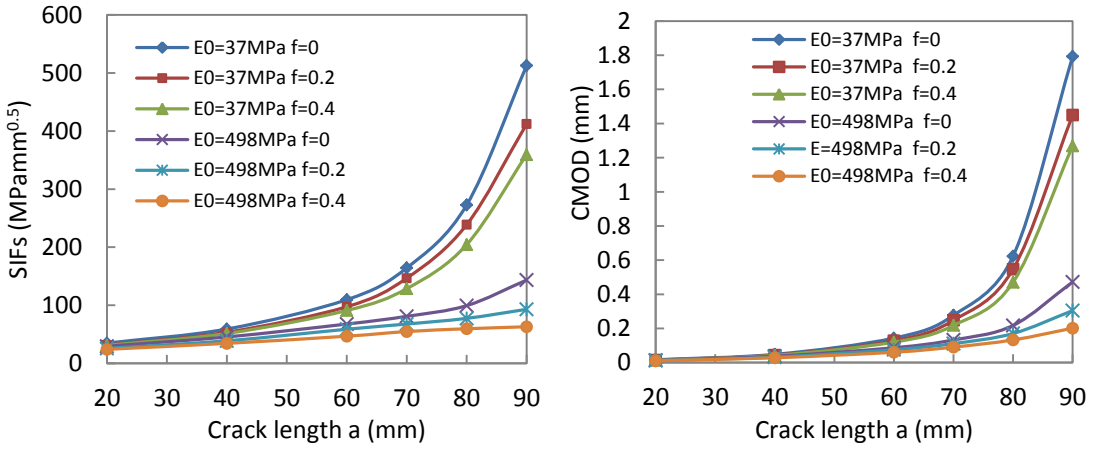

(a) (b)

Figure 8-12 Relationships of SIF and crack length and of CMOD and crack length of unreinforced beam on elastic solid foundation with different friction coefficients (P=100N in 1 mm width, L=500 mm, h=100 mm)

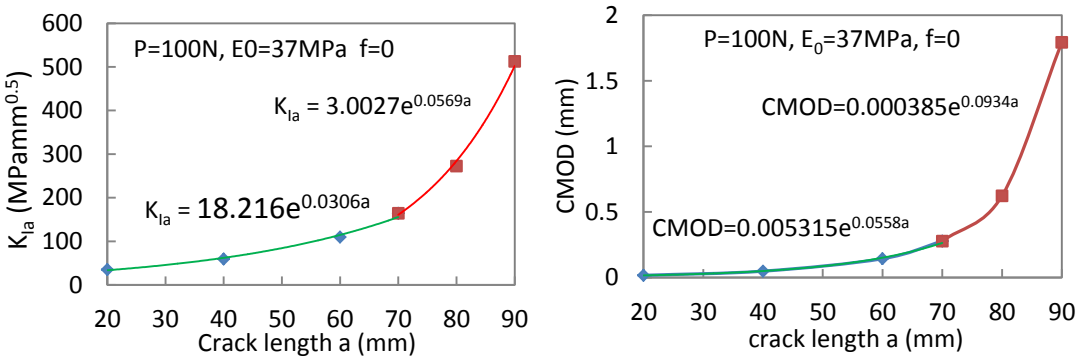

(a) (b)

Figure 8-13 (a) K_{Ia} vs. crack length a; (b) CMOD vs. crack length a.

$$K_{Ia} = \frac{P}{100} \times 18.216e^{0.0306a} \qquad 0 \le a \le 70mm \qquad 8.29$$

$$K_{Ia} = \frac{P}{100} \times 3.0027e^{0.0569a} \qquad 70 \le a \le 90mm \qquad 8.30$$

$$CMOD_a = \frac{P}{100} \times 0.005135e^{0.0558a} \qquad 0 \le a \le 70mm \qquad 8.31$$

$$CMOD_a = \frac{P}{100} \times 0.000385e^{0.0934a} \qquad 70 \le a \le 90mm \qquad 8.32$$

where K_{Ia} is the SIF induced by applied load (MPamm$^{0.5}$); $CMOD_a$ is the crack mouth opening displacement induced by applied load P (mm); P is the applied load (N for 1 mm width of beam); a is the crack length (mm).

8.3 Flexural Behaviour of Notched OPCC Beams on Winkler Foundation

OPCC is the base of the concrete overlay pavement system, and thus the investigation on the overlay pavement system started from the study of the OPCC beam on Winkler foundation. Three groups of OPCC beams were prepared in the study, and each group consisted of three beams. One of the three groups of beams was prepared for MOR test under four-point bend (4PB), one for testing fracture toughness and the third for testing the flexural behaviour on elastic foundation. The mix proportion of OPCC was shown in Table 8-14. All the beams were consolidated on the vibrating table and cured in water till testing date. The ages of beams for MOR test and fracture toughness test were 28 days, while the age of beams tested on foundation was 35 - 45 days. Young's modulus and Poisson's ratio were measured in compression using cylinders with the dimensions 100 mm x 180 mm in diameter and height. The fracture toughness and the corresponding critical $CTOD_c$ and MORs under three-point bend (3PB) are listed in Table 8-5. It is noted that the MOR obtained by notched beam

under 3PB was 7.04 MPa, which was evaluated using the maximum loads in fracture test for K_{Ic} and $CTOD_c$, whose beams were pre-notched to the depth of 33 mm, and the loading rate was controlled by CMOD at the constant incremental rate of 0.0001 mm/s (This has been described in Section 6.2.4 in detail). It can be seen that the MORs measured by 4PB and 3PB test are greatly different from each other, which may be attributed mainly to the size effect and experimental scatter.

Table 8-5 Mechanical properties of OPCC

K_{IC} (MPamm$^{0.5}$)	$CTOD_c$ (mm)	MOR under 4PB (MPa)	MOR of notched beam in 3PB (MPa)	E (MPa)	ν
46.81	0.0229	4.66	7.04	25200	0.21

The dimensions of the beams are tabulated in Table 8-6. The experimental setup and beam with instrumentation are illustrated in Figure 8-14. A clip gauge, mounted at 13 mm above the bottom of the beam, was used to measure the crack opening displacement (denoted COD_{13} in this study) and control the loading rate (0.0001 mm/s); one LVDT was glued at the notch tip for measuring notch (crack) tip opening displacement (CTOD), and two LVDTs were used to measure the vertical displacement at load point and the vertical displacement at the top of the point 200 mm away from the middle, respectively. The LVDT at the top point 200 mm away from central line was used to indicate whether the beam end curled up without contact with the foundation. All the readings of the four meters were automatically recorded by computer at the frequency of 5 Hz. One of the three beams failed abruptly at the beginning without an obvious cause, and thus only two beams were successfully tested.

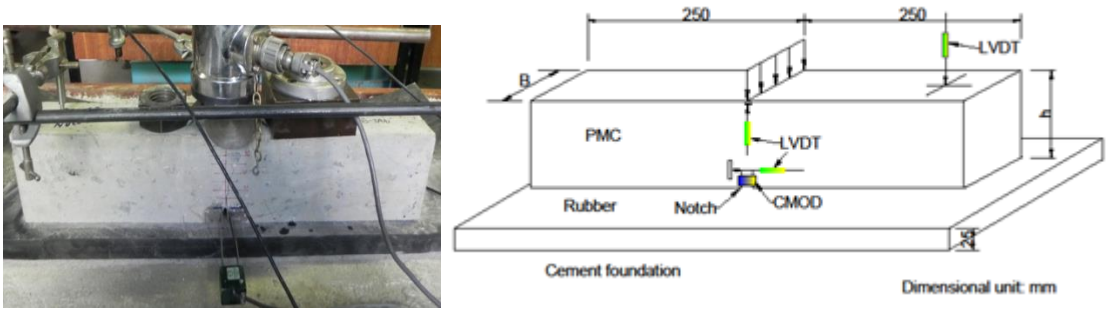

(a) (b)

Figure 8-14 (a) Experimental setup for beam on RF under central pointed load; (b) Beam dimension and instrumentation

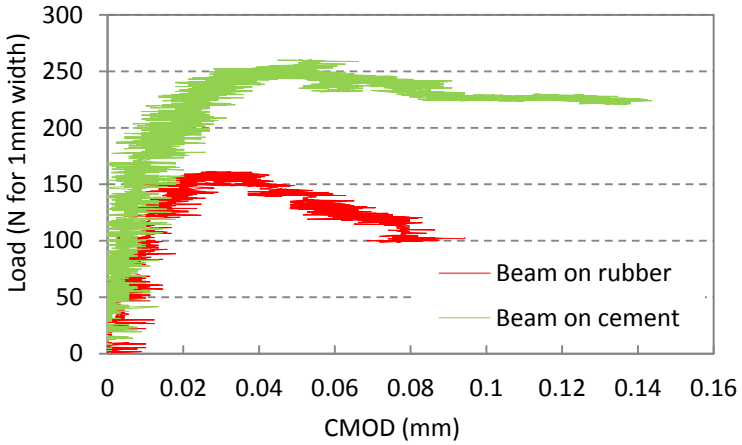

Figure 8-15 P- CMOD relationship of OPCC notched beams on RF and CF

Table 8-6 Dimensions of two notched OPCC beams and experimental results

No.	ID of mix	Foundation	L (mm)	B (mm)	h (mm)	a_0 (mm)	P_{max} (for 1mm width beam) (N)
1	OPCC	RF	500	100	120	20	161.7
2		CF	500	102	123	17	260.0

The experimental results showed that the two beams on RF and CF failed after peak load, and maximum load readings were obtained, which are tabulated in Table 8-6. The load-CMOD curves are plotted in Figure 8-15. The reading of the LVDT at the top point 200 mm away from middle indicated that the beam end was always in contact with the foundation during test.

Estimation of maximum load carrying capacity by fracture mechanics method

With the knowledge of the fracture properties of OPCC (Table 8-5), the maximum load carrying capacity of OPCC beams was evaluated and compared with the experimental results. As a quasi-brittle material, the maximum load of a concrete beam is dependent on two mechanical parameters, i.e. fracture toughness (K_{IC}) and critical crack tip opening displacement ($CTOD_C$). The two-parameter model for concrete structures in flexure was proposed by Jenq and Shah (1985), and adopted by RILEM (1991). The maximum load can be obtained by solving the two eqns. 8.33 and 8.34 below:

$$K_a - K_{Ic,M} = 0 \quad (8.33)$$

$$CTOD_a - CTOD_c = 0 \quad (8.34)$$

where K_a is evaluated using eqns. 8.14, 8.16 and 8.9, $K_{Ic,M} = 46.81 MPamm^{0.5}$, $CTOD_c = 0.0229\ mm$, listed in Table 8-5; $CTOD$ is notch tip opening displacement, and can

be evaluated through *CMOD* by eqn.8.22; and the *CMOD* is determined by eqns.8.15 and 8.16.

As an alternative, the relationship of *CMOD* and *CTOD* proposed by Jenq and Shah (1986) is:

$$CTOD_a = CMOD_a \cdot \sqrt{\left\{\left(1-\frac{a_0}{a}\right)^2 + \left(1.081 - 1.149\frac{a}{h}\right)\left[\frac{a_0}{a} - \left(\frac{a_0}{a}\right)^2\right]\right\}} \qquad 8.35$$

where a, a_0 and h are the crack length, depth of initial notch and height of beam, respectively, which are defined in Figure 8-5. In fact, similar results were obtained using eqns.8.22 and 8.35.

Numerical computation iterative scheme was used to evaluate the maximum load. For the two beams with the dimensions listed in Table 8-6 and mechanical properties listed in Table 8-5, the maximum load carrying capacity for the two OPCC beams is predicted as:

$P_{max} = 174N(for\ 1mm\ width\ of\ beam)$ for beam-1 on RF;

$P_{max} = 231N(for\ 1mm\ width\ of\ beam)$ for beam-2 on CF;

It is seen that the maximum loads of the two beams predicted by Parmerter's theory and Winkler foundation model are in good agreement with the experimental results, listed in Table 8-6. This confirms that Parmerter's fracture method and the Winkler foundation are applicable to evaluate the load carrying capacity of unreinforced beams on elastic foundation.

Estimation of load carrying capacity by material mechanics method

The maximum load carrying capacity can also be evaluated based on a material-mechanics criterion. The bending moment at notched section can be evaluated by using Parmerter's method described above, and the tensile stress at the notch tip is calculated by eqns.8.9 and 8.16. Setting tensile stress at notch tip equal to the flexural strength (7.04MPa) listed in Table 8-5, and noting M_0 and h should be replaced by M_c and $(h\text{-}a_0)$, respectively, the maximum loads predicted are below:

beam-1 on RF: $P_{max} = 191N\ (for\ 1mm\ width)$

beam-2 on CF: $P_{max} = 244N\ (for\ 1mm\ width)$

It can be observed that the predicted load carrying capacity of beam-1 on RF is 191N, which is slightly higher than the experimental value of 161.7 N, which is listed in Table 8-6. Comparison of the predicted load carrying capacity determined by both fracture mechanics

and material mechanics methods indicates that both are applicable to analysing OPCC beams on elastic foundation.

Load carrying capacity of un-notched OPCC beams

The applicability of the fracture mechanics method for evaluating the load carrying capacity of the OPCC beams on a Winkler foundation has been experimentally verified above, and is now used for OPCC beams on foundations with different reaction modulus. The OPCC beams (with no crack) are of the dimensions 500 mm x 100 mm in length and height, 1 mm width of beam is considered, and the fracture parameters are listed in Table 8-5. An initial crack of 2 mm depth in the bottom of the middle section is assumed, and the loading configuration is illustrated in Figure 8-4. The predicted values are tabulated in Table 8-7 and shown in Figure 8-16. The predicted load carrying capacity of OPCC beams will be compared with that of un-notched SFRC beams in Section 8.4.4. It should be pointed out that the load carrying capacity evaluated by the material mechanics method is nearly identical to that listed in Table 8-7.

Table 8-7 Predicted load carrying capacity of OPCC beam on Winkler foundation with various stiffness (L=500mm, h=100mm, K_{Ic}=46.81 MPamm$^{0.5}$, $CTOD_c$=0.0229 mm)

K_0 (N/mm^3)	0.648	2	4	6	8.22	10
Load P (N, for 1mm width)	182	196	209	224	242	250

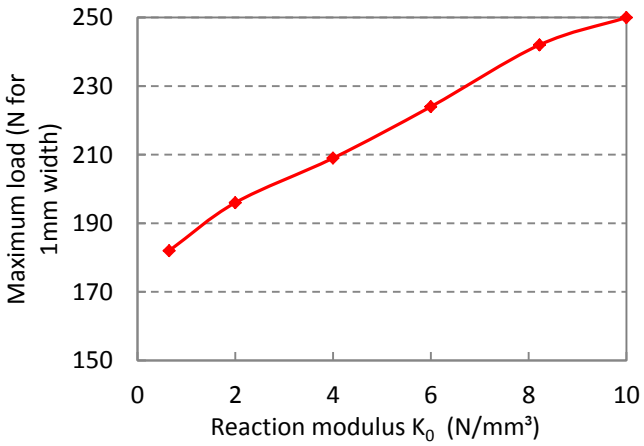

Figure 8-16 Predicted load carrying capacity of un-notched OPCC beam on Winkler foundation

8.4 Notched SBRPMC1.5%-35 Beams

The composite beam may be decomposed into the OPCC base and the SFRC overlay, and thus the flexural performance of the composite beam may be separately simulated by an OPCC beam and a SFRC beam on an elastic foundation. For this purpose, six intact beams of

mix SBRPMC1.5%-35 were prepared. The formation and curing procedures of specimens were the same as those used for the three-point bending test presented in Chapter 5. The beams were sawn cut to produce notches, whose depths are listed in Table 8-8. Figure 8-14 shows the experimental setup, while Figure 8-17 illustrates the definition of the geometrical parameters of the beam. A clip gauge mounted at a position 13 mm above the bottom of the beam was to measure the crack opening displacement and control the loading rate. The crack opening rate measured by the clip gauge was controlled by the following procedure: 0.0001 mm/s till CMOD was equal to 0.2 mm; then 0.0033 mm/s till test termination. The testing data were automatically recorded by computer at the frequency of 5 Hz. The test procedure was the same as that used in the three-point bending test, described in Chapter 5. Two beams were tested on cement stabilized aggregate foundations, whereas the other four beams on rubber foundations. A thin layer of cement was sprayed to minimize the effect of friction. Every test was terminated at CMOD about equal to 1.4 - 1.6 mm.

The experimental results are tabulated in Table 8-8, and plotted in Figures 8-19 and 8-20. It is seen that the flexural behaviour of SFRC beams is different from that of beams with no fibres. The load reading of unreinforced concrete reached the maximum and failed abruptly in a small notch opening; maximum load existed for OPCC beams on both foundations (see Figure 8-15). However, no maximum load existed for SFRC beams; the load reading increased with the CMOD increasing. The increased load was carried mainly by the foundation.

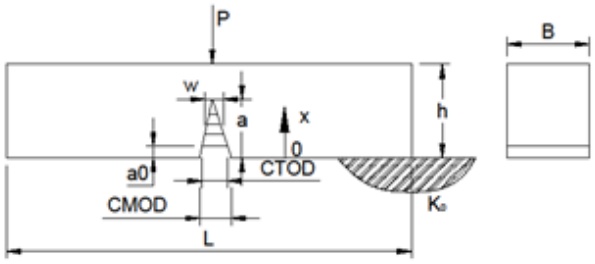

Figure 8-17 Steel fibre-reinforced PMC notched beam on elastic foundation subjected to a central point load

8.4.1 Crack Initiation at Notch Tip

It is seen from Figure 8-19 and Figure 8-20 that, all the load-CMOD curves had a linear segment at the initial region, and then behaved nonlinearly after a certain point. It can be easily identified by analysing load-CMOD curves, i.e. the conversion point from linearity to nonlinearity. The loads corresponding to the conversion point are denoted as P_1 and listed in

Table 8-8. Before cracking, the steel fibres are inactive, and thus the stress field at the notch tip was dominated by the matrix.

Table 8-8 Dimensions of beams, experimental results and the calculated stress intensity factors K_I at notch tip (mix SBRPMC1.5%-35)

ID of beam	Foundation	Geometrical parameters			Experimental	Calculated
		L (mm)	h (mm)	a_0 (mm)	P_1 (for 1mm width) (N)	K_I ($MPamm^{0.5}$)
1	RF	500	100.5	43	42.25	22.3
2	RF	500	100	40.5	54.28	26.83
3	CF	500	101	43.5	53.33	18.57
4	RF	500	100	19	82.78	24.13
5	RF	500	100	19	94.59	27.58
6	CF	500	100	28	82.78	22.63

Note P_1 is the load corresponding to the point of linearity to nonlinearity of the load-COD_{int} curve.

The stress intensity factors were calculated using eqn.8.14. The average of the SIFs of the six beams above was $23.67MPamm^{0.5}$. The value is very close to the critical stress intensity factor of the matrix (the mix SBRPMC0%), $K_{IC,M}^{ini}$ which was $24.63MPamm^{0.5}$, presented in Table 6-4. This clearly demonstrates the flexural performance of SFRC, i.e. that fibres in concrete are inactive before cracking, and the flexural behaviour is mainly dependent on the matrix.

8.4.2 Simulation of Load-CMOD Relationship

With the available experimental load-CMOD relationships, an attempt was made to use Parmerter's theory and Winkler foundation model, and the regression equations established by using FEA and elastic solid foundation model, to simulate the experimental load-CMOD relationship. The SIFs and CMODs induced by fibre bridging effect are the same for the two methods, which were calculated by eqns.8.19 - 8.22. The fibre bridging law for the mix SBRPMC1.5%-35 was investigated in Chapter 6, and is shown by eqn.8.38 for convenience. The SIFs and CMOD induced by applied load were calculated by eqns.8.9 - 8.18

Since the loading rate was slow, resulting in slow crack propagation, and thus indicating that the fracture criteria were satisfied for any crack extension, namely it is:

$$\left|K_{Ia} - K_{Ib} - K_{IC,M}\right| \leq \varepsilon 1 \qquad 8.36$$

$$|CMOD_i - CMOD| \leq \varepsilon 2 \qquad 8.37$$

where K_{Ia} and K_{Ib} and $CMOD$ are the calculated values; $K_{IC,M}$ is the critical stress intensity

factor of matrix of SBRPMC1.5%-35, i.e. $48.76 MPamm^{0.5}$, listed in Table 6-4; ε_1 and ε_2 are allowable tolerances.

A special MATLAB routine with iterative scheme was developed, in which the computation procedure was: (1) For a given *CMOD*, *CTOD* was calculated using eqn.8.22; (2) Crack length *a* and load *P* were varied to calculate K_{Ia} using eqn.8.14, $CMOD_a$ using eqn.8.15 for Parmerter's theory method; or to compute K_{Ia} using eqns.8.29 and 8.30, $CMOD_a$ using eqns.8.31 and 8.32 for elastic solid foundation model; (3) Stress intensity factor K_{Ib} was computed using eqn. 8.19, and $CMOD_b$ was computed using eqn.8.20; (4) The *P* and *CMOD* and *a* were the solutions if the eqns.8.36 and 8.37 were satisfied; otherwise, the crack length *a* and load *P* were varied, and the computation procedure above was repeated until the solutions were found.

The fibre bridging law for mix SBRPMC1.5%-35 established in Chapter 6 and listed in Table 6-7, with which the fracture mechanics is valid, is

$$\sigma(w) = -59.786w^5 + 146.64w^4 - 122.85w^3 + 37.82w^2 - 2.7337w + 5.193$$

$$0 \leq w \leq 0.958 \text{ mm} \qquad 8.38$$

where $\sigma(w)$ is the fibre tensile stress (MPa); *w* is the crack opening displacement (mm).

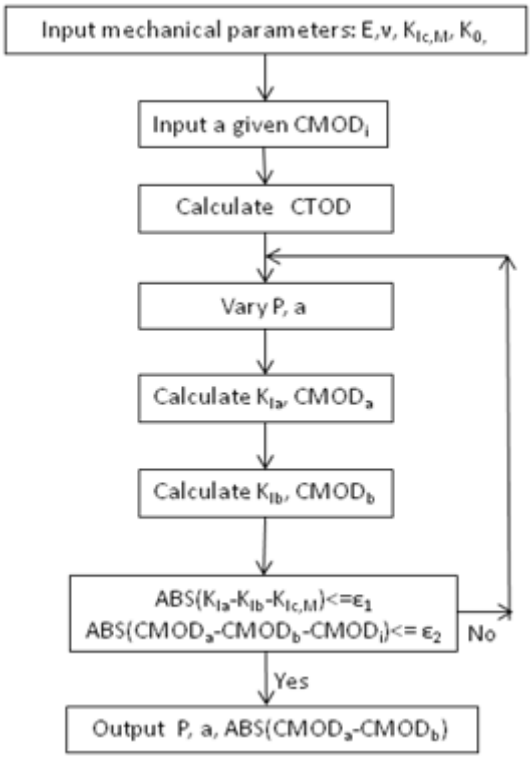

Figure 8-18 Calculation procedure for establishing load-CMOD relationships of SFR-PMC beam on elastic foundation

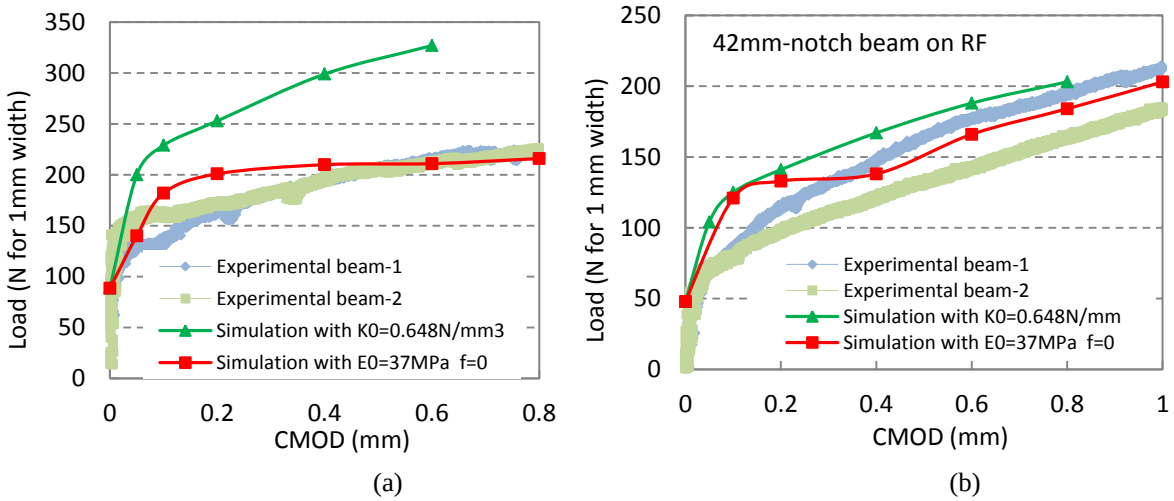

(a) (b)

Figure 8-19 Experimental load-CMOD curves of notched SBRPMC1.5%-35 beams on rubber foundation, and theoretical simulation with K and E foundation respectively:(a) 19mm-notch beam, (b) 42mm-notch beam

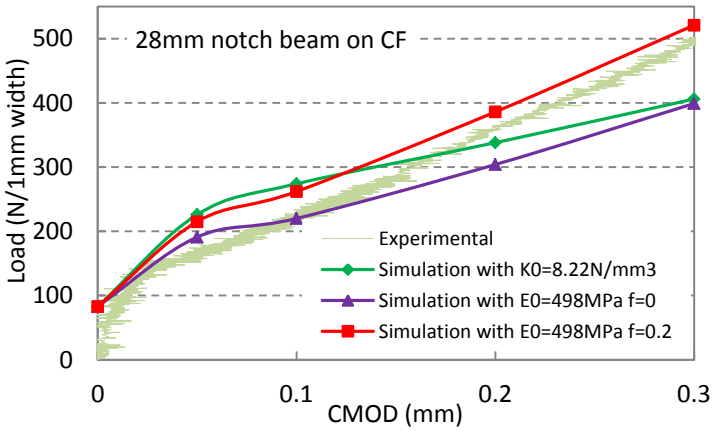

Figure 8-20 Experimental load-CMOD curve of 28 mm-notch SBRPMC1.5%-35 beam on CF, and theoretical simulation with K and E foundation respectively

Figure 8-19 and Figure 8-20 show the experimental load-CMOD curves, and the simulated load-CMOD curves by Winkler foundation model (Parmerter's theory) and elastic solid foundation model, respectively. It is observed from the two figures that load-CMOD curves simulated by Winkler foundation greatly deviated from the experimental ones, whereas the elastic solid foundation model can properly simulate SFRC beams on elastic foundation. For the SFRC beam on CF, friction between beam and foundation influenced the flexural performance; for SFRC beam on RF, the friction between the beam and foundation did not. Therefore, the following conclusion can be drawn:

(1) Winkler foundation model is not capable of characterizing the performance of a SFRC beam on elastic foundation, even if the foundation is a simple rubber.

(2) Elastic solid foundation model is suitable for the simulation of SFRC beam on elastic foundation. For the SFRC beam on RF, friction between beam and foundation can be

ignored, i.e. f=0, while for the SFRC beam on CF, the friction between the beam and foundation should be taken into account. In this study, the coefficient of friction for CF is 0.2, i.e. f=0.2.

It should be pointed out that the beam with the 43.5 mm-deep notch (number 3 in Table 8-8) on CF is not investigated, because the vertical displacement measured at the point of the top of beam 200 mm away from the middle, indicated that the end of beam was curling up away from the foundation, even at low load level.

8.4.3 Load Carrying Capacity of Un-notched SBRPMC1.5%-35 Beam

The experimental results presented in the preceding section showed that peak load did not exist in SFR-PMC beams on elastic foundation, but the load increased with increasing CMOD. This is due to the support from foundation increasing with the increase of deflection, even with the crack reaching the top of the beam. However, the crack reaching the top implies structure failure in pavement engineering, because surface water will penetrate into the cracks, resulting in steel fibre corrosion in a short time. Therefore, in practical engineering crack length should be restricted to a certain level. Therefore in this study, the steel fibre-reinforced roller compacted polymer modified concrete beam under three-point bending test showed that applied loads achieved a maximum as crack lengths were around 0.65h - 0.80h in the three-point bending test (h is the height of the beam). It seems rational in pavement engineering that the load of SFRPMC beams at $CTOD = CTOD_c$ be defined as the load carrying capacity, at which the crack lengths are approximately 0.65h - 0.8h.

In this section, the load carrying capacity of non-notch beams is considered. The $CTOD_c$ at maximum load under the three-point bend conducted in this study and the corresponding ligament depth are listed in Table 8-9, and are plotted in Figure 8-21. The regression relationship of $CTOD_c$ and the depth of ligament of beam is also shown in Figure 8-21, where D is the depth of ligament.

Table 8-9 Relationship of CTOD in maximum load and the depth of ligament of beams of mix SBRPMC1.5%-35 under three-point bend

Depth of ligament, (mm)	40	60	80	125
$CTOD_c$, (mm)	0.423	0.523	0.590	0.636

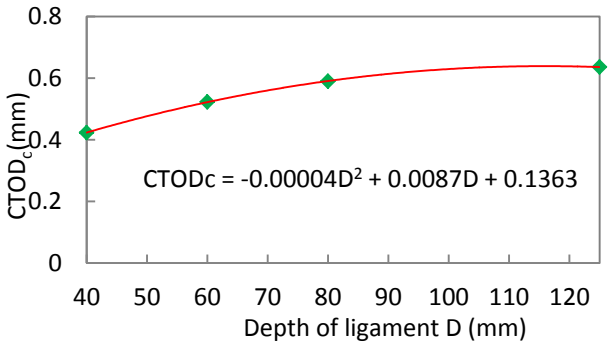

Figure 8-21 Relationship of CTODc at maximum load and depth of ligament of beam of mix SBRPMC1.5%-35 under three-point bend

Consider the un-notched beam of mix SBRPMC1.5%-35 resting on an elastic solid foundation with modulus E_0 and subjected to centrally placed point load P, shown in Figure 8-22. The dimensions of the beam is 100 mm x 500 mm in height and length, and only 1 mm width of beam is considered, i.e. B=1 mm. The $CTOD_c$ for 100 mm-height beam is 0.6 mm, determined by the relationship shown in Figure 8-21.

It has been experimentally confirmed in Section 8.4.2 that the friction coefficients between SBRPMC1.5%-35 beam and RF, and CF are 0 and 0.2, respectively. The relationships of K_{Ia} and load P and crack length a, and $CMOD_a$ and load P and crack length a, can be established using the calculated data listed in Table 8-4, by regression fitting technique. Eqns. 8.29-8.32 are these relationships for rubber pad foundation. The procedure for calculating the load at $CTOD=CTOD_c$ is similar to that presented in Section.8.4.2. Note that in this case, $a_0=0$, $CTOD=CMOD$. However, the denominator of eqn.8.20 for calculating $CMOD_b$ is zero due to the Gauss' integrating points being symmetrically distributed in the same interval of [-1, +1] for variables of x and a', thus a_0 should be taken a small value instead of zero to avoid a zero denominator. In the study, a_0 was taken as 2 mm, i.e. a_0=2mm. The relative tolerance of ε_1 and ε_2 for the iterative scheme were 1-3% and about 0.1%, respectively. The variable tolerable differences for ε_1 were to obtain a unique calculated result for load P. It is seen from the values of ε_1 and ε_2 that P and $CTOD$ were accurately obtained.

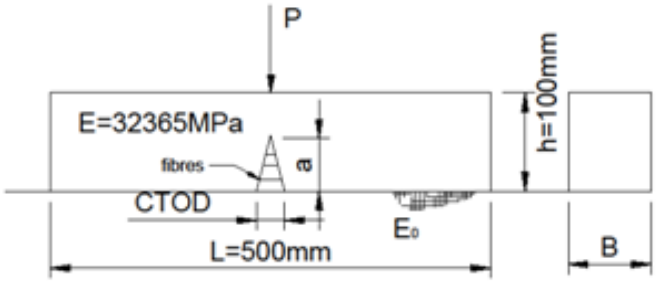

Figure 8-22 Un-notch beam of mix SBRPMC1.5% subjected to central pointed load

The load carrying capacity predicted by using the fracture mechanics-based method described above, including load P and the corresponding bending moment M_c at cracked section are tabulated in Table 8-10. The maximum flexural strength of mix SBRPMC1.5%-35 is 15.22 MPa, measured under three-point bend and presented in Chapter 5, and thus the corresponding maximum bending moment M_{max} is 25366N·mm, determined below. It is seen that the ratios of M_c to M_{max} are in the range of 0.82 to 2.62.

$$M_{max} = \frac{f_p h^2}{6} = \frac{15.22 \times 100^2}{6} = 25366N \cdot mm$$

Table 8-10 Load carrying capacity of un-notched SBRPMC1.5%-35 beam at CTODc=0.6 mm on RF (E_0=37MPa, ν_0=0.3, f=0) and CF (E_0=498MPa, ν_0=0.3, f=0.2) (non-notch beam, L=500 mm, h=100 mm)

E_0 (MPa)	37	498
Load P for CTOD=0.6mm (N for 1 mm width)	357	1314
M_c (N.mm)	21861	66347
M_c/M_{max}	0.86	2.62

8.4.4 Comparison of Load Carrying Capacity of Un-notched SBRPMC1.5%-35 and OPCC Beams

For the beams with the same dimensions of 1 mm x 100 mm x 500 mm in width, height and length subjected to centrally placed point load, the maximum load of the un-notched OPCC beams with the MOR of 7.04 MPa was calculated using Hetenyi's theory, previously presented in Section 8.3. Both the load carrying capacities of OPCC and SBRPMC1.5%-35 beams are plotted in Figure 8-23 for comparison. It can be seen that the load carrying capacity of the SBRPMC1.5%-35 beams is 1.96 times that of the OPCC beams on RF, and 5.4 times that of the OPCC beams on CF foundations, respectively. It indicates that steel fibres in concrete greatly improve the load carrying capacity of beams on elastic foundation.

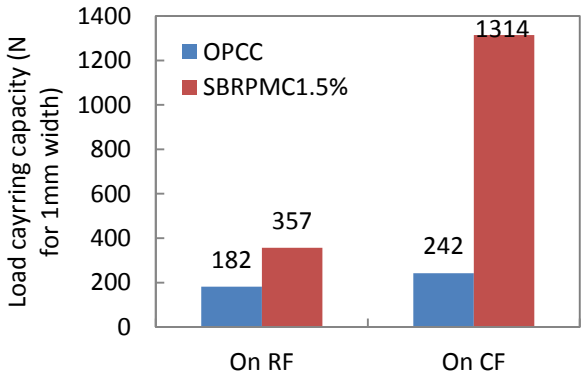

Figure 8-23 Comparison of load carrying capacity of un-notched SBRPMC1.5%-35 and un-notched OPCC beams on RF (K_0=0.648N/mm^3,E_0=37MPa, ν_0=0.3, f=0) and CF (K_0=8.22N/mm^3,E_0=498MPa, ν_0=0.3, f=0.2)

8.5 SFRPMC-on-OPCC Composite Beams

The flexural performance of steel fibre-reinforced polymer modified concrete (SFRPMC) on OPCC composite beams is dominated by both OPCC base and SFRC overlay, respectively, depending on the crack propagation. During the process of crack initiation to interface, the flexural behaviour may be dominated by the OPCC base. During the crack propagation in the SFRC overlay, the overlay itself may dominate the flexural performance. It has been experimentally verified that the Winkler foundation model is suitable to model OPCC beams (unreinforced beam) on elastic foundations, but not suitable for SFRC beams, while the elastic solid foundation model is suitable to model SFRC beams. In this study, since the composite beam consisted of an OPCC base and a SFRC overlay, the Winkler foundation model is used to investigate the flexural behaviour of OPCC base, and the elastic solid foundation model is used to study the SFRC overlay.

8.5.1 Formulation

SBRPMC-on-OPCC composite beam with no notch (crack)

Gere and Timoshenko (1999) employed classic beam theory (plane assumption) to analyse fully-bonded composite beams, and provided the following eqns.8.39 and 8.40 for locating the neutral axis z and the flexural rigidity *FR* (see Figure 8-24(b)):

$$E_1\int_1 ydA + E_2\int_2 ydA = 0 \qquad 8.39$$

$$FR = E_1 I_1 + E_2 I_2 \qquad 8.40$$

where $E_1$and E_2 are the elasticity modulus of top layer material and bottom layer material, respectively; I_1 and I_2 are moments of inertia of top layer and bottom layer with respect to neutral axis, respectively; *FR* is flexural rigidity of the beam with no crack (notch).

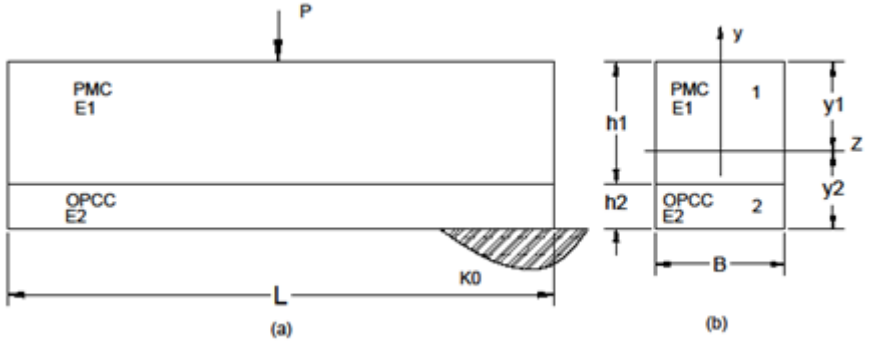

Figure 8-24 (a) SFRPMC-on-OPCC composite beam with no crack on Winkler foundation; (b) cross-section of composite beam

Hence, consider a SFRPMC-on-OPCC composite beam with no crack resting on a Winkler foundation subjected to a centrally placed point load (Figure 8-24(a)). The flexure rigidity of a single material section is *EI*, while it is $(E_1I_1 + E_2I_2)$ for a two-material composite section. Application of both, beam on a Winkler foundation theory (Hetenyi 1946) and composite beam theory (Gere and Timoshenko 1999) results in:

$$M_0 = \frac{P}{4\lambda}\frac{cosh\lambda L - cos\lambda L}{sinh\lambda L + sin\lambda L} \quad 8.41$$

$$k = Bk_0 \quad 8.42$$

$$\lambda = \sqrt[4]{\frac{k}{4(E_1I_1 + E_2I_2)}} \quad 8.43$$

$$\sigma_B = \frac{M_0E_2y_2}{E_1I_1 + E_2I_2} \quad 8.44$$

where M_0 is the bending moment of beam with no crack at load-line section; k_0 is the reaction coefficient of Winkler foundation; B is the width of beam; E_1 and E_2 are the Young's modulus of the top layer and the bottom layer, respectively; I_1 and I_2 are the moment of inertia of the top and the bottom layers with respect to the neutral axis; σ_B is the stress at the bottom of the beam; y_2 is the distance of the neutral axis to the bottom. Note B is usually taken as 1 mm in this study, for convenience.

Crack in OPCC base

Now consider a SFRPMC-on-OPCC composite beam with a crack (or notch) in the OPCC base. The stress field at the notch tip is dominated by the OPCC base, and thus the flexural performance of the composite beam can be properly simulated by using Parmerter's theory and the Winkler foundation model. In order to use Parmerter's method, it is necessary to convert the top layer material to the bottom layer material by keeping flexural rigidity and width constant (see Figure 8-25). The equivalent height of the section is given by:

$$E_2 \times \frac{1}{12}Bh_e^{\,3} = E_1I_1 + E_2I_2 \quad 8.45$$

Solving eqn.8.45, the equivalent height of the section with respect to material 2 is:

$$h_e = 2.29\sqrt[3]{\frac{E_1I_1 + E_2I_2}{E_2B}} \quad 8.46$$

where h_e is the equivalent height with respect to material 2; B is the width of beam; E_1, I_1, E_2 and I_2 have been defined previously. The bending moment at the cracked section, M_c, can be

obtained by substituting h_e into eqns.8.9 - 8.13 (h=h_e). However, the stress at the notch tip should be evaluated in the ligament section by the following equation:

$$\sigma_N = \frac{M_c E_2 y_2'}{E_1 I_1' + E_2 I_2'} \qquad 8.47$$

where M_c is bending moment at the cracked (notched) section; y_2', I_1' and I_2' are evaluated over the ligament area of the cracked section. Note that the I_1 and I_2 in eqns.8.45 and 8.46 are evaluated over the whole depth of the cross section.

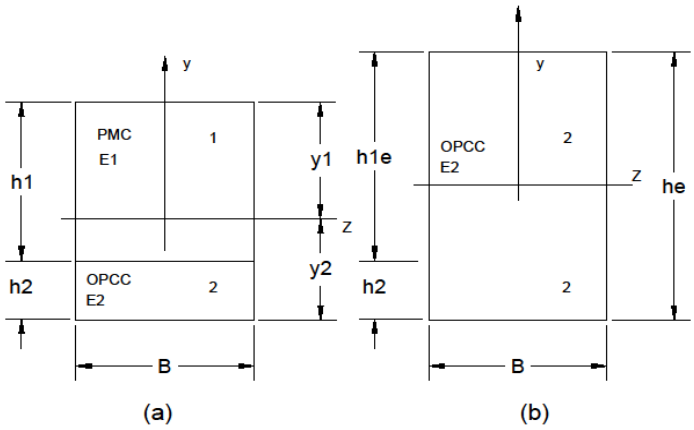

Figure 8-25 (a) cross-section of SFRPMC-on-OPCC composite beam; (b) equivalent cross-section with respect to OPCC base with identical flexural rigidity

Crack reaching interface

Now, consider a PMC-on-OPCC composite beam with a crack (or notch) through the OPCC base impinging the interface. In this case the overlay dominates the stress field at the bottom of the overlay. Therefore, the bottom layer material is necessarily converted to the top layer material by keeping flexural rigidity and width constant. Similarly to the formulation above, the equivalent height of the section is determined as:

$$E_1 \times \frac{1}{12} B h_e^{\,3} = E_1 I_1 + E_2 I_2 \qquad 8.48$$

The equivalent height with respect to material 1 (top layer) by solving eqn.8.48 is given by:

$$h_e = 2.29 \sqrt[3]{\frac{E_1 I_1 + E_2 I_2}{E_1 B}} \qquad 8.49$$

where h_e is equivalent height with respect to material 1; B is the width of beam; E_1, I_1, E_2 and I_2 have been defined previously. The bending moment at the cracked section, M_c, can be calculated by substitution of h_e into eqns. 8.9 - 8.13 (h=h_e). Since the bending moment is carried by the overlay alone, the stress at the bottom of overlay is evaluated in the overlay section by the following equation:

$$\sigma_N = \frac{6M_c}{Bh_1^2} \quad 8.50$$

where M_c is the bending moment at the cracked (notched) section; B and h_1 are the width of the beam and height of the overlay, respectively. Note that the I_1 and I_2 in eqn.8.48 and 8.49 are evaluated over the whole depth of the cross section.

Crack in SFRPMC overlay

After the crack penetrates into the top overlay, the top material dominates the stress field at the vicinity of the crack tip, and thus the flexural behaviour is dependent on the steel fibre-reinforced PMC. It has been confirmed in Section 8.4.2 that the Winkler foundation is no longer suitable for simulating the flexural performance of the SFRC beams, and the elastic solid foundation is an appropriate model. It has been previously stated that the analytical solution to the load-CMOD relationship for beams on elastic solid foundations is not available to date, hence the relationship needs to be established using the FEA method.

As an example, a SBRPMC1.5%-on-OPCC composite beam with a notch through OPCC base shown in Figure 8-29 is analysed using FE code ANSYS12.0. The analysis procedure was the same as that described in Section 8.2.5. The dimensions of the composite beam are 1 mm x 500 mm in width and length, and the heights of the top and the bottom layers are 70 mm and 49 mm respectively. The dimensions are the averages of the three tested beams listed in Table 8-12. The three composite beams were tested on a rubber foundation, and the Young's modulus of the foundation is 37 MPa (listed in Table 8-1). Two coefficients of friction between the beam and the foundation, i.e. f=0 and f=0.2, were considered. Table 8-11 and Figure 8-26 demonstrate the SIF-crack length and CMOD-crack length relationships under the action of the applied load of 100 N.

Table 8-11 SIFs and CMODs of SBRPMC1.5%-on-OPCC beam with a notch through OPCC base on the elastic solid foundations in different crack lengths and friction coefficients (Figure 8-29) calculated using FE code.

P=100N, L=500mm, B=1mm,h_1=70mm, h_2=49mm, E_1=32365MPa, E_2=25200MPa,E_0=37MPa								
a0	Δa	a	f=0			f=0.2		
(mm)	(mm)	(mm)	K_I (MPamm$^{0.5}$)	CTOD (mm)	CMOD (mm)	K_I (MPamm$^{0.5}$)	CTOD (mm)	CMOD (mm)
49	10	59	59.1	0.0202	0.0675	51.2	0.0177	0.059
49	20	69	78.8	0.0427	0.1077	67.6	0.0367	0.0927
49	40	89	165.3	0.1733	0.3472	144.3	0.1516	0.3039
49	50	99	277.4	0.4122	0.7726	236.7	0.3527	0.6612
49	60	109	514.3	1.2249	2.1778	396.9	0.9500	1.6881

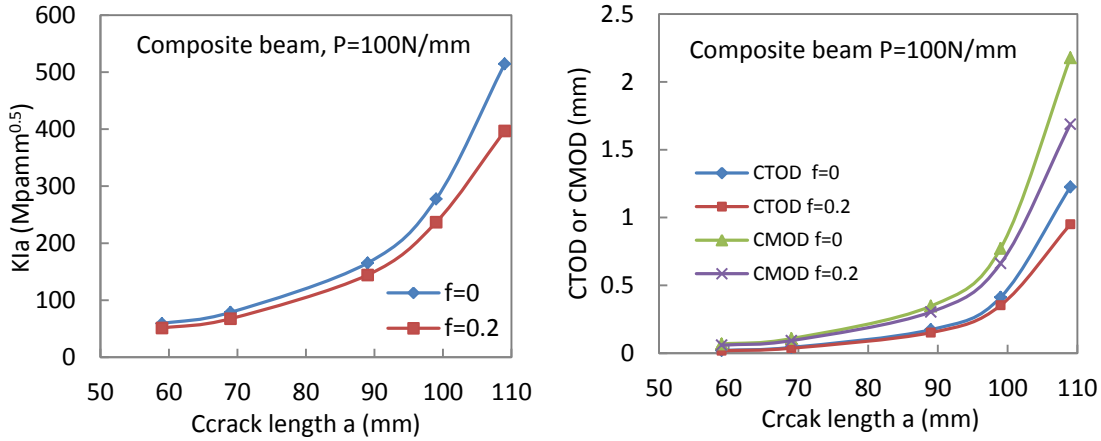

Figure 8-26 Relationships of SIF-crack length and CMOD-crack length of SBRPMC1.5%-on-OPCC composite on rubber beam (E_0=37MPa, ν_0=0.3).

Regression-fitting the data in Figure 8-26, and by noting the linear relationships between SIF and *P*, CMOD and *P*, the following relationships for f=0 are:

$$K_{Ia} = 0.074601P \cdot \mathrm{e}^{0.0347a} \quad \text{for } 49 \le a \le 90\text{mm} \qquad 8.51$$

$$K_{Ia} = 0.01041P \cdot e^{0.0347a} \quad \text{for } 89 \le a \le 110\text{mm} \qquad 8.52$$

$$CMOD_a = 0.000025P \cdot \mathrm{e}^{0.0552a} \quad \text{for } 49 \le a \le 90\text{mm} \qquad 8.53$$

$$CMOD_a = 0.0000009P \cdot \mathrm{e}^{0.0918a} \quad \text{for } 89 \le a \le 110\text{mm} \qquad 8.54$$

where K_{Ia} is the stress intensity factor induced by the applied load (MPamm$^{0.5}$); $CMOD_a$ is the crack mouth opening displacement (mm) induced by applied load; *P* is the applied load (N); *a* is the crack length (mm). The relationships above will be used to simulate the flexural behaviour of SBRPMC1.5%-on-OPCC composite beam on the rubber pad foundation, with crack propagation in the SFR-PMC overlay, and will be presented in Section 8.5.3.

8.5.2 Specimen Preparation and Test Procedure

In this study, three SBRPMC1.5%-on-OPCC composite beams with a notch through OPCC base, two SBRPMC1.5%-on-OPCC composite beams with a notch in the OPCC base, and three PVAPMC1.5%-on-OPCC composite beams with a notch in the OPCC bases, were tested on rubber and cement foundations. The preparation procedure for the composite beams was presented in Section 4.4 in detail. A clip gauge was mounted on the notch at 13 mm above the bottom of the beam to measure the crack opening displacement. Three LVDTs were used: one for measuring crack opening displacement at the interface, one for measuring vertical displacement at load-point, and a third for measuring the deflection at the top, 200 mm away from the central line. A thin layer of cement was evenly sprayed between the beam

and the foundation to minimize the friction between them. Figures 8-27 and 8-28 clearly illustrate the experimental setup, the dimensions of the composite beam, and the instrumentation. The test procedure was the same as that for intact SBRPMC1.5%-35 beams on an elastic foundation. The loading rate was controlled by CMOD, namely 0.0001 mm/s till CMOD was equal to 0.2 mm, and after that the loading rate was 0.0033 mm/s till termination of the test.

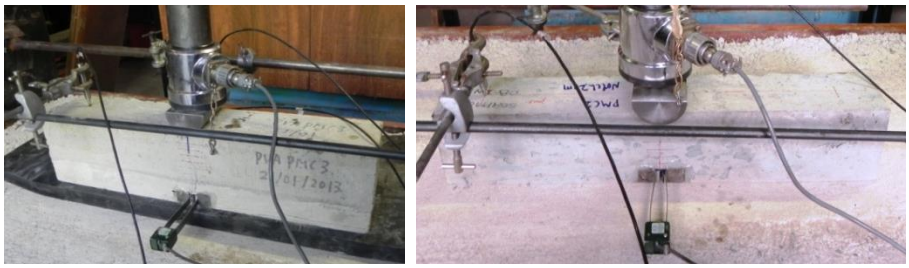

(a) (b)

Figure 8-27 Experimental setup for SFRPMC-on-OPCC composite beam: (a) on RF, (b) on CF

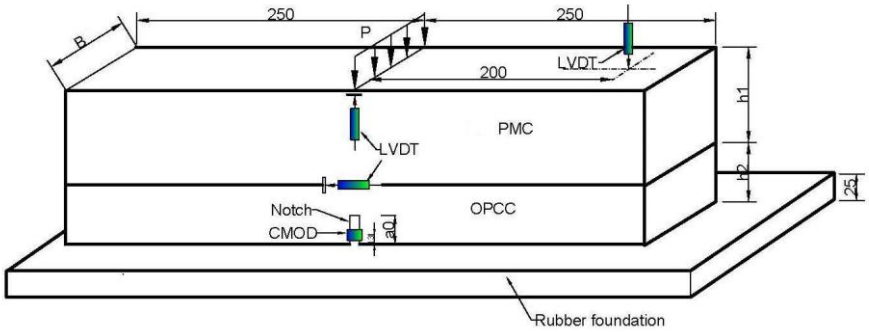

Figure 8-28 Dimensions and instrumentation of PMC-on-OPCC composite beam on elastic foundation

8.5.3 Composite Beams with a Notch through OPCC

Three composite beams with notch through OPCC base were prepared for the test. Each OPCC base was assembled with two half bases to form the notch through OPCC base during the three composite beams formation. The top of the OPCC base was roughened. The mix of the overlay was SBRPMC1.5%-35. The mix proportion of SBRPMC1.5%-35 was listed in Table 5-1, and that of OPCC in Table 4-14. The experimental setup was shown in Figures 8-27 and 8-28. All three beams were tested on rubber foundation. The dimensions of the three specimens are tabulated in Table 8-12. The three curves of load-crack opening displacement ($COD_{int.}$) at the interface are plotted in Figure 8-30.

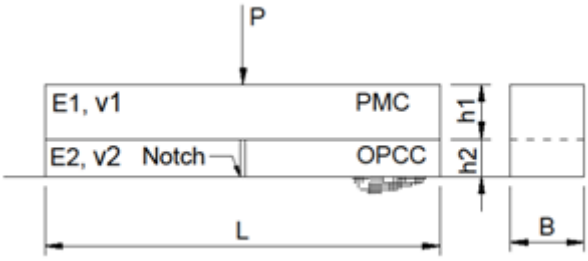

Figure 8-29 SFRPMC-on-OPCC beam with notch through OPCC base on elastic solid foundation

Table 8-12 Dimensions of SBRPMC1.5%-on-OPCC composite beams with notch through OPCC base, on rubber pad foundation; tested load P1 at cracking initiation and calculated stress at notch tip

No.	ID of mix	Geometrical parameters of beam					Experimental	Calculated
		L (mm)	B (mm)	h_1 (mm)	h_2 (mm)	a_0 (mm)	P_1 (for 1mm width) (N)	σ_N at notch tip (MPa)
1	SBRPMC1.5%	500	100	75	48	48	121	7.81
2		500	100	66	50	50	80	6.6
3		500	100	69	47.5	47.5	125	9.47

Note P_1 is the load for 1mm width of beam, not the total load.

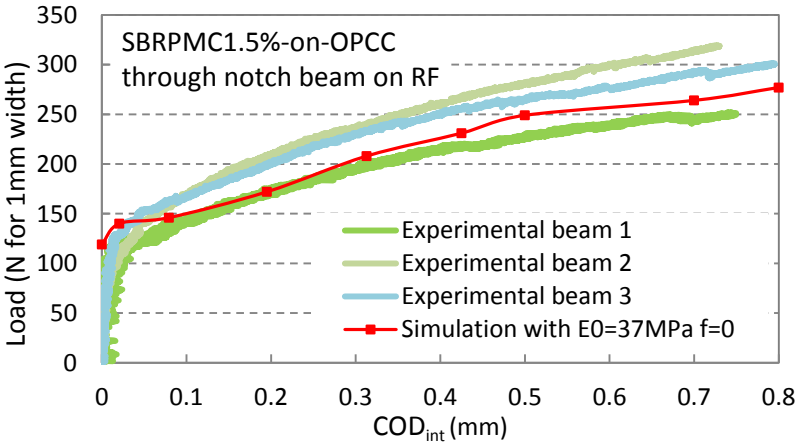

Figure 8-30 Load vs. crack opening displacement at interface.

It is seen from Figure 8-30 that there exists a conversion point of linearity to nonlinearity for all three beams, and after that the incremental rate of load decreased. The loads at conversion points are easily identified in enlarged load-COD_{int} graphs, and denoted as P_1 and listed in Table 8-12.

Mechanism of conversion point from linearity to nonlinearity

The decrease of slope of load-COD_{int} curve indicates a decrease in flexural rigidity of the load-line section. Thus, the conversion point might indicate the cracking initiation in the SFRPMC overlay.

With the knowledge of P_1 and the mechanical properties of SBRPMC1.5%-35 and OPCC, the stress at the notch tip (i.e. the bottom of the overlay) can be evaluated using the method presented in Section 8.5.1, in which the OPCC base was converted to SBRPMC1.5%-35 overlay using eqn.8.49, which is based on the principle of equivalent flexural rigidity. The calculated stress at the notch tip (i.e. the bottom of the overlay) of the three beams is listed in Table 8-12. The average of the three calculated stresses at the bottom of the overlay is 7.96 MPa, very close to the flexural strength of the matrix of mix SBRPMC1.5%-35, which is 7.93 MPa, measured under three-point bending test, and listed in Table 6-4.

Therefore, the following conclusion can be drawn: (1) Crack initiation in the SFRC overlay led to the flexural behaviour of the composite beam changing from linearity to nonlinearity and at the same time resulting in the reduction of flexural rigidity of the beam; (2) The load corresponding to crack initiation is only dependent on the flexural strength of the matrix.

Simulation of load-COD_{int}

The relationship of load-COD_{int} was simulated using eqns.8.51 - 8.54, with involving to eqn.8.55. The eqns. 8.51 - 8.54 was purposely established for the three specific beams listed in Table 8-12. In the computation for the simulation of the load-COD_{int} relationship, K_{Ia} and $CMOD_a$ were evaluated by eqns.8.51 - 8.54, whereas K_{Ib} and $CMOD_b$ induced by fibre bridging traction, were calculated by using eqns.8.19 and 8.20. The fibre bridging law is described by eqn.8.38, and the Young's modulus was taken as the elasticity modulus of the SFRPMC overlay, i.e. E=32365 MPa, since the overlay dominated the mechanical behaviour. It is worth noting that COD_{int} was calculated through CMOD by eqn. 8.55, which is essentially the same as eqn.8.22:

$$COD_{int} = CMOD \cdot \frac{a-a_0}{a} \qquad 8.55$$

where CMOD is the crack mouth opening displacement, $\mathrm{CMOD} = \mathrm{CMOD_a} - \mathrm{CMOD_b}$; a and a_0 are crack length and the initial notch length, $a_0=h_2$ here.

The calculation procedure was the same as that described in detail in Section 8.4.2. The fibre bridging law for SBRPMC1.5%-35 is described by eqn. 8.38. The simulated load-COD_{int} curve is plotted in Figure 8-30. It can be observed that the simulation of load-COD_{int} is in very good agreement with the experimental results. It confirms again that elastic solid foundation model is suitable for modelling the system of SFRC beam on elastic foundation.

8.5.4 Composite Beam with a Notch in OPCC Base

The PMC-on-OPCC composite beam on elastic foundation can partially simulate the overlay on old concrete pavements in the field. The objective of this section was to simulate the bonded SFRC overlay on old concrete pavements. For this purpose, two SBRPMC1.5%-35-on-OPCC composite beams with a notch in the OPCC were tested on rubber pad foundation; and three PVAPMC1.5%-on-OPCC composite beams with a notch in the OPCC were prepared: one was tested on CF, the other two beams were tested on RF. Figure 8-31 and Table 8-13 show the loading configuration and dimensions of the composite beams.

The experimental results are listed in Table 8-13, and the load vs. COD_{int} is plotted in Figures 8-32 and 8-33. It is seen from these figures that: (1) the beam on a cement foundation exhibited much higher load bearing capacity; (2) the beams on a rubber foundation experienced a first peak load, then the load dropped down to a lower level and then increased with the CMOD. The beam on a cement foundation did not exhibit the same phenomenon of load drop. The first peak load appears to be related to the cracking of OPCC base. This is further analysed in the following.

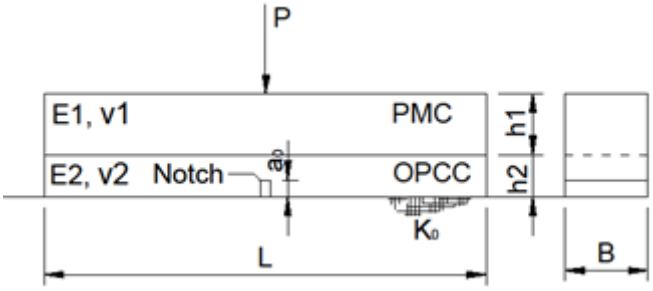

Figure 8-31 SFRPMC-on-OPCC beam with a notch in OPCC on elastic foundation

Table 8-13 Dimensions of PMC-on-OPCC composite beams and experimental results of first peak load P_1 and drop-down load P_2

No.	ID of overlay mix	Foun.	Geometrical parameters					Experim.(for 1mm width)	
			L (mm)	B (mm)	h_1 (mm)	h_2 (mm)	a_0 (mm)	P_1 (N)	P_2 (N)
1	SBRPMC1.5%	RF	500	100	73	47	20	202	168.6
2		RF	500	100	68.5	52	18	212	180.9
3	PVAPMC1.5%	CF	500	100	73	47	20	268	246.5
4		RF	500	100	73	49	22	178	110.3
5		RF	500	100	73	48	20	200	157.7

Table 8-14 Prediction of maximum load carrying capacity (P_1) of OPCC base of PMC-on-OPCC composite beam with notch in OPCC base

No.	ID of mix of overlay	Found.	a_0 (mm)	he (mm)	P_1 (N ,for 1 mm width beam) Experim.	Predicted by fracture mech.	Predicted by material mech.
1	SBRPMC1.5%	RF	20	125	202.3	180	210
2		RF	18	126	211.5	196	220
3	PVAPMC1.5%	CF	20	128	267.9	243	260
4		RF	22	130	177.5	197	222
5		RF	20	129	200.3	199	226

Note h_e is the equivalent height with respect to the bottom material OPCC.

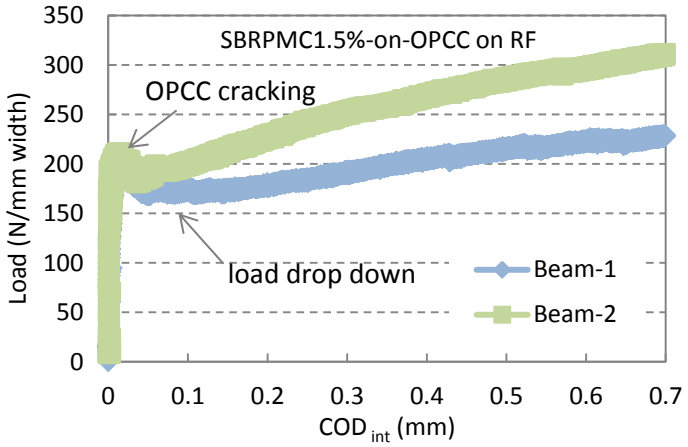

Figure 8-32 Load vs. COD_{int} of SBRPMC1.5%-on-OPCC composite beams on rubber foundation

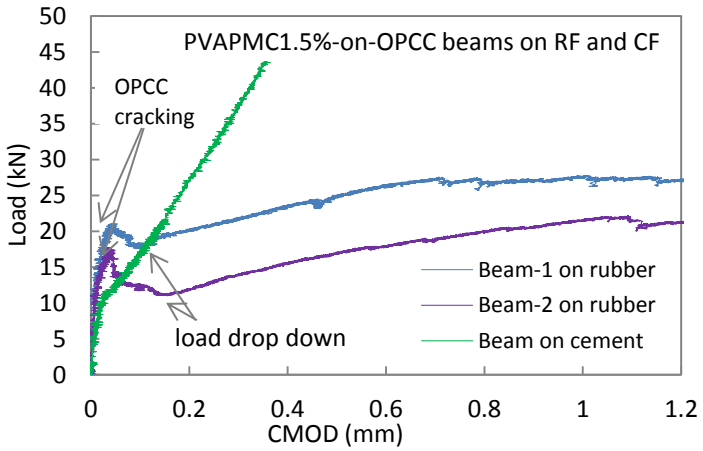

Figure 8-33 Load vs. CMODs of PVAPMC1.5%-on-OPCC composite beam on RF and CF

First peak load P_1

It seemed that the first peak loads of composite beams on a rubber pad foundation might also correspond to OPCC base cracking. It has been confirmed in Section 8.3 that the flexural behaviour of OPCC beams can be properly simulated by the Winkler foundation model and Parmerter's theory (Parmerter 1976), and both fracture mechanics and material mechanics

methods are suitable for predicting the load bearing capacity of OPCC beams. Now, it is further extended to predict the first peak load of composite beam, since it seems to be related to OPCC cracking.

As described in Section 8.5.1, the overlay material is necessarily converted to the bottom layer material OPCC, and then both fracture mechanics and material mechanics are used to determine the load carrying capacity of the OPCC base. The equivalent heights of section with respect to the OPCC base and the predicted load carrying capacity determined by both methods are tabulated in Table 8-14. It is seen that the predicted values are close to the corresponding experimental results. This indicates that the method for evaluating the load bearing capacity of the OPCC base of the PMC-on-OPCC composite beam by combining Parmerter's theory, the equivalent flexural rigidity concept and the Winkler model is verified.

The phenomenon of load drop

It has previously been presented that SFRPMC-on-OPCC composite beams on a rubber pad foundation exhibited load drop down after OPCC base cracking. The magnitude of load drop was clearly affected by the type of elastic foundation, the loading rate and the combination of stiffness of the top and the bottom layers. This study is only concerned with the bearing capacity of the OPCC base and overlays, and it is not intended to further investigate the flexural performance of the composite beam on an elastic foundation.

Load carrying capacity of SFRPMC-on-OPCC composite beams

For SFRC-on-OPCC composite beams on an elastic foundation, it seems reasonable to define two special loads to characterise the load carrying capacity: One is the load corresponding to cracking of OPCC base, the other corresponds to the crack opening displacement at the interface being equal to a certain value, i.e. $CTOD_c$, which corresponds to maximum load of notched beam under a three-point bending test.

It has been previously confirmed that a Winkler foundation and Parmerter's theory and a material strength-based criterion is capable to properly characterize the performance of an OPCC beam on elastic foundation, and to predict the load carrying capacity of the OPCC base of a composite beam. On the other hand whereas the elastic solid foundation model must be employed for simulating the flexural performance of an SFRC beam, and FEA is needed to establish the relationship of load-CMOD.

8.6 Summary

The main conclusions are presented below, while the specific conclusions can be found at the end of each sub-section. The composite beam on a rubber pad foundation exhibited a load drop after cracking of OPCC base; it is not the aim of this study to further investigate the flexural performance.

(1) Peak load did not exist in steel fibre-reinforced roller compacted polymer modified concrete beams subjected to the centrally placed point load test. The improvement of load carrying capacity was mainly contributed by the reaction of the foundation. OPCC beams exhibited a peak load and failed soon after. For the same dimension of beam on elastic foundation, SFRC beams exhibited much higher load bearing capacity than OPCC beams.

(2) Parmerter's theory and a Winkler foundation are suitable for modelling OPCC beams on elastic foundations, but not suitable for SFRC beams. Load bearing capacity of OPCC beam can be properly predicted by Parmerter's theory with the Winkler foundation model.

(3) The elastic solid foundation model is suitable for modelling SFRC beams on elastic foundations, and FEA is needed to establish the load-CMOD relationship. The simulation of load-CMOD using the method proposed by the study was in good agreement with experimental results.

(4) As for SFRC-on-OPCC composite beams, a method for calculating the load of OPCC base cracking and the load for crack initiation of SFRC beams was proposed and experimentally verified. The method combines Parmerter's cracked beam theory and the section conversion concept based on the principle of equivalent flexural rigidity. The method is presented in detail in Section 8.5.1.

9 Analysis of Overlay Pavement System

In this section, the strain energy release rate (ERR) of the interface of overlay pavement system is first analysed, and a design method for overlay thickness is presented in brief.

9.1 Strain Energy Release Rate of Interface of Overlay Pavement System

General literature review by Ioannides (2006) presented the eighty years history of stress analysis of concrete pavements. Gaedicke and Roesler (2009) reviewed the state-of-the art of the application of fracture mechanics in concrete pavements, and pointed out the lag time in usage of fracture mechanics is caused by several factors, and one of them is the difficulty in developing simple fracture mechanic analysis for slabs. Ramsamooj (1999) presented a method for analysing stress intensity factors of K_I and K_{II} of cracks in infinite-length concrete slab by combining FEA and general analytical solutions. Gotlif et al. (2006) analysed the SIFs of partial crack in concrete pavements. All the literatures aforementioned were about stress or SIFs in the single material. Jayawickrama and Lytton (1987) analysed the SIF K_I and K_{II} in overlay of overlay pavement system. Kazimierowicz-Frankowska (2008) analysed the stress at the crack tip with the assumption of 1 mm-width crack in overlay pavement system, but did not consider the interfacial crack problems. It is clear that the method for calculating the ERR of interface in overlay pavements is not available to date.

9.1.1 Fundamentals

It is well known that three-dimensional crack problems are difficult to analyse due to the orientation of crack initiation and that a very fine mesh is needed in the vicinity of the crack tip to capture the stress singularity. The concrete overlay pavement system is more difficult to model because it is usually very large in volume, resulting in a great number of elements being needed. Two dimensional crack problems are much more easily analysed by using existing analysis tools such as the FE method. For these reasons it is always expected to simplify the three-dimensional model to the two-dimensional. For interfacial cracks, a three-dimensional model can be reasonably simplified to two-dimensional model thanks to the fact that bond strength of interface is usually weaker than both the materials, and consequently the crack propagation is constrained in the interface surface. For this purpose, consider the overlay pavement system subjected to the two loading configurations shown in Figure 9-1(a) and (b). An interfacial crack exists through the pavement width. The loading mode-a is the

overlay pavement system subjected to two-wheel vehicular load. Mode-b is the same pavement, but subjected to the same pressure on the zone through the pavement width, and the width of pressured zone is equal to the width of contact area of the wheel. A three-dimensional coordinate system is built for convenience, in which the interface belongs to *x*-*z* plane, and the *x*-axis coincides with the intersection line AB and x-y plane. Figure 9-1 clearly demonstrates the relative position of overlay pavement and the coordinate system. The interfacial crack of section AB in Figure 9-1(a) and section EF in Figure 9-1(b) extending in the *x* direction is considered, and the interfacial ERR is analysed in the following:

Analysis presented later in Section 9.1.3 confirms that the assumption of the interfacial crack extending in *x*-direction is reasonable by comparing the relative displacements δ_x, δ_y and δ_z.

Referring to Figure 9-1 and denoting the interfacial strain energy release rates of mode-a and mode-b as $G_i^{(a)}$ and $G_i^{(b)}$, respectively; the ratio $G_i^{(a)}/G_i^{(b)}$ is reasonably assumed to be a constant for given geometrical and mechanical parameters. The mode-b loading system is clearly a plane strain problem. Thus it can be simplified to mode-c loading, which is a two-dimensional model and thus is easily analysed. Now, the analysis starts from the establishment of the ratio $G_i^{(a)}/G_i^{(b)}$. According to the relationship proposed by Shi et al. (2006), which has been presented in Section 7.3.1, the strain energy release rates of mode-a and mode-b for the crack extending in the direction of the *x* axis is:

$$G_i^{(a)} = \frac{1}{cosh^2(\pi\varepsilon)} \frac{(K_I^2 + K_{II}^2)^{(a)}}{E^*} \tag{9.1}$$

$$G_i^{(b)} = \frac{1}{cosh^2(\pi\varepsilon)} \frac{(K_I^2 + K_{II}^2)^{(b)}}{E^*} \tag{9.2}$$

Where, $G_i^{(a)}$ and $G_i^{(b)}$ are the interfacial ERRs of mode-a and mode-b loading (Figure 9-1), respectively; E^* and ε are material constant, and has been previously defined in Section 7.3.1; K_I and K_{II} are the stress intensity factors of mode-I loading and mode-II loading, respectively. Eqn. 9.1 divided by eqn.9.2 results in:

$$\frac{G_i^{(a)}}{G_i^{(b)}} = \frac{(K_I^2 + K_{II}^2)^{(a)}}{(K_I^2 + K_{II}^2)^{(b)}} \tag{9.3}$$

It is noted that for given mechanical parameters of a overlay pavement system, a chosen characteristic length and the node on the crack face, *D*, Q and ε in mode-a are identical to those in mode-b. Substituting *A* and *B* from eqns. 7.30 and 7.31 into eqn. 9.3 and after involving eqns. 7.19 and 7.20 results in:

$$\frac{G_i^{(a)}}{G_i^{(b)}} = \frac{(\delta_x^2+\delta_y^2)^{(a)}}{(\delta_x^2+\delta_y^2)^{(b)}} \cdot \frac{(1+4\varepsilon^2)^{(a)}}{(1+4\varepsilon^2)^{(b)}} \qquad 9.4$$

It is noted that for given mechanical parameters of a overlay pavement system, ε in mode-a is identical to that in mode-b. Thus simplification of eqn. 9.4 results in:

$$\frac{G_i^{(a)}}{G_i^{(b)}} = \frac{(\delta_x^2+\delta_y^2)^{(a)}}{(\delta_x^2+\delta_y^2)^{(b)}} \qquad 9.5$$

where δ_x and δ_y are the relative sliding displacement in *x*-axis and relative opening displacement in *y*-axis, of crack face behind the crack tip (Figure 9-2), respectively; the superscripts *(a)* and *(b)* indicate the mode-a and mode-b loading, respectively.

It is clear that the ratio $G_i^{(a)}/G_i^{(b)}$ is dependent on the relative crack face displacements of mode-a and mode-b. The ratio may be obtained from FEA of three-dimensional overlay pavement system. The FE model may be coarse meshed to avoid generating great number of elements. Mode-b is a plane strain problem and can be simplified to mode-c, which is a two-dimensional model, and thus the interfacial ERR $G_i^{(c)}$ and its phase angle of mode-c can be determined by using the calculation procedure presented in Section 7.3.1. With the knowledge of the ratio $G_i^{(a)}/G_i^{(b)}$, the $G_i^{(a)}$ of mode-a can be easily obtained via $G_i^{(b)}$ of mode-b, which is equal to $G_i^{(c)}$.

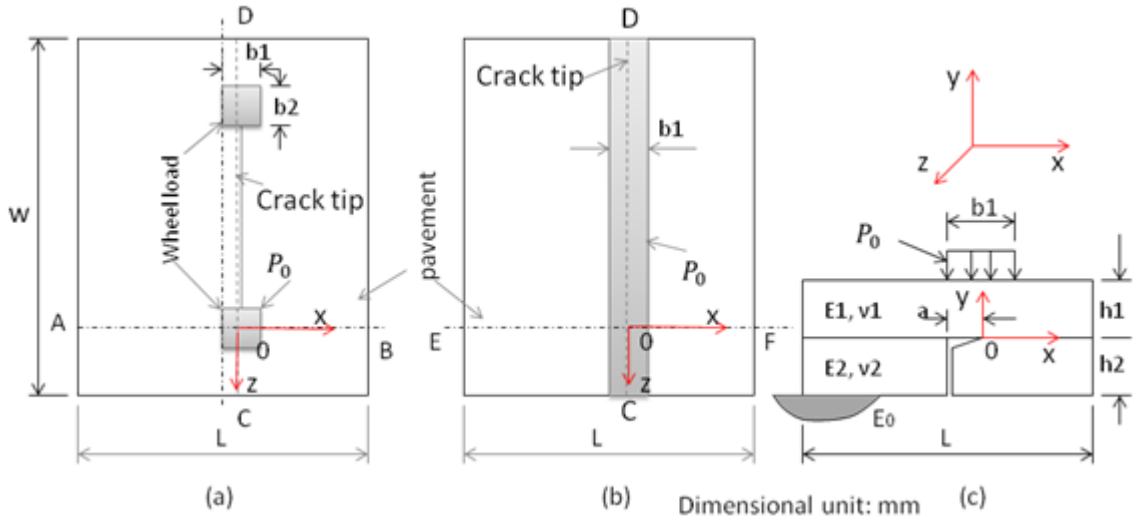

Figure 9-1 (a) a lane-width pavement subjected to vehicular wheel loading, (b) a lane width pavement subjected to a pressure load through the width, (c) simplified model for loading mode (b)

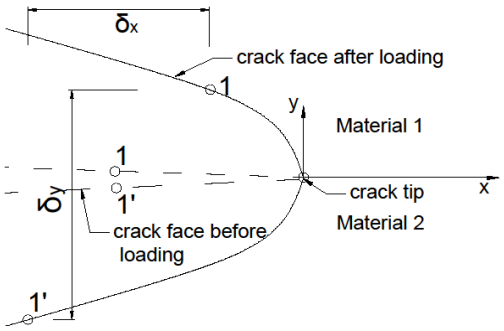

Figure 9-2 Relative displacement of interfacial crack face in the vicinity of the crack tip of bi-material

9.1.2 Interfacial ERR Induced by Vehicular Loads

It has been previously described that the analytical solution for calculating interfacial ERR of overlay pavement system is not available to date; and thus FEA is needed. In this study, the Winkler foundation was adopted for calculating the ratio $G_i^{(a)}/G_i^{(b)}$ because it could easily be handled in finite element (FE) code ANSYS. An elastic solid foundation needs a great number of elements for mesh; contact elements are needed to simulate the interface between the slab and the foundation. This may result in slow or not convergence in computation, and a number of elements in excess of the limit of capacity. The materials of overlay and existing old concrete pavement considered are the mixes developed by the present study, i.e SBRPMC1.5%-35 and OPCC, which have been extensively investigated in previous sections. The mechanical properties of the two materials are relisted in Table 9-1 for convenience.

Table 9-1 Mechanical properties of SBRPMC1.5%-35, OPCC and their composite specimens

Mix ID	E (MPa)	ν
SBRPMC1.5%-35	32365	0.187
OPCC	25200	0.21
Interfacial toughness of SBRPMC1.5%-on-OPCC (J/m^2)	Roughened interface	52.0
	Smooth interface	22.6
Splitting tensile bond strength of SBRPMC1.5%-on-OPCC (MPa)	Roughened interface	2.96
	Smooth interface	1.80

The pavements in service may be subjected to various vehicular loads, including standard vehicle and lorry. British Standard (BS EN 1991-2:2003) illustrates various lorries for bridge design. The interfacial ERRs of the typical overlay pavement systems subjected to the standard axle and the lorry axle loads are calculated in the following:

Elastic modulus and reaction coefficient of elastic foundation

In the highway pavement design manual (Highway Agency UK 2013), foundations for pavement design are divided into four classes based on the following elasticity moduli: 50MPa, 100MPa, 200MPa and 400MPa. The relationships given by British Standard (BS EN 1997-2: 2007) for evaluating the modulus of the elastic solid foundation and the reaction coefficient of the Winkler foundation are described by eqns.8.2 and 8.3. When the Poisson's ratio v_0 of the elastic solid foundation is taken as 0.3 and the diameter of loading circular plate is taken as 760 mm (which is the diameter of the standard plate (Croney1998)), the relationship of K_0 and E_0 is given by:

$$K_0 = \frac{E_0}{543} \qquad 9.6$$

where E_0 is the modulus of the elastic solid foundation (MPa); K_0 is the reaction coefficient of the Winkler foundation (N/mm^3). The E_0 and the corresponding K_0 are listed in Table 9-2. In this study, Winkler foundation was adopted to analyse the model-a and model-b shown in Figure 9-1 for the reasons described previously, to calculate the ratio $G_i^{(a)}/G_i^{(b)}$; while elastic solid foundation was used in analysing the model-c shown in the same figure to calculate the interfacial ERRs $G_i^{(c)}$ and phase angles, in accordance with the highway pavement design manual (Highway Agency UK 2013).

Table 9-2 Elasticity modulus of elastic solid foundation and the corresponding reaction coefficients of Winkler foundation

E_0 (MPa)	37	50	100	200	400	500
K_0 (N/mm^3)	0.068	0.092	0.184	0.37	0.74	0.92

Interfacial ERR induced by standard 80kN - axle load

The SBRPMC1.5%-on-OPCC overlay pavement system shown in Figure 9-3(a) subjected to standard two-wheel axle load is considered. The system consists of 3600 mm x 1500 mm in width and length in planar dimension, and a 20 mm-length interfacial defect through the pavement. The overlay pavement, consisting of 100 mm–thickness SBRPMC1.5% overlay and 200 mm–thickness OPCC base is considered. The mechanical properties of the two materials are listed in Table 9-1. The weight of the standard axle is 80 kN; and the equivalent square of each standard wheel is 240 mm x 240 mm, and the pressure is 0.7 MPa. The wheel load partially acts on the right hand side with respect to the crack (see Figure 9-3). The length of the overlay pavement system of 1500 mm was considered, since the typical crack spacing of CRCP is 1000 to 2000 mm (McCullough 1988). The assumption of interfacial crack length of 20 mm seems reasonable, due to the fact that the maximum size of coarse aggregate used

on sites is usually around 20 mm.

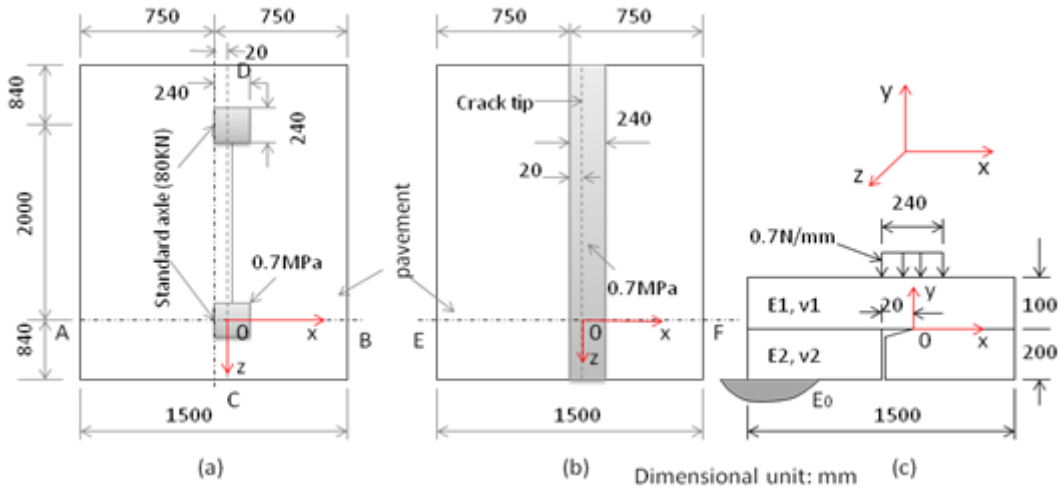

Figure 9-3 (a) Overlay pavement system subjected to standard 80kN - axle load; (b)a lane width pavement subjected to a pressure load through the width, (c) simplified model for loading mode (b)

For the mode-a and model-b shown in Figure 9-3, the critical position is at the crack tip beneath the loading wheel (the origin 0 of Figure 9-3). The general FE code ANSYS 12.0 was employed; the eight-node Solid45 element was used for the two-layer composite slab; while the element Surf153, which is able to simulate Winkler foundation, was used for modelling the foundation. The two nodes on upper and lower faces of the crack, whose displacements were extracted to evaluate the ratio $G_i^{(a)}/G_i^{(b)}$, were 1mm behind the crack tip. The specified two nodes were sufficiently close to the crack tip. Total number of nodes was about 38000. The whole meshed model and the fine–mesh zone surrounding the crack tip are shown in Figure 9-4(a) and (b). Figure 9-5 demonstrates the deformed model under two-wheel loading and through width pressure loading, respectively; the former corresponds to Figure 9-3(a) and the latter to Figure 9-3(b). The calculated ratios of $G_i^{(a)}/G_i^{(b)}$ are listed in Table 9-3.

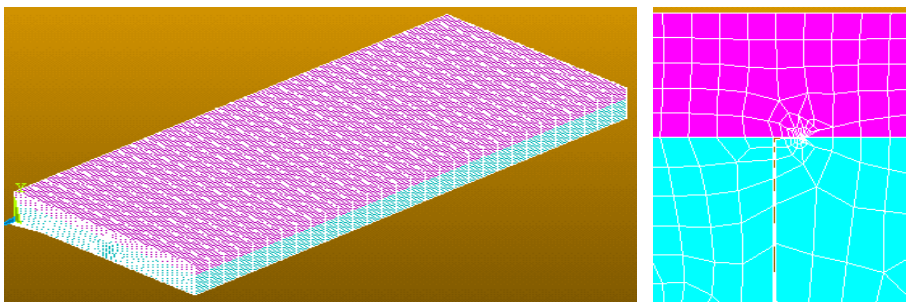

(a) (b)

Figure 9-4 (a) meshed three-dimensional overlay pavement model, (b) fine meshed zone

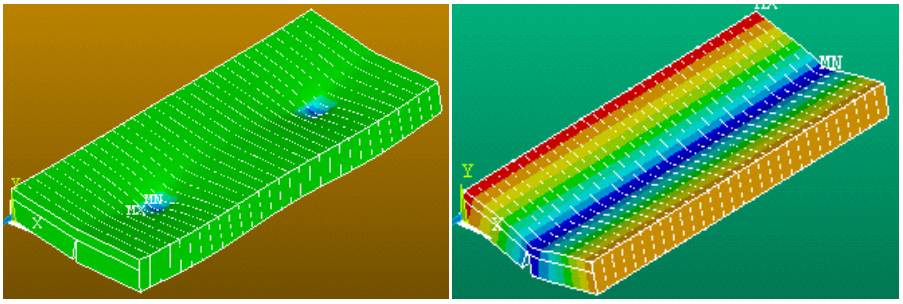

(a) (b)

Figure 9-5 (a) deformed overlay pavement system subjected to two - wheel load corresponding to Fig. 9-3(a), (b) deformed overlay pavement system subjected to a pressure through the width corresponding to Fig. 9-3(b)

It is seen from Table 9-3 that the ratio $G_i^{(a)}/G_i^{(b)}$ is insensitive to the elasticity modulus of the foundation, i.e. the ratio increased from 0.029 to 0.036 as the modulus varied from 37MPa to 500MPa, whereas the average of the six values is 0.031.

Table 9-3 Calculated strain energy release rate of the interface of the overlay pavement system shown in Figure 9-3 (a) subjected to the 80kN - axle load (E_1=32365MPa, ν_1=0.187, h_1=100mm; E_2=25200MPa, ν_2=0.21, h_2=200mm) (Note: Gi= $Gi^{(a)}$, $Gi^{(b)}$=$Gi^{(c)}$ in this table)

E_0 (MPa)	K_0 (N/mm^3)	$G_i^{(a)}/G_i^{(b)}$	$G_i^{(c)}$ (J/m^2)	G_i at interface of overlay pavement (J/m^2)
37	0.068	0.029	92.6	2.69
50	0.092	0.029	88.5	2.57
100	0.184	0.029	72.5	2.1
200	0.37	0.031	50.5	1.57
400	0.74	0.034	29.7	1.01
500	0.92	0.036	12.9	0.46

The two-dimensional model-c shown in Figure 9-3(c) is easily modelled. The calculation procedure presented in detail in Section 7.3.1 was used. Plane strain was assumed, and the four-node Plane42 element was used for modelling the overlay pavement and the elastic solid foundation, and the contact element CONTA172 was used for simulating the interface between OPCC base and the foundation. The friction between the composite beam and the foundation was assumed to be zero. The length of the square elements in the fine-meshed zone was 0.1 mm; and crack extension (Δa) was 0.1 mm. The calculated G_i of model-c is listed in Table 9-3. With the knowledge of the ratio of $G_i^{(a)}/G_i^{(b)}$ and the $G_i^{(c)}$ of model-c, the G_i of the interface of the overlay pavement system subjected to standard vehicular load (Figure 9-3(a)) is readily obtained by simple multiplication of the ratio and $G_i^{(c)}$. The calculation results are tabulated in Table 9-3. The results will be compared with the measured interfacial fracture toughness in the end of this section.

It is worth pointing out that the calculation of the models shown in Figure 9-3(c), Figure 9-8(c) and Figure 9-10(c) for 80kN-axle, 2 x 120kN-axle and 190kN-axle loads respectively, showed that the relative position of the two nodes 1 and 1′ after crack extension (see Figures 7-18(b) and 9-12(c)), which are originally at the same position before crack extension, is located between the original position, like the one shown in Figure 7-17(a).

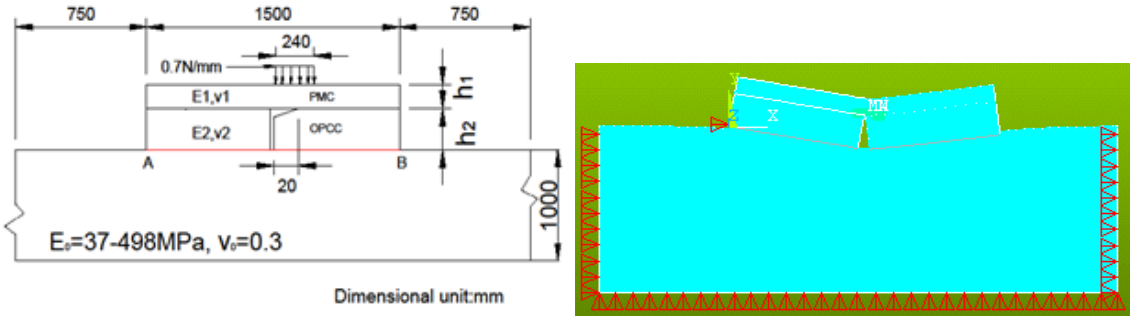

Figure 9-6 The model of Figure 9-3(c) with a 20mm-length interfacial crack subjected to standard vehicular wheel load (the wheel load acting on the right side of the existing crack in old OPCC pavement)

Interfacial ERR induced by 2 x 120kN-axle load

British Standard (BS EN 1991-2:2003) illustrates a lorry, shown in Figure 9-7(a), for the structural design of bridges. The total weight of the lorry is 630 kN; the three rear axles weigh 3 x 120 kN; the spacing of them is identically 1.3 m, and the area of each wheel of the three axles is 270 mm x 320 mm, shown in Figure 9-7(b). Two axles acting on the overlay pavement shown in Figure 9.8(a) may constitute another unfavourable condition for the interfacial ERR of the overlay pavement system. The wheel contact pressure is 0.694MPa, determined using the weight of the wheel and its area shown in Figure 9-7(b). The overlay pavement system subjected to the two-axle load is analysed to obtain the energy release rate of the interface in the following:

The pavement is of the dimensions 3.76 m x 2.05 m in length and width. A 20mm-long interfacial crack through the width exists between the overlay and the existing pavement. The materials of the overlay and the concrete base are SBRPMC1.5%-35 and OPCC, respectively.

Figure 9-8 shows the dimensions of the overlay pavement system and the loading configuration. The calculation procedure was the same as that described previously. The results are listed in Table 9-4 and will be compared with the measured interfacial fracture toughness at the end of the section.

(a) (b)

Figure 9-7 (a) Silhouette of 630 kN-lorry; (b) wheel axle type for the three rear axles (BS EN 1991-2:2003 (E))

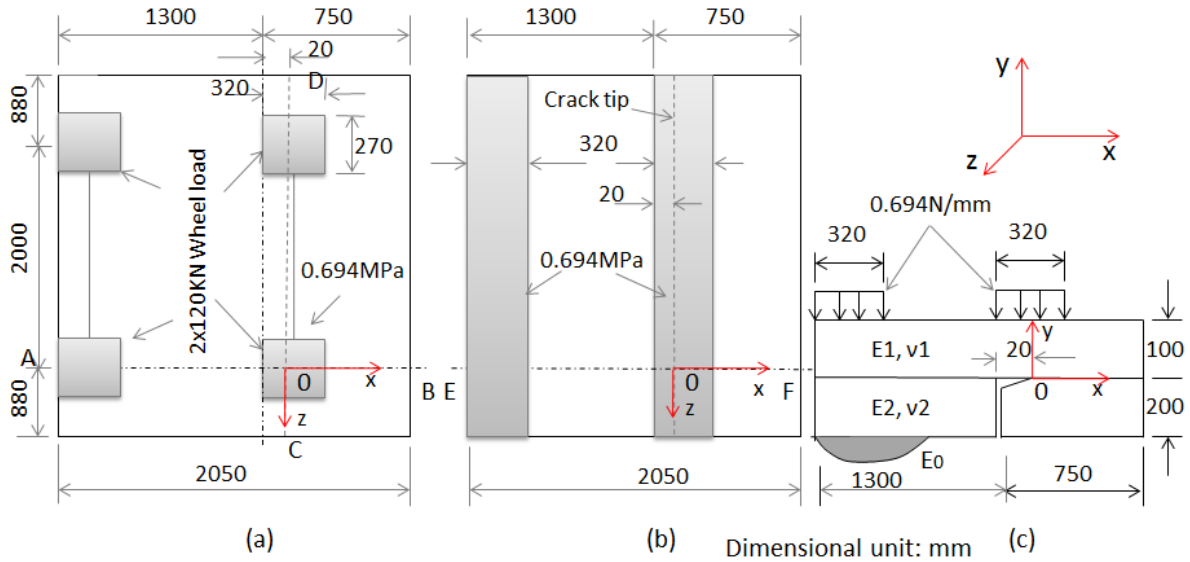

Figure 9-8 (a) Overlay pavement system subjected to two-axle load (2 x 120kN) of 630kN-lorry; (b) a lane width pavement subjected to pressure load through the width, (c) simplified model for loading mode (b)

Table 9-4 Calculated ERRs of the interface of the overlay pavement system shown in Figure 9-8(a) subjected to the 2 x120kN-axle load (E_1=32365MPa, ν_1=0.187, h_1=100mm; E_2=25200MPa, ν_2=0.21, h_2=200mm)

E_0 (MPa)	K_0 (N/mm^3)	$G^{(a)}/G^{(b)}$	$G^{(c)}$ (J/m^2)	G_i of interface of overlay pavement (J/m^2)
37	0.068	0.119	34.6	4.1
50	0.092	0.112	34.0	3.8
100	0.184	0.11	28.1	3.1
200	0.37	0.087	22.6	2.0
400	0.74	0.079	16.7	1.3
500	0.92	0.078	14.5	1.1

Interfacial ERR induced by a 190kN-axle load

British Standard (BS EN 1991-2:2003) illustrates another lorry, shown in Figure 9-9, for the structural design of bridges. The total weight of this lorry is 560 kN; the second axle of the lorry weighs 190 kN; and the contact area of the wheel of the axle is shown in Figure 9-9(b).

The wheel contact pressure is 0.675 MPa, determined using the weight and the area of the wheel shown in Figure 9-9(b). Figure 9-10(a) shows an overlay pavement subjected to the 190 kN-axle load. This may constitute an unfavourable condition for the interfacial ERR of the overlay pavement system, and is analysed in the following.

The overlay pavement system and the materials are the same as that shown in Figure 9-3. The wheel contact area shown in Figure 9-9(b) is simplified to that shown in Figure 9-10(a) by keeping the area constant. The calculation procedures are the same as that described previously, and the results are listed in Table 9-5.

(a) (b)

Figure 9-9 (a) Silhouette of 560 kN-lorry; (b) wheel axle type B for the 190kN-axle (BS EN 1991-2:2003 (E))

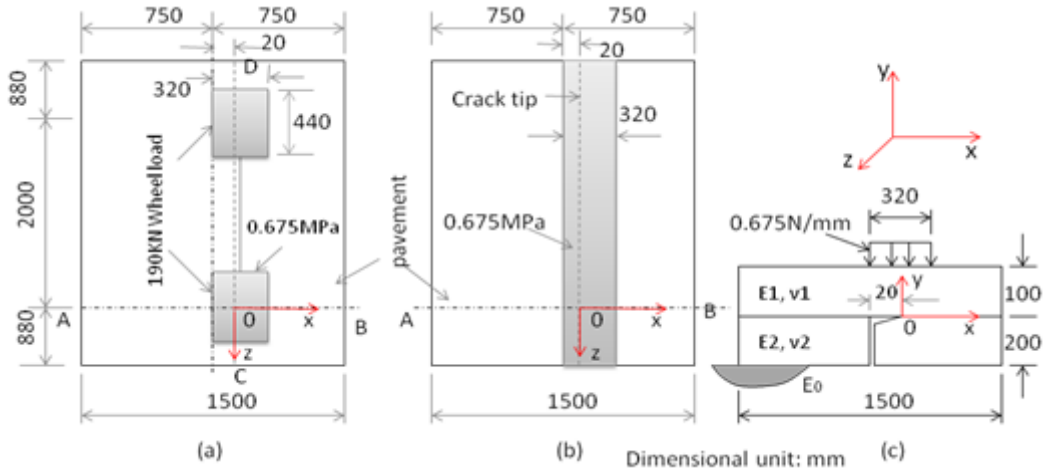

Figure 9-10 (a) Overlay pavement system subjected to a 190kN-axle loading of 560kN-lorry; (b)a lane width pavement subjected to pressure load through the width, (c) simplified model for loading mode (b)

Table 9-5 Calculated strain ERRs of the interface of the overlay pavement system shown in Figures 9-10 subjected to 190kN-axle load (E_1=32365MPa, ν_1=0.187, h_1=100mm; E_2=25200MPa, ν_2=0.21, h_2=200mm)

E_0 (MPa)	K_0 (N/mm^3)	$G^{(a)}/G^{(b)}$	$G^{(c)}$ (J/m^2)	G_i at interface of overlay pavement (J/m^2)
37	0.068	0.1003	126.4	12.7
50	0.092	0.1003	122	12.2
100	0.184	0.103	98.6	10.2
200	0.37	0.1098	67.2	7.4
400	0.74	0.1193	40.2	4.8
500	0.92	0.1243	33.1	4.1

9.1.3 Three-dimensional interfacial crack

All the analyses conducted previously on the interfacial ERRs of overlay pavement systems were simplified to two-dimensional interface crack. Namely, the ERR obtained previously corresponds to the crack on *x*-*y* plane extending in *x* direction (see Figure 9-12), only contained the ERR in mode-I and mode-II. However, the interfacial crack of overlay pavement is actually three-dimensional. In a three-dimensional crack, the total energy release rate is the sum of ERRs in mode-I, mode-II and mode-III. Therefore, it is necessary to validate the simplification used previously.

For two–dimensional interfacial crack, substituting eqns. 7.19 – 7.20 and 7.30 – 7.31 into eqn. 7.21 results in:

$$G_i = \frac{(1+4\varepsilon^2)}{D^2 E^* cosh^2(\pi\varepsilon)}(\delta_x^2 + \delta_y^2) \qquad 9.7$$

It is seen from eqn. 9.7 that for a given overlay pavement system and for a chosen characteristic length and node on the crack face, interfacial ERR is linearly proportional to the value of $(\delta_x^2 + \delta_y^2)$ for two-dimensional interfacial crack. For three-dimensional interfacial crack, it is reasonable to deduce that the interfacial ERR is linearly proportional to the value of $(\delta_x^2 + \delta_y^2 + \delta_z^2)$, i.e. the equations below hold:

$$G_i^{(I+II)} \propto (\delta_x^2 + \delta_y^2) \qquad 9.8$$

$$G_i^{(I+II+III)} \propto (\delta_x^2 + \delta_y^2 + \delta_z^2) \qquad 9.9$$

$$G_i^{(I+II)} = G_I + G_{II} \qquad 9.10$$

$$G_i^{(I+II+III)} = G_I + G_{II} + G_{III} \qquad 9.11$$

where G_I , G_{II} and G_{III} are the energy release rates for mode-I, mode-II and mode-III (see Figure 9-11), respectively; $G_i^{(I+II)}$ is the total interfacial ERR for two-dimensional crack, containing ERRs for mode-I and mode-II; $G_i^{(I+II+III)}$ is the total interfacial ERR for three-dimensional crack, containing ERRs for mode-I, mode-II and mode-III; δ_x, δ_y and δ_z are the relative opening, sliding and tearing displacements of both crack surfaces (see Figure 9-11 and Figure 9-12). Therefore, the value of $(\delta_x^2 + \delta_y^2)/(\delta_x^2 + \delta_y^2 + \delta_z^2)$ is equal to the ratio of $G_i^{(I+II)}$ to $G_i^{(I+II+III)}$, given by:

$$\frac{G_i^{(I+II)}}{G_i^{(I+II+III)}} = \frac{\delta_x^2+\delta_y^2}{\delta_x^2+\delta_y^2+\delta_z^2} \quad 9.12$$

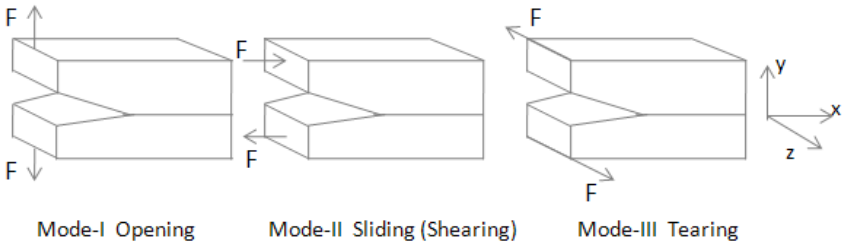

Figure 9-11 Cracks subjected to opening loading, sliding loading and tearing loading

The overlay pavement system shown in Figure 9-12(a), with a 20mm-long interfacial crack subjected to the 190kN-axle load was analysed to obtain the displacements of nodes 1 and 1′. The nodes 1 and 1′ (see Figure 9-12(c)), purposely created in the upper and lower faces of the crack respectively, in the model shown in Figure 9-12(a) were 1 mm behind the crack tip, and very close to each other in y – direction. The displacements of the two nodes were extracted for further calculation. The relative displacements were calculated using the equations below:

$$\delta_x = |u_{1x} - u_{1'x}| \quad 9.13$$

$$\delta_y = |u_{1y} - u_{1'y}| \quad 9.14$$

$$\delta_z = |u_{1z} - u_{1'z}| \quad 9.15$$

where u_{1x}, u_{1y}, u_{1z}, $u_{1'x}$, $u_{1'y}$ and $u_{1'z}$ are the displacements of node 1 and 1′ in x, y and z directions respectively, extracted from the model shown in Figure 9.12(a).

For the overlay pavement system shown in Figure 9-12(a), the mechanical properties of the two materials are shown in Table 9-1. The calculated relative displacements of nodes 1 and 1′, using finite element code ANSYS 12.0, are tabulated in Tables 9-6 and 9-7. Analysing the calculated relative displacements listed in the two tables, the following conclusions can be summarised:

(1) The interfacial crack experiences opening and sliding and tearing deformations under the vehicular loading. In all cases, the relative opening displacement δ_y is much larger than the relative sliding displacements δ_x, and the relative tearing displacements δ_z are much smaller than both the opening and sliding relative displacements.

(2) The ratio of $(\delta_x^2 + \delta_y^2)/(\delta_x^2 + \delta_y^2 + \delta_z^2)$ is very close to 1 for overlay with the thickness of 50 mm and 150 mm, for elastic foundation with the modulus varying in the

range of 37 MPa to 500 MPa, indicating that the interfacial ERR G_{III} dissipated in tearing mode is negligible, and thus the crack is likely to extend in *x*-direction in *x*-*y* plane. This validates the interfacial ERRs obtained in Section 9.1.2.

(3) The interfacial crack really experiences opening and sliding deformation under the vehicular action, i.e. mode-I loading and mode-II loading, although the pavement system is supported by the elastic foundation. This also validates the test beam and loading configuration for measuring the interfacial fracture toughness of bi-material beam in flexure for concrete overlay pavement design, illustrated in Figures 7-23 (b) and 7-24 (a), in which a bi-material beam with interfacial crack exhibited opening and sliding deformation under three-point bending test, previously presented in Section 7.3.2.1.

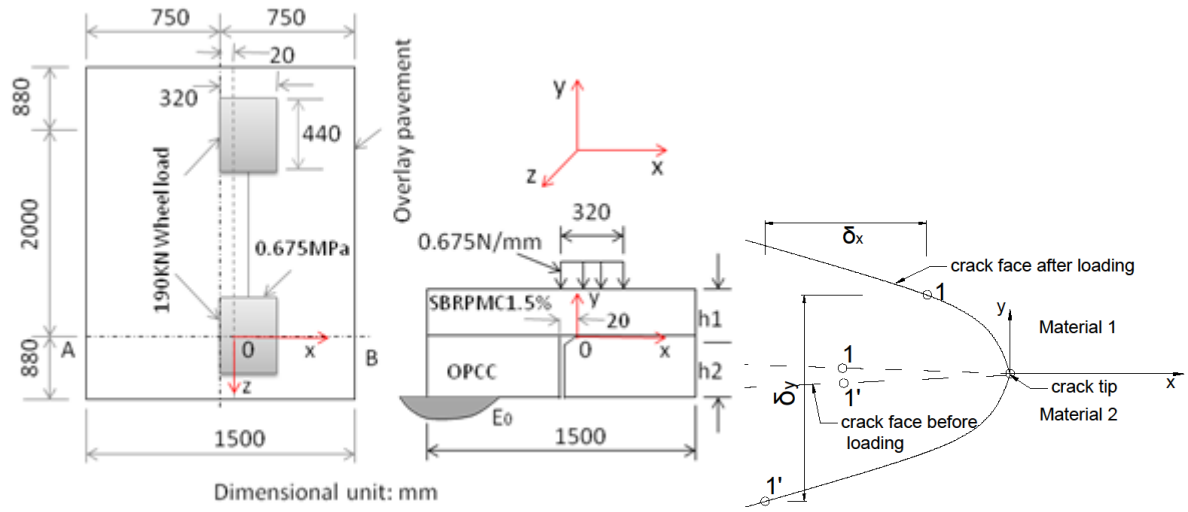

(a) (b) (c)

Figure 9-12 (a) SBRPMC1.5%-35 overlay on OPCC pavement with an interfacial defect through width ,subjected to 190kN axle loading, (b) cross – section of AB, (c) the relative position of two nodes in the vicinity of crack tip before loaded and after loaded

Table 9-6 Relative displacements of interfacial crack face of overlay pavement subjected to 190kN – axle load (E_1=32365MPa, ν_1=0.187, h_1=150mm; E_2=25200MPa, ν_2=0.21, h_2=200 mm)

Stiffn. of found.		h_1=150 mm, h_2=200 mm					
E_0	K_0	δ_x	δ_y	δ_z	$\delta_x^2+\delta_y^2$	$\delta_x^2+\delta_y^2+\delta_z^2$	$(\delta_x^2+\delta_y^2)/(\delta_x^2+\delta_y^2+\delta_z^2)$
MP	N/mm^3	X 10^{-3} mm	X 10^{-3} mm	x 10^{-4} mm	x $10^{-6}mm^2$	x $10^{-6}mm^2$	
37	0.068	0.154	0.99	0.1295	1.003816	1.003984	0.999833
50	0.092	0.176	0.98	0.1281	0.991376	0.991540	0.999835
100	0.184	0.202	0.97	0.1246	0.981704	0.981859	0.999842
200	0.37	0.2062	0.93	0.1221	0.907418	0.907568	0.999836
400	0.74	0.1933	0.874	0.1229	0.801241	0.801392	0.999812
500	0.92	0.1861	0.851	0.1241	0.758834	0.758988	0.999797

Table 9-7 Relative displacements of interfacial crack face of overlay pavement subjected to 190kN – axle load (E_1=32365MPa, ν_1=0.187, h_1=50mm; E_2=25200MPa, ν_2=0.21, h_2=200 mm)

Stiffn. of found.		h_1=50 mm, h_2=200 mm					
E_0 MPa	K_0 N/mm^3	δ_x X 10^{-2}mm	δ_y X 10^{-2}mm	δ_z x 10^{-4}mm	$\delta_x^2+\delta_y^2$ x 10^{-4}mm^2	$\delta_x^2+\delta_y^2+\delta_z^2$ x 10^{-4}mm^2	$(\delta_x^2+\delta_y^2)/(\delta_x^2+\delta_y^2+\delta_z^2)$
37	0.068	0.3065	0.406	0.103	0.258778	0.258779	0.999996
50	0.092	0.2911	0.385	0.111	0.232964	0.232965	0.999995
100	0.184	0.2445	0.327	0.134	0.166709	0.166711	0.999989
200	0.37	0.1904	0.261	0.16	0.104373	0.104376	0.999975
400	0.74	0.1422	0.202	0.175	0.061025	0.061028	0.999950
500	0.92	0.1294	0.187	0.1821	0.051713	0.051717	0.999936

9.1.4 Discussion and Summary

The calculation results listed in Tables 9-3 – 9-5 are rearranged and discussed in the following:

Interfacial ERRs induced by different axle loads

Table 9-8 and Figure 9-13 show the interfacial ERRs of 100mm-thick SBRPMC1.5%-35 overlay on 200mm-thick OPCC base pavement induced by 80kN – axle, 2 x 120kN – axle and 190kN – axle loads. They demonstrate that 190kN – axle load produces much higher interfacial ERRs than the 80kN - axle load and 2 x 120kN - axle load, for the same overlay pavement. For the pavement system of 100mm-thick SBRPMC1.5%-35 overlay on 200mm-thick OPCC base, the ERRs induced by 190kN – axle for the overlay pavements on weak foundation (the modulus is less than 100 MPa) is lower than the average interfacial fracture toughness measured from the composite beam with smooth interface listed in Table 9-1, but exceeds the minimum one, which was in the range of 10.3 J/m to 28.9 J/m^2 (Table 7-12), while the interfacial ERRs are much lower than the interfacial fracture toughness, which is 52 J/m^2, measured from the roughened interface composite beams. This implies that the roughening treatment of the surface of existing concrete pavement is necessary.

Table 9-8 Calculated ERRs of the interface of the overlay pavement system shown in Figures 9-3(a), 9-8(a) and 9-10(a) subjected to 80kN-axle, 2x120kN-axle and 190kN-axle loads (h_1=100mm, h_2=200mm)

E_0	K_0	80kN axle	2 x 120kN axle		190kN axle	
(MPa)	(N/mm^3)	G_i (J/m^2)	G_i (J/m^2)	ψ_G (Deg.)	G_i (J/m^2)	ψ_G (Deg.)
37	0.068	2.69	4.1	3.51	12.7	7.37
50	0.092	2.57	3.8	4.02	12.2	6.18
100	0.184	2.1	3.1	3.69	10.2	7.16
200	0.37	1.57	2.0	2.76	7.4	7.09
400	0.74	1.01	1.3	2.40	4.8	7.46
500	0.92	0.46	1.2	2.40	4.1	6.77

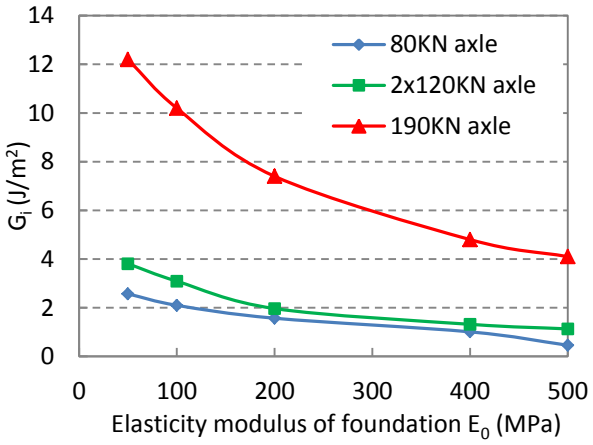

Figure 9-13 Interfacial ERRs of 100mm-thick SBRPMC1.5%-35 overlay on 200mm-thick OPCC base vs. elastic modulus of foundation subjected to three types of vehicular axle loads

Interfacial ERR affected by overlay thickness

Further investigation was conducted to reveal the overlay thickness effect on the interfacial ERR in this study. The pavement consisted of SBRPMC1.5%-35 overlay and 200mm-thick OPCC base, subjected to 190kN – axle load. The calculated interfacial ERRs for overlay thickness of 50mm, 100mm and 150mm are listed in Table 9-9 and plotted in Figure 9-14. It is seen that: (1) the interfacial ERRs considerably decrease with the increase in overlay thickness and in elastic modulus of foundation; (2) the 50mm-thick overlay pavement exhibits very high interfacial ERR in the overlay pavements on weak foundations, even exceeding the interfacial fracture toughness of roughened interface composite specimen, which is 52 J/m^2 listed in Table 9-1. Therefore, thin overlay (less than 100mm) should not be considered in overlay pavement design to avoid interfacial delamination, induced by heavy vehicular loading.

Table 9-9 Interfacial ERR of the overlay pavement system with different overlay thicknesses subjected to 190kN-axle load (h_2=200 mm)

E_0 (MPa)	K_0 (N/mm^3)	h_1=50 mm G_i(J/m^2)	ψ_G(Deg.)	h_1=100 mm G_i(J/m^2)	ψ_G(Deg.)	h_1=150 mm G_i(J/m^2)	ψ_G(Deg.)
37	0.068	53.4	7.40	12.7	7.37	5.4	10.38
50	0.092	45.1	7.44	12.2	6.18	4.9	9.02
100	0.184	28.2	6.10	10.2	7.16	4.6	9.50
200	0.37	17	6.18	7.4	7.09	3.9	9.46
400	0.74	9.7	6.08	4.8	7.46	3	10.01
500	0.92	8	6.06	4.1	6.77	2.7	10.05

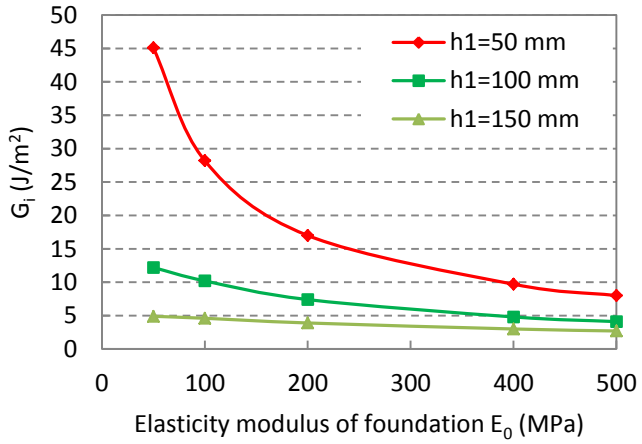

Figure 9-14 Interfacial ERRs of SBRPMC1.5% overlay on OPCC pavement system subjected to 190kN – axle load at different overlay thicknesses (h_2=200mm)

Phase angles for interfacial ERR

Table 9-10 shows the calculated interfacial ERRs and phase angles of the 100mm–thick SBRPMC1.5%-35 overlay on 200mm-thick OPCC base, as well as a series of modulus of elasticity representing the foundation, and two types of axle loads. The phase angles were obtained by analysing the two-dimensional models illustrated in Figures 9-8(c) and 9-10(c). According to the definition of phase angle for interfacial ERR, the tangent value of phase angle is equal to the ratio of the interfacial ERR dissipated in sliding and opening mode, respectively; given by

$$\frac{G_{II}}{G_I} = \tan(\psi_G) \qquad 9\text{-}16$$

where G_I and G_{II} are the interfacial ERRs in opening mode and sliding mode, respectively; ψ_G is the phase angle. Table 9-10 presents that, the mean phase angles for 2 x 120kN - axle load and 190kN - axle load are 3 and 7 degrees, respectively; implying that the G_{II} is about 5% G_I for the 2 x 120kN - axle loading, and the G_{II} is about 12% G_I for the 190kN - axle loading. This indicates that the interfacial crack of overlay pavement system subjected to vehicular loading suffers mainly from opening damage, and that the damage due to sliding is much smaller than that of opening damage. Consequently, from the investigation point of view the appropriate test for evaluating the interfacial bond quality is splitting test instead of direct shear test.

Table 9-10 Calculated interfacial ERRs and phase angles of the interface of the overlay pavement system shown in Figures. 9-8(a) and 9-10(a) subjected to 2 x 120kN-axle and 190kN-axle load (h_1=100mm, h_2=200mm)

E_0 (MPa)	K_0 (N/mm^3)	2x120kN axle G_i (J/m^2)	ψ_G (Deg.)	190kN axle G_i (J/m^2)	ψ_G (Deg.)
50	0.092	3.8	4.02	12.2	6.18
100	0.184	3.1	3.69	10.2	7.16
200	0.37	2.0	2.76	7.4	7.09
400	0.74	1.3	2.40	4.8	7.46
500	0.92	1.1	2.40	4.1	6.77

9.2 Overlay Thickness Designs

It has been described in Chapter 2 that 'Guide to Concrete Overlays', recommended by the National Concrete Pavement Technology Centre of the USA (NCPTC USA 2008), provides a procedure of evaluating existing concrete pavement and the thickness design method for the conventional concrete overlay. Recently, Altoubat et al. (2008) proposed a thickness design method for SFRC pavements, which converted flexural strength of SFRC into the equivalent flexural strength of OPCC. The standard equivalent flexural strengths of six mixes have been presented in Section 5.3.3, and are relisted in Table 9-11 for convenience. As it has been discussed in Section 5.5, the mix SBRPMC1.5%-35 was deemed to be the optimum. It is worth noting that the concept of equivalent flexural strength did not take the steel fibre effect on the fatigue life into account.

It is not intended for this study to further investigate the thickness design method. This study adopts the thickness design method recommended by NCPTC USA 2008 and the equivalent flexural strength concept for the design of the steel fibre-reinforced roller-compacted polymer modified concrete bonded overlay.

It should be noting that the thickness design method for SFR-RC-PMC overlay presented above should be regarded as an expedience; and further specific investigation is needed.

Table 9-11 Standard equivalent flexural strengths $f_{e,3}$ of six mixes

Mix ID	Equivalent flexural strength $f_{e,3}$ (Mpa)
SBRPMC1%-35	5.93
SBRPMC1.5%-35	7.27
SBRPMC2%-35	9.4
Con.SBRPMC1.5%-35	6.79
SBRPMC1.5%-50	9.53
PVAPMC1.5%-35	6.49

9.3 Summary

The main conclusions drawn from the above are presented below, while the specific conclusions can be found at the end of each sub-sections.

(1) A calculation procedure for the interfacial strain energy release rate of the overlay pavement system is proposed, in which a three-dimensional pavement system is converted to two-dimensional model via a theoretical approach. The simplified method for calculating the interfacial ERR of overlay pavement, proposed by the study, was validated.

(2) For the typical overlay pavement system, the interfacial energy release rate of the concrete overlay pavement system induced by the heavy axle of the lorry exceeds the measured interfacial toughness of SBRPMC1.5%-35 -on- OPCC with smooth interface. Thus, the surface treatment of old concrete pavements is necessary for bonded concrete overlay, even if the overlay material is the mix SBRPMC1.5%, which contains the SBR polymer to enhance the bond strength.

(3) For the typical overlay pavement system, the interfacial ERR induced by 190kN–axle loading considerably decreases with the increase in overlay thickness and in elastic modulus of foundation; the 50mm-thick overlay exhibits much high interfacial ERR in the overlay pavements on weak foundations, even exceeding the interfacial toughness of roughened interface composite specimen. Therefore, thin overlay (less than 100mm) should be avoided in overlay pavement design due to interfacial delamination problem, induced by heavy vehicular loading.

(4) The interfacial crack overlay pavement subjected to vehicular loading really experiences opening and sliding deformation under the vehicular action, i.e. mode-I loading and mode-II loading, although the pavement system is supported by the elastic foundation; and the tearing deformation is negligible.

(5) For the typical overlay pavement system, an interfacial crack subjected to vehicle load suffers mainly from opening damage. The sliding damage is much smaller than the opening damage. Namely, the ERR for sliding is only about 3% - 12% the ERR for opening. Consequently, from the engineering point of view the appropriate test for evaluating the interfacial bond quality in fields is splitting tensile test instead of direct shear test.

(6) An expedient thickness design method for steel fibre-reinforced, roller-compacted, polymer modified concrete bonded overlay is proposed, which combines the design method

recommended by NCPTC of USA (2008) for plain concrete overlay and the equivalent flexural strength concept for the conversion of SFRC strength into plain concrete strength.

10 Conclusions

The main intention of this thesis was to develop a design method for mixes of high bond strength, suitable for placement by asphalt pavers and compaction by rollers, and to reveal its flexural performance. With that general aim in mind, during the progress of the research, the two main objectives were achieved. In addition to the main objectives, a method for establishing a fibre bridging law was developed, and a simple method for calculating the interfacial energy release rate of the composite specimen and concrete overlay pavement system with the aid of FEA was proposed. These findings provide deeper insight into the flexural behaviour and interfacial delamination performance.

This chapter summarises the main contributions of the thesis, and presents the constraints of the conclusions drawn from the research. Finally, a series of suggestions are proposed for possible further studies.

10.1 Scientific Contributions of the Thesis

Detailed conclusions were presented at the end of each chapter; the major scientific contributions of the research are presented in below:

10.1.1 Mixes and Mix Design Method

1. A new mix design method for determining the optimal water content, the modified-light (M-L) compaction method, was proposed for steel fibre-reinforced, roller-compacted, polymer modified, bonded concrete overlays. This method employs devices of the Standard Proctor compaction test and a compaction effort of 4 layers and 20 hammer blows for each layer. The mixes designed by this method have high bond strength with the concrete substrate, and at the same time are suitable to be placed by an asphalt paver and compacted by a roller.

This M-L method for determining the optimal water content was experimentally validated when both dry density of the dry density of the mix and the splitting tensile strength of compacted samples reached maximum simultaneously at the same water content. Furthermore, the bond strength criterion (splitting tensile bond strength of 2.17 MPa) for the investigation of mix design was experimentally verified by suitable tests of PMC-on-OPCC composite beams under four-point bending regimes, i.e. the interface of composite beams

with roughened interface did not separate, while interfacial debonding actually occurred when the bond strength was lower than 2.17 MPa.

2. Mixes having high flexural and bond strengths and appropriate workability for placement by asphalt pavers and compaction by roller were developed and are listed in Table 5-1. Mix SBRPMC1.5%-35 was deemed to be optimal for both strength and workability. Mix PVAPMC1.5%-35 exhibited very high flexural and bond strengths, but not so good workability and toughness.

The special mixes developed in this study exhibited much higher bond strengths with OPCC than OPCC-to-OPCC. Splitting tensile strengths measured from the prisms cut from tested composite beams with rough interface (Table 7-7) were 2.96 MPa for SBRPMC1.5%-35-on-OPCC and 3.70 MPa for PVAPMC1.5%-35-on-OPCC, while that of OPCC-on-OPCC was 2.68 MPa.

10.1.2 Flexural Strength and Fibre Efficiency

3. The flexural strengths of SFR-RC-PMC beams formed with five mixes under three-point bending, i.e. SBRPMC1.0%-35, SBRPMC1.5%-35, SBRPMC2%-35, SBRPMC1.5%-50 and PVAPMC1.5%-35, were extensively investigated in the laboratory, and are listed in Table 5-4. The equivalent flexural strengths of four mixes (Table 5-8), were evaluated using the method developed in this study. These equivalent strengths can be directly used in overlay thickness design, which was proposed by Altoubat et al. (2008).

4. Mix SBRPMC1.5%-35 was deemed to be the optimal for both flexural strength and workability. Compared to the conventional steel fibre-reinforced polymer-modified concrete, Con.SBRPMC1.5%-35, the maximum flexural and standard flexural strengths of mix SBRPMC1.5%-35 are 1.47 and 1.07 times those of the former. Compared to unreinforced plain concrete (OPCC), mix SBRPMC1.5%-35 developed 3.3 times the maximum flexural strength and 1.56 times the equivalent flexural strength than the OPCC (MOR=4.66MPa, listed in Table 4-14).

5. The efficiency of steel fibre in SFR-RC-PMC is higher than that in conventional SFRC (Table 6-11), indicating the former being economically viable compared to the latter, which has been widely used in engineering applications.

10.1.3 Fibre Bridging Law

6. A new method for establishing a fibre bridging law in flexure using inverse analysis was developed. The fibre bridging law consisted of two phases: the initial phase was set up by the fracture mechanics method before hinge formation, and the second phase was established by the material mechanics method utilised after hinge formation. The fibre bringing law established by the method proposed is able to properly simulate the flexural performance of SFRC beam, and has been experimentally verified. The calculation procedure for establishing the fibre bridging law is presented in Section 6.2.3 in detail.

7. Fibre bridging laws for the three mixes SBRPMC1.5%-35, SBRPMC1.5%-50 and Con.SBRPMC1.5%-35 were established using the inverse analysis method proposed, and listed in Table 6-7. The combination of fibre bridging law established by this study and the size effect law described by Equation 5.22 can properly predict the flexural behaviour of the SFRC beam, and thus can be regarded as a material property.

10.1.4 Calculation of Interfacial Energy Release Rate and Measurement of Interfacial fracture Toughness

8. A new simple method for calculating the interfacial energy release rate by using the finite element code ANSYS was proposed and verified by comparison with the existing analytical solutions. This method can be readily and easily used by engineers. The calculation procedure is presented in Section 7.3.1 in detail.

9. A test specimen and loading configuration for measuring interfacial fracture toughness for concrete overlay pavement was developed. The measured interfacial fracture toughness of SBRPMC1.5%-35-on-OPCC composite beam was 52 J/m^2 and 22.6 J/m^2 for rough and smooth interfaces, respectively. They can be used in PMC overlay design.

10.1.5 Interfacial Energy Release Rate of Concrete Overlay Pavement

10. A new method for calculating strain energy release rate (ERR) at the interface of concrete overlay pavement system was also proposed. The three-dimensional concrete overlay pavement system can be theoretically converted to two-dimensional model using this method. A typical concrete overlay pavement subjected to various vehicular loadings was analysed using the proposed method. The calculation of the ERRs at interface of SBRPMC1.5%-on-OPCC pavement system induced by vehicular loading showed that:

(a) Thin overlay (thickness less than 100mm) subjected to heavy axle (190kN) exhibited very high ERRs, even higher than the interfacial toughness of composite specimens with roughened interface, and therefore in overlay design, thin overlays should be avoided. Also, surface treatment of the old concrete pavement should be considered for bonded overlay pavements.

(b) Splitting tensile test is an appropriate test for evaluating bond quality of concrete overlay pavement, whereas the direct shear test is not.

(c) For the typical overlay pavement system subjected to vehicular loading, the interfacial crack suffers mainly from opening damage. The opening damage is much higher than both sliding and tearing damages, i.e., the ERR for sliding is only about 3% - 12% the ERR for opening, while the ERR for tearing is so small that is negligible.

10.1.6 Flexural Behaviour of Beams on Elastic Foundation

11. The applicability of Parmerter's theory (Parmerter 1976) on a foundation model was investigated. The results indicate that the flexural performance of OPCC beam on elastic foundation can be simulated using Parmerter's theory and Winkler's foundation model, whereas SFRC beam can be simulated more rigorously by the elastic solid foundation model instead of Winkler foundation.

10.2 The Thesis Constraints

The limitations of this research are identified below:

Ingredient materials and mixes

1 All the experimental results were measured using the materials and test methods previously presented. Some of the materials are local, such as coarse aggregate, sand, cement and PFA, which may exhibit specific characteristics.

Experimental results

2. All experiments were carried out to measure the static mechanical properties, while the material in overlay pavements is under the cyclic and dynamic action of vehicles.

3. All specimens of steel fibre-reinforced roller compacted polymer modified concrete were formed by the vibrating compactor, used in field work but specially modified for the research project.

4. All conclusions were drawn from the experimental results in the laboratory and theoretical analysis, and have not been validated with full-scale field tests.

10.3 Further Work

The following are indications for possible future work in the research field addressed in this study.

1. Test road is needed to verify the mixes proposed by the study and develop the construction method, especially the construction procedure for obtaining good bond with existing concrete pavements.

2. The moisture loss during construction, such as moisture evaporation and cement hydration, should be considered in mix design for an actual engineering project. Retarder for slowing down cement hydration may be needed for workability stabilisation.

3. The overlay thickness design method needs further investigation. The simplified overlay thickness design method proposed by Altoubat et al. (2008) is based on OPCC overlay thickness design, in which the fibre effect is taken into account by adopting a simplified method. The fatigue life of fibres has not been considered, and it should thus be regarded as an expedient method, hence further investigation is needed.

4. How the steel fibre content affects flexural performance of SFRC beam on elastic foundation needs further experimental investigation.

5. Stress analysis of the bonded overlay pavement system needs further extensive investigation, probably using advanced numerical technology.

References

AASHTO, 1993, Guide for Design of Pavement Structures, American Association of State Highway and Transportation Officials.

Abdalla, H.M.; Karihaloo, B.L.;2003, Determination of size-independent specific fracture energy of concrete from three-point bend and wedge splitting tests, Magazine of Concrete Research, v 55, n 2, p 133-141.

ACI Committee 207, 1999, Roller-Compacted Mass Concrete (ACI 207.5R-99), ACI, USA.

ACI Committee 211, 2002, Guide for selecting proportions for no-slump concrete (ACI 211.3R-02), ACI, USA.

ACI Committee 360R-92 (Reapproved 1997), 1997, Design of Slabs on Grade, USA.

ACI Committee 544, 1988, Measurement of properties of fibre-reinforced concrete, ACI Materials Journal, 85(1988), 583-593.

ACI Committee 544.2R-89, 1988, Measurement of properties of fibre-reinforced concrete, Reapproved in 2009.

ACI Committee 548, 2003, Polymer-Modified Concrete (ACI 548.3R-03), USA.

Altoubat, S.A; Roesler, J.R.; Lange, D.A.; Rieder, K. A.; 2008, Simplified method for concrete pavement design with discrete structural fibres, Construction and building materials, 22 (2008) 384-393.

ANSYS 12.0, 2009, SAS *IP* Inc.

Armelin, H.S.; Banthia, N.; 1997, Predicting the flexural post-cracking performance of steel fibre reinforced concrete from the pullout of single fibres, ACI Materials Journal, V.94, No.1, January- February, 1997, pp.18-31.

ASTM C 1170-06, 2006, Standard test method for determining consistency and density of roller-compacted concrete using a vibrating table, ASTM Committee C09, USA.

ASTM C 1176-05, 2006, Standard practice for making roller-compacted concrete in cylinder moulds using a vibrating table, ASTM Committee C09, USA.

ASTM C 138/C138M-01a, 2001, Standard test method for density (unit weight), yield, and air content (Gravimetric), ASTM Committee C09, USA.

ASTM C 1435/C 1435M-06, 2006, Standard practice for moulding roller-compacted concrete in cylinder moulds using a vibrating hammer, ASTM Committee C09, USA.

ASTM C 1439-99, 1999, Standard test methods for polymer-modified mortar and concrete, ASTM Committee C-9, USA.

ASTM C 1609/C 1609M-06 (2006); 2006, Standard Test Method for Flexural Performance of Fiber-Reinforced Concrete (Using Beam with Third-Point Loading), ASTM International, USA.

ASTM Committee C-9 and C099.44 1999, Standard test methods for polymer-modified mortar and concrete (ASTM C 1439-99$^{\varepsilon 1}$), USA.

ASTM C 1018-92, 1992, Standard Test Method for Flexural Toughness and First-Crack Strength of Fiber Reinforced Concrete(using Beam with Third-Point Loading), , ASTM Annual Book of Standards,Vol.*04.22*, ASTM Philadelphia, USA, 1992, pp. 510-516.

Baggott, R.; Abdel-monem, A.E.S., 1992, Aspects of bond in high volume fraction steel fibre reinforced calcium silicates, High Performance Fibre Reinforced Cement Composites, 15th Proceedings of RILEM and ACI workshop, Edited by H.W. Reinhard and A. E. Naanman.

Ballarini, R.; Shah, S.P.; Keer, L.M.; 1984, Crack growth in cement-based composites, Engineering Fracture Mechanics, Vol.20, No.3, pp.433-445.

Banthia, N.; Trottier, J.F.; 1995a, Test method for flexural toughness characterization of fibre reinforced concrete: some concerns and a proposition, ACI Materials Journal, V.92, No.1, pp.48-57.

Banthia, N.; Trottier, J.F.; 1995b, Concrete reinforced with deformed steel fibres Part II: Toughness characterization, ACI Materials Journal, V.92,No.2, pp.146-154.

Bazant, Z. P., Chen, E. P., 1997, Scaling of structural failure, Applied Mechanics Reviews, v 50, n 10, p 593-627.

Bazant, Z.P., 1989, Fracture energy of heterogeneous materials and similitude, in Fracture of Concrete and Rock, edited by Shah, S.P., and Swartz, S.E., Pringer-Verlag, New York, 1989, pp.229-241.

Bazant, Z.P.; Kazemi, M.T., 1990, Determination of fracture energy, process zone length brittleness number from size effect, with application to rock and concrete, International Journal of Fracture, Vol.44, pp.111-131.

Bazant, Z.P.; Pfeiffer, P.A., 1987, Determination of fracture energy from size effect and brittleness numbers, ACI Materials Journal, Vol.84, No.6, pp.463-480.

Bazant,Z.P., 1984, Size effect in blunt fracture: concrete, rock, metal.Journal of Engineering Mechanics, Vol. 81, N. 5, pp. 456-468.

Belletti, B.; Cerioni, R.; Meda, A.; Plizzari, G.; 2008, Design aspects on steel fibre-reinforced concrete pavements, Journal of Materials in Civil Engineering, Vol. 20,No. 9, pp.599–607.

Bjerkén, C.; Persson, C.; 2001, A numerical method for calculating stress intensity factores for interface cracks in biomaterials, Engineering Fracture Mechanics, 68 (2001) 235-246.

British Standard BS EN 12390-6:2009, Testing hardened concrete Part 6: Tensile splitting strength of test specimens, British Standard Institute, UK.

British Standard BS EN 12390-7:2009, Testing hardened concrete Part 7: Density of hardened concrete, British Standard Institute, UK.

British Standard BS EN14651:2005+A1:2007, Test method for metallic fibre concrete — Measuring the flexural tensile strength (limit of proportionality (LOP), residual), British Standard Institute, UK.

British Standard BS EN1997-2:2007, Geotechnical design, Ground investigation and testing.

British Standard, BS 1377-4:1990, 2002, Methods of test for Soils for civil engineering purposes—part 4: Compaction-related tests, British Standard Institute, UK.

British Standard, BS 598-105:1990, 1998, Sampling and examination of bituminous mixtures forroads and other pavement areas- part 105: Methods of tests for determination of texture depth, UK.

British Standard, BS 812: Part 2: 1995, Testing aggregates- Part 2. Methods of determination

British Standard, BS EN 1991-2:2003, Eurocode 1: Actions on structures, part 2: Traffic loads on bridges.

British Standard, BS812-110.1990; Testing aggregates -Part 110: Methods for determination of aggregate crushing value (ACV), British Standard Institute, UK.

Broek, D., 1986; Elementary Engineering Fracture Mechanics, 4th rev.ed.,MartinusNijhoff, Dordrecht, The Netherlands, 1986.

Büyüköztürk, O.; Lee, K.M.; 1993, Assessment of interfacial fracture toughness in concrete composite, Cement and Concrete Composite, 15(1993) 143-151.

Carpinteri, A.; Ferro, G.; 1994, Size effects on tensile fracture properties: a unified explanation based on disorder and fractality of concrete microstructure, Materiaux et constructions, v 27, n 174, p 563-571.

Chabot, A.; Hun, M.; Hammoum, F., 2013, Mechanical analysis of a mixed mode debonding test for 'composite' pavements, Construction and Building Materials 40 (2013) 1076–1087.

Charalambides, P.G.; Lund, J.; Evans, A.G.; McMeeking, R.; 1989; A test specimen for determining the fracture resistance if biomaterial interfaces, Journal of Applied Mechanics, Vol. 56, pp. 77 – 82.

Cox, B.N. and Marshall D.B.; 1991, Stable and unstable solutions for bridged cracks in various specimens, Acta, Metallic materials, Vol.39, No.4, pp.579-589.

Croney, D.; Croney, P.; 1998, Design and performance of road pavements, third edition, McGraw-Hill Companies, Inc, 1998.

Delatte, N. J.; Sehdev, A.; 2003, Mechanical properties and durability of bonded-concrete overlays and ultrathin white-topping concrete, Journal of Transportation Engineering, 2003, pp.16-23.

Delatte, N.J.; 1998; Investigating performance of bonded concreteoverlays, Journal of performance of constructed facilities, May 1998, pp.62-70.

Denneman, E.; Wu, R.; Kearsley, E.P.; Visser, A.T.; 2011, Discrete fracture in high performance fibre reinforced concrete materials, Engineering Fracture Mechanics, 78 (2011) 2235-2245.

Falkner, H.; Huang, Z.; Teutsch, M.; 1995, Comparative study of plain and steel fibre reinforced concrete ground slabs, Concrete International, Jan. 1995, pp.45-51.

Filho, J.,M.; Paulon, V.A.; Monteiro, P.J.M.; Andrade, W.P.D.; 2008,Development of laboratory device to simulate roller-compacted concrete placement, ACI Materials Journal, March-April 2008, Vol.105, No.2, pp125-130.

Foote, R.M.L.; Mai, Y.W.; Cotterell, B.; 1986, Crack growth resistance curves in strain-softening materials, Journal of Mechanics and Physics of Solids, Vol. 34, No.6, pp.593-607.

Fwa, T.F.; 1991, Remaining-life consideration in pavement overlay design, Journal of Transportation Engineering, November/December, 1991, Vol. 117, No.6, pp.585-601.

Gaedicke, C.; Roesler, J.; 2009, Fracture-based method to determine the flexural load capacity of concrete slabs, Department of Civil and Environmental Engineering, University of Illinois at Urbana-Champaign.

Gallagher, A.P., 1983, Bending a free beam on an elastic foundation, ASME Journal of Applied Mechanics, Vol.50, pp. 463-465.

Gere, J.M.; Timoshenko, S.P.; 1999, Mechanics of Materials, Stanley Thornes Ltd, UK.

Giaccio, G.; Tobes, J.M.; Zerbino, R.; 2008, Use of small beams to obtain design parameters of fibre reinforced concrete, Cement and Concrete Composites, v 30, n 4, pp. 297-306.

Gopalaratnam, V. S.; Shah, S. P.; Batson, G. B.; Criswell, M. E.; Ramakrishnan, V.; Wecharatana, M., 1991, Fracture toughness of fibre reinforced concrete, ACI Materials Journal, v 88, n 4, pp. 339-353.

Gotlif, A.; Mallela, J.; Khazanovich, L.; 2006, Finite element study of partial-depth cracks in restrained PCC slabs, International Journal of Pavement Engineering, Vol. 7, No. 4, 2006, 323–329.

Guo, X.H.; Tin-Loi, F.; Li, H.; 1999, Determination of quasi-brittle fracture law for cohesive models, Cement and Concrete Research, 29 (1999) pp. 1055-1059.

He, M.Y.; Hutchinson, J.W.; 1989, Crack deflection at an interface dissimilar elastic materials,International Journal of Solids and Structures, Vol. 25, No. 9, p 1053-1067.

Hetenyi, M.; 1946, Beams on elastic foundation, University of Michigan Press, Ann Arbor, Michigan, USA.

Highway Agency, UK, 2013, Design Manual for Roads and Bridges.

Huang, Z.; Suo, Z.; Xu, G.; He, J.; Prevost, J.H.; Sukumar, N. 2005, Initiation and arrest of an interfacial crack in a four-point bend test, Engineering Fracture Mechanics 72 (2005) 2584–2601.

Hughes, B.P.; 2006, Optimum design of sustainable concrete Pavements, Proceedings of

Institute of Civil Engineers, Engineering Sustainability 159, September 2003, pp. 127-132.

Hughes, B.P.; Karadelis, J.; 2007, Discussion: Optimum design of sustainable concrete pavements, Proceedings of Institute of Civil Engineers, March 2007.

Hughes, B.P.; Lubis, B.; 1996, Roller compacted sheets of polymer modified mortar, Cement and Concrete Composites, 18(1996), pp41-46.

Illinois Department of Transportation, 2002, Bonded Concrete Overlay Performance in Illinois, USA.

Illinois Department of Transportation, Bureau of Materials and Physical Research, 2005, Pavement Technology Advisory-Bonded Concrete Overlay-PTA-M3. International Journal of Fracture, v 95, n 1-4, pp. 379-390.

Ioannides, A., 2006, Concrete pavement analysis: the first eighty years, International Journal of Pavement Engineering, December 2006, Vol. 7, No. 4, 233–249.

Irwin, G.R., Fracture, Handbuch der Physic. 6, 551 (1958).

Japan Society of Civil Engineers JSCE-SF4 (1984), Methods of tests for flexural strength and flexural toughness of steel fibre reinforced concrete, Concrete Library International, Part III-2, No.3; 1984, pp. 58-61.

Jayawickrama, P.W.; Lytton, R.L.; 1987, Methodology for predicting asphalt concrete overlay life against reflection cracking, Proceedings of the 6th International Conference on Structural Design, Vol.1 PT, pp. 912-924.

Jeng, F.; Lin, M.L.; Yuan, S.C.; 2002, Performance of toughness indices for steel fibre reinforced shotcrete, Tunnelling and underground space technology, 17 (2002) 69-82.

Jenni, A; Holzer, L.; Zurbriggen, R.; Herwegh, M.; 2005, Influence of polymers on microstructure and adhesive strength of cementitious tile adhesive mortars, Cement and Concrete Research 35 (2005) 35–50.

Jenq, Y.S., Shah, S. P., 1986, Crack propagation in fibre-reinforced concrete, Journal of Structural Engineering, 1986, Vol.112, No.1, pp. 19-34.

Jenq, Y.S.; Shah, S. P.; 1985; Two-parameter fracture model for concrete, Journal of Engineering Mechanics, 1985, Vol.111, No.10, pp.1227-1241.

Johnston, C. D.; Zemp, R. W.; 1991, Flexural fatigue performance of steel fibre reinforced concrete. Influence of fibre content, aspect ratio, and type; ACI Materials Journal, v 88, n 4, pp. 374-383.

Kagaya,M.; Suzuki,T.; Kokubun,S.; Tokuda, H.; 2001, A study on mix proportions and properties of steel fibre reinforced roller-compacted concrete for pavements, (Translation from Proceedings of JSCE, No.669/V-50, February 2001).

Karihaloo, B.L., 1999, Size effect in shallow and deep notched quasi-brittle structures

Karihaloo, B.L.; Abdalla, H.M.; Xiao, Q.Z.; 2003, Size effect in concrete beams, Engineering Fracture Mechanics, v 70, n 7-8, pp. 979-993

Kazemi, M.T., Fazilah, F.; Ebrahiminezhand, M.A., 2007, Cohesive crack model and fracture energy of steel-fibre-reinforced-concrete notched cylindrical specimens, Journal of Materials in Civil Engineering, Vol. 19, No. 10, pp. 884- 890.

Kazimierowicz-Frankowska, K., 2008, Comparison of stress and strain states in pavements with and without reflective cracks, Journal of Transportation Engineering, Vol. 134, No. 11, pp.483-492.

Klingbeil, N.W.; Beuth, J.L.; 1997, Interfacial fracture testing of deposit metal layers under four-point bending, Engineering Fracture Mechanics, Vol. 56, No.1, pp. 113-126.

Kohn, S.D.; Rollings, R.; 1988, Overlay design, Concrete Pavements, edited by Stock A.C., Elsevier applied science publisher LTD, New York, USA, 1988.

Koutselas, K. 2011, Sustainable 'Green' overlays for strengthening and rehabilitation of concrete pavements, PhD Thesis, Civil Engineering, Faculty of Engineering and Computing, Coventry University UK.

Kwon, S.H.; Zhao, Z. Shah, S.P.; 2008; Effect of specimen size on fracture energy and softening curve of concrete: Part II. Inverse analysis and softening curve; Cement and Concrete Research, 38 (2008) 1061–1069.

Laranjeira, F.; Molins, C., Aguado, A., 2010, Predicting the pullout response of inclined hooked steel fibres, Cement and Concrete Research, 40 (2010) 1471-1487.

Lau, D.; Büyüköztürk, O.; 2010, Fracture characterization of cement/epoxy interface affected by moisture, Mechanics of Materials, 42 (2010) 1031-1042.

Li, V.C., Chan, Y.M., 1994, Determination of interfacial debond mode for fibre-reinforced cementitious composites, Journal of Engineering Mechanics, Vol.120, No.4, pp. 707-719.

Li, V.C.; 1992, Performance driven design of fiber reinforced cementitious composites, Proceedings of the International Symposium on Fibre Reinforced Cement and Concrete, p 12, Fibre Reinforced Cement and Concrete.

Lindhagen, J.E.; Gamstedt, E.K; Berglund L.A.; 2000, Application of bridging-law concepts to short-fibre composites Part 3: Bridging law derivation from experimental crack profiles, Composites Science and Technology 60, 2883-2894.

Lok, T. S.; Pei, J. S.; 1998, Flexural behaviour of steel fibre reinforced concrete, Journal of Materials in Civil Engineering, v 10, n 2, p 86-97.

Maalej, M.; Li, V.C. ; 1994, Flexural strength of fibre cementitious composites, Journal of Materials in Civil Engineering, Vol. 6, No. 3, pp. 390-406.

Malysev, B.M.; Salganik, R.L.; 1965, The strength of adhesive joints using the theory of cracks, International Journal of Fracture, 1, 114-127.

Matos, P.P.L.; McMeeking, R.M.; Charalamides, P.G.; and Drory, D.; 1989, A method for calculating stress intensities in bimaterial fracture, International Journal of Fracture, 40, 313-322.

McCullough, B.F.; 1988, Criteria for the design and construction of continuously reinforced concrete pavement, Concrete Pavements, edited by Stock A.C., Elsevier applied science publisher LTD, New York, USA, 1988.

Meda, A.; Plizzari, G.A.; 2004, New design approach for steel fibre-reinforced concrete slabs-on-ground based on fracture mechanics, *ACI Structural Journal*, V. 101, No. 3, pp.1-6.

Mokarem, D.W.; Galal, K.A.; Sprinkel, M.M.; 2007. Performance evaluation of bonded concrete pavement overlays after 11 Years, Transportation Research Record, Vol. 2007, No. 2005, pp. 3-10.

NCPTC (National Concrete Pavement Technology Centre), USA; 2008, Guide to concrete overlays (second edition), September. 2008.

NCPTC (National Concrete Pavement Technology Centre), USA; 2010, Guide for roller-compacted concrete pavements, Aug. 2010.

NCPTC, USA, 2008,*'Guide to Concrete Overlays'*, Second edition, National Concrete Pavement Technology Centre, USA, September 2008.

Neocleous, K.; Angelakopoulos, H.; Pilakoutas, K.; Guadagnini, M.; 2011, Fibre-reinforced roller-compacted concrete transport pavements, Proceedings of the Institution of Civil Engineers, UK, Transport 164, May 2011 Issue TR2, pp.97-109.

Neocleous, K.; Tlemat, H.; Pilakoutas, K.2006, Design issues for concrete reinforced with steel fibres, including fibres recovered from used tires, Journal of Materials in Civil Engineering, v 18, n 5, p 677-685.

Nevill, A.M.; 1986, Properties of Concrete, Harlow: Longman Scientific & Technical, UK.

Nguyen, D. L.; Kim, D. J.; Ryu, G. S.; Koh, K. T.;2013, Size effect on flexural behaviour of ultra-high-performance hybrid fibre-reinforced concrete, Composites Part B:Engineering, v 45, n 1, p 1104-1116.

Nour, A.; Massicotte, B.; Montaignac, R.D.; Charron, J.P.; 2011, Derivation of a crack opening deflection relationship for fibre reinforced concrete panels using a stochastic model: Application for predicting the flexural behaviour of round panels using stress crack opening diagrams, Cement and Concrete Research, 41 (2011) 964-974.

Ohama, Y., 1995, Handbook of Polymer-modified concrete and mortar-Properties and Process Technology, Noyes Publications, USA.

Ohama,Y.; 1997, Recent progress in concrete-polymer composite, Advanced cement based materials, 5, pp.31-40.

Olesen, J.F.; 2001, Fictitious crack propagation in fibre-reinforced concrete beams, Journal of Engineering Mechanics, Vol. 127, No. 3, pp.272-280.

Parmerter, R.R. 1976, A method for calculating the reduction in stress intensity factor due to an elastic foundation, Engineering Fracture Mechanics, 1976, Vol.8, pp.539-546.

Parmerter, R.R.; Mukherji, B. 1975, Stress intensity factors for a notched beams on an elastic foundation, Engineering Fracture Mechanics,1975, Vol.7, pp.291-298.

Paskova, T.; Meyer, C.; 1997, Low-cycle fatigue of plain and fibre-reinforced concrete, ACI Materials Journal, V.94, No.4, pp 273-284.

Quinn, G.D, 2003, Weibull strength scaling for standardized rectangular flexure specimens. Journal of American Ceramics Society, 86:508-10.

Ramsamooj, D.V.; 1999, Stresses in jointed rigid pavements, Journal of Transportation Engineering, March/April 1999, Vol. 125, No.2, pp101-107.

Richard L.; Burden, J.; Douglas F., 2005, Numerical Analysis, 8th edition, Thomson Brooks/Cole.

RILEM, 1991, Fracture mechanics test method for concrete, Report 5, Edited by Shah, S.P. and Carpinteri, A.

RILEM, Committee on Fracture mechanics of concrete, 1985,Test methods: Determination of the fracture energy of mortar and concrete by means of three-point bend test on notched beams, Materials and Structures, Vol.10, No.106, 1985,pp. 285-290.

Rodezno, M.C.; Kaloush, K.E.; 2010, Effect of different dosage of polypropylene fibres in thin white-topping concrete pavements, ACI Materials Journal, V.107, N0.1, Jan.-Feb. 2010.

Rybicki, E.F.; Kanninen, M.F.; 1977, A finite element calculation of stress intensity factors by a modified crack closure integral, Engineering Fracture Mechanics, 1977, 9:931-938.

Ryu, S.W.; Won, H.; Choi, S. ; Won, M.C.; 2013, Continuously reinforced bonded concrete overlay of distressed jointed plain concrete pavements, Construction and Building Materials 40 (2013) 1110–1117.

Saleh, M.F.; Yeow, T.; MacRae, G.; Scott, A.; 2012, Effect of steel fibre content on the fatigue of behavior of steel fibre reinforced concrete, 7th RILEM International Conference on Cracking in Pavements, Edited by Scarpas, et al, pp.815-825.

Satoh, A.; Yamada, K.; Ishiyama, S.; 2010, A discussion on major factors affecting crack path of concrete-to-concrete interfacial surfaces, Engineering Fracture Mechanics 77 (2010) 2168–2181.

Scarpas, A.T.; Kringos, N.; Al-Qadi, I.L.; Loizos, A.; 2012, Preface, 7th RILEM International Conference on Cracking in Pavements, Vol.1.

Shi, X.Q.; Zhang, X.R.; Pang, J.H.L.; 2006, Determination of interface fracture toughness of adhesive joint subjected to mixed-mode loading using finite element method, International Journal of Adhesion and Adhesives, 26 (2006) 249-260.

Singh, S.P.; Kaushik, S.K.; 2001, Flexural fatigue analysis of steel fibre-reinforced concrete, ACI Materials Journal, Vol.98, No.4, pp. 306-312.

Slowik, V.; Villmann, B.; Bretschneider, N.; Villmann, T.; 2006, Computational aspects of inverse analysis for determining softening curves of concrete, Computer. Methods in Applied Mechanics and Engineering, 195 (2006) 7223–7236.

Soares, J.B.; Tang, T.; 1998, Bimaterial Brazilian specimen for determining interfacial fracture toughness, Engineering Fracture Mechanics, Vol. 59, No. 1, pp. 57-71, 1998.

Song, G.M.; Zhou, Y.; Sun. Y.; 1999, Modeling of fibre toughening in fibre-reinforced ceramic composites, Ceramics International, (25) 1999 257-260.

Sousa, J.L.A.O., Gettu, R. 2006, Determining the tensile stress-crack opening curve of concrete by inverse analysis, Journal of Engineering Mechanics, Vol. 132, No. 2, pp.141–148.

Stang, H.; Oleson, J.F.; 1998, On the interpretation of bending test on FRC materials, Proceedings, FRAMCOS-3, Fracture Mechanics of Concrete Structures, H. Mihashi and K. Rokugo, eds. Vol. I, Aedificatio Publisher, Freiburg, Germany, 511-520.

Stang, H.; Oleson, J.F.;2000, A fracture mechanics based design approach to FRC, Proceedings, 5th RILEM Symposium on Fibre-reinforced Concretes (FRCs), BEFIB 2000.

Stroeven, P.; Shah, S.P.; deHaan, Y.M.; and Bouter, C.; 1978, Pull-out tests of steel fibres, Proceedings of International Symposium, RILEM-ACI-ASTM, Sheffield, England, pp.345-353.

Sun, C.T. and Qian, W.; 1997, The use of finite extension strain energy release rates in fracture of interfacial cracks, International Journal of Solids and Structures, Vol.34, No.20, pp. 2595-2609.

Sun, C.T.; Jih, C.J.; 1987, On strain energy release rates for interfacial cracks in biomaterial media, Engineering Fracture Mechanics, Vol. 28, No. 1, pp. 13-30.

Sun, W.; Guo, J. Yan, Y.; 1996, Study of the fatigue performance and damage mechanism of steel fibre reinforced concrete, ACI Materials Journal, Vol.93, No.3, pp. 206-211.

Tada, H.; Paris, P.C.; Irwin, G.R.; 2000, The stress analysis of cracks handbook, (third edition), Professional Engineering Publishing.

Texas Department of Transportation, 2011, Pavement Design Guide, USA.

Tong, J.; Wong, K. Y.; Lupton, C. 2007, Determination of interfacial fracture toughness of

bone–cement interface using sandwich Brazilian disks, Engineering Fracture Mechanics 74 (2007) 1904–1916

Tschegg, E.K.; Tan, D.M.; Kircher, H.O.K; Stanzl, S.E.; 1993, Interfacial and sub-interfacial fracture in concrete, Acta, Metallurgica et Materialia, Vol.41, No.2, pp.569-576.

Valentine, D.T.; Hanhn, B.D.; 2007, Essential MATLAB for engineers and scientists (Electronic book), 3th edition.

Visalvanich, K.; Naaman, A.; 1983,Fracture model for fibre reinforced concrete, ACI Materials Journal, v 80, n 2, pp.128-138.

Wang, J.-S.; Suo, Z.; 1990, Experimental determination of interfacial toughness curves using Brazil-nut-sandwiches, Acta, metal, materials, Vol. 38, No. 7, pp. 1279 – 1290.

Watanabe, T.; 2009, Interfacial fracture mechanics approach to delamination resistance between cement-based materials, Journal of Engineering Mechanics, Vol. 135, No.10, pp.1198-1205.

Xiao, Q.Z., Karihaloo, B.L., 2002, A Proximate Green's functions for singular and higher order terms of an edge crack in a finite plate, Engineering Fracture Mechanics, 69 (2002), 959-981.

Xie, D.; Biggers Jr., S.B.; 2006, Strain energy release rate calculation for a moving delamination front of arbitrary shape based on the virtual crack closure technique. Part II: Sensitivity study on modelling details, Engineering Fracture Mechanics 73 (2006).786–801.

Xu, S.; Reinhardt, H.W.; 1999, Determination of double-K criterion for crack propagation in quasi-brittle fracture, Part II: Analysis evaluating and practical measuring methods for three-point bending notched beams, International Journal of Fracture, 98: 151 - 177, 1999.

Zhang, J.; Stang, H.; 1998b, Fatigue performance in flexure of fibre reinforced concrete, ACI Materials Journal, Vol. 95, No.1, pp58-67.

Zhang, J.; Ju, X.; 2011, Investigation on stress-crack opening relationship of engineering cementitious composites using inverse approach, Cement and Concrete Research, 41 (2011) 903 - 912.

Zhang, J.; Leung, K.Y.; Xu, S.; 2010, Evaluation of fracture parameters of concrete from

bending test, Materials and Structures, Vol.43, No.6, pp. 857-874.

Zhang, J.; Li, V.C., 2004, Simulation of crack propagation in fibre-reinforced concrete by fracture mechanics, Cement and Concrete Research, 34 (2004) 333-339.

Zhang, J.; Stang, H., 1998a, Applications of stress crack width relationship in predicting the flexural behavior of fibre-reinforced concrete, Cement and Concrete Research, Vol. 28, No. 3, pp. 439-452.

Appendix

Construction and Building Materials 48 (2013) 333–341

Contents lists available at SciVerse ScienceDirect

Construction and Building Materials

journal homepage: www.elsevier.com/locate/conbuildmat

A new mix design method for steel fibre-reinforced, roller compacted and polymer modified bonded concrete overlays

Yougui Lin, John N. Karadelis *, Yi Xu

Department of Civil Engineering Architecture and Building, Faculty of Engineering and Computing, Coventry University, W Midlands CV1 5FB, UK

HIGHLIGHTS

- A new mix design method for polymer modified, bonded concrete overlays is proposed.
- Main requirements for the mix were: roller compactability and paver placeability.
- Optimal water content was a key element for the roller-compacted, concrete overlay.
- The modified light compaction method (M-L) guarantees high strength and good bond.

ARTICLE INFO

Article history:
Received 4 February 2013
Received in revised form 20 May 2013
Accepted 14 June 2013
Available online 31 July 2013

Keywords:
Steel fibre reinforced
Roller compacted
Polymer modified
Bonded concrete overlays

ABSTRACT

For roller compacted concrete used in pavements, optimal water content is one of main concerns for mix design. However the mix design method aiming at achieving both high bond strength and roller *compactability* is not available so far. The modified Proctor compaction method and modified Vebe method were investigated and found to be inappropriate to the type of mixes in terms of durability. In this paper a method for determining optimal water content is proposed for steel fibre-reinforced, roller compacted and polymer modified bonded concrete overlays. Two types of mixes suitable for asphalt paver placement and roller compaction were developed: They were the SBR and the SBR–PVA hybrid polymer modified cement concrete mixes with the optimal water contents determined by the proposed method. Both mixes achieved good bond with the old concrete substrate.